Sidra Iftekhar

SYNTHESIS OF HYBRID BIO-NANOCOMPOSITES AND THEIR APPLICATION FOR THE REMOVAL OF RARE EARTH ELEMENTS FROM SYNTHETIC WASTEWATER

ACTA UNIVERSITATIS LAPPEENRANTAENSIS 856

Sidra Iftekhar

SYNTHESIS OF HYBRID BIO-NANOCOMPOSITES AND THEIR APPLICATION FOR THE REMOVAL OF RARE EARTH ELEMENTS FROM SYNTHETIC WASTEWATER

Dissertation for the degree of Doctor of Science (Technology) to be presented with due permission for public examination and criticism in the Mikkeli University Consortium (MUC) auditorium, Mikkeli, Finland on the 3rd of June, 2019, at noon.

Acta Universitatis
Lappeenrantaensis 856

Supervisors Professor Mika Sillanpää
LUT School of Engineering Science
Lappeenranta-Lahti University of Technology LUT
Finland

Dr. Varsha Srivastava
LUT School of Engineering Science
Lappeenranta-Lahti University of Technology LUT
Finland

Reviewers Professor Koen Binnemans
Department of Chemistry
Katholieke Universiteit (KU) Leuven
Belgium

Professor Karen Hudson-Edwards
Camborne School of Mines
University of Exeter
United Kingdom

Opponent Professor Marie-Odile Simonnot
Laboratoire Réactions et Génie des Procédés (LRGP)
Université de Lorraine - CNRS (UMR 7274)
France

ISBN 978-952-335-378-7
ISBN 978-952-335-379-4 (PDF)
ISSN-L 1456-4491
ISSN 1456-4491

Lappeenranta-Lahti University of Technology LUT
LUT University Press 2019

Abstract

Sidra Iftekhar
Synthesis of hybrid bio-nanocomposites and their application for the removal of rare earth elements from synthetic wastewater
Lappeenranta 2019
93 pages
Acta Universitatis Lappeenrantaensis 856
Diss. Lappeenranta-Lahti University of Technology LUT
ISBN 978-952-335-378-7, ISBN 978-952-335-379-4 (PDF), ISSN-L 1456-4491, ISSN 1456-4491

In recent decades, the application of rare earth elements (REEs) has become apparent in numerous technological sectors. The gap in the supply and demand of REEs, as well as the increasing pollution of REEs, has raised the need for the removal and recovery of these elements from both secondary sources and waste streams. Hybrid bio-nanocomposites synthesised using various combinations of organic-inorganic matrices have the potential to remove and recover REEs from aqueous medium. The research focuses on the synthesis of five different bio-nanocomposites using different organic-inorganic matrices, the characterisation of prepared bio-nanocomposites, their application for the removal of REEs, the kinetic, isotherm and thermodynamic studies, the determination of possible REEs adsorption mechanism on bio-nanocomposites and their regeneration abilities.

The bio-nanocomposites, including cellulose intercalated zinc-aluminium layered double hyrdoxides (CL-Zn/Al LDH), sulfuric acid modified cellulose based silica nanocomposite (CLN/SiO_2), Gum Arabic grafted polyacrylamide based silica (GA-g-PAM/SiO_2), exfoliated biopolymeric-LDH (GA-LDH) and LDH encapsulated in xanthan gum anchored by metal ions (M@XG-ZA) nanocomposites were used to study the adsorptive behaviour towards REEs. The fusion of organic-inorganic matrices combined the advantages of both matrices. The application of CL and GA with LDH for the removal of REEs exhibited promising results compared to LDH encapulation in XG, modification of CL and grafting of PAM chain on GA backbone with SiO_2 incorporation. The selection of organic-inorganic matrix and method of synthesis is very important.

The adsorption assays for the removal of REEs were performed in batch mode in order to attain maximum removal. The adsorption of REEs was pH dependent and a fast removal of REEs was indicated by all bio-nanocomposites. The knowledge about surface properties, nature and adsorption mechanism was attained by using different adsorption isotherm and kinetic models. Moreover, the adsorption mechanism, adsorption in a multi-component system with or without competing ions and intra-series adsorption behaviour were also discussed. On the whole, the bio-nanocomposites exhibited the potential for the removal and recovery of REEs.

Keywords: rare earth elements, bio-nanocomposites, hybrids, cellulose, gum Arabic, xanthan gum, layered double hydroxides, silica, adsorption, adsorption kinetics, adsorption isotherms, thermodynamics, adsorption mechanism, intra-series adsorption

Acknowledgements

The research work of this thesis was conducted at the Department of Green Chemistry, Lappeenranta-Lahti University of Technology LUT, Mikkeli during March 2016-November 2017 and financially supported by LUT graduate school.

Firstly, I am sincerely grateful to my supervisor Prof. Mika Sillanpää for his support, motivation and providing me with a platform to perform this research. I could not have envisioned having a better mentor for my doctoral studies. I learned so much from you and will always admire your exceptional research and management skills. I would like to thank Dr. Varsha Srivastava for her devoted help and precious guidance in the experimental work, data analysis, writing of manuscripts and for being my officemate. I would not have been able to work on my research this far without you.

I express my sincere gratitude to Prof. Dr. Koen Binnemans and Prof. Karen Hudson-Edwards, the reviewers of my thesis, for their valuable comments and suggestions, which are helpful in improving the thesis.

I would like to thank all the members of DGC for their help and support. It has been an honour and pleasure to conduct research with such creative and inspiring people. Special thanks to Deepika, Indu, Zhao, Sarra and Bhairavi for all the happy moments and joy. I would like to thank Sanna Tomperi for administration help. I am also thankful to my colleagues from the Environmental Engineering Department, UET, Taxila, Pakistan for being in touch and especially to M. Bilal Asif, Shamas Tabraiz and Rasikh Habib for their help and encouragement throughout my PhD study.

Lastly, to my parents, thank you for being my champions throughout the past 30 years. Your unconditional love and support has meant the world to me. I hope that I have made you proud. I would like to thank my family, especially siblings and in-laws for their support, love, understanding and encouragement. Saving the most important for last, I wish to give my heartfelt thanks to my husband, Noman Ashraf, whose unconditional love, patience, and continual support of my academic endeavours over the past several years enabled me to complete this thesis.

Finally, to my son, Shazain Ashraf, my little bundle of joy and laughter, your birth has brightened up my world. I am so blessed to have you both by my side.

Sidra Iftekhar

Mikkeli, September 2018

Contents

List of Publications

I. **Iftekhar, S.**, Srivastava, V., & Sillanpää, M., Synthesis and application of LDH intercalated cellulose nanocomposite for separation of rare earth elements (REEs), *Chemical Engineering Journal* 309 (2017) 130-139.

II. **Iftekhar, S.**, Srivastava, V., & Sillanpää, M., Enrichment of lanthanides in aqueous system by cellulose based silica nanocomposite, *Chemical Engineering Journal* 320 (2017) 151-159.

III. **Iftekhar, S.**, Srivastava, V., Casas, A., & Sillanpää, M., Synthesis of novel GA-g-PAM/SiO2 nanocomposite for the recovery of rare earth elements (REE) ions from aqueous solution, *Journal of Cleaner Production* 170 (2018) 251-259.

IV. **Iftekhar, S.**, Srivastava, V., Ramasamy, D. L., Naseer, W. A., & Sillanpää, M., A novel approach for synthesis of exfoliated biopolymeric-LDH hybrid nanocomposites via in-situ coprecipitation with gum Arabic: Application towards REEs recovery, *Chemical Engineering Journal* 347 (2018) 398-406.

V. **Iftekhar, S.**, Srivastava, V., Hammouda, S. B., & Sillanpää, M., Fabrication of novel metal ion imprinted xanthan gum-layered double hydroxide nanocomposite for adsorption of rare earth elements, *Carbohydrate polymers* 194 (2018) 274-28.

VI. **Iftekhar, S.**, Ramasamy, D. L., Srivastava, V., Asif, M. B., Sillanpää, M., Understanding the factors affecting the adsorption of Lanthanum using different adsorbents: A critical review, *Chemosphere 204* (2018) 413-430.

The author's contribution in the publications

I. The author conducted all the experiments, analysed the data and had the main responsibility of writing the manuscript.

II. The author conducted all the experiments, analysed the data and had the main responsibility of writing the manuscript.

III. The author conducted or supervised all the experiments, analysed the data and had the main responsibility of writing the manuscript. Alba Casas helped with some adsorption experiments.

IV. The author conducted or supervised all the experiments, analysed the data and had the main responsibility of writing the manuscript. Waqar Ahmad Naseer helped with some adsorption experiments.

V. The author conducted all the experiments, analysed the data and had the main responsibility of writing the manuscript.

VI. The author had the main responsibility of writing the manuscript.

Other Publications by the Author

I. **Iftekhar, S.**, Farooq, M. U., Sillanpää, M., Asif, M. B., Habib, R., Removal of Ni (II) Using Multi-walled Carbon Nanotubes Electrodes: Relation Between Operating Parameters and Capacitive Deionization Performance, *Arabian Journal for Science and Engineering 42*-1 (2017) 235-240.

II. Srivastava, V., **Iftekhar, S.**, Wang, Z., Babu, I., Sillanpää, M., Synthesis and application of biocompatible nontoxic nanoparticles for reclamation of Ce3+ from synthetic wastewater: Toxicity assessment, kinetic, isotherm and thermodynamic study, *Journal of Rare Earths* (2018). DOI: 10.1016/j.jre.2018.03.005.

III. **Iftekhar, S**., Küçük, M. E., Srivastava, V., Repo, E., Sillanpää, M., Application of zinc-aluminium layered double hydroxides for adsorptive removal of phosphate and sulfate: Equilibrium, kinetic and thermodynamic, *Chemosphere* 209 (2018) 470-479.

IV. Habib, R., Asif, M. B., **Iftekhar, S.**, Khan, Z., Gurung, K., Srivastava, V., Sillanpää, M., Influence of relaxation modes on membrane fouling in submerged membrane bioreactor for domestic wastewater treatment, *Chemosphere 181* (2017) 19-25.

V. Hammouda, S. B., Zhao, F., Safaei, Z., Srivastava, V., Ramasamy, D. L., **Iftekhar, S.**, Sillanpää, M., Degradation and mineralization of phenol in aqueous medium by heterogeneous monopersulfate activation on nanostructured cobalt based-perovskite catalysts ACoO3 (A= La, Ba, Sr and Ce): Characterization, kinetics and mechanism study, *Applied Catalysis B: Environmental 215* (2017) 60-73.

VI. Gao, B., Safaei, Z., Babu, I., **Iftekhar, S.**, Iakovleva, E., Srivastava, V., Doshi, B., Hammouda, S.B., Kalliola, S., Sillanpää, M., Modification of ZnIn2S4 by anthraquinone-2-sulfonate doped polypyrrole as acceptor-donor system for enhanced photocatalytic degradation of tetracycline, *Journal of Photochemistry and Photobiology A: Chemistry 348* (2017) 150-160.

VII. Asif, M. B., Habib, R., **Iftekhar, S.**, Khan, Z., Majeed, N., Optimization of the operational parameters in a submerged membrane bioreactor using box behnken response surface methodology: Membrane fouling control and effluent quality, *Desalination 82* (2017) 26-38.

VIII. Ramasamy, D. L., Puhakka, V., **Iftekhar, S.**, Wojtuś, A., Repo, E., Hammouda, S. B., Iakovleva, E., Sillanpää, M., N-and O-ligand doped mesoporous silica-chitosan hybrid beads for the efficient, sustainable and selective recovery of rare earth elements (REE) from acid mine drainage (AMD): Understanding the significance of physical modification and conditioning of the polymer, *Journal of hazardous materials 348* (2018) 84-91.

IX. Hamida, S. B., **Iftekhar, S.**, Ambat, I., Srivastava, V., Sillanpää, M., Amri, Z., Ladhari, N., Dry and wet ozonation of denim: Degradation products, reaction mechanism, toxicity and cytotoxicity assessment, *Chemosphere 203* (2018) 514-520.

X. Gao, B., **Iftekhar, S.**, Srivastava, V., Doshi, B., Sillanpää, M., Insights into the generation of reactive oxygen species (ROS) over polythiophene/ZnIn2S4 based on different modification processing, *Catalysis Science & Technology 8*-8 (2018) 2186-2194.

XI. Wang, Z., Srivastava, V., **Iftekhar, S.**, Ambat, I., Sillanpää, M., Fabrication of Sb2O3/PbO photocatalyst for the UV/PMS assisted degradation of carbamazepine from synthetic wastewater, *Chemical Engineering Journal*, 354 (2018) 663-671.

XII. Hammouda, S.B., Salazar, C., Zhao, F., Ramasamy, D.L., Laklova, E., **Iftekhar, S.**, Babu, I., Sillanpää, M., Efficient heterogeneous electro-Fenton incineration of a contaminant of emergent concern-Cotinine-in aqueous medium using the magnetic double perovskite oxide Sr2FeCuO6 as a highly stable catalyst: Degradation kinetics and oxidation products, *Applied Catalysis B: Environmental*, 240 (2019) 201-214.

XIII. Ramasamy, D.L., Puhakka, V., Doshi, B., **Iftekhar, S.** and Sillanpää, M., Fabrication of carbon nanotubes reinforced silica composites with improved rare earth elements adsorption performance, Chemical Engineering Journal, 365 (2019) 291-304.

Nomenclature

List of Symbols

A	Temkin isotherm constants	L/g
B	Constant related to heat of sorption	J/mol
C	Intra-particle diffusion constant	-
C_f	Equilibrium concentrations of REEs	mg/L
C_o	Initial concentrations of REEs	mg/L
G	Gibbs free energy	kJ/mol
H	Enthalpy	kJ/mol
k_1	Rate constants for pseudo first order	min^{-1}
k_2	Rate constants for pseudo second order	g mg^{-1} min^{-1}
K_c	Thermodynamic equilibrium constant	L/g
K_e	Elovich isotherm constants	L/mg
K_f	Freundlich isotherm constants	L/mg
K_L	Langmuir isotherm constants	L/mg
M	Mass of bio-nanocomposite	g
n	Freundlich heterogeneity factor	-
pH_{zpc}	Isoelectric point	-
Q_0	Maximum adsorption capacity	mg/g
q_e	Equilibrium adsorption capacity	mg/g
q_t	Adsorption capacity at time t	mg/g
R^2	Correlation coefficient	-
RE	Removal efficiency	%
S	Entropy	J/mol/K
t	Time	min
T	Temperature	K
V	Volume of solution	L
wt.	Weight percentage	%

Abbreviations

Acac	Acetylacetone
Adogen 464	Methyltrialkyl(C8-C10)ammonium chloride
ALG-PGA	Alginate polyglutamic acid
Aliquat 336	Tri-octyl methylammonium chloride
AMD	Acid mine drainage water
AMPS	2-acrylamido 2-methyl propane sulfonic acid
APTES-C3-PAN	APTES silica-chitosan-PAN
CA 100	Sec-nonylphenoxy acetic acid
CA 12	Sec-octylphenoxy acetic acid
CA@Fe_3O_4	Citric acid functionalised magnetic nanoparticles
CATU	Acryloylthiourea crosslinked chitosan
CL	Cellulose
CLN/SiO_2	Modified cellulose based silica nanocomposites
CL-Zn/Al LDH	Cellulose intercalated zinc-aluminium layered double hydroxides
CMC-g-PAA	Cellulose grafted polyacrylic acid hydrogel
CMCH	O-carboxymethyl chitosan
CTS-g-PAA/APT	Acrylic acid grafted chitosan with attapulgite
Cyanex 272	Di-2,4,4,-trimethylpentyl phosphinic acid
Cyanex 301	Di-2,4,4-trimethylpentyl-dithiophosphinic acid
Cyanex 302	Di-2,4,4-trimethylpentyl-monothiophosphinic acid
Cyanex 921	Tri-n-octylphosphine oxide
Cys@CHI-magnetic	Cysteine functionalised chitosan magnetic nano-based particles
D2EHPA	Di-2-ethylhexyl phosphoric acid
DBBP	Dibutylbutylphosphonate
DETA	Dithylenetriamine
DETA@CHI-magnetic	Diethylenetriamine functionalised chitosan magnetic nano-based particles

DGA-g-PAA	Polyacrylic acid grafted carboxylic acid functionalised diatomite
DODGAA	*N*, *N*-dioctyldiglycol amic acid
DPTA	Dithylenetriaminepentaacetic acid
EDTA	Ethylenediaminetetra acetic acid
EDTA Cu-Al LDH	Ethylenediaminetetra acetic acid intercalated Cu-Al layered double hydroxide
EDTA-β-CD	EDTA-β-cyclodextrin
EHEHPA	2-ethylhexylphosphonic acid mono-2-ethylhexyl ester
EnSA	Ethylenediaminepropylesalicylaldimine
Fe_3O_4/CS	Magnetite nanoparticles/chitosan composites
Fe_3O_4@Alg-CHI	Magnetic calcium alginate beads
Fe_3O_4@Ca-Alg	Magnetic calcium alginate-chitosan beads
Fe_3O_4@CD	Cyclodextrin magnetic composite
Fe_3O_4@CMC	Carboxymethyl cellulose modified Fe_3O_4
Fmoc-SBA-15	Lysine modified silica
GA	Gum Arabic
GA5MA	Gum Arabic exfoliated LDH
GA-g-PAM/SiO_2	Gum Arabic grafted polyacrylamide based silica nanocomposites
GLA-chit	Glutaraldehyde crosslinked chitosan
HDEHP	Di-2-ethylhexyl phosphoric acid
HDH	HemiDiHydrate
HEHEHP	2-ethylhexylphosphonic acid mono-2-ethylhexyl ester
HEOPPA	1-hexyl-4-ethyloctyl-isopropylphosphonic acid
HESI	N-(2-hydroexyethyl) salicylaldimine
HH	Calcium sulfate hemihydrate
HMBP-ED	Poly (2-hydroxy-4-methoxybenzophenone) ethylene
HPC-g-PAA/APT	Acrylic acid grafted hydroxypropyl cellulose with attapulgite
HREEs	Heavy rare earth elements
IDAAR	Imino-diacetic acid resin

IE	Ion exchange
Ionquest 801	2-ethylhexylphosphonic acid mono-2-ethylhexyl ester
IUPAC	International union of pure and applied chemistry
KCL-g-PAM/HA	Poly(methylacrylate) grafted kenaf cellulose based poly(hydroxamic acid) ligand
LDH	Layered double hydroxide
Ln	Lanthanides
LREEs	Light rare earth elements
M@XG-ZA	Metal ion anchored xanthan gum encapsulated LDH
MAH	Maleic anhydride
MBA	N,N-methylenebisacrylamide
MePhPTA	N-methyl-N-phenyl-1,10-phenanthroline-2-carboxamide
MNSP	Silica modified maleic anhydride
P229	Di-2-ethylhexylphosphinic acid
P507	2-ethylhexylphosphonic acid mono-2-ethylhexyl ester
PAA	Polyacrylic acid-silica hydrogel nanofibres
PAA-S HNFs	Polyacrylic acid
PAN	1-(2-pyridylazo)-2-naphthol
PC88A	2-ethylhexylphosphonic acid mono-2-ethylhexyl ester
PCM-chit	Poly(aminocarboxymethylation) chitosan
PEI-CNC	Polyethylenimine-cross-linked cellulose
REEs	Rare earth elements
REO	Rare earth oxides
SA	N-propyl salicylaldimine
SBA-15-ZMVP	11-molybdo-vanadophosphoric acid supported on Zr modified silica
SX	Solvent extraction
TBP	Tri-n-butyl phosphate
TEOS	Tetraethylene-ortho-silicate
TEPA	Tetraethylenepentaamine

Thio-CL	Thiourea functionalised cellulose
TOPO	Tri-n-octylphosphine oxide
USGS	U.S. Geological Survey
VP-AMPS	2-acrylamido 2-methyl propane sulfonic acid onto polyvinylpyrilidone
XG	Xanthan gum
Zr@XG-ZA	Zirconium anchored xanthan gum encapsulated LDH

1. Introduction

According to International union of pure and applied chemistry (IUPAC), REEs consists of total 17 elements including scandium (Sc), yttrium (Y), lanthanum (La), cerium (Ce), praseodymium (Pr), neodymium (Nd), promethium (Pm), samarium (Sm), europium (Eu), gadolinium (Gd), terbium (Tb), dysprosium (Dy), holmium (Ho), erbium (Er), thulium (Tm), ytterbium (Yb) and lutetium (Lu) [1]. The series of elements are often termed as lanthanides (Ln) excluding Sc and Y [1]. These REEs are further subdivided into two main groups as per U.S. Geological Survey (USGS), the light rare earth elements (LREEs) also known as cerium sub-group and the heavy rare earth elements (HREEs) sometimes referred as yttrium sub-group [2, 3]. The LREEs consist of elements from La to Eu and HREEs includes elements from Gd to Lu as well as Y because its properties are like the other elements of HREE group [4]. On the other hand, Sc does not belong to either of these groups due to extraction from different ores and unique properties compared to other elements of the lanthanide series [5].

The term REEs is a misnomer [6]. Despite their name as rare earth, these elements are present in abundance in the earth crust especially in the upper crust [5]. The average occurrence of REEs in earth's crust varies from 150 to 200 ppm indicating that most of these elements are not rare at all [7-9]. The most abundant Ce is present in Earth's crust in quantities equal to that of Cu and Zn, likewise, La and Nd are more common than Pb. The Earth's crust is even more abundant for the scarcest of REEs, Lu and Tm compared to Se, Au, Ag, Pt and Cd [10-12]. Among REEs, Pm is the only element, which is very rare since it does not form stable isotopes [11, 13]. The crustal presence of HREEs is far lower than LREEs [14].

Nevertheless, the similar chemical properties of these REEs makes it difficult to separate. Except REEs, in periodic table other group of elements does not exhibit the similarity in properties [11]. The ionic radii vs atomic number trend of Ln is shown in Figure 1. Typically, REEs exists in the trivalent state, whereas, some of them also known to be present in oxidation state of divalent and tetravalent in chemical compounds. The elements including Ca, Th and U have almost similar ionic radii as REEs and makes the exploitation of REEs difficult from ores [14].

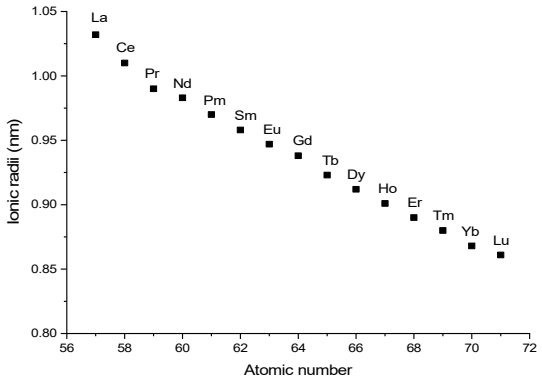

Figure 1: The ionic radii vs atomic number trend of lanthanides

1.1. Applications of REEs

REEs have been used in a wide variety of applications around the globe and are thus termed as "seed for technology" [15-17]. The REEs have astounding optical, magnetic, catalytically and electrical characteristics making them useful for several applications. The REEs market is divided into various sectors including magnets, catalysts, lasers, polishing, batteries, pigments, ceramics, metallurgy, glass etc. [14, 18]. The element specific uses of REEs are listed in Table 1.

1.2. Global resources, demand and problems

At present, the worldwide REEs are mainly extracted from deposits located in China (85%) and Australia (10%) [14]. The existing REE deposits are divided into primary and secondary rare earth deposits constituting off igneous rocks such as ion adsorption or placer deposits and sedimentary deposits including sand and clay, respectively [19-21]. The igneous rocks of alkaline nature in Russia are substantially rich with HREEs [22], whereas, the ion adsorption deposits in southern China are of low grade but contain a high content of easily mineable HREEs. Likewise, the placer deposits in Malaysia and India contain radioactive elements along with REEs [14]. Overall, around 200 minerals are known to contain REEs [23], out of which the primary sources include monazite, bastnaesite, xenotime, apatite, ion adsorption clay and loparite [3]. Monazite, bastnaesite and xenotime formed about 95% of REEs reserves [4, 24], whereas, rare earth oxides (REO) are

extracted from loparite in Russia only [25]. In addition, monazite, bastnaesite and loparite are main sources of LREEs while ion adsorption clay and xenotime are sources of HREEs [5]. The LREEs dominated deposits of monazite-carbonatite and bastnaesite-carbonatite are located in Australia and the US with an average grade of 14.8% and 12% REO, respectively [5]. The unique deposits of ion adsorption clays in southern China are formed by weathering of igneous rocks where REEs are adsorbed on the surface of clay as ions [23, 26]. Although, these deposits contain only 0.05-0.2% REO but extraction of REO from these are the most economical and easy [5].

Table 1: REEs applications in different products [4, 9, 20, 27]

REEs	Uses
Sc	Street lamps, high performance aerospace frameworks
Y	Catalysts, LED lights, screens of computers and television, cancer drugs, alloys
La	Battery electrodes, carbon lights i.e. projector and studio lights, camera lenses
Ce	Catalytic convertors, refining of crude oil, steel, coloured glass
Pr	Lasers, special goggles e.g. welding goggles, engine of aircrafts, strong magnets
Nd	Lasers, strong magnets, hybrid cars, wind turbines
Pm	Rarely found in nature
Sm	Lasers, cancer treatment, controlling rods of nuclear reactors
Eu	Colour screens of computers and television, controlling rods of nuclear reactors, fluorescent glass, genetic testing devices
Gd	Green phosphor in screens television, nuclear reactors, MRI and X-ray devices, alloys to increase their durability
Tb	Solar system, screens of computers and television, fuel cell
Dy	Transducers, hard disk devices, commercial lighting
Ho	Lasers, coloured glass, strong magnets
Er	Metallurgical instruments, coloured glass, optical fibres for amplification of signals
Tm	Superconductors, handheld X-ray devices, lasers
Yb	Lasers, stainless steel, ground sensing devices, catalysts
Lu	In oil refineries for cracking of hydrocarbons

All over the world, 851 deposits of REEs have been discovered but only 178 of these are exploited as per data published in 2017 [19]. The amount of REEs resources located globally is 478 Mt illustrated in Figure 2. The global REEs demand and consumption in 2010 was 136 Kt [28], which decreased slightly in 2012 due to increase in price and quotas on Chinese export [9], and the demand in 2016 was reported to be 160 Kt. The expected increases of 5% in global consumption of REEs was predicted in USGS, 2016 report [29]. China is the biggest supplier of REEs and dominated the global market. But overall reduction in their export quota of REEs from 65 Kt to 30 Kt put stress on the European market as 90% or raw REEs was imported from China. The increasing concern regarding the supplies of REEs led European Commission focus towards recycling of REEs along with extraction [30].

Although the crustal deposits have enough REEs to meet the world demand for hundred years, however, due to the challenges involved in the extraction of REEs from their ores recycling could be the most suitable option. On the other hand, only 1% of total REEs were recycled up to 2012 [29], which is very little compared to other recyclables.

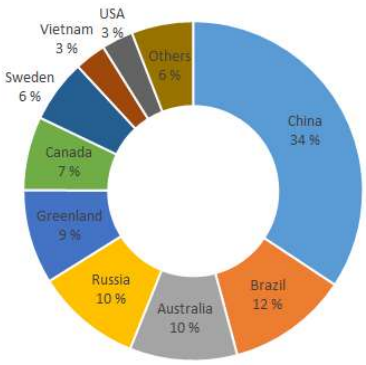

Figure 2: REE resources located globally (data used from ref [14])

The need for the recycling and recovery of REEs not only arises as an alternate to meet the global demand but also due to several environmental impacts related to their exploitation and increased applications. Most of the REEs deposits contain a high concentration of radioactive

elements like thorium and uranium. The extraction from such deposits involves excess water, chemicals and energy consumptions while long-term storage and disposal of such radioactive waste is another problem. Therefore, reusing and recycling REEs waste instead of extracting it from new mines seems to be a more environmentally friendly option [31]. However, the recycling techniques also have a lot of limitations and environmental impacts like excessive use of chemicals, high energy requirements and generation of waste chemicals and wastewater [5]. For instance, the recycling of REEs from magnets using a hydrometallurgical process involves the use of NaOH, H_2SO_4 and HF and thus generates a large amount of wastewater [31].

Researchers have, therefore, focused on the recovery and extraction of REEs from wastewater which could be another source of REEs like acid mine drainage water (AMD). AMD, acidic in nature is an outflow of coal and metal mines and known to contain a high amount of REEs and metals [32-34]. Many studies in past reported the recovery of metals or uranium by either bio-sorption or ion exchange resins [35, 36], however, the potential to recover REEs from AMD is mainly unexplored [34].

1.3. Technological developments for the recovery of REEs

The extensive application of REEs has become apparent in numerous agricultural and industrial technologies in recent decades [37]. This surge in the consumption of REEs has also produced huge amounts of wastes, if cannot dispose properly, it will seriously endanger human health and the ecosystem. The database related to the biological effect of REEs has been limited up to 1990 as the major technological development happened in the last two decades [38]. As a consequence of these activities, REEs have been detected in wastewater, runoff and aquatic ecosystems [39]. According to studies, large amount of REEs entered every year to Chinese agricultural systems [40]. Moreover, to improve animal growth REEs have been used as a food supplement and entered to the soil through animal waste [41]. Almost 10% of total REEs are soluble and migrate from the soil, polluting groundwater and other water bodies including rivers and lakes [42]. The bioaccumulation of REEs might occur in the ecosystem in the same way as many other heavy metals. Considering their relative toxicity, more studies related to REEs effects

was published in the last decade and after 2010. Moreover, the number of publications doubled in the last five years compared to last decade. This pointed towards the growing concern of community towards the health effects related to the bioaccumulation of REEs in the ecosystem, which are not yet known clearly. It is noteworthy that most of the studies published so far are related to La and Ce effects, fewer on Eu, Nd, Y, Tm and Yb and scanty numbers for other REEs [37, 42, 43]. The studies on animals also showed the adverse effects on liver, lungs and blood [43]. Thus, due to relative health effects with increasing REEs pollution, the need of removal also arose from water bodies and waste streams.

To date, several methods have been employed for the recovery and removal of REEs from waste streams including precipitation, solvent extraction, ion-exchange and adsorption. These methods were not only used for recovery purposes but also for removal of REEs from waste streams. As if not handled properly REEs waste will end up polluting the water and soil like many other metal ions and toxic chemicals which was extensively used in past. The relevant literature related to the methods is briefly discussed in the following sections.

1.3.1. Precipitation

Precipitation is the simplest and easiest technique used for the removal and recovery of metal ions from the aqueous medium. Compared to the conventional solvent extraction and ion-exchange method, precipitation is cheaper as process can be carried out with simpler equipment and less expensive chemicals [44]. The schematic illustration of the process is shown in Figure 3. The process is typically conducted by using NaOH, oxalic acid and ammonium oxalate and precipitates of REEs in the form of respective insoluble salts are obtained followed by calcination to get pure REE oxides. The method was mostly employed for the recovery of REEs from the leachates of fluorescent lamps, batteries and magnets [44].

For the precipitation of Y_2O_3 from lamp leachates, oxalic acid was used [45]. The yttrium recovered at pH 2.5-3 from cathode ray tube and lamp leachates showed low recovery efficiencies due to the co-precipitation of other metal ions viz. Zn, Ca, Fe, Ni, Pb, Mn, Co, Cr and Ca present in leachates [45]. The recovery improved up to 80% when leachate of fluorescent

lamp was precipitated using various hydration grades of oxalic acid and obtain purity of Y_2O_3 was 90-95% wt. with impurities (Fe and Ca) as low as 1.5% wt. [46]. Nd and Dy precipitation in the form of oxalates from leachates of magnets was explored by Rabatho et al. (2013) [47]. In another work, Nd and Dy were precipitated using oxalic acid and the impurities of Mn, Cu and Co were extracted using trihexyl(tetradecyl)phosphoniumchloride ionic liquid [48]. The studies were also conducted by a two-stage precipitation technique using oxalic acid and ammonia [49, 50].

The combine leaching-precipitation approach was studied for the recovery of REEs from batteries. The REEs was precipitated from sulfuric acid-based leachate at higher temperatures implying that increasing temperature resulted in lower solubility of REEs sulfates [51, 52]. Furthermore, to obtain the high purity products of La and Ce, pH was adjusted below 1.5 using alkaline solution to avoid precipitation of impurities like Fe which starts at pH 2.5-3 [53, 54]. Likewise, La, Ce, Pr and Nd were recovered by keeping pH 1.6 using a mixture of NaOH and Na_2CO_3 [55]. Solvent extraction was used to remove the impurities of Ni, Co, Mn, Zn, Fe [54] and Cu, Co and Ni [55]. REEs could be recovered via selective precipitation from leachates of magnets easily compared to lamps and batteries due to the presence of few metal ions [44]. Mostly Nd, Dy and Sm were recovered from such waste. Double-salt precipitation was investigated for recovery of Nd and Sm by Lee et al. (2013) and Koshimura (1987), respectively [56, 57]. Onoda and Nakamura (2014) reported 100% Nd recovery from Nd-Fe solution by selective phosphate precipitation [58].

To date, the method was only used for the extraction of REEs from its deposits and waste stream. No literature is available related to the application of this method for the recovery of REEs from AMD. The major disadvantages include low product purity due to the precipitation of other metal ions along with REEs from leachate and generation of secondary chemical waste.

1.3.2. Solvent Extraction

The physio-chemical properties of REEs make it difficult to separate from one another, however, methods like solvent extraction (SX) and ion-exchange (IE) which were developed and employed in the past for the recovery/separation of REEs. The SX is the most appropriate for the separation

of REEs due to its ability to deal with larger volumes [6]. SX is most commonly employed for the recovery/separation of REEs from leachates using different types of extractants including acidic (cationic), neutral (solvation) and basic (anionic) extractants [6, 59]. The details of various extractants used for REEs separation/recovery are given in Table 2.

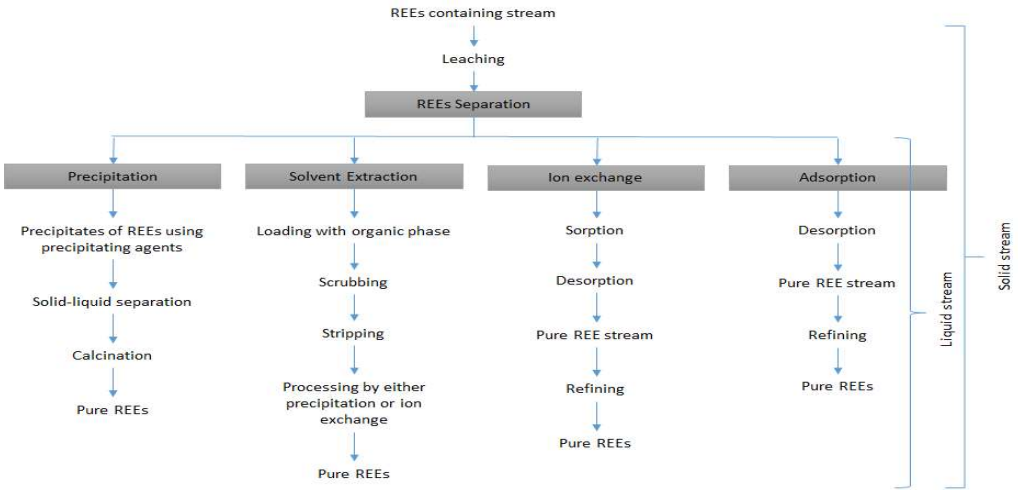

Figure 3: Schematic illustration of precipitation, solvent extraction, ion-exchange and adsorption process for REEs recovery from solid and liquid waste stream

Naphthenic acid was utilised for Y extraction from Ln [60], however, reagent losses and change in composition were reported due to solubility in water [61]. To overcome this, CA 12 [62] and CA 100 [63] were examined and it was concluded that, compared to Versatic 10, CA 100 extract REEs at lower pH [63]. Likewise, the addition of 2-bromo groups in alkanoic structures was effective for the recovery of REEs at a lower pH [64]. Other carboxylic based acid developed and used for REEs include cekanoic and neo-heptanoic [65]. D2EHPA is the most widely used extractant for REEs followed by HEHEHP (also marketed as EHEHPA, PC88A, P507) due to its extractability to strip REEs at lower acidities. Notably, extraction of REEs by various extractants like TBP, D2EHPA, HEHEHP etc. increased with increasing atomic number [6].

Table 2: Various extractants used for REEs separation

Extractants	Details
Acidic	
a. Carboxylic acids	Versatic acid e.g. Versatic 10 and Versatic 911 Naphthenic acids
b. Phosphorous acids	Phosphoric acids e.g. Di-2-ethylhexyl phosphoric acid (D2EHPA) Phosphonic acids e.g. 2-ethylhexylphosphonic acid mono-2-ethylhexyl ester (HEHEHP or EHEHPA, PC88A, P507) Phosphinic acids e.g. Di-2-ethylhexylphosphinic acid (P229), Cyanex 272 Monothiophosphorous acid e.g. Cyanex 302 Dithiophosphorous acid e.g. Cyanex 301
Neutral	Phosphorous ester e.g. Tri-n-butyl phosphate (TBP), Di-butylbutylphosphonate (DBBP), Cyanex 921, Cyanex 923, tri-n-octylphosphine oxide (TOPO)
Basic	Primary amines e.g. N1923, Primene JMT Quaternary amines e.g. Adogen 464, Aliquat 336

SX and precipitation can be used in combination, either precipitation can be carried out before or after SX from stripping solution. A high purity REEs could be obtained by this combination which was reported by Thakur (2013) in patent employing TBP, D2EHPA, Aliquat 336 and HEHEHP extractants [66].

Besides these conventional solvents, ionic liquids have also gained considerable attention due to flame resistance and negligible vapor pressure [67]. In addition, the bifunctional ionic liquids showed promising results for the extraction and recovery of REEs. The extractants for REEs were prepared from HEHEHP, HDEHP and Aliquat 336 and the results showed that bifunctional ionic liquids had better extractability compared to TBP and HDEHP but lower efficiency than Cynaex 923 [68]. DODGAA (*N*, *N*-dioctyldiglycol amic acid) was used to recover Eu, La, Ce and Y from lamp leachates, though, during stripping losses in ionic liquid and reduction in ability to extract both in sulfuric and nitric acid media after five cycles were observed [69].

Although, the process was used extensively for the extraction and recovery of REEs but has some major drawbacks including the release of solvent/extractant in water bodies. In addition, the process is efficient enough to recover REEs from the concentrated solution, whereas, when the concentration of REEs was lower (0.5-1 g/L), the method has limited competitiveness because of the contamination of the aqueous phase [70].

1.3.3. Ion-exchange

Although, for the recovery of REEs, solvent extraction is the preferred method, the application of ion exchange and chelating resins are used preferably over solvent extraction due to their ability to extract REEs from dilute leached solutions [71]. The other advantages of the process over solvent extraction include less waste generation, organic solvent free process, compacted equipment and easy operational process [72]. The process diagram is shown in Figure 3. These resins are mainly natural or synthetic and have an ability to exchange ions with REEs. The resins were prepared by using various types of functional groups viz. carboxylic, amines, organophosphorus, sulfonic etc. Among these, sulfonic and carboxylic acid based resins are referred as strong and weak acidic resins, respectively [35, 73]. Due to higher selectivity and large adsorption capacities of strong acidic cation exchange resins towards REEs had been investigated in past [74, 75]. Some of the cation exchange resins like D72, HMBP-ED (Poly(2-hydroxy-4-methoxybenzophenone) ethylene), HH (hemihydrate) and HDH (hemidihydrate) have been used recently by researchers to explore their potential for the recovery of REEs from waste streams and mining wastewater [76-79]. Likewise, the extractability of REEs with weak acidic resins containing carboxylic functional groups viz. D113-III and D152 resins was reported by Xiong et al. (2008, 2009) [80, 81]. Moreover, chelating resins containing iminodiacetic or phosphonic functional groups instead of sulfonic acid was also studied for REEs [82]. A higher affinity was shown by resins with phosphonic acid groups attached on copolymer matrix towards REEs recovery from acidic liquors [83, 84]. In addition, REEs adsorbed selectively over such resins compared to other trivalent metal ions such as Al, Bi and Cr [84]. IDAAR, an iminodiacetic resin, showed pH dependence for Yb adsorption [85]. Iminodiacetic chelating resin was also compared with amino-phosphonic, sulfonic-phosphonic and sulfonic resins for REEs extraction from sulfuric

acid medium. The performance of iminodiacetic chelating resin was superior compared to other resins [86].

A lot of researchers also investigated the application of strong (quaternary amine, type I and II) and weak (primary and tertiary amines) anion exchange resins with amines as a main functional group [87]. It was reported that compared to primary [72] and tertiary [88] pyridinium anionic resins over silica support, the resistance of quaternary pyridinium anionic resins was higher towards oxidising agents [89]. Another class of resins known as extraction resins (or Levextrel resins) has gained considerable attention as they offer the combined advantages of solvent extraction and ion-exchange processes. The high purity HREEs oxides were extracted with high yield by Wang et al. (1998, 2002) and Jia et al. (2004) using extraction resins containing HEOPPA, DEHPA, Cynaex 272 and Cynaex 302 [90-92].

The studies related to the removal and recovery of metal ions like uranium from AMD has been found, but the literature lacks sufficient information regarding the recovery of REEs via ion-exchange [34]. Due to difficulties in column scale-up, large feed volumes and initial large-scale separation steps, the method can be problematic and thus used preferably for the purification of the final concentrates [44].

1.3.4. Adsorption

Adsorption is one the most commonly used alternative technique for the treatment of wastewater containing heavy metal ions [93]. The method has been reported as the most economical, eco-friendly and efficient for the removal and recovery of REEs [15]. The application of various materials including low cost naturally occurring bio-based raw and modified materials [94, 95], agro-based materials [96], nanocomposites [97], hybrids prepared by modifying physically or chemically [98, 99], commercially available carbon-based materials [100] etc. have been reported in the literature for the removal and recovery of REEs. Figure 4 illustrated the publication data extracted from Scopus for various adsorbents extensively examined for the removal and recovery of REEs.

Recently, the application of bio-based materials consisting of natural polymers has gained wide attention due to their easy availability, low cost, biodegradability and non-toxicity [101]. Many research groups have investigated the use of raw bio-sorbents such as neem sawdust [102], *Platanus orientalis* and *Pinus brutia* leaf powder [103, 104], *Sargassum fluitans* and *Spirulina* [15, 105], fish scale [102], fresh water algae [106], prawn carapace [107], malt spent rootlets [108], orange, tangerine and grapefruit peels [109-111] etc. for the uptake of REEs from aqueous medium. In addition, to improve the adsorption ability of REEs, various bio-sorbents like cactus fibres [112, 113], rice husk [96], apricot shells [114], bamboo charcoal [115], carb shells [116], *agrobacterium sp.* [117], *Sargassum polycystum* [95] and *Sargassum* biomass [94] were also investigated after chemical modification. On the other hand, Figure 4 shows the increasing trend in the use of hybrids and nanocomposites for the removal of REEs.

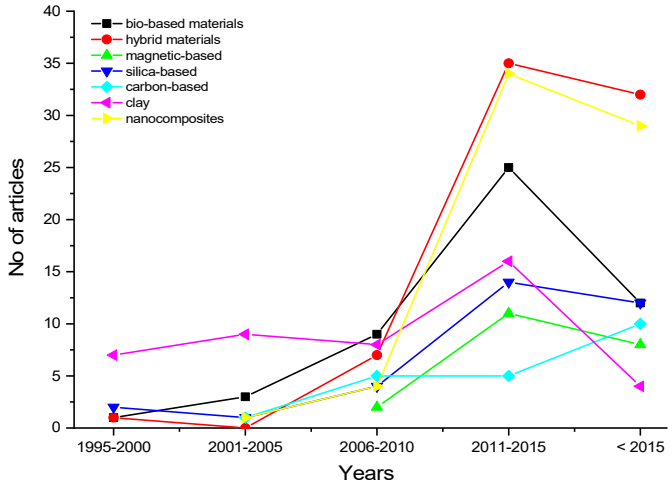

Figure 4: Extracted Scopus data of annual publications using the keywords: adsorption and REEs

Composites are the materials synthesised by combining different matrices like polymers or metals with some reinforcements (particles, fibres, whiskers etc.) [118]. The materials resulting from the combination of different matrices are often termed hybrids. These hybrids are generally synthesised by merging two matrices viz. inorganic-inorganic, inorganic-organic and organic-organic. The composite materials with at least one dimension in nano-range (nm) are referred as

nanocomposites [119]. Different hybrid and nanocomposites used for the removal of REEs are summarised in Table 3.

Table 3: Adsorption parameters and capacities for REEs on various hybrids and nanocomposites

Adsorbent	REEs	pH	Dose (g/L)	Time (h)	Conc. (mg/L)	Ads. Capacity (mg/g)	Ref
KCL-g-PAM/HA	La	6	15	3	0.1[a]	260	[120]
	Ce					245	
	Pr					235	
	Gd					220	
	Nd					210	
	Eu					195	
	Sm					192	
CMC-g-PAA	La	-	0.8	0.5	400	384.62	[121]
	Ce			0.67		333.33	
HPC-g-PAA/APT	La	6	1	1	300	264.17	[101]
	Ce					192.43	
CTS-g-PAA/APT	La	6	1	1.33	400	319.77	[122]
	Ce					232.41	
DGA-g-PAA	La	7	0.5	0.67	100	139.5	[123]
PAC	La	5	0.2	3	100	170	[70]
PEI-CNC	La	5.4	1	6	100	84.73	[124]
	Eu					101.82	
	Er					120.26	
Thio-CL	Eu	-	4	0.5	50	27	[125]
	Nd					73	
Thio-CL	Er	5	0.2	4	100	69.11	[126]
GLA-chit	Er	5	0.2	4	100	45.83	[126]
PCM-chit	Er	5	0.2	4	100	123.64	[126]
CATU	La	5	1	4	110	291.7	[127]
ALG-PGA	Nd	3.6	1.6	24	290	237.99	[128]
EDTA-β-CD	La	4	2	0.75	1.33[a]	47.64	[17]
	Ce					49.46	
	Eu					57.63	
MePhPTA-SiO_2	Dy	4	2	3	2	125.44	[129]

	Lu					129.77	
SiO_2/UF	Eu	3	10	2	-	157.03	[130]
	Nd					134.63	
SBA/SA	Eu	4	4	5	10	4.7	[131]
SBA/EnSA	Eu	4	1	2	10	15	[131]
MSNP	Gd	4	1	4	20	76.89	[132]
HESI-SBA-15	La	7	2.33	0.75	20	8.32	[133]
P(VP-AMPS-SiO_2)	La	5	5	6	100	116	[134]
	Ce					103	
	Nd					92	
	Eu					76	
PAA-S HNFs	La	5	0.1	3	-	232.6	[135]
	Eu					268.8	
	Tb					250	
Fmoc-SBA-15	Sc	5	0.25	0.17	20	135.29	[136]
SBA-15-ZMVP	Sm	4	5	1	10	41.66	[137]
	Dy					52.63	
P-SBA-15	Gd	4	0.5	0.03	200	204.42	[138]
2SilP	La	4	1	30	25	85.72	[139]
	Sc					75.5	
	Y					62.92	
SiO_2/CMCH	Nd	6.9	1.9	6	48	37.17	[140]
EDTA-chitosan-silica	Nd	-	2.5	3	72	38.9	[141]
DPTA-chitosan-silica	Nd	-	2.5	2	72	38.9	[141]
APTES-C3-PAN	La	4	1	1.5	25	116.27	[142]
	Sc					172.41	
	Y					140.85	
P507 magnetic-silica hybrid	La	5.5	1	1	35	55.9	[97]
Cys@Fe_3O_4	La	7	0.25	0.5	5	57.2	[143]
	Gd					85.5	
	Nd					98	
	Y					73	
CA@Fe_3O_4	La	7	0.25	0.25	5	32.5	[143]
	Gd					41	
	Nd					52	

	Y					35.8	
Fe_3O_4/CS	La	11	0.65	0.73	100	342.46	[144]
DETA@CHI-magnetic	Nd	5	0.2	1	100	52.1	[145]
	Dy					52.4	
	Yb					52.6	
Fe_3O_4@Ca-Alg	La	5	2	28	140	123.5	[146]
Fe_3O_4@Alg-CHI	La	2.8	1	10	140	97.1	[147]
Fe_3O_4@CD	Eu	5	0.8	3	5	12.69	[148]
Fe_3O_4@CMC	Eu	5.5	0.2	7	7.5	42.24	[149]
Cys@CHI-magnetic	La	5	2.5	4	100	17.9	[150]
	Nd					17.6	
	Yb					19.3	
EDTA Cu-Al LDH	La	6	2.6	2	1 [a]	-	[151]
	Sc						
	Y						

[a] Units are in mmol/L

The organic-organic hybrids are fabricated by modifying the number of natural biopolymers, consisting of various functional groups, mostly by using “grafting from” approach to improve the adsorption ability of these materials. The process involves the propagation of the monomer chain on biopolymers backbone by initiating sites [152]. The selection of monomer or crosslinker thus used is of key importance and functional groups normally grafted on biopolymers includes carboxyl, hydroxyl and amines. The two most abundant natural polymers used for the removal of REEs after modification is cellulose and chitosan. Methylenebisacrylamide (MBA) was used as monomer for the grafting of cellulose [101, 120, 121] and chitosan [122], while, studies also reported the cross-linking of cellulose by thiourea [125, 126], polyethylenimine (PEI) [124] and tetraethylenepentaamine (TEPA) [70] and with acrylothiourea [127] and glutaraldehyde (GLA) [126] for crosslinking chitosan. The optimum pH for the grafted materials like acrylic acid grafted hyroxypropyl cellulose and chitosan with attapulgite (HPC-g-PAA/APT and CTS-g-PAA/APT) [101, 122], poly(methylacrylate) grafted kenaf cellulose based poly(hydroxamic acid) ligand (KCL-g-PAM/HA) [120] and polyacrylic acid grafted carboxylic acid functionalized diatomite (DGA-g-PAA) [123] showing promising results for REEs ranges from 5-7 (Table 3). The adsorption of REEs on PEI-CNC and EDTA-β-cyclodextrin (EDTA-β-CD) was chemisorption [17, 124]. The presence of

secondary amines was noticed in cellulose grafted polyacrylic acid (CMC-g-PAA) [121], whereas the amines of HPC-g-PAA/APT [101] did not take part in the adsorption of La and Ce due to the blockage of channels which occur sometimes in case of modification with polymers [153].

The organic-inorganic nanocomposites, a novel class of material, substantially improved the properties of parent materials simply by the addition of modified nanoparticles into a polymer matrix or by grafting polymers on inorganic matrices. The nanocomposites thus present the distinct features of both matrices [154]. The most widely reported inorganic matrix modified with polymers for REEs removal was silica. The functionalisation of silica was achieved by various ligands including MePhPTA [129], Ionquest 801 [130], SA [131], EnSA [131], MAH [132], HESI [133], APMS [134], PAA [135], PAN [155, 156], Acac [155, 156], lysine [136], ZMVP [137] and phosphorous acid [138] containing carboxylic, amine, phosphoryl and sulphonyl functional groups. Equilibrium was achieved in 2 min for the adsorption of Gd when silica was modified with inorganic phosphorous acid (P-SBA-15) and interfering ions did not affect the Gd adsorption [138]. The REEs was adsorbed at lower pH on silica immobilised chemically by PAN and Acac via coupling agents, however, the optimum pH shifted to 7 when the same ligand groups were loaded physically [157]. HREEs adsorption was more influenced compared to LREEs with the rise in temperature [139, 155, 158]. Like many synthetic polymers reported for the modification of silica, silica-chitosan (biopolymer) composites were also used for REEs adsorption by entrapping silica in biopolymer matrix. The silica entrapped in chitosan was also functionalised by EDTA [141], DPTA [141], PAN [158] and Acac [158]. The adsorption occurred at acidic pH 2-3 for chitosan-silica composites functionalised with amino groups [158]. On the other hand, phosphoryl functional groups are responsible for the exceptional adsorption of La as reported by Wu et al. (2013) on hybrid magnetic-silica nanocomposite modified with P507 [92].

Another most commonly utilised matrix for the synthesis of organic-inorganic hybrids via encapsulation or functionalisation is magnetic nanoparticles. Ashour et al. (2017) reported the functionalisation of magnetic nanoparticles by citric acid and L-cysteine [143]. In addition, magnetic nanoparticles were encapsulated in chitosan [144, 145], chitosan-alginate [147] and Ca-alginate [146], cyclodextrin [148] and carboxymethyl cellulose [149] bio-polymeric matrices,

whereas, chitosan-magnetic composite was also prepared via the in-situ co-precipitation technique using cysteine (Cys) as a crosslinker [150]. At optimum pH, the adsorption of La occurred by complexation with surface functional groups [146, 150] while for Eu adsorption, hydroxyl and carboxyl groups served as active sites [148, 149]. The pH of the solution did not alter due to Cys@CHI-magnetic buffering capacity [150] but despite having similar functional groups i.e. amine and carboxylic, Cys@Fe_3O_4 did not exhibit similar buffering properties [143]. Layered double hydroxides (LDH), another inorganic matrix based materials generally offered comparable buffering capacity against pH [159]. The EDTA intercalated LDH matrix had been used by Kameda et al. (2011, 2013) for the adsorption of La, Sc and Y [151, 159]. Although present in the interlayers of LDH, EDTA ions retain their chelating functions and formed complexes with REEs [151].

Several studies related to the uptake of REEs via hybrids and nanocomposites have been published. However, the different combinations of organic (i.e. the abundantly occurring natural biopolymers like cellulose, gums etc.) and inorganic matrices for the synthesis of novel hybrid bio-nanocomposites (or green nanocomposites) and their potential for the uptake of REEs has yet to be explored. As this emerging class of hybrids are prepared by combining natural polymers with nanometre-sized inorganic matrix and open new prospects by adding the inherent features of biopolymers to hybrid nanocomposites i.e. biodegradability making such materials more environmentally friendly.

2. Objectives

The overall aim of the thesis was to explore the potential of hybrid bio-nanocomposites prepared using different organic-inorganic matrices for water treatment applications. The focus of the research was the application of hybrid bio-nanocomposites for the removal and recovery of REEs. The identifiable objectives of the study were:

- To synthesise five different hybrid bio-nanocomposites (1) cellulose intercalated zinc-aluminium LDH (CL-Zn/Al LDH, Paper I); (2) modified cellulose based silica nanocomposites (CLN/SiO_2, Paper II) ; (3) Gum Arabic grafted polyacrylamide based silica nanocomposites (GA-g-PAM/SiO_2, Paper III); (4) Gum Arabic exfoliated LDH (GA5MA, Paper IV) and (5) LDH encapsulated in xanthan gum anchored by metal ions (Zr@XG-ZA, Paper V) for the removal of REEs

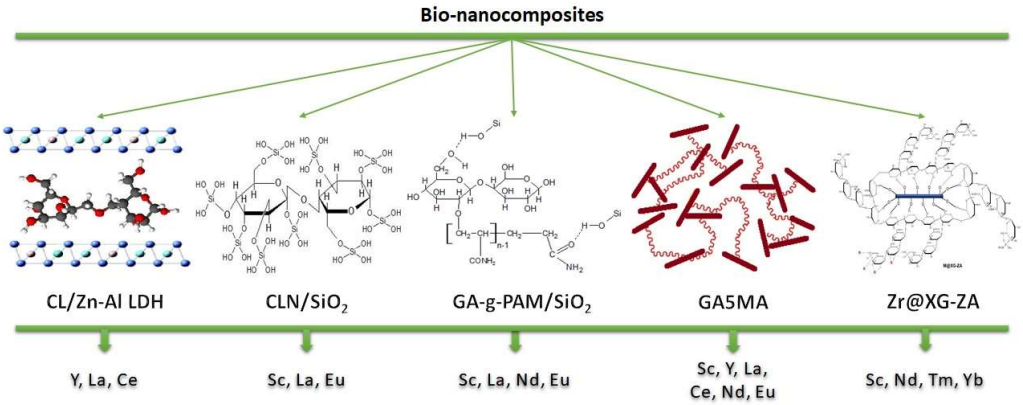

Figure 5: Schematic illustration of thesis contents

- To explore the influence of several operating parameters viz. pH of the solution, bio-nanocomposite dosage, contact time, initial REEs concentration in solution and temperature as well as the reusability potential of used bio-nanocomposite (Paper I-V). In addition, the REEs adsorption mechanism on bio-nanocomposites was studied and explained (Papers IV and V).

- To fit the data obtained experimentally to kinetic, isotherm and thermodynamic models. Papers I-V presented the fitting results of kinetic, isotherm and thermodynamic modelling for the experimented data range.
- To test the adsorptive behaviour of bio-nanocomposites towards REEs in the presence of competing ions (Papers I, II and IV), the removal of REEs in the multi-component system (Papers I, IV and V) and intra-series adsorption behaviour of REEs in a single (Paper I) as well as multi-component system (Paper IV)

3. Materials and methods

3.1. Synthesis of bio-nanocomposites

The five different bio-nanocomposites using cellulose, gum Arabic and xanthan gum were synthesised: the synthesis of cellulose intercalated zinc-aluminium LDH (CL-Zn/Al LDH), modified cellulose based silica (CLN/SiO_2), Gum Arabic grafted polyacrylamide based silica (GA-g-PAM/SiO_2), exfoliated biopolymeric-LDH (GA-LDH) and LDH encapsulated in xanthan gum anchored by metal ions (M@XG-ZA) nanocomposites is described in detail in Papers I-V, respectively.

Briefly, cellulose intercalated Zn/Al-LDH was prepared by a simple co-precipitation method (Paper I). The modification of cellulose was conducted using H_2SO_4 and citric acid prior to silica incorporation for the synthesis of CLx/SiO_2 nanocomposite (Paper II). In-situ radial graft polymerisation technique was used for grafting of PAM chains over Gum Arabic and sol-gel method was employed for the incorporation of silica over grafted monomer (GA-g-PAM) using TEOS as a precursor (Paper III). The in-situ co-precipitation strategy was employed for the preparation of exfoliated LDH nanocomposites in the presence of Gum Arabic using various divalent ions (Paper IV). To improve its properties xanthan gum, LDH as an inorganic matrix was encapsulated in xanthan gum and anchored with Fe and Zr ions (Paper V).

3.2. Characterisation of bio-nanocomposites

The synthesised bio-nanocomposites were analysed by powder X-ray diffraction (XRD) employing PANalytical diffractometer (Netherlands) equipped with Co Kα radiations (λ= 1.790307 Å) operated at accelerating voltage and current of 40 kV and 40 mA, respectively (Papers I-IV). For the identification of functional groups of prepared nanocomposites, the analysis was carried out on Bruker Vertex 70 (Germany) based Fourier transform infrared spectroscopy (FTIR) equipped with platinum ATR in the spectral range of 400 cm^{-1} to 4000 cm^{-1} (Papers I-V). Hitachi H-7700 (Japan) transmission electron microscope (TEM) was used for the determination of particle size (Papers I-V). The surface morphology was evaluated by Hitachi S-4800 (Japan) scanning electron

microscope (SEM) operated at 10 kV (Papers II, IV, V) and equipped with energy dispersive X-ray spectroscopy (EDS) (Papers IV and V). For further morphological characterisation, atomic force microscopy (AFM) analysis was conducted by Park Systems NX-10 (South Korea) using NCHR tip (Papers I-IV). The pore size, pore volume and surface area were obtained from Brunauer, Emmett and Teller (BET) Tristar® II Plus system (USA) using BET and BJH models at 77 K (Papers I-V). The elemental analysis (CHNS/O) was performed on Thermo scientific Flash 2000 analyser (USA) (Paper III). For the determination of isoelectric point, Malvern Zeta potential Nano ZEN3500 (UK) (Papers III-V) and pH_{zpc} method as described in Papers I-II was used.

3.3. Adsorption and Desorption Experiments

The details of the adsorption and desorption experiments conducted are described in Papers I-V. Briefly, a typical adsorption assay was performed by adding a known amount of bio-nanocomposite in REE solution of known concentration and a reaction mixture was then shaken for a specific period. At the end of each adsorption assay, the REE solution was separated from bio-nanocomposite by filtration using syringe filters. The adsorbed amount of REE by bio-nanocomposites was calculated by Eq. (1):

$$q_e = \frac{(C_0 - C_f)V}{M} \qquad \text{(Eq. 1)}$$

Where C_o and C_f are the in solution initial and equilibrium concentrations of REEs (mg/L), V and M represent the solution volume (L) and mass of bio-nanocomposite (g), respectively and q_e is the adsorption capacity (mg/g).

The pH of REEs solutions was adjusted by adding NaOH or HCl solution of known concentration. To study the adsorption kinetics, contact time was varied from one min to the time equilibrium was attained. Similarly, for adsorption isotherm and thermodynamics were investigated by varying the initial concentration of REEs and temperature, respectively.

For desorption experiments, the REE saturated bio-nanocomposite was desorbed using various desorbing agents (Papers I-V). The bio-nanocomposite was then separated by centrifugation, neutralised and used for REE enrichment in succeeding cycles.

Table 4: Adsorption experiments for targeted REEs over bio-nanocomposites (Papers I-V)

Bio-nanocomposite	Targeted REEs
CL-Zn/Al LDH	Y, La, Ce
CLN/SiO_2	Sc, La, Eu
GA-g-PAM/SiO_2	Sc, La, Nd, Eu
GA5MA	Sc, Y, La, Ce, Nd, Eu
Zr@XG-ZA	Sc, Nd, Tm, Yb

3.4. Analysis of solutions

The concentration of REEs and other metals in solution before and after adsorption experiments were analysed by Thermo iCAP 6300 (USA) inductively coupled plasma optical emission spectrometry (ICP-OES) (Papers I-III) and Agilent ICP-OES 5100 (Papers IV and V). The wavelengths used for the detection of various REEs and metal ions were: Sc: 335.373 nm, Y: 360.074 nm, La: 291.139 nm, Ce: 446.021 nm, Pr: 390.843 nm, Nd: 401.224 nm, Sm: 359.259 nm, Eu: 420.504 nm, Gd: 342.246 nm, Tb: 350.914 nm, Dy: 340.780 nm, Ho: 339.895 nm, Er: 337.275 nm, Tm: 342.508 nm, Yb: 369.419 nm, Lu: 291.139 nm, Na: 588.995 nm, Ca: 393.366 nm, Mg: 280.270 nm, Zn: 213.875 nm, Al: 237.12 nm, Fe: 238.204 nm and Zr: 343.823 nm.

3.5. Adsorption isotherms, kinetics and thermodynamics

3.5.1. Adsorption isotherms

During the adsorption process, adsorption isotherm is the quantitative measurement of its equilibrium and is useful in designing an adsorption system. The adsorption isotherms also describe the adsorbate and adsorbent interaction in solution. Langmuir (Papers I-V), Freundlich (Papers I-V), Temkin (Papers I-IV) and Elovich (Paper III) were the isotherm models used for

modelling the adsorption process. The calculations for the modelling were performed using OriginPro 2015 academic software. The equations of models are given in Table 5:

Table 5: Linear equations for various isotherm models

Isotherm model	Linear equation		Ref
Langmuir I	$\frac{C_e}{q_e}=\frac{1}{K_L Q_0}+\frac{C_e}{Q_0}$	(Eq. 2)	[160]
Langmuir II	$\frac{1}{q_e}=(\frac{1}{K_L Q_0})\frac{1}{C_e}+\frac{1}{Q_0}$	(Eq. 3)	
Langmuir III	$q_e=Q_0-(\frac{1}{K_L})\frac{q_e}{C_e}$	(Eq. 4)	
Langmuir IV	$\frac{q_e}{C_e}=K_L Q_0-K_L qe$	(Eq. 5)	
Freundlich	$\ln q_e=\ln K_f+\frac{1}{n}\ln C_e$	(Eq. 6)	[161]
Temkin	$q_e = B\log(A) + B\log(C_e)$	(Eq. 7)	[162]
Elovich	$\ln\frac{q_e}{C_e}=\ln(K_e Q_0)-\frac{q_e}{Q_0}$	(Eq. 8)	[163]

where q_e and C_e are the REEs adsorption capacity (mg/g) and concentration of REEs at equilibrium (mg/L), respectively, Q_0 maximum adsorption capacity (mg/g), n is the heterogeneity factor related to adsorption intensity, K_L, K_f, A (L/g) and K_e present Langmuir, Freundlich, Temkin and Elovich isotherm constants, B is a constant related to heat of sorption (J/mol).

3.5.2. Adsorption Kinetics

For developing an understanding of the adsorption process and to determine the rate controlling step, the kinetic data was analysed using commonly used kinetic models viz. pseudo first order (Papers I-V), pseudo second order (Papers I-V), intra-particle diffusion (Papers I-V) and Boyd models (Papers I-V). The equations of models used are listed in Table 6 below:

Table 6: Linear equations for various kinetic models

Kinetic model	Linear equation		Ref
Pseudo first order (PS1)	$\log(q_e - q_t) = \log q_e - \frac{k_1}{2.303}t$	(Eq. 9)	[164]
Pseudo second order (PS2)	$\frac{t}{q_t} = \frac{1}{k_2 q_e^2} + \frac{1}{q_e}t$	(Eq. 10)	[165]
Intra-particle diffusion	$q_t = k_i t^{1/2} + C$	(Eq. 11)	[166]
Boyd	$-k_b t = \ln(1-F); F = \frac{q_t}{q_e}$	(Eq. 12)	[167]

where q_t and q_e are the adsorption capacity of REEs over bio-nanocomposites at time t and equilibrium (mg/g), respectively, k_1 (min^{-1}) and k_2 (g mg^{-1} min^{-1}) are rate constants for PS1 and PS2, respectively, C is a constant and t is time (min)

3.5.3. Adsorption thermodynamics

The study of thermodynamic parameters including enthalpy (ΔH^o), entropy (ΔS^o) and Gibbs free energy (ΔG^o) is essential to understand the endothermic/exothermic nature, randomness of the adsorbent/adsorbate system and the spontaneity of adsorption process. The thermodynamic parameters including ΔG^o, ΔH^o and ΔS^o were computed from the following equations:

$$\ln K_C = \frac{\Delta S^0}{R} - \frac{\Delta H^0}{RT} \quad \text{(Eq. 8)}$$

$$\Delta G^0 = -RT \ln K_C \quad \text{(Eq. 9)}$$

where K_c is thermodynamic equilibrium constant (L/g), R and T represent universal gas constant (8.314 J/mol/K) and temperature (K), respectively.

4. Results and discussion

4.1. Characterisation of bio-nanocomposites

To visualise the size, morphology and distribution of inorganic matrices in biopolymers, the microscopic investigation of synthesised hybrid bio-nanocomposites is important. The morphological characterisation of bio-nanocomposites was performed with TEM (Papers I-V), SEM (Papers II, IV and V) and AFM (Papers I-IV). TEM images shown in Figure 6 reveal a difference in the morphologies of synthesised bio-nanocomposites. The presence of sheet-like LDH structure appeared in CL-Zn/Al LDH and GA5MA that distributes uniformly in CL and GA matrix (Paper I and IV). The LDH sheets are irregular shaped slanted fibres indicating the exfoliation of sheet structure due to GA loading (Paper IV). In addition, the exfoliated randomly oriented non-uniform size LDH platelets stacking can be seen in SEM image (Figure 7(d)) of GA5MA (Paper IV). However, no free LDH structure can be seen in case of Zr@XG-ZA due to the complete encapsulation of LDH and the presence of a dense organic cluster of XG. On the other hand, the encapsulation of LDH in XG and anchoring with Zr changes the morphology of bio-nanocomposite completely (Paper V). The AFM image of Zr@XG-ZA (Figure 8(e)) is in agreement with TEM and SEM. Similarly, in CLN/SiO_2 and GA-g-PAM/SiO_2, the silica particles were evenly distributed throughout CLN and GA-g-PAM matrix with the particle size in the range of 9-15 nm and 25-60 nm, respectively (Papers II and III). The SEM image of CLN/SiO_2 also indicates the uniform distribution of silica over the surface of CLN (Paper II). The settlement of LDH plates over one another can also be seen in the SEM image of CL-Zn/Al LDH (Figure 7(a)). The AFM images of all the bio-nanocomposites indicate the agglomeration of particles, which vary in height except GA5MA where the topographic image clearly shows the GA being decorated with LDH platelets (Figure 8, Papers I-IV).

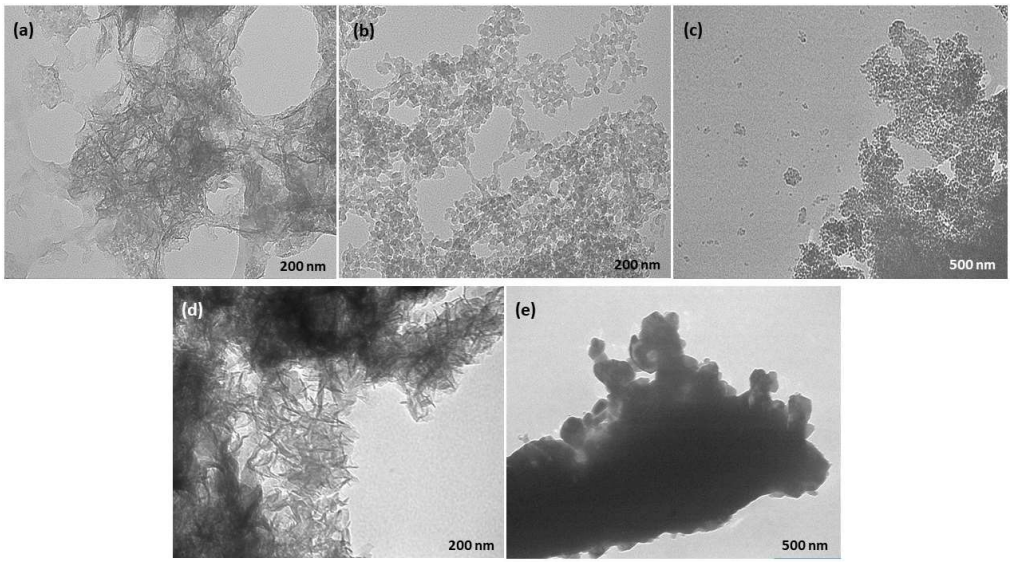

Figure 6: TEM images of (a) CL-Zn/Al LDH, (b) CLN/SiO_2, (c) GA-g-PAM/SiO_2, (d) GA5MA and (e) Zr@XG-ZA (Papers I-V)

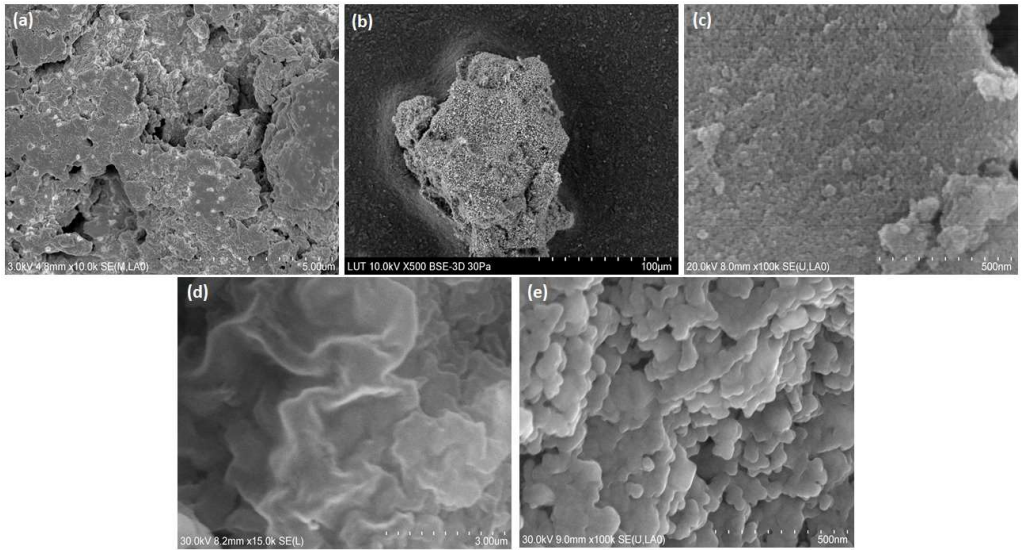

Figure 7: SEM images of (a) CL-Zn/Al LDH, (b) CLN/SiO_2 (Paper II), (c) GA-g-PAM/SiO_2, (d) GA5MA (Paper IV) and (e) Zr@XG-ZA (Paper V)

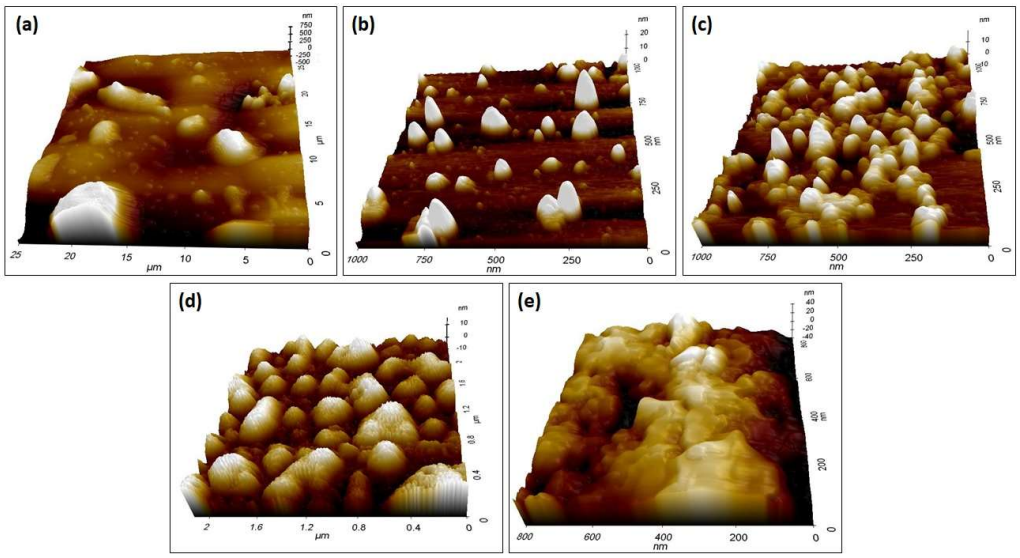

Figure 8: AFM images of (a) CL-Zn/Al LDH (Paper I), (b) CLN/SiO_2 (Paper II), (c) GA-g-PAM/SiO_2 (Paper III), (d) GA5MA (Paper IV) and (e) Zr@XG-ZA

FTIR analysis was used for the identification of functional groups on the surface of bio-nanocomposites (Papers I-V). The bands that appeared during the analysis of CL-Zn/Al LDH, CLN/SiO_2, GA-g-PAM/SiO_2, GA5MA and Zr@XG-ZA (Papers I-V) are listed in Table 7. The presence of the characteristic peaks of CL, GA and XG along with LDH indicates the successful modification and incorporation of the LDH matrix into biopolymers (Papers I, IV and V). The FTIR spectra of cellulose modified with sulfuric acid (CLN) showed several characteristic peaks of CL at 1043, 1370, 1412, 1429, 1636, 2901, 3336 cm^{-1} attributed to the skeletal vibrations of C-O-C ring, C-H bending, CH_2 symmetric scissoring, -CH_2 bending, –OH bending, C-H stretching and –OH stretching vibrations, respectively. In addition, the absence of crystal adsorption peak of cellulose at 1105 cm^{-1} confirmed that the structure of CL was destroyed due to modification (Paper II) as proposed in Figure 10 (Paper VI). The incorporation of silica in modified CL leads to the appearance of both bands of CL and SiO_2 in FTIR spectra. The various bands, which evidenced the grafting of PAM (monomer) over GA, appeared at 1120, 1319, 1390, 1448, 1414 and 1658, 1607, 2927 and 3200-3500 cm^{-1} corresponds to C-O stretching of ester group, CH_2 twisting, C-N

stretching vibrations, CH_2 scissoring, vibrations of COO^- groups, N-H stretching vibrations, C-H stretching vibrations and -OH stretching vibrations, respectively (Figure 9, Paper III). Besides these main peaks, the other peaks originated after addition of SiO_2 in grafted polymer i.e. GA-g-PAM are tabulated in Table 7. Some of the peaks of XG showed a shift to different wavenumber after formation of Zr@XG-ZA due to metal anchoring and encapsulation (Paper V). Furthermore, FTIR spectra of GA5MA and Zr@XG-ZA after adsorption of targeted REEs was measured and used for explaining the adsorption mechanism (Papers IV and V).

Table 7: The FTIR characteristic bands of synthesised bio-nanocomposites (Papers I-V)

Bio-nanocomposite	**Wavenumber (cm^{-1})**	**Process**
CL-Zn/Al LDH	3300-3450	-OH stretching vibrations
	1600-1700	-OH bending vibrations
	1461 and 1595	Symmetrical and asymmetrical vibrations of $–COO^-$
	1152	C-O-C vibrations
	400-800	O-M-O stretching and M-OH vibrations (where M represents metal ions of LDH i.e. Zn and Al)
CLN/SiO_2	1058	Si-O-C vibrations
	465 and 798	Bending and symmetric vibrations of Si-O-Si
GA-g-PAM/SiO_2	1080	Si-O stretching vibrations of Si-O-Si bridges
	966	Si-O vibrations from Si-OH groups
	450 and 792	Bending and symmetric vibrations of Si-O-Si
GA5MA	3200-3700	-OH stretching vibrations
	2800-3000	Stretching vibrations of C-H
	1750	Stretching vibrations of C-O

	1635	Stretching vibrations of carbonyl groups
	1050-1200	Stretching vibrations of C-O-C aliphatic ether
	1410 and 1350	Bending vibration of CH_2 and CH
	400-800	O-M-O stretching and M-OH vibrations (where M represents metal ions of LDH i.e. Mg, Ca, Sr, Ba and Al)
Zr@XG-ZA	3345	-OH stretching vibrations
	1706	C=O stretching
	1620 and 1407	Symmetrical and asymmetrical vibrations of $–COO^-$
	1022	O-H band of XG
	400-800	O-M-O stretching and M-OH vibrations (where M represents metal ions of LDH i.e. Zn and Al)

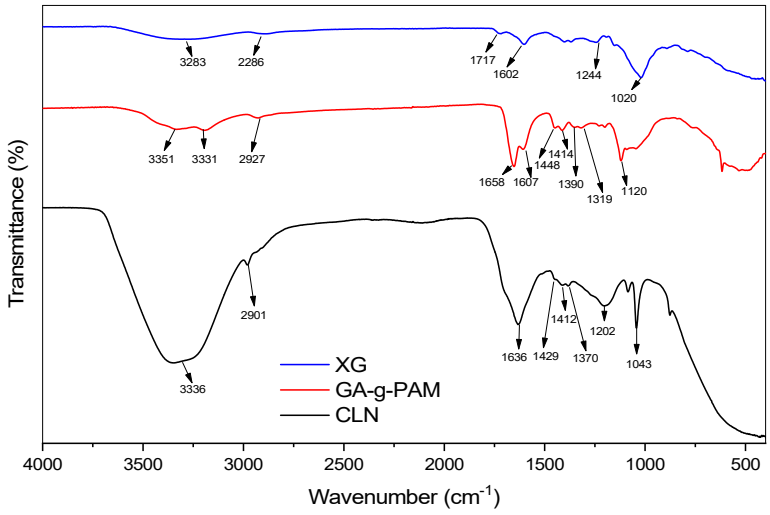

Figure 9: FTIR spectra of CLN, GA-g-PAM and XG

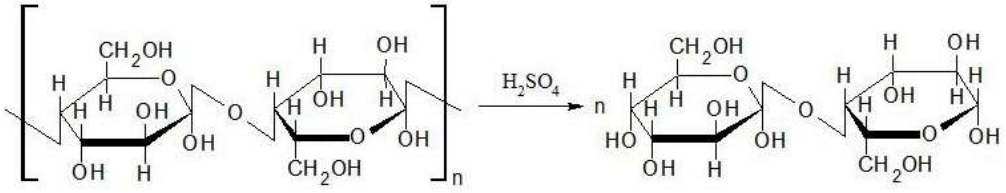

Figure 10: Proposed schematic diagram of sulfuric acid modified cellulose (Paper VI)

XRD analysis was used for the identification of the crystal structure of bio-nanocomposites and illustrated in Figure 11(a-d). XRD patterns of CL-Zn/AL LDH, GA5MA and Zr@XG-ZA demonstrate the peaks forming the planes of (1 1 0) and (1 1 3) indicating a good dispersion of divalent and trivalent metal ions within LDH. Moreover, in GA5MA, the peaks corresponding to the planes of (0 03), (0 0 6), (0 0 9), (0 1 2) and (0 1 8) are characteristic diffraction peaks of LDH (Paper IV), whereas, reflection to the plane (0 0 3) is missing in CL-Zn/Al LDH because of the intercalation of CL in LDH layers (Paper I). The broadness in peaks of GA5MA further exhibits the interlayer galleries are not uniform (Paper IV). All the major planes of LDH in Zr@XG-ZA disappeared due to encapsulation and even the planes of (0 0 9) and (0 1 2) appeared with shift because of metal anchoring as can be seen in Figure 11(e). A board hump of amorphous SiO_2 was indexed in case of CLN/SiO_2 and GA-g-PAM/SiO_2 (Papers II and III).

The results of BET surface area, pore volume and diameter are listed in Table 8 (Papers I-V). Figure 12 illustrates the N_2 adsorption-desorption isotherms of bio-nanocomposites (Papers I-V). According to IUPAC classifications, CL-Zn/Al LDH and GA5MA exhibit type III with H3 hysteretic loop (Papers I and IV) indicating the aggregation of plate-like particles [168, 169]. Likewise, type IV with H2 hysteretic loop for CLN/SiO_2 and GA-g-PAM/SiO_2 for mesoporous materials (Papers II and III) and type II with H4 hysteretic loop for Zr@XG-ZA (Paper V) representing monolayer-multilayer adsorption of non-porous or macroporous materials [168, 169].

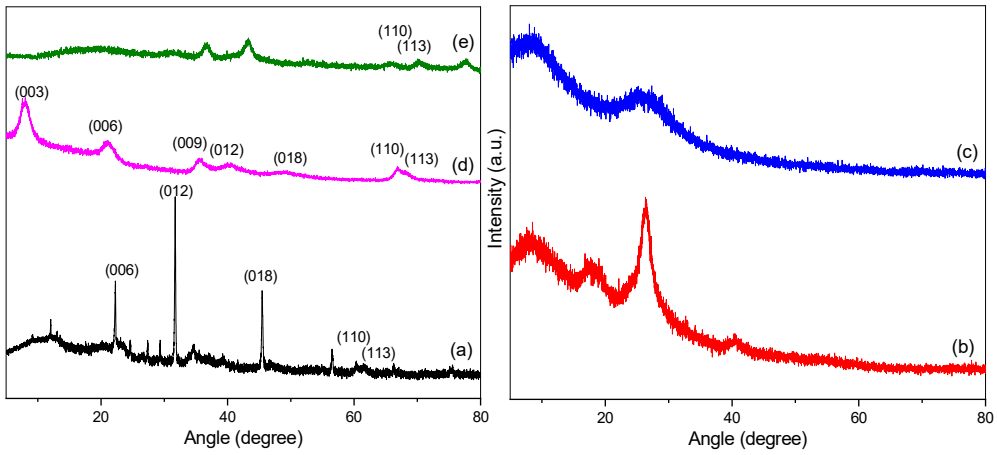

Figure 11: XRD pattern of bio-nanocomposites; (a) CL-Zn/Al LDH (Paper I), (b) CLN/SiO_2 (Paper II), (c) GA-g-PAM/SiO_2 (Paper III), (d) GA5MA (Paper IV) and (e) Zr@XG-ZA

Table 8: BET surface area, pore volume and pore diameter of bio-nanocomposites (Papers I-V)

Bio-nanocomposite	**BET surface area (m^2/g)**	**Pore volume (cm^3/g)**	**Average pore diameter (nm)**
CL-Zn/Al LDH	1.26	9.3×10^{-3}	22.7
CLN/SiO_2	169.74	0.478	11.2
GA-g-PAM/SiO_2	273.55	0.428	6.26
GA5MA	4.169	0.004	7.33
Zr@XG-ZA	21.49	0.041	7.29

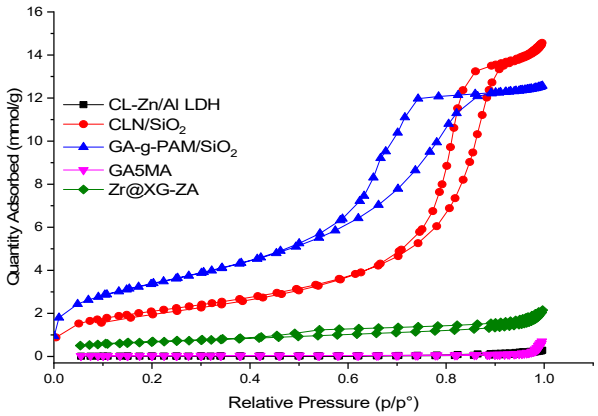

Figure 12: N_2 adsorption-desorption isotherms of bio-nanocomposites (Papers I-V)

The elemental analysis (CHNS/O) was used for the quantitative determination of the amount of functional groups in GA-g-PAM/SiO_2 (Paper III) and findings are summarised in Table 9. Although the GA-g-PAM contained an excess amount of nitrogen from PAM, however, the decree in amount was associated with the release of ammonia gas during hydrolysis. Furthermore, an increased amount of oxygen in GA-g-PAM/SiO_2 compared to GA-g-PAM was due to the addition of silanol-OH groups (Paper III). The EDX analysis was also used for elemental analysis of CL-Zn/Al LDH, CLN/SiO_2, GA-g-PAM/SiO_2, GA5MA and Zr@XG-ZA (Paper V), however, only elements on the surface were determined by EDX. The EDX analysis of bio-nanocomposites presented in Figure 13 indicates the presence of all the elements of both organic (CL, GA and XG) and inorganic matrices (LDH and SiO_2).

Table 9: Elemental analysis result of GA-g-PAM and GA-g-PAM/SiO_2

Sample	% O	% C	% H	% N	% S
GA-g-PAM	38.66	39.55	7.42	14.37	0
GA-g-PAM/SiO_2	46.32	31.66	6.41	7.62	0

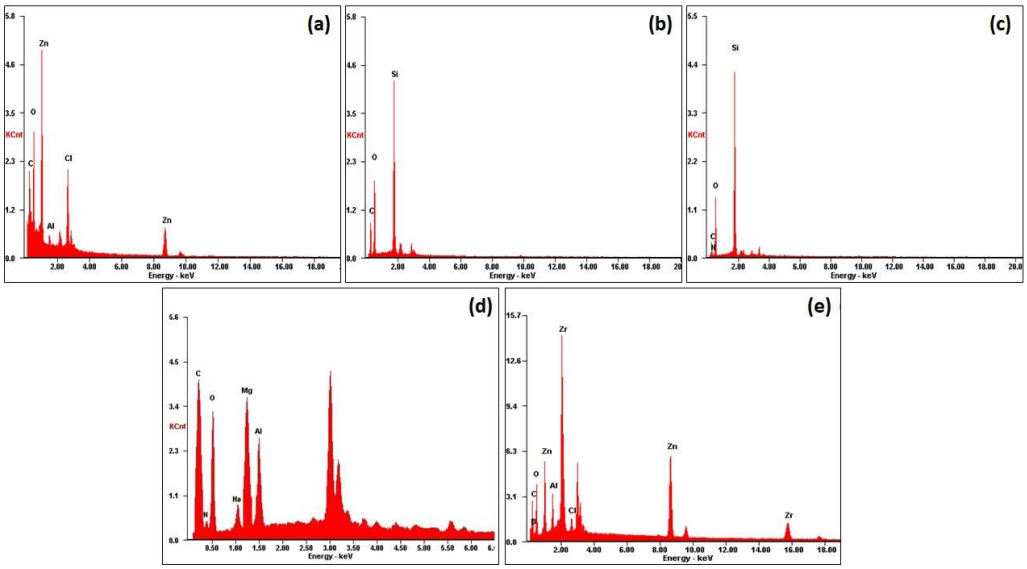

Figure 13: EDX spectra of (a) CL-Zn/Al LDH, (b) CLN/SiO_2, (c) GA-g-PAM/SiO_2 (d) GA5MA and (e) Zr@XG-ZA (Paper V)

The isoelectric point was estimated to be 9.10, 7.06, 3.18, 2.65 and 3.2 for CL-Zn/Al LDH, CLN/SiO_2, GA-g-PAM/SiO_2, GA5MA and Zr@XG-ZA (Papers I-V), respectively. When pH < pH_{zpc} the surface of bio-nanocomposite carries positive charge means protonation occurs and vice versa.

4.2. Adsorption studies

4.2.1. Preliminary adsorption tests

The preliminary adsorption experiments were conducted to screen out the bio-nanocomposites, which showed better adsorbing capacity. Among sulfuric acid modified and citric acid modified cellulose-based silica nanocomposites (CLN/SiO_2 and CLCA/SiO_2), the former showed higher adsorption for targeted REEs (Sc, La, Eu). The higher surface area of CLN/SiO_2 compared to CLCA/SiO_2 (110.29 m^2/g) attributed towards its higher adsorption (Paper II). Similarly, in case of Fe@XG-ZA and Zr@XG-ZA, the adsorption of REEs (Sc, Nd, Tm, Yb) was negligible on Fe@XG-ZA. The higher Fe bridging on XG-ZA emulsion resulting in a lower surface area of Fe@XG-ZA (13.09 m^2/g) compared to Zr@XG-ZA contributed towards its lower adsorption (Paper V). In Paper V,

various exfoliated bio-nanocomposites were synthesised by varying the GA loading (2% and 5%) and changing the divalent ions (Mg, Ca, Sr, Ba) of LDH. All the bio-nanocomposites were tested for selected REEs (Sc, Y, La, Ce, Nd, Eu). The results showed that GA5MA with higher GA loading and smaller ionic radii of divalent ion in LDH offered better adsorption towards REEs.

4.2.2. Effect of pH

The pH of the solution is the main factor that affects the adsorption efficiency and plays a vital role at solid-liquid interface. Thus, pH optimisation is necessary to maximise the REEs adsorption over bio-nanocomposites. The adsorption above pH 6 or 7 was not studied due to the precipitation of REEs as insoluble metal hydrides (Papers I-V).

The removal of REEs in all cases was found to be pH dependent and a considerable increase in the removal of REEs was observed with an increase in pH (Papers I-V). Under strong acidic conditions, all bio-nanocomposites showed poor adsorption towards the targeted REEs due to competitive adsorption between REEs and H^+ ions. The higher concentration under acidic medium and smaller ionic radii of H^+ ion facilitate their adsorption over bio-nanocomposites compared to REEs. Thus, the surface functional groups including carboxylates, amines etc. get protonated resulting in low removal of REEs under acidic conditions (pH 2). Furthermore, the adsorption of REEs was associated with the zero point charge of the bio-nanocomposite. The electrostatic repulsion occurs when the solution pH < pH_{zpc}. This phenomenon was observed for GA-g-PAM/SiO_2 (Paper III), GA5MA (Paper IV) and Zr@XG-ZA (Paper V), where the adsorption increases significantly after a certain pH i.e. when pH > pH_{zpc}. This indicates that the surface of bio-nanocomposites carrying negative charge mainly facilitates the adsorption of REEs (cationic species). On the other hand, the CL-Zn/Al LDH carries positive charge still showed exceptionally high REEs adsorption, which in turn was related to surface properties and buffer action of LDH (Paper I). The maximum removal of targeted REEs was found at pH 7 for CL-Zn/Al LDH (Paper I), at pH 6 for CLN/SiO_2 (Paper II) and GA-g-PAM/SiO_2 (Paper III), at pH 4 for GA5MA (Paper IV) and from 4-6 for Zr@XG-ZA (Paper V). Notably, the bio-nanocomposites synthesised using LDH as an inorganic matrix showed higher adsorption compared to SiO_2 matrix. This was mainly because

carboxyl and amine groups could not serve as active sites due to the addition of SiO_2 (Papers II and III).

The strong dependency on pH indicates the formation of REEs complexes with the surface functional groups. The possible REEs complexes with carboxyl, amine and hydroxyl functional groups are shown in Figure 14.

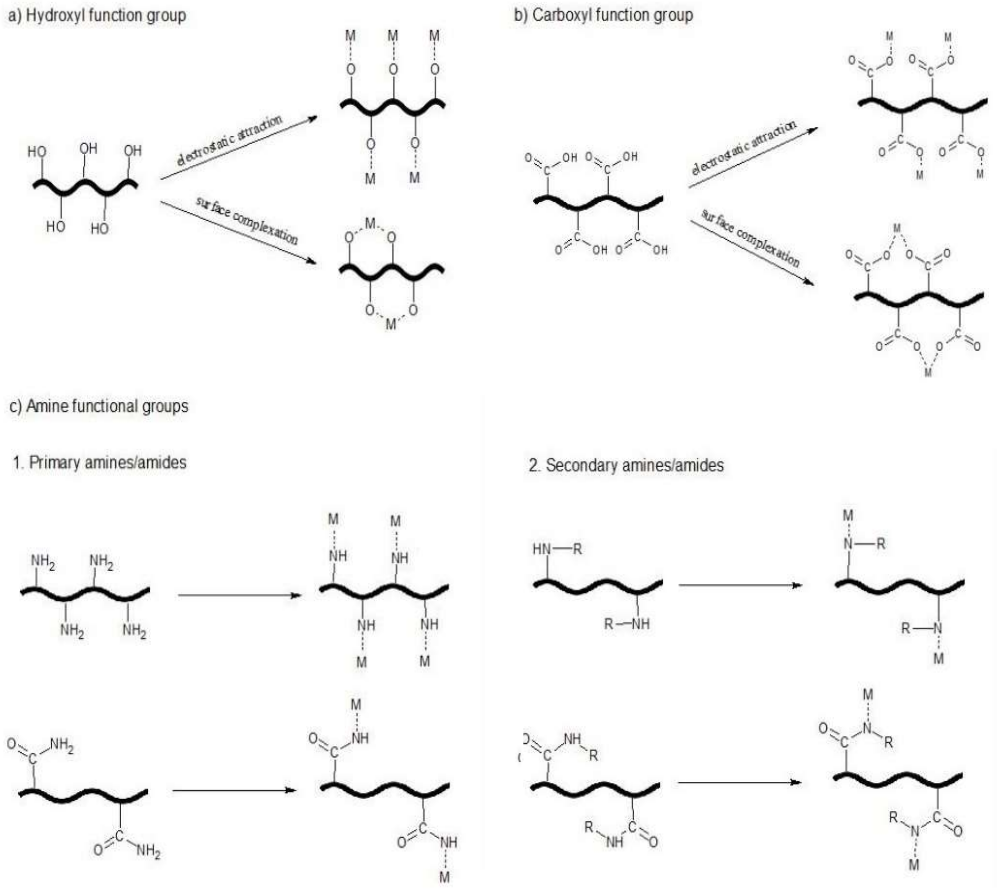

Figure 14: Proposed schematic illustration of REEs complexes with hydroxyl, carboxyl and amine functional group (where M and R represents REEs and other groups, respectively) (Paper VI)

4.2.3. Effect of dose

To determine the optimum dose of bio-nanocomposites for REEs, the adsorption experiments were conducted by varying the dose. For all the studied bio-nanocomposites, the REEs adsorption increased by increasing the dose, as a higher dose provides more active sites for REEs adsorption. The optimum dose was determined to be 1.2 g/L, 3 g/L, 3.5 g/L, 1 g/L and 3 g/L for CL-Zn/Al LDH, CLN/SiO_2, GA-g-PAM/SiO_2, GA5MA and Zr@XG-ZA (Papers I-V), respectively.

4.2.4. Adsorption Kinetics

To determine the equilibrium time for targeted REEs to achieve maximum adsorption, the influence of contact time was investigated on CL-Zn/Al LDH, CLN/SiO_2, GA-g-PAM/SiO_2, GA5MA and Zr@XG-ZA (Papers I-V).

Figure 15 shows the effect of the contact time on bio-nanocomposites for the adsorption of REEs. A rapid increase in the removal of REEs was noticed followed by a slow attainment in all cases. This sheer increase was in turn related to the availability of active sites at the beginning of REEs adsorption over bio-nanocomposites. Once the external active sites were saturated, REEs started to diffuse to the inner pores, which would take longer time. The REEs removal of 99% was observed in 10 mins for CL-Zn/Al LDH (Paper I). The adsorption of Sc on Zr@XG-ZA was faster (30 min) due to smaller ionic radii whereas, equilibrium was achieved in 80 min for Nd. The REEs adsorption reached equilibrium in 50 min, 60 min and 90 min for CLN/SiO_2, GA-g-PAM/SiO_2 and GA5MA (Papers II, III and IV), respectively.

The kinetics of the targeted REEs on CL-Zn/Al LDH, CLN/SiO_2, GA-g-PAM/SiO_2, GA5MA and Zr@XG-ZA (Papers I-V) was also investigated by employing PS1 and PS2 kinetic models. The kinetic parameters for the adsorption of REEs on bio-nanocomposites are listed in Table 10. The higher values of correlation coefficient (R^2) favours the applicability of PS2 model for REEs adsorption on CL-Zn/Al LDH (Paper I). For the adsorption on CLN/SiO_2, PS2 model yielded better fit to the experimental data for La and Eu, whereas, PS1 for Sc (Paper II). Similarly, for GA-g-PAM/SiO_2 and Zr@XG-ZA, the R^2 and kinetic parameter values suggested kinetic data were well

described by PS1 model (Papers III and V). The closer values of $q_{e,exp}$ and $q_{e,cal}$ indicated the favourability of PS2 for REEs adsorption on GA5MA (Paper IV).

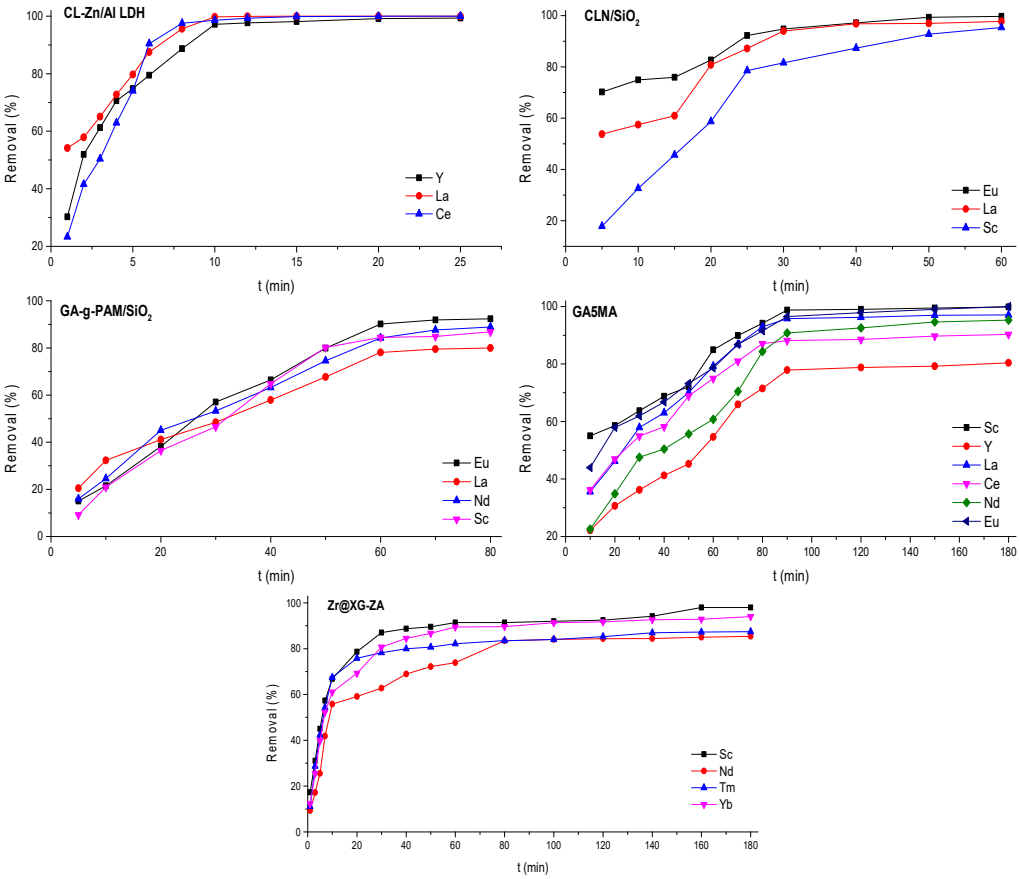

Figure 15: Effect of contact time on the adsorption of targeted REEs over bio-nanocomposites (Papers I-V)

In order to understand the contribution of steps (i.e. intra-particle diffusion or film diffusion) involved in the adsorption process, intra-particle diffusion and Boyd model was used. If the intra-particle curve does not fit linearly to the experimental data, the adsorption process is controlled by intra-particle diffusion and film diffusion [170], which was then validated by Boyd model. The Boyd model helps in distinguishing between intra-particle diffusion and film diffusion. The film

diffusion is the rate governing step if Boyd plot does not pass through origin [167]. In all the cases, film diffusion was found to be the rate controlling step (Papers I-V). Moreover, it was noticeable that intra-particle plot showed multi-linearity indicating that diffusion occurred via three stages including external film, macropore and micropore diffusion. The region of macropore diffusion was only observed for the adsorption of REEs on CL-Zn/Al LDH (Paper I), for Nd and Eu adsorption on GA5MA (Paper IV) and for Nd adsorption on Zr@XG-ZA (Paper V).

Table 10: Kinetics parameters of targeted REEs (Papers I-V)

CL-Zn/Al LDH							
Targeted REEs	$q_{e,exp}$ (mg/g)	Pseudo first order			Pseudo second order		
		$q_{e,cal}$ (mg/g)	k_1 (min^{-1})	R^2	q_e (mg/g)	k_2 (g/mg. min^{-1})	R^2
Y	42.04	68.87	0.46	0.81	53.45	6.07×10^{-3}	0.99
La	45.07	79.92	0.56	0.801	52.74	9.5×10^{-3}	0.98
Ce	49.7	115.85	0.57	0.94	55.83	4.3×10^{-3}	0.95
CLN/SiO_2							
Targeted REEs	$q_{e,exp}$ (mg/g)	Pseudo first order			Pseudo second order		
		$q_{e,cal}$ (mg/g)	k_1 (min^{-1})	R^2	q_e (mg/g)	k_2 (g/mg. min^{-1})	R^2
Sc	9.41	13.33	0.079	0.96	23.28	7.4×10^{-4}	0.80
La	10.55	24.49	0.16	0.85	13.06	7.8×10^{-3}	0.95
Eu	10.57	6.17	0.08	0.93	11.32	0.02	0.99
GA-g-PAM/SiO_2							
Targeted REEs	$q_{e,exp}$ (mg/g)	Pseudo first order			Pseudo second order		
		$q_{e,cal}$ (mg/g)	k_1 (min^{-1})	R^2	q_e (mg/g)	k_2 (g/mg. min^{-1})	R^2
Sc	5.17	7.90	5.64×10^{-3}	0.82	20.81	2.83×10^{-4}	0.56
La	5.64	5.09	3.27×10^{-3}	0.95	6.21	8.4×10^{-3}	0.94

Eu	5.77	6.87	4.23×10^{-3}	0.94	11.47	1.32×10^{-3}	0.82
Nd	7.30	7.51	3.57×10^{-3}	0.97	10.57	2.47×10^{-3}	0.96

GA5MA

Targeted REEs	$q_{e,exp}$ (mg/g)	Pseudo first order			Pseudo second order		
		$q_{e,cal}$ (mg/g)	k_1 (min^{-1})	R^2	q_e (mg/g)	k_2 (g/mg. min^{-1})	R^2
Sc	33.16	53.21	5.0×10^{-2}	0.68	38.77	1.23×10^{-3}	0.95
Y	19.15	47.59	4.21×10^{-2}	0.71	23.28	0.83×10^{-3}	0.77
La	21.45	41.98	5.14×10^{-2}	0.79	28.95	0.96×10^{-3}	0.96
Ce	24.47	49.30	5.53×10^{-2}	0.82	26.74	1.47×10^{-3}	0.96
Nd	24.33	40.51	3.78×10^{-2}	0.73	27.13	0.79×10^{-3}	0.84
Eu	26.89	31.60	3.82×10^{-2}	0.81	31.61	1.37×10^{-3}	0.96

Zr@XG-ZA

Targeted REEs	$q_{e,exp}$ (mg/g)	Pseudo first order			Pseudo second order		
		$q_{e,cal}$ (mg/g)	k_1 (min^{-1})	R^2	q_e (mg/g)	k_2 (g/mg. min^{-1})	R^2
Sc	9.18	9.15	0.13	0.98	4.29	1.94×10^{-2}	0.96
Nd	7.37	7.07	0.08	0.97	4.11	1.23×10^{-2}	0.94
Tm	8.89	8.85	0.14	0.99	3.94	2.18×10^{-2}	0.96
Yb	7.41	7.40	0.11	0.98	3.79	1.59×10^{-2}	0.95

4.2.5. Adsorption Isotherms

In order to investigate the adsorption potential of the used bio-nanocomposites for targeted REEs, the equilibrium adsorption was explored as a function of the initial REEs concentration (Papers I-V).

The adsorption of Y, La and Ce on CL-Zn/Al LDH were investigated by Langmuir, Freundlich and Temkin isotherm models. The results in Table 11 demonstrate that the data fitted well to Langmuir model indicating monolayer adsorption. The order followed by the adsorption

isotherms were: Temkin < Freundlich < Langmuir (Paper I). Langmuir I-IV, Freundlich and Temkin were used in the adsorption studies of REEs (Sc, La, Eu) on CLN/SiO_2. Among various isotherms, the data was well described by Langmuir I with higher values of R^2. Conversely, for the adsorption of Sc, Freundlich isotherm fitted the data well (Paper II). The similar different trend was also observed for Sc adsorption on GA-g-PAM/SiO_2 and GA5MA (Papers III and IV). In addition, the n values obtained for Sc adsorption on CLN/SiO_2, GA-g-PAM/SiO_2 and GA5MA indicating the heterogeneous surface (Papers II, III and IV). The equilibrium data for adsorption of Sc, Y, La, Ce, Nd and Eu on Zr@XG-ZA was fitted to Langmuir and Freundlich isotherms. The results from Table 11 represent that correlation coefficient values of Freundlich isotherm (0.98-0.99) was higher than Langmuir isotherm (0.57-0.96) (Paper V).

Table 11: Isotherm parameters of targeted REEs (Papers I-V)

CL-Zn/Al LDH									
	Langmuir			Freundlich			Temkin		
REEs	Q_o	K_L (L/mg)	R_L^2	K_f (L/g)	n	R_F^2	A (L/g)	B (J/mol)	R_T^2
Y	102.25	0.15	0.93	19.34	2.47	0.90	0.91	20.61	0.86
La	92.51	0.62	0.97	54.84	7.83	0.88	1467.4	7.81	0.80
Ce	96.25	0.08	0.96	41.88	5.78	0.83	31.6	11.15	0.76
CLN/SiO_2									
	Langmuir I			Langmuir II			Langmuir III		
REEs	Q_o	K_L (L/mg)	R_{L1}^2	Q_o	K_L (L/mg)	R_{L2}^2	Q_o	K_L (L/mg)	R_{L3}^2
Sc	93.54	0.014	0.63	41.56	0.056	0.88	49.63	0.044	0.39
La	29.48	0.072	0.964	19.96	1.24	0.509	21.40	1.05	0.28
Eu	24.47	0.85	0.96	18.05	1.80	0.57	18.79	1.58	0.33
REEs	Langmuir IV			Freundlich			Temkin		

	Q_o	K_L (L/mg)	R_{L4}^2	K_f (L/g)	n	R_F^2	A (L/g)	B (J/mol)	R_T^2
Sc	78.42	0.019	0.39	2.70	1.48	0.96	0.25	14.55	0.84
La	24.31	0.35	0.28	8.58	4.24	0.86	5.27	3.96	0.77
Eu	20.55	0.60	0.33	9.57	5.82	0.85	25.65	2.66	0.76

GA-g-PAM/SiO_2

REEs	Langmuir			Freundlich			Temkin		
	Q_o	K_L (L/mg)	R_L^2	K_f (L/g)	n	R_F^2	A (L/g)	B (J/mol)	R_T^2
Sc	35.22	0.02	0.81	1.56	1.64	0.99	0.25	6.74	0.89
La	7.90	0.17	0.99	3.07	4.96	0.76	7.09	1.17	0.76
Nd	12.24	0.07	0.98	2.37	2.92	0.87	0.84	2.49	0.90
Eu	10.11	0.21	0.99	4.98	6.73	0.86	63.81	1.11	0.83

REEs	Elovich		
	Q_o	K_e (L/mg)	R_E^2
Sc	0.06	11.52	0.76
La	0.75	86.72	0.64
Nd	0.29	103.35	0.75
Eu	0.79	1121.86	0.77

GA5MA

REEs	Langmuir			Freundlich			Temkin		
	Q_o	K_L (L/mg)	R_L^2	K_f (L/g)	n	R_F^2	A (L/g)	B (J/mol)	R_T^2
Sc	145.14	0.023	0.91	10.1	2.01	0.94	0.30	28.46	0.88
Y	144.72	0.034	0.84	30.90	4.34	0.68	8.51	13.61	0.55
La	108.69	0.05	0.94	24.75	3.87	0.89	3.28	14.14	0.78
Ce	116.82	0.06	0.90	39.68	6.32	0.74	114.97	9.02	0.59
Nd	141.44	0.053	0.94	20.46	2.59	0.94	1.01	24.48	0.87

Eu	111.73	0.102	0.97	40.30	5.74	0.88	74.41	10.05	0.75

Zr@XG-ZA

REEs	Langmuir			Freundlich		
	Q_o	K_L (L/mg)	R_L^2	K_f (L/g)	n	R_F^2
Sc	76.4	0.48	0.96	1.93	24.96	0.99
Nd	38.42	1.21	0.58	1.63	1.94	0.98
Tm	31.98	1.51	0.75	2.47	4.93	0.99
Yb	41.25	2.66	0.71	2.29	6.31	0.99

Compared to all the used bio-nanocomposites, GA-g-PAM/SiO_2 showed the least adsorption capacities for REEs (Table 12, Paper II), whereas GA5MA exhibited the highest (Paper IV). The adsorption capacities of REEs followed the order: La < Eu < Ce < Nd < Y < Sc on GA5MA (Paper V) and Nd < Tm < Yb < Sc on Zr@XG-ZA (Paper V). This could be explained by the fact that smaller ionic radii revealed better adsorbing capacities [171]. These results were consistent with the previous findings [17, 124].

Table 12: Maximum adsorption capacities (mg/g) for targeted REEs (Papers I-V)

Targeted	**Bio-nanocomposites**				
REEs	**CL-Zn/Al LDH**	**CLN/SiO_2**	**GA-g-PAM/SiO_2**	**GA5MA**	**Zr@XG-ZA**
Sc		96.25	11.05	145.13	132.3
Y	102.25			144.72	
La	92.51	23.76	7.9	108.69	
Ce	96.25			116.82	
Eu		29.48	10.11	141.44	
Nd			12.24	111.73	14.01
Tm					18.15
Yb					25.73

4.2.6. Thermodynamics

The results for the thermodynamic parameters calculated using equations listed in Section 3.5.3. are tabulated in Table 13. An increase in the adsorption of REEs over bio-nanocomposites was observed with a rise in temperature. The spontaneity of the adsorption process was indicated by the obtained negative or decreasing values of ΔG^o (Papers I-V). Moreover, the results in Table 13 show that the values of ΔH^o are positive for all cases pointing towards the endothermic adsorption process (Papers I-V). The values of $\Delta H^o < 50$ KJ/mol suggested the chemisorption process and vice versa [103, 172, 173]**.** The physisorption process was recommended based on the values of ΔH^o for REEs adsorption on GA-g-PAM/SiO_2 and the results are in line with the kinetic study (Paper III). Notably, the different behaviour of Sc towards CLN/SiO_2 compared to La and Eu (Paper II) was probably due to lanthanide contraction [174]. The positive ΔS^o values in Table 13 represents the increase in randomness over the solid-liquid interface (Papers I-V).

Table 13: Thermodynamic parameters for targeted REEs (I-V)

Bio-nanocomposites	Targeted REEs	ΔH^o (kJ/mol)	ΔS^o (J/mol/K)	ΔG^o (kJ/mol)			
				293K	**303K**	**313K**	**323K**
CL-Zn/Al LDH	Y	61.77	222.07	-5.10	-6.03	-6.35	-12.72
	La	50.73	276.81	-15.54	-16.14	-17.69	-19.69
	Ce	58.49	266.78	-9.61	-11.6	-12.40	-13.76
				293K	**303K**	**313K**	**323K**
CLN/SiO_2	Sc	24.12	82.42	-0.75	-4.69	-14.23	-19.12
	La	188.95	644.96	-1.89	-5.88	-8.86	-14.51
	Eu	137.92	470.07	-1.91	-3.16	-4.90	-17.48
				298K	**308K**	**318K**	**328K**
GA-g-PAM/SiO_2	Sc	46.37	157.47	-1.10	-1.41	-3.36	-5.79
	La	32.57	110.14	-0.15	-1.35	-2.82	-3.31
	Eu	12.55	54.92	-3.98	-4.29	-4.53	-5.77
	Nd	41.33	138.51	-0.13	-0.86	-3.15	-3.99

				293K	303K	313K	323K
GA5MA	Sc	62.49	231.56	7.05	7.58	-12.02	-13.32
	Y	78.33	276.16	-2.63	-9.01	-9.19	-11.60
	La	52.12	98.03	-7.84	-9.04	-9.45	-10.98
	Ce	87.55	306.93	-4.5	-6.79	-8.51	-14.30
	Eu	79.87	296.72	-3.29	-4.51	-6.61	-15.41
	Nd	109.94	375.08	-7.79	-12.69	-14.59	-16.94
				298K	**308K**	**318K**	**328K**
Zr@XG-ZA	Sc	105.4	357.93	-1.98	-4.34	-7.11	-13.13
	Nd	51.53	166.85	1.64	0.42	-1.41	-3.37
	Tm	53.62	184.25	-1.34	-2.91	-5.23	-6.17
	Yb	160.78	535.28	-0.83	-2.71	-5.19	-18.32

4.2.7. REE speciation

The concentration distribution of REEs over the pH range of 1 to 13, computed by Visual MINTEQ 3.1 is shown in Figure 16 below, according to which the REEs can form the mentioned species complexes. It can be seen that in speciation study all the REEs demonstrate similar behaviour except Sc. Until pH value of 6-7, Y^{3+}, La^{3+}, Ce^{3+}, Eu^{3+}, Nd^{3+}, Tm^{3+} and Yb^{3+} are the predominant species present in the solution. With a further increase in the pH, the corresponding ionic species of the REEs exist as YOH^{2+}, $LaOH^{2+}$, $CeOH^{2+}$, $EuOH^{2+}$, $NdOH^{2+}$, $TmOH^{2+}$ and $YbOH^{2+}$, reaching the maximum concentration around pH value of 9 to 10. It has to be noted that there are negligible traces of $Y_2(OH)_2^{4+}$ ionic species present in case of Y over the studied pH range. Likewise, the other ionic species of Nd present from pH 7 to 13 are $Nd_2(OH)_2^{4+}$ and $Nd(OH)^{4-}$, while below pH 7 the concentration is very less. Unlike other REEs discussed earlier, Sc exists as multiple ionic species over the entire pH range. Sc^{3+} are distributed until pH of 5 above which the hydroxo complexes are formed. Though the predominant ionic form of Sc at pH > 9 is $Sc(OH)^{4-}$, in the pH range of 4 to 9 it exists simultaneously as $Sc(OH)^{2+}$, $Sc(OH)_3$ (aq) and $ScOH^{2+}$ as well. This might be the reason of different behaviour of Sc compared to other REEs observed over various bio-nanocomposites (Paper II-V).

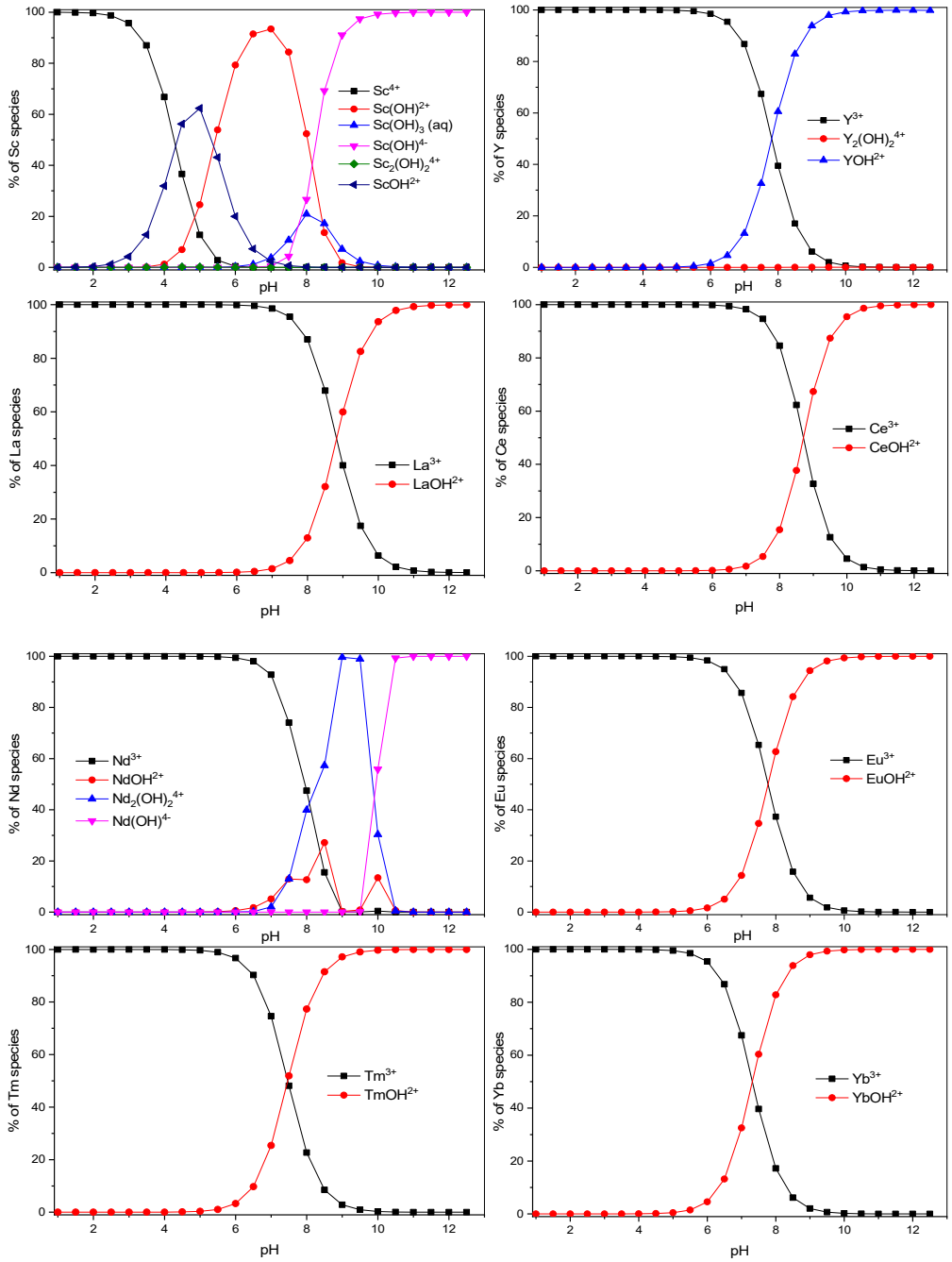

Figure 16: Speciation diagrams of Sc, Y, La, Ce, Nd, Eu, Tm and Yb over pH range of 1-13

4.2.8. Adsorption in the multi-component system

In Paper I, adsorption in a bi-solute system was studied and the adsorption of Y was always less than La and Ce. In Paper IV, 10 mg/L concentration of Sc, Y, La, Ce, Nd and Eu was used to check their affinities on GA5MA, GA5CA, GA5SA and GA5BA. The adsorption in the multi-component system was found to be competitive and significant Sc adsorption was noticed compared to Y and La. The adsorption on hybrids followed the order GA5BA < GA5SA < GA5CA < GA5MA and indicates that the smaller the ionic size of divalent interlayer ions, the better the adsorption of REEs. In Paper V, multi-component adsorption studies were carried out as a function of the pH, time, temperature and REE concentration. Sc demonstrated a higher adsorption and the adsorption in the multi-component system was higher than the single system at pH 4 and 6. However, with rise in temperature from 298-328 K, Sc showed the least sensitivity towards the rise in temperature with negligible effect, whereas Nd had a positive impact on removal. When the experiments were conducted as a function of REEs concentration, the results were different at different concentrations. At the initial REE concentration of 1 mg/L, Sc and Nd showed more removal compared to Tm and Yb. This trend shifted towards Tm and Yb when the concentration was increased to 5 mg/L and 10 mg/L. The comparable shift of trend was reported for adsorption in a multi-component system as a function of the REEs concentration on SEP and SEA [156].

4.2.9. Effect of competing ions

The presence of other cations might influence the adsorption of REEs on bio-nanocomposites. To investigate the effect of competing ions, adsorption experiments were conducted in the presence of a tenfold (Papers I and II) and fivefold (Paper IV) concentration of mono, di and trivalent ions. A decree in 8-10% in the removal of REEs on CL-Zn/Al LDH and CLN/SiO_2 in the presence of Na, K, Ca, Mg and Al ions were mainly due to Al ions which bear a similar ionic charge (Papers I and II).

The similar experiments were performed in a multi-component system with competing ions (Figure 17). The negligible effect on the adsorption of REEs was noticed due to the presence of monovalent ions (Na), whereas, removal was ensued slightly by divalent ions (Ca and Mg). On the other hand, adsorption was hampered significantly due to trivalent ions i.e. Al. In addition,

Sc removal was higher compared to other REEs in the presence of competing ions in the multi-component system (Paper IV).

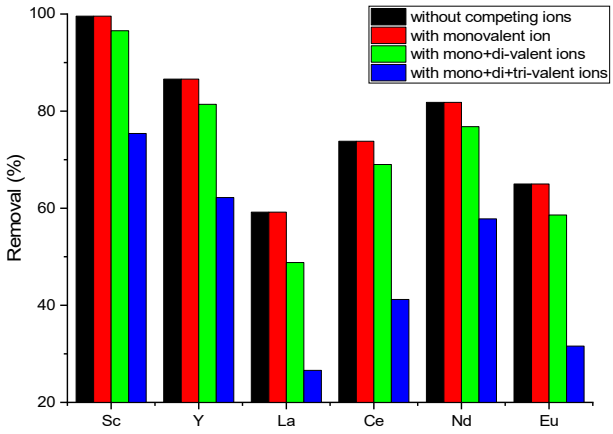

Figure 17: Effect of competing ions on the adsorption of REEs on GA5MA in multi-component

4.2.10. Intra-series adsorption behaviour of REEs

To investigate the REEs affinities towards bio-nanocomposites, intra-series adsorption experiments were performed both in a single and multi-component system (Papers I and IV). The overall removal of REEs on CL-Zn/Al LDH remains above 90% (Papers I).

Furthermore, to investigate the affinities of REEs towards GA5MA, GA5CA, GA5SA and GA5BA, the intra-series adsorption behaviour was performed in the multi-component system with an initial REE concentration of 10 mg/L. The trend obtained is shown in Figure 18. GA5MA compared to the others exhibited the highest REEs removal at pH 4. For all four exfoliated hybrids, La presented the least and Sc the highest adsorption and trend showed the increment w.r.t increasing atomic number. Furthermore, HREEs except Y seems to be more selective over the materials. The similar results were reported by other researchers [139, 156]. In addition, the adsorption of REEs seems to be affected by the size of divalent ions present in the interlayers of

LDH i.e. increasing the size of divalent ions results in lower REEs removal. The REEs tetrad effect found to be possibly responsible for zigzag pattern [175] (Paper IV).

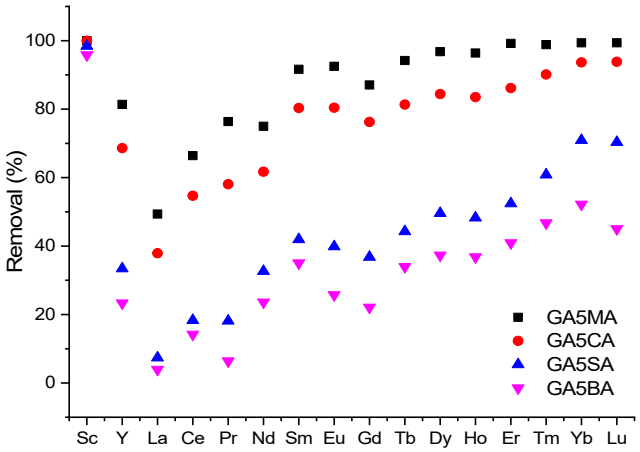

Figure 18: Multi-component intra-series adsorption trend of REEs

4.2.11. Desorption studies:

The reusability of the bio-nanocomposites is an important factor towards its potential use. REEs was desorbed from bio-nanocomposites using various desorbing mediums. In Paper I, REEs (Y, La and Ce) were desorbed effectively from CL-Zn/Al LDH using 0.1 M HCl. The CL-Zn/Al LDH was used up to five cycles and showed good removal efficiency towards REEs. For Sc, La and Eu desorption from CLN/SiO_2, different concentrations of NaOH and HCl was used to find out the better desorbing eluent. The results showed with 0.5 M HCl material could be used up to three cycles (Paper III). Similarly, 0.1 M HCl was selected as a desorbing medium to desorb Sc, La, Eu and Nd from GA-g-PAM/SiO_2 and removal decreased up to 50-55% after three cycles (Paper III). In Paper IV, GA5MA was reused up to eight (08) adsorption-desorption cycles and the removal rate of REEs was decreased in each cycle. The reason for this decrease is the incomplete desorption of REEs from GA5MA and hydraulic sheer force of the adsorption process which damages the surface of GA5MA and thus reduces the REEs removal. The results of the desorption study in Paper V revealed that REEs removal decreased up to 50% at fifth cycle using 0.1 M HNO_3 (Figure

5a in Paper V). It was reported that the decrease in adsorption in each cycle is due to the leaching of Zn from LDH resulting in damage to Zr@XG-ZA structure. In addition, after five cycles, the leftover Zr@XG-ZA was used as a photocatalyst for the degradation of tetracycline using H_2O_2 and PMS as oxidants. Although, nano-based materials do not produce the large volume of waste, however, the used material was reused efficiently for the degradation of tetracycline (Figure 5b in Paper V).

Compared to other bio-nanocomposites, GA5MA showed the potential to be used up to eighth cycles (Paper IV), whereas, SiO_2 based bio-nanocomposites (Papers II and III) showed the least.

4.2.12. Adsorption Mechanism

The adsorption mechanism of REEs on GA5MA and Zr@XG-ZA was suggested in Papers IV and V. The possible mechanism of REEs binding on GA5MA and Zr@XG-ZA might be electrostatic interaction, surface complexation with functional groups and ion exchange. From the results of pH and zeta potential, the surface of GA5MA and Zr@XG-ZA became negative above pH 2.65 and 3.2, respectively manifesting to electrostatic interaction with REEs (Papers IV and V).

The post adsorption FTIR spectra of GA5MA and Zr@XG-ZA pointed towards the surface complexation/chelation of REEs with surface functional groups of GA5MA and Zr@XG-ZA which served as active sites (Papers IV and V). In Paper IV, the carboxyl functional groups served as binding sites as the FTIR bands at 2900 and 1750 cm^{-1} disappeared while other shifted towards lower wavenumbers (Figure SF6 in Paper IV). Likewise, the band corresponding to the carboxylate group was missing and many other peaks shifted to lower wavenumbers in Paper V (Figure SF6a). This ascribed towards REEs binding with COO^- and –OH groups via electrostatic interaction and surface complexation with neighbouring groups (as proposed in Scheme 2 in Paper V). In addition, the binding of REEs with –OH groups of LDH occurred via ion exchange. Therefore, it could be concluded that none of the processes were exclusive and they occurred simultaneously.

In Papers IV and V, the SEM images of GA5MA and Zr@XG-ZA after adsorption illustrated the change in the morphology of materials (Figure SF5 in Paper IV and Figure SF6b-e in Paper V).

Furthermore, the EDX spectra shown in Figure SF6f-i in Paper V confirmed the REEs adsorption over Zr@XG-ZA. The uniform distribution of REEs was also observed in the elemental mapping of Zr@XG-ZA in Figure SF7 in Paper V.

5. Conclusion

The adsorption of REEs from the aqueous medium by five different bio-nanocomposites synthesised using cellulose, gum Arabic and xanthan gum as an organic matrix and LDH and SiO_2 as an inorganic matrix was investigated in this thesis. The bio-nanocomposites, including cellulose intercalated zinc-aluminium LDH (CL-Zn/Al LDH), sulfuric acid modified cellulose based silica nanocomposite (CLN/SiO_2), Gum Arabic grafted polyacrylamide based silica (GA-g-PAM/SiO_2), exfoliated biopolymeric-LDH (GA-LDH) and LDH encapsulated in xanthan gum anchored by metal ions (M@XG-ZA) nanocomposites, were used to study the adsorptive behaviour towards REEs.

The bio-nanocomposites were characterised by an XRD, FTIR, TEM, SEM, EDX, AFM, BET and elemental analyser to verify the surface functional groups, morphology and surface areas. TEM analysis confirmed that all the synthesised materials were in the nano range, whereas the morphologies differ due to different organic and inorganic matrices, which was also shown by the SEM results. The FTIR analysis confirmed the presence of various functional groups.

Experiments were performed in batch mode to optimise various operating parameters in order to attain the maximum removal of REEs. Overall, the bio-nanocomposites exhibited the potential for REEs adsorption. The information regarding surface properties, nature and adsorption mechanism was obtained by using various adsorption isotherm and kinetic models.

The results and major findings of this thesis are presented below:

I. The application of CL and GA with LDH based bio-nanocomposites for the removal of REEs exhibited promising results compared to other used materials. However, the size of the LDH interlayer divalent ion plays a major role in REEs adsorption, i.e. increasing the interlayer ionic size resulted in lower REEs removal. The modification of CL and grafting of PAM chain on the GA backbone did not exhibit good results due to the blockage of the functional groups (carboxyl and amines) after SiO_2 incorporation. This indicated that the active sites were blocked if SiO_2 was present towards the outer edges of the material. Therefore, it

could be concluded that the selection of organic/inorganic matrix and method of synthesis is very important.

II. The adsorption of REEs was found to be pH dependent and a fast removal of REEs was demonstrated by all bio-nanocomposites. The dose requirements seem to be lesser for LDH based bio-nanocomposites compared to SiO_2 materials. Moreover, the highest adsorption capacities of REEs was offered by exfoliated GA5MA.

III. The presence of tri-valent ions affects the adsorption of REEs, whereas, mono-valent had a negligible influence. In multi-component system, Sc exhibit higher adsorption and La the least. Furthermore, LREEs removal was lesser than HREEs. In terms of reusability of material, LDH based hybrids showed better potential compared to SiO_2 based bio-nanocomposites.

The results of this work can serve as a foundation for further research in the future. These bio-nanocomposites provide good alternatives to replace the expensive commercially available materials. These bio-nanocomposites can be studied in column tests prior to their application at the pilot or industrial scale. Future studies will also focus on developing the ways to enhance the adsorptive capacities of SiO_2 based bio-nanocomposites towards REEs. Moreover, other organic and inorganic matrices will be explored for the synthesis of bio-nanocomposites. The bio-nanocomposites will also be tested for the removal and recovery of REEs from acid mine drainage (AMD) wastewater and from seawater. In addition, the application of these bio-nanocomposites in technologies like capacitive deionisation (CDI) and electrodeionisation processes (EDI) need to be studied in the years to come to investigate the potential of this ever-growing and flourishing domain.

References

[1] N.G. Connelly, R.M. Hartshorn, T. Damhus, A.T. Hutton, Nomenclature of inorganic chemistry: IUPAC recommendations 2005, Royal Society of Chemistry2005.

[2] B.S. Van Gosen, P.L. Verplanck, K.R. Long, J. Gambogi, R.R. Seal II, The rare-earth elements: vital to modern technologies and lifestyles, US Geological Survey, 2014.

[3] J. Hedrick, US Geological Survey 2007 minerals yearbook: rare earths, 2007.

[4] A. Jordens, Y.P. Cheng, K.E. Waters, A review of the beneficiation of rare earth element bearing minerals, Minerals Engineering 41 (2013) 97-114.

[5] A. Golev, M. Scott, P.D. Erskine, S.H. Ali, G.R. Ballantyne, Rare earths supply chains: Current status, constraints and opportunities, Resources Policy 41 (2014) 52-59.

[6] F. Xie, T.A. Zhang, D. Dreisinger, F. Doyle, A critical review on solvent extraction of rare earths from aqueous solutions, Minerals Engineering 56 (2014) 10-28.

[7] N.N.E. Greenwood, N. Earnshaw, Alan," Chemistry of the Elements, Oxford, Pergamon Press, 1984.

[8] K.R. Long, B.S. Van Gosen, N.K. Foley, D. Cordier, The principal rare earth elements deposits of the United States: a summary of domestic deposits and a global perspective, Non-Renewable Resource Issues, Springer, 2012, pp. 131-155.

[9] T. Dutta, K.-H. Kim, M. Uchimiya, E.E. Kwon, B.-H. Jeon, A. Deep, S.-T. Yun, Global demand for rare earth resources and strategies for green mining, Environmental Research 150 (2016) 182-190.

[10] G.B. Haxel, J.B. Hedrick, G.J. Orris, P.H. Stauffer, J.W. Hendley II, Rare earth elements: critical resources for high technology, 2002.

[11] G. Tyler, Rare earth elements in soil and plant systems-A review, Plant and Soil 267 (2004) 191-206.

[12] R.L. Rudnick, S. Gao, Composition of the continental crust, Treatise on Geochemistry 3 (2003) 659.

[13] E. Machacek, P. Kalvig, Assessing advanced rare earth element-bearing deposits for industrial demand in the EU, Resources Policy 49 (2016) 186-203.

[14] B. Zhou, Z. Li, C. Chen, Global Potential of Rare Earth Resources and Rare Earth Demand from Clean Technologies, Minerals 7 (2017) 203.

[15] D. Sadovsky, A. Brenner, B. Astrachan, B. Asaf, R. Gonen, Biosorption potential of cerium ions using *Spirulina* biomass, Journal of Rare Earths 34 (2016) 644-652.

[16] J. Ponou, L.P. Wang, G. Dodbiba, K. Okaya, T. Fujita, K. Mitsuhashi, T. Atarashi, G. Satoh, M. Noda, Recovery of rare earth elements from aqueous solution obtained from Vietnamese clay minerals using dried and carbonized parachlorella, Journal of Environmental Chemical Engineering 2 (2014) 1070-1081.

[17] F. Zhao, E. Repo, Y. Meng, X. Wang, D. Yin, M. Sillanpää, An EDTA-β-cyclodextrin material for the adsorption of rare earth elements and its application in preconcentration of rare earth elements in seawater, Journal of Colloid and Interface Science 465 (2016) 215-224.

[18] D. Kingsnorth, Rare earths: is supply critical in 2013?, Proceedings of the Critical Minerals Conference Perth (AusIMM'13), 2013.

[19] G.J. Orris, R.I. Grauch, Rare earth element mines, deposits and occurrences, US Department of the Interior, US Geological Survey2002.

[20] K. Long, B. Van Gosen, N. Foley, D. Cordier, The Principal Rare Earth Elements Deposits of the United States; A Summary of Domestic Deposits and a Global Perspective: USGS. Scientific Investigations Report, 2010–5220, 2010.

[21] K. Goodenough, J. Schilling, E. Jonsson, P. Kalvig, N. Charles, J. Tuduri, E. Deady, M. Sadeghi, H. Schiellerup, A. Müller, Europe's rare earth element resource potential: An overview of REE metallogenetic provinces and their geodynamic setting, Ore Geology Reviews 72 (2016) 838-856.

[22] V. Zaitsev, L. Kogarko, Sources and perspectives of REE in the Lovozero massif (Kola Peninsula, Russia), European Mineralogical Conference, 2012, pp. EMC2012-EMC2290.

[23] Y. Kanazawa, M. Kamitani, Rare earth minerals and resources in the world, Journal of Alloys and Compounds 408 (2006) 1339-1343.

[24] C. Gupta, N. Krishnamurthy, Extractive Metallurgy of Rare Earths CRC Press, ISBN: 0–415-33340-7, 2005.

[25] Y.A. Vereschagin, N. Kudrevatykh, M. Malygin, T. Emelina, Rare-earth magnets in Russia: raw materials, processing, properties control and output issues, Journal of Iron and Steel Research, International 13 (2006) 23-32.

[26] R. Chi, S. Xu, G. Zhu, J. Xu, X. Qiu, Beneficiation of rare earth ore in china, Light Metals 2001 as held at the 130th TMS Annual Meeting, 2001, pp. 1159-1165.

[27] K. Binnemans, P.T. Jones, B. Blanpain, T. Van Gerven, Y. Yang, A. Walton, M. Buchert, Recycling of rare earths: a critical review, Journal of cleaner production 51 (2013) 1-22.

[28] M. Humphries, Rare earth elements: the global supply chain, Diane Publishing2010.

[29] United States Geological Survey mineral commodity summaries (Rare Earth) 2016., 2016.

[30] D. Guyonnet, M. Planchon, A. Rollat, V. Escalon, J. Tuduri, N. Charles, S. Vaxelaire, D. Dubois, H. Fargier, Material flow analysis applied to rare earth elements in Europe, Journal of Cleaner Production 107 (2015) 215-228.

[31] K. Binnemans, P.T. Jones, K. Van Acker, B. Blanpain, B. Mishra, D. Apelian, Rare-earth economics: the balance problem, The Journal of The Minerals, Metals & Materials Society 65 (2013) 846-848.

[32] A. Akcil, S. Koldas, Acid Mine Drainage (AMD): causes, treatment and case studies, Journal of Cleaner Production 14 (2006) 1139-1145.

[33] J. Delgado, R. Pérez-López, L. Galván, J.M. Nieto, T. Boski, Enrichment of rare earth elements as environmental tracers of contamination by acid mine drainage in salt marshes: a new perspective, Marine Pollution Bulletin 64 (2012) 1799-1808.

[34] K. Binnemans, P.T. Jones, B. Blanpain, T. Van Gerven, Y. Pontikes, Towards zero-waste valorisation of rare-earth-containing industrial process residues: a critical review, Journal of Cleaner Production 99 (2015) 17-38.

[35] F. Fu, Q. Wang, Removal of heavy metal ions from wastewaters: a review, Journal of Environmental Management 92 (2011) 407-418.

[36] R. Geremias, R. Pedrosa, J. Benassi, V. Favere, J. Stolberg, C. Menezes, M. Laranjeira, Remediation of coal mining wastewaters using chitosan microspheres, Environmental Technology 24 (2003) 1509-1515.

[37] G. Pagano, M. Guida, F. Tommasi, R. Oral, Health effects and toxicity mechanisms of rare earth elements—Knowledge gaps and research prospects, Ecotoxicology and Environmental Safety 115 (2015) 40-48.

[38] S. Hirano, K.T. Suzuki, Exposure, metabolism, and toxicity of rare earths and related compounds, Environmental Health Perspectives 104 (1996) 85.

[39] G. Protano, F. Riccobono, High contents of rare earth elements (REEs) in stream waters of a Cu–Pb–Zn mining area, Environmental Pollution 117 (2002) 499-514.

[40] T. Liang, S. Zhang, L. Wang, H.-T. Kung, Y. Wang, A. Hu, S. Ding, Environmental biogeochemical behaviors of rare earth elements in soil–plant systems, Environmental Geochemistry and Health 27 (2005) 301-311.

[41] M. He, D. Ranz, W. Rambeck, Study on the performance enhancing effect of rare earth elements in growing and fattening pigs, Journal of Animal Physiology and Animal Nutrition 85 (2001) 263-270.

[42] V. Gonzalez, D.A. Vignati, C. Leyval, L. Giamberini, Environmental fate and ecotoxicity of lanthanides: are they a uniform group beyond chemistry?, Environment International 71 (2014) 148-157.

[43] G. Pagano, F. Aliberti, M. Guida, R. Oral, A. Siciliano, M. Trifuoggi, F. Tommasi, Rare earth elements in human and animal health: state of art and research priorities, Environmental Research 142 (2015) 215-220.

[44] C. Tunsu, M. Petranikova, M. Gergorić, C. Ekberg, T. Retegan, Reclaiming rare earth elements from end-of-life products: a review of the perspectives for urban mining using hydrometallurgical unit operations, Hydrometallurgy 156 (2015) 239-258.

[45] V. Innocenzi, I. De Michelis, F. Ferella, F. Vegliò, Recovery of yttrium from cathode ray tubes and lamps' fluorescent powders: experimental results and economic simulation, Waste Management 33 (2013) 2390-2396.

[46] I. De Michelis, F. Ferella, E.F. Varelli, F. Vegliò, Treatment of exhaust fluorescent lamps to recover yttrium: Experimental and process analyses, Waste Management 31 (2011) 2559-2568.

[47] J.P. Rabatho, W. Tongamp, Y. Takasaki, K. Haga, A. Shibayama, Recovery of Nd and Dy from rare earth magnetic waste sludge by hydrometallurgical process, Journal of Material Cycles and Waste Management 15 (2013) 171-178.

[48] T. Vander Hoogerstraete, B. Blanpain, T. Van Gerven, K. Binnemans, From NdFeB magnets towards the rare-earth oxides: a recycling process consuming only oxalic acid, RSC Advances 4 (2014) 64099-64111.

[49] X. Wang, G. Mei, C. Zhao, Y. Lei, Notice of Retraction Recovery of Rare Earths from Spent Fluorescent Lamps, 5th International Conference on Bioinformatics and Biomedical Engineering (iCBBE) 2011, IEEE, 2011, pp. 1-4.

[50] R. Otto, A. Wojtalewicz-Kasprzak, Method for recovery of rare earths from fluorescent lamps, Google Patents, 2011.

[51] W. Fang, S.-M. Xu, L.-Y. Li, S.-Z. Chen, X. Gang, J.-M. Xu, Recovery of valuable metals from anode material of hydrogen-nickel battery, Transactions of Nonferrous Metals Society of China 19 (2009) 468-473.

[52] L. Li, S. Xu, Z. Ju, F. Wu, Recovery of Ni, Co and rare earths from spent Ni–metal hydride batteries and preparation of spherical Ni (OH) 2, Hydrometallurgy 100 (2009) 41-46.

[53] V. Innocenzi, F. Vegliò, Recovery of rare earths and base metals from spent nickel-metal hydride batteries by sequential sulphuric acid leaching and selective precipitations, Journal of Power Sources 211 (2012) 184-191.

[54] L. Pietrelli, B. Bellomo, D. Fontana, M. Montereali, Rare earths recovery from NiMH spent batteries, Hydrometallurgy 66 (2002) 135-139.

[55] J. Nan, D. Han, M. Yang, M. Cui, X. Hou, Recovery of metal values from a mixture of spent lithium-ion batteries and nickel-metal hydride batteries, Hydrometallurgy 84 (2006) 75-80.

[56] C.-H. Lee, Y.-J. Chen, C.-H. Liao, S.R. Popuri, S.-L. Tsai, C.-E. Hung, Selective leaching process for neodymium recovery from scrap Nd-Fe-B magnet, Metallurgical and Materials Transactions A 44 (2013) 5825-5833.

[57] H. Koshimura, Recovery of samarium from scrap of samarium–cobalt alloy with double salt of samarium sulfate, Report of Tokyo Metropolitan Industrial Technology Center, 1987, pp. 113-118.

[58] H. Onoda, R. Nakamura, Recovery of neodymium from an iron–neodymium solution using phosphoric acid, Journal of Environmental Chemical Engineering 2 (2014) 1186-1190.

[59] M.K. Jha, A. Kumari, R. Panda, J.R. Kumar, K. Yoo, J.Y. Lee, Review on hydrometallurgical recovery of rare earth metals, Hydrometallurgy 165 (2016) 2-26.

[60] L. Deqian, W. Zhonghuai, S. Wenzhong, M. Shulan, M. Gengxiang, Recommended separation processes for ion-absorbed rare earth minerals, Hydrometallurgy'94, Springer, Dordrecht, 1994, pp. 627-634.

[61] D.Q. Li, Chemical engineering problems in hydrometallurgical industry of rare earths, Progress in Chemistry (in Chin.) 7 (1995) 209-213.

[62] W. Li, X. Wang, S. Meng, D. Li, Y. Xiong, Extraction and separation of yttrium from the rare earths with sec-octylphenoxy acetic acid in chloride media, Separation and Purification Technology 54 (2007) 164-169.

[63] Y. Wang, S. Yue, D. Li, M. Jin, C. Li, Solvent extraction of scandium (III), yttrium (III), lanthanides (III), and divalent metal ions with sec-nonylphenoxy acetic acid, Solvent Extraction and Ion Exchange 20 (2002) 701-716.

[64] J. Preston, Solvent extraction of the trivalent lanthanides and yttrium by some 2-bromoalkanoic acids, Solvent Extraction and Ion Exchange 12 (1994) 29-54.

[65] D. Singh, H. Singh, J. Mathur, Extraction of rare earths and yttrium with high molecular weight carboxylic acids, Hydrometallurgy 81 (2006) 174-181.

[66] N.V. Thakur, Rare earth recovery from phosphor, Google Patents, 2013.

[67] G. Cevasco, C. Chiappe, Are ionic liquids a proper solution to current environmental challenges?, Green Chemistry 16 (2014) 2375-2385.

[68] H. Yang, W. Wang, H. Cui, D. Zhang, Y. Liu, J. Chen, Recovery of rare earth elements from simulated fluorescent powder using bifunctional ionic liquid extractants (Bif-ILEs), Journal of Chemical Technology & Biotechnology 87 (2012) 198-205.

[69] F. Yang, F. Kubota, Y. Baba, N. Kamiya, M. Goto, Selective extraction and recovery of rare earth metals from phosphor powders in waste fluorescent lamps using an ionic liquid system, Journal of Hazardous Materials 254 (2013) 79-88.

[70] A.A. Tolba, S.I. Mohamady, S.S. Hussin, T. Akashi, Y. Sakai, A.A. Galhoum, E. Guibal, Synthesis and characterization of poly (carboxymethyl)-cellulose for enhanced La (III) sorption, Carbohydrate polymers 157 (2017) 1809-1820.

[71] B. Esma, A. Omar, D.M. Amine, Comparative study on lanthanum (III) sorption onto Lewatit TP 207 and Lewatit TP 260, Journal of Radioanalytical and Nuclear Chemistry 299 (2014) 439-446.

[72] T. Arai, Y. Wei, M. Kumagai, K. Horiguchi, Separation of rare earths in nitric acid medium by a novel silica-based pyridinium anion exchange resin, Journal of alloys and compounds 408 (2006) 1008-1012.

[73] F. Gode, E. Pehlivan, Removal of chromium (III) from aqueous solutions using Lewatit S 100: the effect of pH, time, metal concentration and temperature, Journal of Hazardous Materials 136 (2006) 330-337.

[74] F.W. Strelow, R. Rethemeyer, C. Bothma, Ion Exchange Selectivity Scales for Cations in Nitric Acid and Sulfuric Acid Media with a Sulfonated Polystyrene Resin, Analytical Chemistry 37 (1965) 106-111.

[75] F. Strelow, C. Baxter, Separation of tervalent rare earths and scandium from aluminium, iron (III), titanium (IV), and other elements by cation-exchange chromatography in hydrochloric acid-ethanol, Talanta 16 (1969) 1145-1151.

[76] C. Koopman, G. Witkamp, Extraction of lanthanides from the phosphoric acid production process to gain a purified gypsum and a valuable lanthanide by-product, Hydrometallurgy 58 (2000) 51-60.

[77] N. Shokobayev, C. Bouffier, T. Dauletbakov, Rare earth metals sorption recovery from uranium in situ leaching process solutions, Rare Metals 34 (2015) 195-201.

[78] S. Al-Thyabat, P. Zhang, In-line extraction of REE from Dihydrate (DH) and HemiDihydrate (HDH) wet processes, Hydrometallurgy 153 (2015) 30-37.

[79] M. Patel, M. Kapadia, G. Patel, J. Joshi, Synthesis, characterization, ion-exchange and antimicrobial study of poly [(2-hydroxy-4-methoxy benzophenone) ethylene] resin and its polychelates with lanthanides (III), Reactive and Functional Polymers 67 (2007) 746-757.

[80] C. Xiong, L. Xiaozheng, Y. Caiping, Effect of pH on sorption for RE (III) and sorption behaviors of Sm (III) by D152 resin, Journal of Rare Earths 26 (2008) 851-856.

[81] C. XIONG, M. Yuan, Y. Caiping, S. Chen, Adsorption of erbium (III) on D113-III resin from aqueous solutions: batch and column studies, Journal of Rare Earths 27 (2009) 923-931.

[82] Z. Hubicki, D. Kołodyńska, Selective removal of heavy metal ions from waters and waste waters using ion exchange methods, Ion Exchange Technologies, InTech, 2012.

[83] A. Jyo, K. Yamabe, H. Egawa, Metal ion selectivity of a macroreticular styrene-divinylbenzene copolymer-based methylenephosphonic acid resin, Separation science and technology 32 (1997) 1099-1105.

[84] K. Yamabe, T. Ihara, A. Jyo, Metal ion selectivity of macroreticular chelating cation exchange resins with phosphonic acid groups attached to phenyl groups of a styrene-divinylbenzene copolymer matrix, Separation science and technology 36 (2001) 3511-3528.

[85] C. Xiong, C. Yao, Y. Wang, Sorption behaviour and mechanism of ytterbium (III) on imino-diacetic acid resin, Hydrometallurgy 82 (2006) 190-194.

[86] M.J. Page, K. Soldenhoff, M.D. Ogden, Comparative study of the application of chelating resins for rare earth recovery, Hydrometallurgy 169 (2017) 275-281.

[87] K.L. Ang, D. Li, A.N. Nikoloski, The effectiveness of ion exchange resins in separating uranium and thorium from rare earth elements in acidic aqueous sulfate media. Part 1. Anionic and cationic resins, Hydrometallurgy 174 (2017) 147-155.

[88] T. Suzuki, K. Itoh, A. Ikeda, M. Aida, M. Ozawa, Y. Fujii, Separation of rare earth elements by tertiary pyridine type resin, Journal of Alloys and Compounds 408 (2006) 1013-1016.

[89] J. Ludek, Y. Wei, K. Mikio, Adsorption of Ce (IV) anionic nitrato complexes onto anion exchangers and its application for Ce (IV) separation from rare earths (III), Journal of Rare Earths 24 (2006) 385-391.

[90] Z. Wang, G. Ma, D. Li, Extraction and separation of heavy rare earth (III) with extraction resin containing di (2, 4, 4-trimethyl pentyl) phosphinic acid (Cyanex 272), Solvent Extraction and Ion Exchange 16 (1998) 813-828.

[91] Z. Wang, G. Ma, J. Lu, W. Liao, D. Li, Separation of heavy rare earth elements with extraction resin containing 1-hexyl-4-ethyloctyl isopropylphosphonic acid, Hydrometallurgy 66 (2002) 95-99.

[92] Q. Jia, Z. Wang, D. Li, C. Niu, Adsorption of heavy rare earth (III) with extraction resin containing bis (2, 4, 4-trimethylpentyl) monothiophosphinic acid, Journal of Alloys and Compounds 374 (2004) 434-437.

[93] M. Barakat, New trends in removing heavy metals from industrial wastewater, Arabian Journal of Chemistry 4 (2011) 361-377.

[94] V. Diniz, B. Volesky, Biosorption of La, Eu and Yb using *sargassum* biomass, Water Research 39 (2005) 239-247.

[95] V. Diniz, B. Volesky, Effect of counterions on lanthanum biosorption by *Sargassum polycystum*, Water research 39 (2005) 2229-2236.

[96] N. Awwad, H. Gad, M. Ahmad, H. Aly, Sorption of lanthanum and erbium from aqueous solution by activated carbon prepared from rice husk, Colloids and Surfaces B: Biointerfaces 81 (2010) 593-599.

[97] D. Wu, Y. Sun, Q. Wang, Adsorption of lanthanum (III) from aqueous solution using 2-ethylhexyl phosphonic acid mono-2-ethylhexyl ester-grafted magnetic silica nanocomposites, Journal of hazardous materials 260 (2013) 409-419.

[98] S. Pal, S. Ghorai, C. Das, S. Samrat, A. Ghosh, A.B. Panda, Carboxymethyl tamarind-g-poly (acrylamide)/silica: a high performance hybrid nanocomposite for adsorption of methylene blue dye, Industrial & Engineering Chemistry Research 51 (2012) 15546-15556.

[99] S. Zhang, F. Xu, Y. Wang, W. Zhang, X. Peng, F. Pepe, Silica modified calcium alginate–xanthan gum hybrid bead composites for the removal and recovery of Pb (II) from aqueous solution, Chemical engineering journal 234 (2013) 33-42.

[100] S.M.A. Koochaki-Mohammadpour, M. Torab-Mostaedi, A. Talebizadeh-Rafsanjani, F. Naderi-Behdani, Adsorption isotherm, kinetic, thermodynamic, and desorption studies of lanthanum and dysprosium on oxidized multiwalled carbon nanotubes, Journal of Dispersion Science and Technology 35 (2014) 244-254.

[101] Y. Zhu, Y. Zheng, A. Wang, A simple approach to fabricate granular adsorbent for adsorption of rare elements, International journal of biological macromolecules 72 (2015) 410-420.

[102] D. Das, C.J.S. Varshini, N. Das, Recovery of lanthanum (III) from aqueous solution using biosorbents of plant and animal origin: Batch and column studies, Minerals Engineering 69 (2014) 40-56.

[103] Ş. Sert, C. Kütahyali, S. İnan, Z. Talip, B. Çetinkaya, M. Eral, Biosorption of lanthanum and cerium from aqueous solutions by *Platanus orientalis* leaf powder, Hydrometallurgy 90 (2008) 13-18.

[104] C. Kütahyali, Ş. Sert, B. Cetinkaya, S. Inan, M. Eral, Factors affecting lanthanum and cerium biosorption on *Pinus brutia* leaf powder, Separation Science and Technology 45 (2010) 1456-1462.

[105] M.C. Palmieri, B. Volesky, O. Garcia, Biosorption of lanthanum using *Sargassum fluitans* in batch system, Hydrometallurgy 67 (2002) 31-36.

[106] Z. Birungi, E. Chirwa, The kinetics of uptake and recovery of lanthanum using freshwater algae as biosorbents: Comparative analysis, Bioresource technology 160 (2014) 43-51.

[107] D. Das, N. Das, Optimization of parameters for cerium (III) biosorption onto biowaste materials of animal and plant origin using 5-level Box-Behnken design: Equilibrium, kinetic, thermodynamic and regeneration studies, Journal of Rare Earths 32 (2014) 745-758.

[108] V. Anagnostopoulos, B. Symeopoulos, Sorption of europium by malt spent rootlets, a low cost biosorbent: effect of pH, kinetics and equilibrium studies, Journal of Radioanalytical and Nuclear Chemistry 295 (2013) 7-13.

[109] M. Torab-Mostaedi, M. Asadollahzadeh, A. Hemmati, A. Khosravi, Biosorption of lanthanum and cerium from aqueous solutions by grapefruit peel: equilibrium, kinetic and thermodynamic studies, Research on Chemical Intermediates 41 (2015) 559-573.

[110] M. Torab-Mostaedi, Biosorption of lanthanum and cerium from aqueous solutions using tangerine (Citrus reticulata) peel: equilibrium, kinetic and thermodynamic studies, Chemical Industry and Chemical Engineering Quarterly/CICEQ 19 (2013) 79-88.

[111] D. Das, N. Das, Optimization of parameters for praseodymium (III) biosorption onto biowaste materials using response surface methodology: equilibrium, kinetic and regeneration studies, Ecological engineering 81 (2015) 321-327.

[112] M. Prodromou, I. Pashalidis, Europium adsorption by non-treated and chemically modified opuntia ficus indica cactus fibres in aqueous solutions, Desalination and Water Treatment 57 (2016) 5079-5088.

[113] L. Hadjittofi, S. Charalambous, I. Pashalidis, Removal of trivalent samarium from aqueous solutions by activated biochar derived from cactus fibres, Journal of Rare Earths 34 (2016) 99-104.

[114] H. Gad, N. Awwad, Factors affecting on the sorption/desorption of Eu (III) using activated carbon, Separation Science and Technology 42 (2007) 3657-3680.

[115] C. Qing, Study on the adsorption of lanthanum (III) from aqueous solution by bamboo charcoal, Journal of Rare Earths 28 (2010) 125-131.

[116] K. Vijayaraghavan, A. Mahadevan, U.M. Joshi, R. Balasubramanian, An examination of the uptake of lanthanum from aqueous solution by crab shell particles, Chemical Engineering Journal 152 (2009) 116-121.

[117] X. Shuxia, S. Zhang, C. Ke, H. Jinfeng, L. Huashan, W. Kun, Biosorption of La^{3+} and Ce^{3+} by *Agrobacterium sp*. HN1, Journal of Rare Earths 29 (2011) 265-270.

[118] M.R. Bockstaller, R.A. Mickiewicz, E.L. Thomas, Block copolymer nanocomposites: perspectives for tailored functional materials, Advanced Materials 17 (2005) 1331-1349.

[119] H. Hu, L. Onyebueke, A. Abatan, Characterizing and modeling mechanical properties of nanocomposites-review and evaluation, Journal of Minerals and Materials Characterization and Engineering 9 (2010) 275.

[120] M.L. Rahman, T.K. Biswas, S.M. Sarkar, M.M. Yusoff, M.S. Sarjadi, S.E. Arshad, B. Musta, Adsorption of rare earth metals from water using a kenaf cellulose-based poly (hydroxamic acid) ligand, Journal of Molecular Liquids 243 (2017) 616-623.

[121] Y. Zhu, W. Wang, Y. Zheng, F. Wang, A. Wang, Rapid enrichment of rare-earth metals by carboxymethyl cellulose-based open-cellular hydrogel adsorbent from HIPEs template, Carbohydrate Polymers 140 (2016) 51-58.

[122] Y. Zhu, Y. Zheng, A. Wang, Preparation of granular hydrogel composite by the redox couple for efficient and fast adsorption of La (III) and Ce (III), Journal of Environmental Chemical Engineering 3 (2015) 1416-1425.

[123] Q. Zhou, H. Yang, C. Yan, W. Luo, X. Li, J. Zhao, Synthesis of carboxylic acid functionalized diatomite with a micro-villous surface via UV-induced graft polymerization and its adsorption properties for Lanthanum (III) ions, Colloids and Surfaces A: Physicochemical and Engineering Aspects 501 (2016) 9-16.

[124] F. Zhao, E. Repo, Y. Song, D. Yin, S.B. Hammouda, L. Chen, S. Kalliola, J. Tang, K.C. Tam, M. Sillanpää, Polyethylenimine-cross-linked cellulose nanocrystals for highly efficient recovery of rare earth elements from water and a mechanism study, Green Chemistry 19 (2017) 4816-4828.

[125] A. Negrea, A. Gabor, C.M. Davidescu, M. Ciopec, P. Negrea, N. Duteanu, A. Barbulescu, Rare Earth Elements Removal from Water Using Natural Polymers, Scientific reports 8 (2018) 316.

[126] M.O.A. El-Magied, A.A. Galhoum, A.A. Atia, A.A. Tolba, M.S. Maize, T. Vincent, E. Guibal, Cellulose and chitosan derivatives for enhanced sorption of erbium (III), Colloids and Surfaces A: Physicochemical and Engineering Aspects 529 (2017) 580-593.

[127] M.M. Khalil, M. Atrees, A. Abd El Fatah, H. Salem, R. Roshdi, Synthesis and application studies of chitosan acryloylthiourea derivative for the separation of rare earth elements, Journal of Dispersion Science and Technology 39 (2018) 605-613.

[128] F. Wang, J. Zhao, X. Wei, F. Huo, W. Li, Q. Hu, H. Liu, Adsorption of rare earths (III) by calcium alginate–poly glutamic acid hybrid gels, Journal of Chemical Technology & Biotechnology 89 (2014) 969-977.

[129] M.R. Awual, N.H. Alharthi, Y. Okamoto, M.R. Karim, M.E. Halim, M.M. Hasan, M.M. Rahman, M.M. Islam, M.A. Khaleque, M.C. Sheikh, Ligand field effect for Dysprosium (III) and Lutetium (III) adsorption and EXAFS coordination with novel composite nanomaterials, Chemical Engineering Journal 320 (2017) 427-435.

[130] A. Naser, G.S. El-deen, A.A. Bhran, S. Metwally, A. El-Kamash, Elaboration of impregnated composite for sorption of europium and neodymium ions from aqueous solutions, Journal of Industrial and Engineering Chemistry 32 (2015) 264-272.

[131] L. Dolatyari, M.R. Yaftian, S. Rostamnia, Adsorption characteristics of Eu (III) and Th (IV) ions onto modified mesoporous silica SBA-15 materials, Journal of the Taiwan Institute of Chemical Engineers 60 (2016) 174-184.

[132] X. Zheng, C. Wang, J. Dai, W. Shi, Y. Yan, Design of mesoporous silica hybrid materials as sorbents for the selective recovery of rare earth metals, Journal of Materials Chemistry A 3 (2015) 10327-10335.

[133] A. Tadjarodi, V. Jalalat, R. Zare-Dorabei, Adsorption of La (III) in aqueous systems by N-(2-hydroxyethyl) salicylaldimine-functionalized mesoporous silica, Materials Research Bulletin 61 (2015) 113-119.

[134] E. Borai, M. Hamed, A. El-Kamash, T. Siyam, G. El-Sayed, Template polymerization synthesis of hydrogel and silica composite for sorption of some rare earth elements, Journal of colloid and interface science 456 (2015) 228-240.

[135] M. Wang, X. Li, W. Hua, L. Shen, X. Yu, X. Wang, Electrospun Poly (acrylic acid)/silica hydrogel nanofibers scaffold for highly efficient adsorption of Lanthanide ions and its photoluminescence performance, ACS applied materials & interfaces 8 (2016) 23995-24007.

[136] J. Ma, Z. Wang, Y. Shi, Q. Li, Synthesis and characterization of lysine-modified SBA-15 and its selective adsorption of scandium from a solution of rare earth elements, RSC Advances 4 (2014) 41597-41604.

[137] H. Aghayan, A. Mahjoub, A. Khanchi, Samarium and dysprosium removal using 11-molybdo-vanadophosphoric acid supported on Zr modified mesoporous silica SBA-15, Chemical Engineering Journal 225 (2013) 509-519.

[138] Q. Gao, J.-F. Xie, Y.-T. Shao, C. Chen, B. Han, K.-S. Xia, C.-G. Zhou, Ultrafast and high-capacity adsorption of Gd (III) onto inorganic phosphorous acid modified mesoporous SBA-15, Chemical Engineering Journal 313 (2017) 197-206.

[139] D.L. Ramasamy, V. Puhakka, E. Repo, S.B. Hammouda, M. Sillanpää, Two-stage selective recovery process of scandium from the group of rare earth elements in aqueous systems using activated carbon and silica composites: Dual applications by tailoring the ligand grafting approach, Chemical Engineering Journal 341 (2018) 351-360.

[140] F. Wang, J. Zhao, H. Zhou, W. Li, N. Sui, H. Liu, O-carboxymethyl chitosan entrapped by silica: preparation and adsorption behaviour toward neodymium (III) ions, Journal of Chemical Technology & Biotechnology 88 (2013) 317-325.

[141] J. Roosen, J. Spooren, K. Binnemans, Adsorption performance of functionalized chitosan–silica hybrid materials toward rare earths, Journal of Materials Chemistry A 2 (2014) 19415-19426.

[142] D.L. Ramasamy, A. Wojtuś, E. Repo, S. Kalliola, V. Srivastava, M. Sillanpää, Ligand immobilized novel hybrid adsorbents for rare earth elements (REE) removal from waste water:

Assessing the feasibility of using APTES functionalized silica in the hybridization process with chitosan, Chemical Engineering Journal 330 (2017) 1370-1379.

[143] R.M. Ashour, R. El-sayed, A.F. Abdel-Magied, A.A. Abdel-khalek, M. Ali, K. Forsberg, A. Uheida, M. Muhammed, J. Dutta, Selective Separation of Rare Earth Ions from Aqueous Solution using Functionalized Magnetite Nanoparticles: Kinetic and Thermodynamic Studies, Chemical Engineering Journal 327 (2017) 286-296.

[144] Y. Haldorai, A. Rengaraj, T. Ryu, J. Shin, Y.S. Huh, Y.-K. Han, Response surface methodology for the optimization of lanthanum removal from an aqueous solution using a Fe_3O_4/chitosan nanocomposite, Materials Science and Engineering: B 195 (2015) 20-29.

[145] A.A. Galhoum, M.G. Mahfouz, S.T. Abdel-Rehem, N.A. Gomaa, A.A. Atia, T. Vincent, E. Guibal, Diethylenetriamine-functionalized chitosan magnetic nano-based particles for the sorption of rare earth metal ions [Nd (III), Dy (III) and Yb (III)], Cellulose 22 (2015) 2589-2605.

[146] D. Wu, J. Zhao, L. Zhang, Q. Wu, Y. Yang, Lanthanum adsorption using iron oxide loaded calcium alginate beads, Hydrometallurgy 101 (2010) 76-83.

[147] D. Wu, L. Zhang, L. Wang, B. Zhu, L. Fan, Adsorption of lanthanum by magnetic alginate-chitosan gel beads, Journal of chemical technology and biotechnology 86 (2011) 345-352.

[148] Z. Guo, Y. Li, S. Pan, J. Xu, Fabrication of Fe3O4@ cyclodextrin magnetic composite for the high-efficient removal of Eu (III), Journal of Molecular Liquids 206 (2015) 272-277.

[149] Y. Cai, F. Yuan, X. Wang, Z. Sun, Y. Chen, Z. Liu, X. Wang, S. Yang, S. Wang, Synthesis of core–shell structured Fe 3 O 4@ carboxymethyl cellulose magnetic composite for highly efficient removal of Eu (III), Cellulose 24 (2017) 175-190.

[150] A.A. Galhoum, M.G. Mafhouz, S.T. Abdel-Rehem, N.A. Gomaa, A.A. Atia, T. Vincent, E. Guibal, Cysteine-functionalized chitosan magnetic nano-based particles for the recovery of light

and heavy rare earth metals: uptake kinetics and sorption isotherms, Nanomaterials 5 (2015) 154-179.

[151] T. Kameda, K. Hoshi, T. Yoshioka, Preparation of Cu–Al layered double hydroxide intercalated with ethylenediaminetetraacetate by coprecipitation and its uptake of rare earth ions from aqueous solution, Solid State Sciences 17 (2013) 28-34.

[152] D. Roy, M. Semsarilar, J.T. Guthrie, S. Perrier, Cellulose modification by polymer grafting: a review, Chemical Society Reviews 38 (2009) 2046-2064.

[153] X. Sun, B. Peng, Y. Ji, J. Chen, D. Li, Chitosan (chitin)/cellulose composite biosorbents prepared using ionic liquid for heavy metal ions adsorption, AIChE journal 55 (2009) 2062-2069.

[154] J. Jancar, J. Douglas, F.W. Starr, S. Kumar, P. Cassagnau, A. Lesser, S.S. Sternstein, M. Buehler, Current issues in research on structure–property relationships in polymer nanocomposites, Polymer 51 (2010) 3321-3343.

[155] D.L. Ramasamy, E. Repo, V. Srivastava, M. Sillanpää, Chemically immobilized and physically adsorbed PAN/acetylacetone modified mesoporous silica for the recovery of rare earth elements from the waste water-comparative and optimization study, Water Research 114 (2017) 264-276.

[156] D.L. Ramasamy, V. Puhakka, E. Repo, S. Khan, M. Sillanpää, Coordination and silica surface chemistry of lanthanides (III), scandium (III) and yttrium (III) sorption on 1-(2-pyridylazo)-2-napththol (PAN) and acetylacetone (acac) immobilized gels, Chemical Engineering Journal 324 (2017) 104-112.

[157] D.L. Ramasamy, S. Khan, E. Repo, M. Sillanpää, Synthesis of mesoporous and microporous amine and non-amine functionalized silica gels for the application of rare earth elements (REE) recovery from the waste water-understanding the role of pH, temperature, calcination and mechanism in Light REE and Heavy REE separation, Chemical Engineering Journal 322 (2017) 56-65.

[158] D.L. Ramasamy, V. Puhakka, S. Iftekhar, A. Wojtuś, E. Repo, S.B. Hammouda, E. Iakovleva, M. Sillanpää, N-and O-ligand doped mesoporous silica-chitosan hybrid beads for the efficient, sustainable and selective recovery of rare earth elements (REE) from acid mine drainage (AMD): Understanding the significance of physical modification and conditioning of the polymer, Journal of Hazardous Materials 348 (2018) 84-91.

[159] T. Kameda, K. Hoshi, T. Yoshioka, Uptake of Sc^{3+} and La^{3+} from aqueous solution using ethylenediaminetetraacetate-intercalated Cu–Al layered double hydroxide reconstructed from Cu–Al oxide, Solid State Sciences 13 (2011) 366-371.

[160] I. Langmuir, The adsorption of gases on plane surfaces of glass, mica and platinum, Journal of the American Chemical society 40 (1918) 1361-1403.

[161] H. Freundlich, Over the adsorption in solution, J. Phys. Chem 57 (1906) 1100-1107.

[162] A. Dada, A. Olalekan, A. Olatunya, O. Dada, Langmuir, Freundlich, Temkin and Dubinin–Radushkevich isotherms studies of equilibrium sorption of Zn2+ unto phosphoric acid modified rice husk, IOSR Journal of Applied Chemistry 3 (2012) 38-45.

[163] S.Y. Elovich, O. Larinov, Theory of adsorption from solutions of non electrolytes on solid (I) equation adsorption from solutions and the analysis of its simplest form,(II) verification of the equation of adsorption isotherm from solutions, Izv. Akad. Nauk. SSSR, Otd. Khim. Nauk 2 (1962) 209-216.

[164] S. Lagergren, About the theory of so-called adsorption of soluble substances, (1898).

[165] Y.-S. Ho, G. McKay, Pseudo-second order model for sorption processes, Process Biochemistry 34 (1999) 451-465.

[166] V. Srivastava, M. Sillanpää, Synthesis of malachite@ clay nanocomposite for rapid scavenging of cationic and anionic dyes from synthetic wastewater, Journal of Environmental Sciences 51 (2017) 97-110.

[167] G. Boyd, A. AW, LS, Myers Exchange adsorption of ions by organic zeolites II: Kinetics J, Am. Chem. Soc 69 (1947) 2836-2848.

[168] K.S. Sing, Reporting physisorption data for gas/solid systems with special reference to the determination of surface area and porosity (Recommendations 1984), Pure and Applied Chemistry 57 (1985) 603-619.

[169] M. Thommes, K. Kaneko, A.V. Neimark, J.P. Olivier, F. Rodriguez-Reinoso, J. Rouquerol, K.S. Sing, Physisorption of gases, with special reference to the evaluation of surface area and pore size distribution (IUPAC Technical Report), Pure and Applied Chemistry 87 (2015) 1051-1069.

[170] V. Srivastava, Y. Sharma, M. Sillanpää, Green synthesis of magnesium oxide nanoflower and its application for the removal of divalent metallic species from synthetic wastewater, Ceramics International 41 (2015) 6702-6709.

[171] G.A. Moldoveanu, V.G. Papangelakis, Recovery of rare earth elements adsorbed on clay minerals: I. Desorption mechanism, Hydrometallurgy 117 (2012) 71-78.

[172] N. Ünlü, M. Ersoz, Adsorption characteristics of heavy metal ions onto a low cost biopolymeric sorbent from aqueous solutions, Journal of Hazardous Materials 136 (2006) 272-280.

[173] Y.R. Smith, D. Bhattacharyya, T. Willhard, M. Misra, Adsorption of aqueous rare earth elements using carbon black derived from recycled tires, Chemical Engineering Journal 296 (2016) 102-111.

[174] A.N. Turanov, V.K. Karandashev, N.S. Sukhinina, V.M. Masalov, G.A. Emelchenko, Adsorption of lanthanides and scandium ions by silica sol-gel material doped with novel bifunctional ionic liquid, trioctylmethylammonium 1-phenyl-3-methyl-4-benzoyl-5-onate, Journal of Environmental Chemical Engineering 4 (2016) 3788-3796.

[175] T. Monecke, U. Kempe, J. Monecke, M. Sala, D. Wolf, Tetrad effect in rare earth element distribution patterns: a method of quantification with application to rock and mineral samples from granite-related rare metal deposits, Geochimica et Cosmochimica Acta 66 (2002) 1185-1196.

Publication I

Iftekhar, S., Srivastava, V., and Sillanpää, M.
Synthesis and application of LDH intercalated cellulose nanocomposite for separation of rare earth elements (REEs)

Reprinted with permission from
Chemical Engineering Journal
Vol. 309, pp. 130-139, 2017

Chemical Engineering Journal 309 (2017) 130–139

Contents lists available at ScienceDirect

Chemical Engineering Journal

journal homepage: www.elsevier.com/locate/cej

Synthesis and application of LDH intercalated cellulose nanocomposite for separation of rare earth elements (REEs)

Sidra Iftekhar [a,*], Varsha Srivastava [a], Mika Sillanpää [a,b]

[a] Laboratory of Green Chemistry, School of Engineering Science, Lappeenranta University of Technology, Sammonkatu 12, FI-50130 Mikkeli, Finland
[b] Department of Civil and Environmental Engineering, Florida International University, Miami, FL 33174, USA

HIGHLIGHTS

- Layered double hydroxide intercalated cellulose nanocomposite was synthesized.
- CL-Zn/Al LDH was used to investigate the adsorption behavior of REEs in batch mode.
- Adsorption followed pseudo second order kinetics and Langmuir isotherm model.
- CL-Zn/Al LDH showed good regeneration and reusability.
- CL-Zn/Al LDH seems to be a relatively effective adsorbent for REEs.

ARTICLE INFO

Article history:
Received 26 August 2016
Received in revised form 7 October 2016
Accepted 7 October 2016
Available online 8 October 2016

Keywords:
Layered double hydroxide
Adsorption
Rare earth elements
Kinetics

ABSTRACT

Present study deals with the synthesis of Zn/Al Layered double hydroxide (LDH) intercalated cellulose (CL) nanocomposite. The CL-Zn/Al LDH nanocomposite was characterized by XRD, FTIR, BET, TEM and AFM. XRD analysis showed the crystalline nature of LDH nanocomposite. TEM analysis confirmed the formation of a sheet like structure of LDH. The synthesized CL-Zn/Al LDH nanocomposite was found to have a capacity of rapid uptake of Y^{3+}, La^{3+} and Ce^{3+}. Kinetic experiments revealed that equilibrium was achieved in 10 min for Y^{3+}, La^{3+} and Ce^{3+}. The kinetic data was well predicted by pseudo second order with higher correlation coefficient (R^2) compared to pseudo first order. The adsorption capacities of Y^{3+}, La^{3+} and Ce^{3+} was found to be 102.25, 92.51 and 96.25 mg/g, respectively, according to Langmuir model. Analysis of thermodynamic studies for Y^{3+}, La^{3+} and Ce^{3+} showed that the process of adsorption is spontaneous and endothermic in nature. The CL-Zn/Al LDH nanocomposite revealed a good reusability up to five cycles. The CL-Zn/Al LDH showed good adsorption and selectivity for Y^{3+}, La^{3+} and Ce^{3+} in the presence of other ions. Therefore, CL-Zn/Al LDH nanocomposite has a great potential to be used for the adsorption of Y^{3+}, La^{3+} and Ce^{3+}.

1. Introduction

Rare earth elements (REEs) consists of 17 elements of the periodic table including 15 lanthanides along with yttrium and scandium [1,2]. They are further subdivided into: light rare earth elements (LREEs) and heavy rare earth elements (HREEs); on the basis of their atomic number. Almost all of these exhibit similar chemical and physical properties and often termed as "seeds of technology" because of their wide applications in batteries, lasers, superconductors, fiber optics, automotive catalytic converters, permanent magnets, electronic devices, ceramics, fertilizers and medicines [1,3,4]. In 2010, the world demand for REEs was 136,000 tons per year and the global demand is projected to rise to at least 160,000 tons annually by 2016 [5,6]. Despite of their wide use, the amount of REEs recycled up to 2012 was estimated to be only 1% which is very low compared to other recyclable elements [1]. Considering the relative toxicity associated with the uptake of REEs toward living organisms [2], there is a need of suitable method for the separation and preconcentration of REEs. Several methods have been developed for the treatment of REEs viz membrane separation, ion exchange, chemical precipitation, solvent extraction, adsorption etc. [1,3,4]. Researchers found adsorption as one of the most cost efficient, eco-friendly and economical method for the treatment and recovery of REEs compared to the conventional methods [1,2].

In recent years, nanocomposites have gained significant attention for adsorption process because of their phenomenal properties

* Corresponding author.
E-mail addresses: sidra.iftekhar@lut.fi, sidra_iftekhar@yahoo.com (S. Iftekhar).

http://dx.doi.org/10.1016/j.cej.2016.10.028
1385-8947/

[7,8]. Nanocomposites are the composite materials which have at least one dimension in nano-range (1–100 nm). A large variety of nanocomposites have been prepared based on various organic and inorganic matrices. Among these cellulose based nanowhiskers and nanocomposites are extensively used as it is the most abundantly available biopolymer and is promising raw material available at low cost [7]. Although cellulose is biodegradable and inexpensive still its application is limited because of low adsorption capacities. However, chemical or surface modification have been conducted by researchers to increase the adsorption capacities in order to use them as an efficient scavenger for heavy metals and REEs [9,10].

Layered double hydroxides (LDH) often referred as anionic clays are bi-dimensional solids having brucite like layer structure [11]. LDH layers poses excess positive charge which is due to the replacement of divalent cations by trivalent cations and to compensate the positive charge various anions are introduced between the layers. In spite of their positive charge layered structure, LDH has been extensively used in various applications, such as catalysts, antacids, anion exchangers etc. as well as for the treatment of organic, inorganic and anionic pollutants [11,12]. LDH can act as a host matrix for the synthesis of organic-inorganic nanocomposite. Commonly the methods employed for the synthesis of such organic-LDH intercalation are ion exchange, co-precipitation and reconstruction of calcined LDH in the presence of organic polymers [12]. The intercalation of several biopolymers in LDH has been reported including alginate, pectic, xanthan gum, κ-carrageenan and ι-carrageenan and are used in development of sensors applied to the potentiometric determination of ions in areas of high relevance such as clinical diagnosis, food analysis and water quality control [13]. Similarly, ligand embedded diverse mesoporous materials are shown very effective for REEs separation [14–16]. However, the application of these unique LDH intercalated biopolymer nanocomposites as an adsorbent for the removal of heavy metals and REEs is limited.

In this way the objective of this study was the synthesis of hybrid nanocomposite based on the intercalation of polymer (cellulose), whose structure is shown in Fig. 1, in the LDH denoted as CL-Zn/Al LDH. The nanocomposite was characterized by FTIR, XRD, BET, TEM and AFM. The resulting CL-Zn/Al LDH nanocomposite was then used as an adsorbent for the removal of Y^{3+}, La^{3+} and Ce^{3+}. The variables (pH, dose, time, concentration and temperature) affecting the adsorption performance were investigated for the optimization of removal process. In addition, adsorption kinetics, equilibrium and thermodynamic data were processed to understand the adsorption mechanism. The reusability, effect of competing ions on adsorption and intra-series adsorption behavior of REEs on CL-Zn/Al LDH nanocomposite were also evaluated.

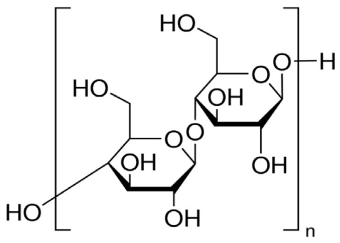

Fig. 1. Structure of cellulose.

2. Materials and methods

2.1. Reagents

Cotton linters cellulose (CL), urea (CH_4N_2O), sodium hydroxide (NaOH), hydrochloric acid (HCl), zinc chloride ($ZnCl_2$), aluminum chloride hexahydrate ($AlCl_3{\cdot}6H_2O$), cerium chloride heptahydrate ($CeCl_3{\cdot}7H_2O$), lanthanum nitrate hexahydrate ($La(NO_3)_3{\cdot}6H_2O$), yttrium chloride (YCl_3) were purchased from Sigma Aldrich and used as received without further purification.

2.2. Synthesis of CL-Zn/Al LDH nanocomposites

The solution of cellulose was prepared as reported [8]. A solution of 7:12:81 of NaOH:Urea:H_2O was pre-cooled to −12 °C. 3.24 g of cellulose was added to NaOH:Urea solution under vigorous stirring (Solution A). The prepared solution was used for the preparation of CL-Zn/Al LDH nanocomposites.

The CL-Zn/Al LDH nanocomposite was prepared simply by co-precipitation method. 0.75 M $ZnCl_2$ and 0.25 M $AlCl_3{\cdot}6H_2O$ (Zn:Al = 3:1) was added in 50 ml deionized water (Solution B). Then solution B was added dropwise in Solution A in an hour under constant stirring at 300 rpm and pH of solution was adjusted to 10 by addition of NaOH and HCl. The precipitates were then aged for 18 h, filtered and washed with water and ethanol. The prepared CL-Zn/Al LDH nanocomposite was then dried in oven (TERMAKS) at 80 °C for 12 h and ground to fine powder by Tubemill (IKA Tube mill control).

2.3. Characterization of CL-Zn/Al LDH nanocomposites

X-ray Diffraction (XRD, PANalytical X-ray diffractometer), Fourier transform infrared spectroscopy (FTIR, Bruker Vertex 70), Brunauer, Emmett and Teller (BET, Tristar® II Plus) surface area, transmission electron microscopy (TEM, Hitachi H-7600), and Atomic force microscopy (AFM, Park Systems NX10) analysis were techniques used for the characterization of prepared nanocomposites. pH_{zpc} of CL-Zn/Al LDH was calculated by method reported earlier [17]. 0.2 g of CL-Zn/Al LDH was added in a solution of 0.01 M NaCl and pH was adjusted from 2–12 by addition of NaOH and HCl. After 48 h the final pH of solutions was measured and the point of intersection of pH_{final} vs $pH_{initial}$ was noted as pH_{zpc} of nanocomposites.

2.4. Adsorption studies

A stock solution of Y^{3+}, La^{3+} or Ce^{3+} with the initial concentration of 1000 mg/L was prepared by dissolving the appropriate amount of salts in deionized water and was used for the preparation of the working solutions of desired concentrations. All the experiments were conducted in a 15 ml polypropylene tube by contacting 10 ml of Y^{3+}, La^{3+} or Ce^{3+} (50 mg/L) solution with 10 mg of CL-Zn/Al LDH nanocomposite in an orbital shaker (IKA KS 4000 ic control) at a constant speed (150 rpm) and temperature (25 °C) for a given time. The reaction mixture was filtered using 0.2 μm PTFE membrane filter and analyzed for the concentrations of Y^{3+}, La^{3+} and Ce^{3+} by ICP-OES (Thermo iCAP 6300 series). The optimum initial pH, adsorbent dose and contact time were investigated for the maximum removal of Y^{3+}, La^{3+} and Ce^{3+}. For the effect of pH, the initial pH was adjusted by dropwise addition of 0.1 M HCl and NaOH. The pH was tested in a range of 2 to 7 in order to avoid precipitation of Y^{3+}, La^{3+} and Ce^{3+} during adsorption. The nanocomposite dose of 2 to 20 mg/10 mL (0.2–2 g/L) was tested to select the optimum dose of CL-Zn/Al LDH nanocomposite. For kinetic, isotherm and thermodynamic experiments, the procedure

was conducted as detailed except that the time (1 to 25 min), concentration (50 to 150 mg/L) and temperature (20–50 °C) was varied.

The amount of Y^{3+}, La^{3+} or Ce^{3+} adsorbed by CL-Zn/Al LDH nanocomposite was calculated by using Eq. (1):

$$Q = \frac{(C_0 - C_f)V}{M} \quad (1)$$

where Q is the adsorption capacity in mg/g, V is the volume of solution (L), M is the mass of nanocomposite (g), C_o and C_f is the initial and equilibrium concentrations of Y^{3+}, La^{3+} or Ce^{3+} in solution (mg/L).

2.5. Desorption studies

Desorption experiments were performed in the same way as adsorption tests except, in this case, experiments were started with Y^{3+}, La^{3+} and Ce^{3+} loaded CL-Zn/Al LDH nanocomposite which was separated by centrifugation, washed with deionized water and desorbed with different concentrations of HCl and NaOH. The solution was filtered and desorbed concentration of Y^{3+}, La^{3+} and Ce^{3+} was estimated. The process was repeated several times and efficiency of CL-Zn/Al LDH nanocomposite for Y^{3+}, La^{3+} and Ce^{3+} uptake was investigated.

3. Results and discussion

3.1. Factors affecting the uptake of Y^{3+}, La^{3+} and Ce^{3+} concerning the synthesis of CL-Zn/Al LDH

There are several factors affecting the uptake of Y^{3+}, La^{3+} and Ce^{3+}. Zn/AL ratio is one of the major factor concerning the synthesis of CL-Zn/Al LDH. The effect of changing the Zn/Al ratio in the preparation of CL-Zn/Al LDH was studied. The uptake of Y^{3+}, La^{3+} and Ce^{3+} increased by changing the Zn/AL ratio from 1 to 3 (Supplementary Material: Table S1). The results showed that the uptake reached maximum after reaching the Zn to Al ratio to 3. The adsorption of Y^{3+}, La^{3+} and Ce^{3+} on CL-Zn/Al LDH occurred by two phases (Supplementary Material: Fig. S1) [18]. In the first phase, adsorption occurred rapidly. The reconstruction of LDH occurred simultaneously accompanied with the adsorption of carriers (Y^{3+}, La^{3+} or Ce^{3+}) in the first phase. In the second phase, the small amount of hydroxide produced by the slight dissociation of the compounds promoted the coagulation of the carriers onto the compound. The hydroxide induced coagulates adsorbed onto the compounds resulting in sludge with very low water content. The slow ion exchange between the intercalating ligands or polymers in the compound and carrier substance would also occur during second phase. The amount of adsorption increased by increasing the Zn/Al ratio. Although the Al(III) ions in the brucite layer produce the anions exchange site, the amount of adsorption increased with decreasing the Al(III) ions in the compound. The results implies the adsorption of Y^{3+}, La^{3+} or Ce^{3+} at the hydroxyl groups of Zn (II) as well as the inner layer anion exchange site. The surface hydroxyl groups of the compounds would work as the coagulation sites. The carrier substances with large molecular sizes should be adsorbed onto the surface of LDH and not intercalate into the inner layers. Thus, CL-Zn/Al LDH showed very large adsorption capacity for Y^{3+}, La^{3+} and Ce^{3+} with the Zn/Al ratio of 3.

3.2. Characterization of CL-Zn/Al LDH nanocomposites

Fig. 2(a) represents the XRD pattern of CL-Zn/Al LDH nanocomposite. The diffraction peaks at $2\Theta = 34.5°$ is assigned to CL [10]. The peaks corresponding to plane (0 0 6), (0 1 2) and (0 1 8) are the characteristic diffraction peaks of Zn/Al LDH. The symmetry and sharpness of these peaks indicates the highly crystalline phase LDH. Besides, the low intense peaks are the characteristic reflections of ZnO phase. Also, the peaks that form (1 1 0) and (1 1 3) planes reveal a good dispersion of metal ions in the LDH layer [19]. However, in our sample the peak corresponding to plane (0 0 3) is absent which is due to intercalation of cellulose in LDH. The average crystal size calculated by using Scherrer equation is 22.47 nm [20].

FTIR spectra of CL-Zn/Al LDH is shown in Fig. 2(b). The bands at 3300–3450 cm^{-1} are assigned to –OH stretching vibrations, peak at 1600–1700 cm^{-1} attributed to –OH bending, peaks at 1461, 1595 cm^{-1} are related to symmetrical and asymmetrical stretching vibrations of the carboxylate groups and the characteristic peak at 1152 cm^{-1} for C-O-C from the glucosidic bonds [10]. The peaks in a region of low wave number from 400 to 800 cm^{-1} corresponds to M-OH vibrations and O-M-O stretching (where M = Zn and Al). These peaks confirmed the formation of the characteristic Zn/Al LDH intercalated CL network.

For TEM analysis, synthesized nanocomposite was dispersed in ethanol and sonicated for 15 min and a drop of suspension was placed on carbon coated Cu grid. The TEM images (Fig. 3(a–b)) of CL-Zn/Al LDH nanocomposite confirms the formation of sheet like structure with a particle size of 25–60 nm. However, the aggregation of particles is also observed. AFM images of CL-Zn/Al LDH also confirms the agglomeration of particles. The peak height of particles shown in Fig. 3(c–d) is in a range of 20–80 nm. The results of both TEM and AFM are in good agreement with XRD.

The N_2 adsorption-desorption isotherm for CL-Zn/Al LDH nanocomposite was also obtained (Fig. 3(e)). The prepared LDH nanocomposite shows type III with H3 hysteretic loop isotherm which suggests the presence of mesoporous materials comprises of aggregates of plate like particles. According to results of BET analysis the surface area is estimated to be 1.216 m^2/g for the CL-Zn/Al LDH nanocomposite. Also, the pore volume and pore diameter is estimated to be 9.3 mm^3/g and 22.7 nm, respectively by BJH analysis. The CL-Zn/Al LDH nanocomposite offers a very low surface area if compared to the mesoporous materials reported in literature [21–25], still they offer very large adsorption capacities due to their structural properties as explained earlier.pH_{zpc} plot for CL-Zn/Al LDH nanocomposite is shown in Fig. 3(f). pH_{zpc} for CL-Zn/Al LDH is estimated to be 9.10. It is evident that CL-Zn/Al LDH has excess of positive charge.

3.3. Effect of initial pH

For controlling the process of adsorption pH is an important factor. 50 mg/L solution of Y^{3+}, La^{3+} and Ce^{3+} was treated separately with 10 mg of CL-Zn/Al LDH. The adsorption at pH higher than 7 was not considered as the precipitation started above this, resulting in the formation of insoluble metal hydroxides [10]. In highly acidic pH region (pH 2), H^+ ions compete with Y^{3+}, La^{3+} and Ce^{3+} over the CL-Zn/Al LDH reducing the adsorption. The carboxyl groups present in CL-Zn/Al LDH as main functional group are highly sensitive to H+. Most of the carboxylate ions ($-COO^-$) will be converted to carboxyl groups (–COOH) in acidic range, thus, reducing the adsorption of Y^{3+}, La^{3+} and Ce^{3+} [10]. Also the surface of Zn/Al LDH has large number of binding sites which were occupied by H^+ ions due to protonation reaction on the surface of LDH at low pH. The increase in (Y^{3+}, La^{3+} and Ce^{3+}) uptake with increasing pH of the solution was attributed due to the surface properties of LDH in terms of surface charge and dissociation of functional groups. Furthermore, buffer action was also observed by LDH when added at different pH values. In acidic range, the excess of H^+ ions dominated resulting in the decrease in the pH of the final solution. However, as the pH increased LDH resulted

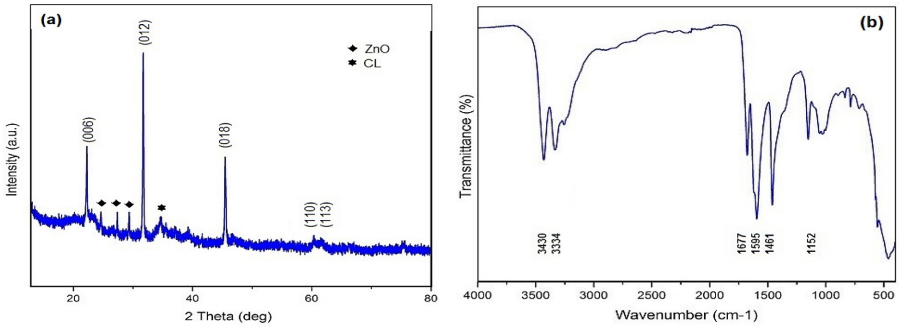

Fig. 2. XRD plot (a), FTIR spectra; (b) of CL-Zn/Al LDH.

in the increase of pH of the final solution. Other researchers also reported the buffering properties of LDH [26–28]. Thus the results suggests that the high uptake of Y^{3+}, La^{3+} and Ce^{3+} was not only because of the cellulose in the interlayers but also due to the chemical properties of Zn/Al LDH. The maximum adsorption was observed at pH 7 (Fig. 4(a)).

3.4. Effect of dose

The adsorption of Y^{3+}, La^{3+} and Ce^{3+} with 50 mg/L solution was studied as a function of dose at pH 7 (Fig. 4(b)). The adsorption of Y^{3+}, La^{3+} and Ce^{3+} increases by increasing the dose and reached almost 100% at a dose of 12 mg/10 mL (1.2 g/L) for Y^{3+},La^{3+} and Ce^{3+}. Therefore, 12 mg/10 mL of CL-Zn/Al LDH was used for further experiments.

3.5. Effect of time and adsorption kinetics

According to Fig. 4(c), adsorption of Y^{3+}, La^{3+} and Ce^{3+} on CL-Zn/Al LDH reached equilibrium in 10 min indicating a faster adsorption kinetics. The uptake was very fast and almost 99% of total uptake occur in 10 min. The adsorption kinetics was analyzed by pseudo first order (Eq. (2)) [29] and pseudo second order kinetic model (Eq. (3)) [30].

$$\log(q_e - q_t) = \log\ q_e - \frac{k_1}{2.303}t \tag{2}$$

$$\frac{t}{q_t} = \frac{1}{k_2 q_e^2} + \frac{1}{q_e}t \tag{3}$$

where t is time (min); q_e and q_t are adsorption capacity of Y^{3+}, La^{3+} and Ce^{3+} over CL-Zn/Al LDH at equilibrium and at time t (mg/g), respectively; k_1 (min^{-1}) and k_2 (g/mg. min^{-1}) are rate constants for pseudo first order and second order, respectively.

The correlation coefficient R^2 and the parameters for pseudo first order and pseudo second order kinetic model are listed in Table 1. The correlation coefficient R^2 were higher for pseudo second order equation for Y^{3+}, La^{3+} and Ce^{3+}. Furthermore, the adsorption capacity at equilibrium estimated from pseudo second order rate equation were in agreement with the experimental data. Therefore, the results suggested that the experimental data was well described by pseudo second order rate kinetics. It could be stated that the adsorption of Y^{3+}, La^{3+} and Ce^{3+} supports the assumption of chemisorption [31]. Similar results showing the compliance of Y^{3+}, La^{3+} and Ce^{3+} adsorption to the pseudo second order kinetics were previously reported [1,32–34].

To further develop the understanding of adsorption process, intra-particle diffusion model was used to analyze the kinetic behavior of adsorption process. The intra-particle diffusion model is expressed as:

$$q_t = k_i t^{1/2} + C \tag{4}$$

where k_i is the intra-particle diffusion rate constant and C is a constant. The linear fitting of experimental data to (Eq. (4)) indicates that the adsorption process is only controlled by intra-particle diffusion. However, in case of deviation the process is composed by two or three steps [35,36]. It can be seen from Fig. 5(c); the adsorption process is comprised of different stages as the plot shows multi-linearity. The first linear stage corresponds to adsorption over the external surface of CL-Zn/Al LDH (diffusion adsorption stage). The second linear region corresponds to the intra-particle diffusion of Y^{3+}, La^{3+} or Ce^{3+} through the pores of CL-Zn/Al LDH (gradual adsorption stage). The final linear region corresponds to the stage in which intra-particle diffusion begins to slow down either due to the low concentration of Y^{3+}, La^{3+} or Ce^{3+} left in the solution or because of the decrease in the available active adsorption sites (equilibrium adsorption stage). Although, the coefficient of correlation (R^2) for all the three plots is above 0.9 still none of the linear region passes through origin. This indicates that intra-particles diffusion though involved in adsorption process but is not the only rate controlling step, which mean that both intra-particle diffusion and film diffusion occurred simultaneously.The Boyd model is mainly used to distinguish between intra-particle diffusion and film diffusion; expressed as (Eq. (5)). Therefore, the kinetic data were also analyzed by Boyd model (liquid film diffusion model) in order to determine the actual rate controlling step involved in the adsorption process.

$$\ln\left(1 - \frac{q_t}{q_e}\right) = k_f t \tag{5}$$

where k_f is the film diffusion rate constant. If the straight line does not pass through the origin the adsorption process is governed by film diffusion, otherwise, it is governed by intra-particle diffusion process [37]. The results of the Boyd model are consistent with that of intra-particle diffusion model as the plot does not pass through the origin indicating that the film diffusion mainly governs the adsorption rate of Y^{3+}, La^{3+} and Ce^{3+} over CL-Zn/Al LDH.

3.6. Effect of concentration and adsorption isotherms

The variation of Y^{3+}, La^{3+} and Ce^{3+} on CL-Zn/Al LDH as a function of concentration is shown in Fig. 4(d). The uptake of Y^{3+}, La^{3+} and

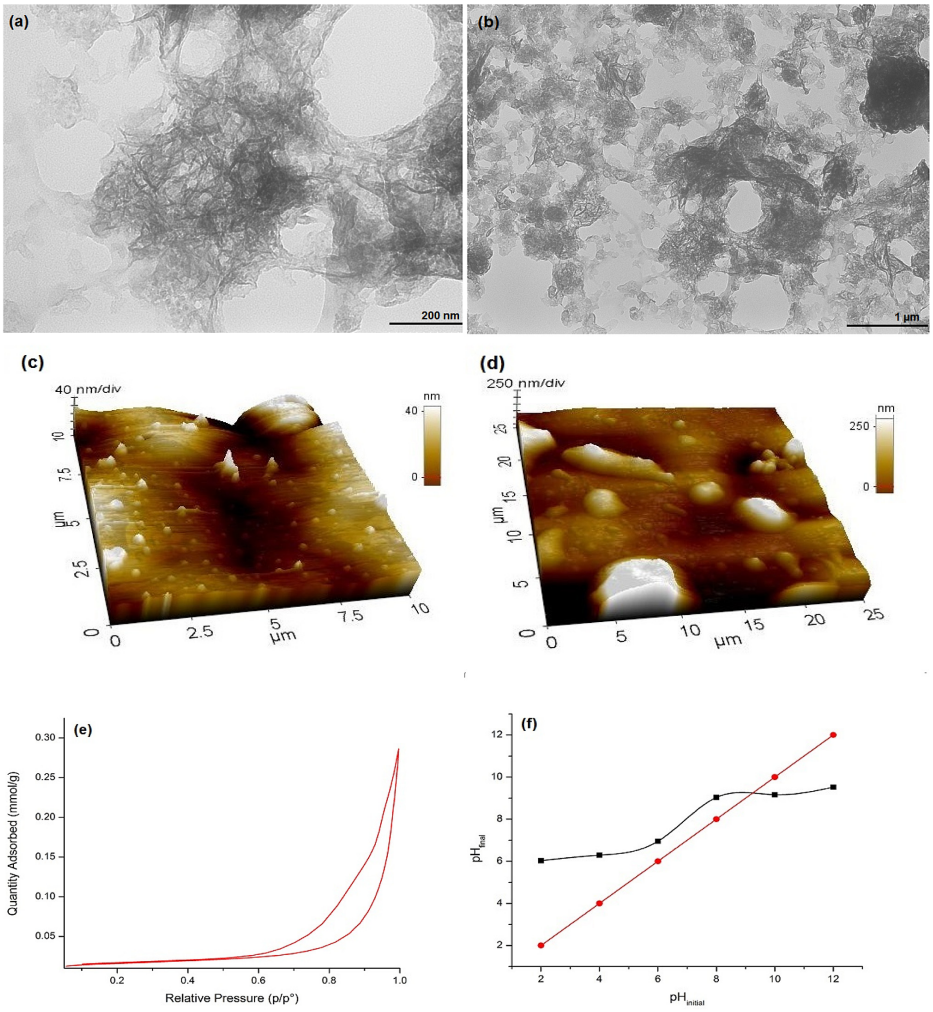

Fig. 3. TEM images (a–b), AFM (c–d), N_2 adsorption-desorption isotherm (e) and pH_{zpc} plot (f) of CL-Zn/Al LDH.

Ce^{3+} on CL-Zn/Al LDH decreases as the initial concentration increase. The fact is explained as with the increase in the initial concentration (Y^{3+}, La^{3+} and Ce^{3+}), the more number of ions are competing for the available binding sites and also due to lack of binding sites of CL-Zn/Al LDH. Thus, at higher concentrations more Y^{3+}, La^{3+} and Ce^{3+} ions left unadsorbed in the solution due to saturation of binding sites.

To elucidate the adsorption performance of CL-Zn/Al LDH Langmuir, Freundlich and Temkin models were employed [10,38,39]. The equations are given below;

$$\frac{C_e}{q_e} = \frac{1}{K_L Q_0} + \frac{C_e}{Q_0} \tag{6}$$

$$\log q_e = \log K_f + \frac{1}{n} \log C_e \tag{7}$$

$$q_e = B \log(A) + B \log(C_e) \tag{8}$$

where q_e and Q_0 are the equilibrium adsorption capacity and the maximum adsorption capacity (mg/g), respectively; C_e is equilibrium concentration of metal ions (mg/L); K_L, K_f and 1/n are empirical constants, $B = RT/b$ is a constant related to heat of sorption (J/mol), A is Temkin constant at equilibrium (L/g), R is the gas constant (J/mol K), T is temperature in kelvin and b is Temkin constant related to heat of sorption.

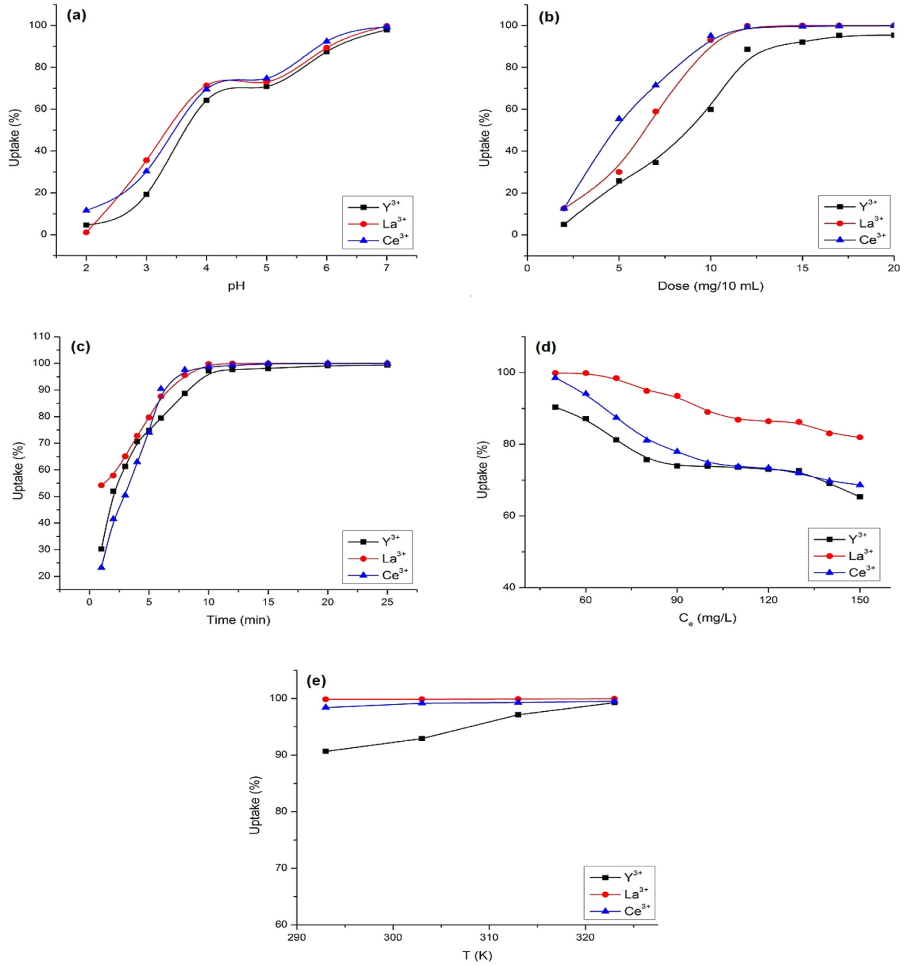

Fig. 4. Adsorption of Y^{3+}, La^{3+} and Ce^{3+} on CL-Zn/Al LDH nanocomposite as a function of pH (a), dose (b), time (c), concentration (d) and temperature (e).

Table 1
Kinetics parameters for Y^{3+}, La^{3+} and Ce^{3+} adsorption onto CL-Zn/Al LDH.

REEs	$q_{e,exp}$ (mg/g)	Pseudo first order			Pseudo second order		
		$q_{e,cal}$ (mg/g)	k_1 (min^{-1})	R^2	q_e (mg/g)	k_2 (g/mg. min^{-1})	R^2
Y^{3+}	42.04	68.87	0.46	0.81	53.45	6.07×10^{-3}	0.99
La^{3+}	45.07	79.92	0.56	0.801	52.74	9.5×10^{-3}	0.98
Ce^{3+}	49.7	115.85	0.57	0.94	55.83	4.3×10^{-3}	0.95

The Langmuir, Freundlich and Temkin plots for Y^{3+}, La^{3+} and Ce^{3+} onto CL-Zn/Al LDH are shown in Fig. 6(a), (b), (c), respectively and the parameters corresponding to isotherms are listed in Table 2. From Fig. 6(a) and Table 2, high coefficient of correlation (R^2) value derived by fitting the experimental data fitted well to Langmuir model indicating the monolayer adsorption of Y^{3+}, La^{3+} and Ce^{3+} over the CL-Zn/Al LDH. The results also strongly supported the validity of pseudo second order kinetics [33]. The order of isotherm models best fit to the experimental data in this study is Langmuir > Freundlich > Temkin. Also, the maximum adsorption

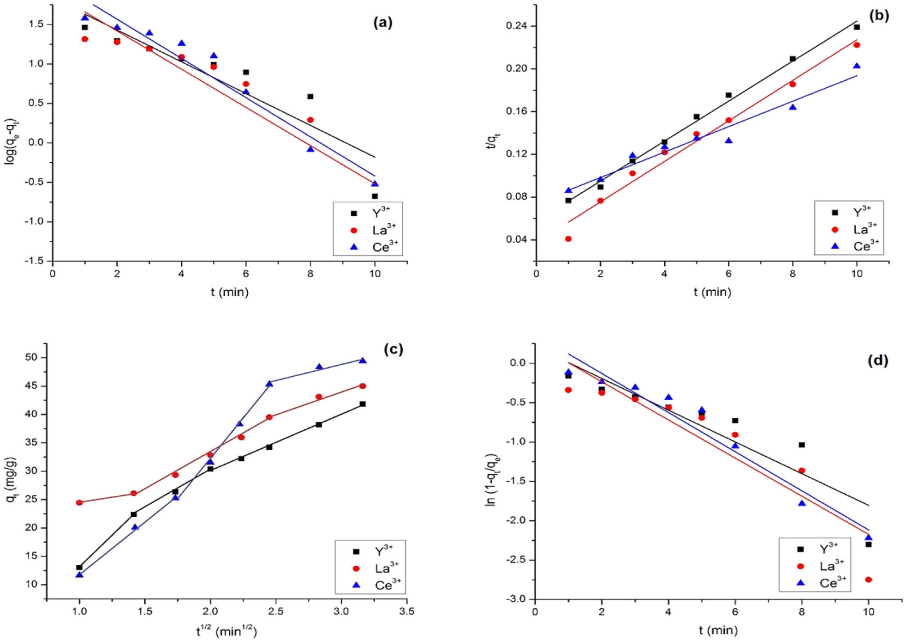

Fig. 5. Plot of pseudo first order model (a), pseudo first order model (b), intra-particle diffusion model (c) and Boyd model (d) for adsorption of Y^{3+}, La^{3+} and Ce^{3+} onto CL-Zn/Al LDH.

capacity calculated for Y^{3+}, La^{3+} and Ce^{3+} was 102.25, 92.51 and 96.25 mg/g, respectively.

Comparisons of adsorptive property between the adsorbents have been performed with synthesized CL-Zn/Al LDH nanocomposite, as summarized in Table 3. The comparative results demonstrate that this CL-Zn/Al LDH nanocomposite shows faster adsorption kinetics than other adsorbents reported and good adsorption capacity.

3.7. Effect of temperature and adsorption thermodynamics

Fig. 4(e) shows that increasing temperature does not affect the uptake of La^{3+} and Ce^{3+}, but there is a slight increasing effect for Y^{3+}.

Thermodynamic parameters (i.e. ΔH^0, ΔS^0, ΔG^0) were calculated using following equations;

$$\ln K_C = \frac{\Delta S^0}{R} - \frac{\Delta H^0}{RT} \quad (9)$$

$$\Delta G^0 = -RT \ln K_C \quad (10)$$

where K_c is thermodynamic equilibrium constant (L/g), R is universal gas constant (8.314 J/mol/K), T is temperature (K), ΔG^0 is Gibbs free energy (kJ/mol), ΔS^0 is entropy (J/mol/K) and ΔH^0 is enthalpy (kJ/mol) [38]. The values of ΔH^0, ΔS^0, ΔG^0 can be calculated using Eq. (9) and Eq. (10) and listed in Table 4. The negative values of ΔG^0 free energy change for Y^{3+}, La^{3+} and Ce^{3+} indicated the spontaneous nature of adsorption. Furthermore, the positive values of ΔH^0 indicates the adsorption process was endothermic. The enthalpy values obtained also suggests the chemisorption process ($\Delta H^0 > 50$ kJ/mol) [32,43,44]. In addition, the value of ΔS^0 was found to be positive due to the exchange of the metal ions with more mobile ions present on the exchanger, which would cause increase in the entropy, during the adsorption process [43,44].

3.8. Desorption and regeneration

The adsorbent is considered to be good if along with high adsorption capacities it posseses good regeneration and reuseabilities. To desorb Y^{3+}, La^{3+} and Ce^{3+} from CL-Zn/Al LDH different concentrations of HCl and NaOH were used. Preliminary experiments revealed that CL-Zn/Al LDH loaded with Y^{3+}, La^{3+} and Ce^{3+} could desorb effectively in 0.1 M HCl. The reusability of CL-Zn/Al LDH was evaluated for five (05) adsorption-desorption cycles (Fig. 7). After 5 cycles, slight decreases in the adsorption capacity for Y^{3+}, La^{3+} and Ce^{3+} was observed. This demonstrates that CL-Zn/Al LDH nanocomposite was high performance recyclable adsorbent for treatment of Y^{3+}, La^{3+} and Ce^{3+}.

3.9. Effect of competing ions

The Y^{3+}, La^{3+} and Ce^{3+} can be substituted by other cations due to similar ionic radius and effect the adsorption of Y^{3+}, La^{3+} and Ce^{3+} on CL-Zn/Al LDH [14,16,45]. Therefore it is important to check the competing ion effect on the adsorption of Y^{3+}, La^{3+} and Ce^{3+} on CL-Zn/Al LDH. The experiments was then performed in a multicomponent system with or without competing ions. Additionally, experiments were also carried out in a bi-solute system at different pH to check the selectivity of CL-Zn/Al LDH toward Y^{3+}, La^{3+} and Ce^{3+}.

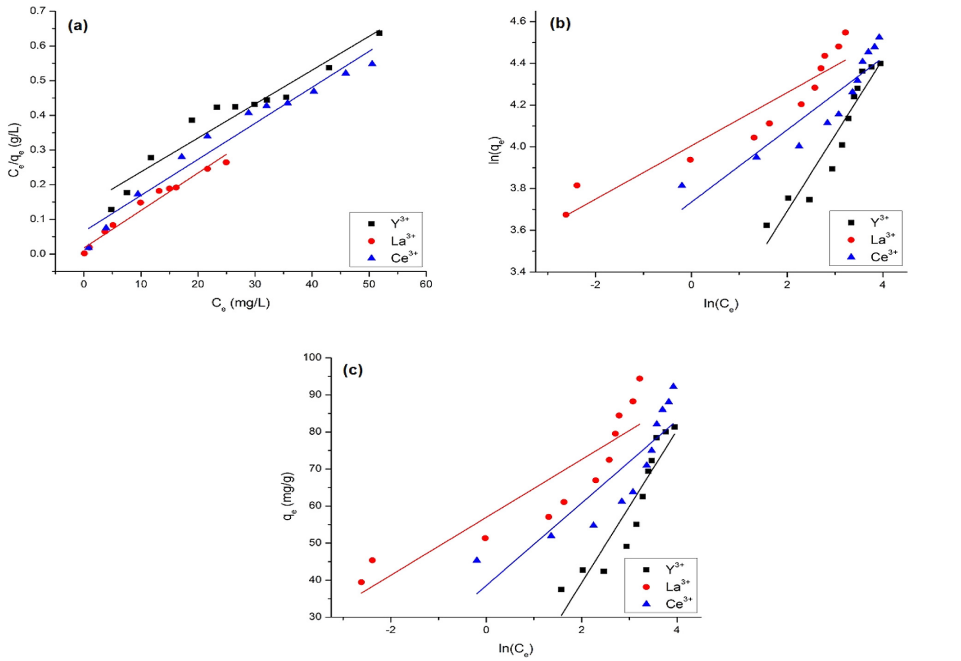

Fig. 6. Plot of Langmuir (a), Freundlich (b) and Temkin (c) for adsorption Y^{3+}, La^{3+} and Ce^{3+} onto CL-Zn/Al LDH.

Table 2
Isotherm constant for Y^{3+}, La^{3+} and Ce^{3+} adsorption onto CL-Zn/Al LDH.

REEs	Langmuir			Freundlich			Temkin		
	Q_o	K_L (L/mg)	R_L^2	K_f (L/g)	n	R_F^2	A (L/g)	B (J/mol)	R_T^2
Y^{3+}	102.25	0.15	0.93	19.34	2.47	0.90	0.91	20.61	0.86
La^{3+}	92.51	0.62	0.97	54.84	7.83	0.88	1467.4	7.81	0.80
Ce^{3+}	96.25	0.08	0.96	41.88	5.78	0.83	31.6	11.15	0.76

Table 3
Comparison of Y^{3+}, La^{3+} and Ce^{3+} adsorption among different adsorbents.

Adsorbent	Adsorption conditions	Adsorption Time (min)			Adsorption Capacity (mg/g)		
		Y^{3+}	La^{3+}	Ce^{3+}	Y^{3+}	La^{3+}	Ce^{3+}
Carbon black derived from recycled tires [32]	C_0:100 mg/L, Dosage:10 g/200 mL, pH: natural	500	500	200	1.79	1.91	5.04
Cellulose hydrogel [10]	C_0:200 mg/L, Dosage: 20 mg/25 mL, pH: natural		30	30		241.72	245.22
Kaolin [38]	C_0:120 mg/L, Dosage:1 g/40 mL, pH: 4.8	30	30		0.974	1.73	
Chitosan-g-poly (acrylic acid)/attapulgite [40]	C_0:400 mg/L, Dosage:25 mg/25 mL, pH: 6		40	40		333.33	243.9
Functionalized (TPDP) mesoporous silica [41]	C_0:20 mg/L, Dosage:70 mg/20 mL, pH: 7		40				
Mesoporous conjugate adsorbent [14]	C_0:5 mg/L, Dosage:8 mg/30 mL, pH: 3.5			25			192.31
Pleurotus ostreatus biomass [42]	C_0:200 mg/L, Dosage:500 mg/50 mL, pH: 7	30			45.45		
Present study	C_0:50 mg/L, Dosage:12 mg/10 mL, pH: 7	10	10	10	102.25	92.51	96.25

The decrease of up to 10% in overall uptake of Y^{3+}, La^{3+} and Ce^{3+} on CL-Zn/Al LDH was observed when present in a same system which might be because of the same ionic charge (Supplementary Material: Fig. S2(a)). However, a slight decrease in uptake of Y^{3+}, La^{3+} and Ce^{3+} in presence of 10-fold concentration of Na^+, K^+, Ca^{2+}, Mg^{2+}, Al^{3+} was observed (Supplementary Material: Fig. S2(b)). This was probably due to the presence of Al^{3+} with similar ionic charge as that of Y^{3+}, La^{3+} and Ce^{3+} [15]. In a bisolute system, La^{3+} and Ce^{3+} always show higher uptake compare to Y^{3+} except at pH 2 when La^{3+} adsorption was lesser than Y^{3+} and Ce^{3+}. Therefore, the CL-Zn/Al LDH exhibited a good selectivity towards Y^{3+}, La^{3+} and Ce^{3+} and also Y^{3+}, La^{3+} and Ce^{3+} can be uptaken with good selectivity from multi-mixture solution.

Table 4
Thermodynamic parameters for adsorption Y^{3+}, La^{3+} and Ce^{3+} onto CL-Zn/Al LDH.

REEs	ΔH^0 (kJ/mol)	ΔS^0 (J/mol/K)	ΔG^0 (kJ/mol)			
			293 K	303	313	323
Y^{3+}	61.77	222.07	−5.10	−6.03	−6.35	−12.72
La^{3+}	50.73	276.81	−15.54	−16.14	−17.69	−19.69
Ce^{3+}	58.49	266.78	−9.61	−11.6	−12.40	−13.76

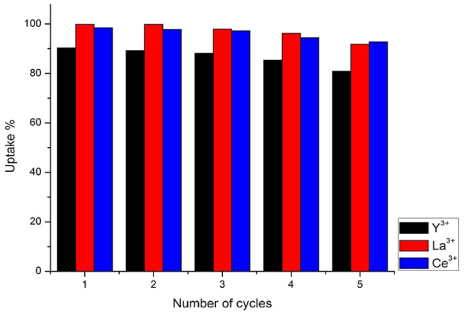

Fig. 7. Adsorption-desorption cycles for Y^{3+}, La^{3+} and Ce^{3+} (C_0:50 mg/L pH 7, dosage 12 mg/10 ml, time 10 min, temp 25 °C).

3.10. Intra-series adsorption behavior of LREEs

To determine the intra-series adsorption behavior of LREE on CL-Zn/Al LDH nanocomposite, 12 mg/ 10 mL adsorbent were tested under each LREEs ion concentration of 50 mg/L (Supplementary Material: Fig. S4). The selectivity order of CL-Zn/Al LDH among LREEs cations follow:

$$Tb^{+3} > Gd^{+3} > Pr^{+3} > Yb^{+3} > Ho^{+3} > Tm^{+3} > Eu^{+3} > Sm^{+3} > La^{+3} > Dy^{+3} > Nd^{+3} > Er^{+3} > Ce^{+3} > Y^{+3} > Sc^{+3} > Lu^{+3}$$

The change presented in intra-series adsorption behavior of LREEs because the series of LREEs filled electron only inner 4f orbit with the increase of atomic number. The same electron configuration in the outer orbit led to the similar chemical properties within the series. Also, with the increase of atomic number the ionic radius decreased due to lanthanide contraction [45]. Thus, the adsorption quantity of REEs on CL-Zn/Al LDH showed different change order based on the above reason. However, the overall adsorption of LREEs on CL-Zn/Al LDH was observed to be more than 90%.

4. Conclusion

The CL-Zn/Al LDH nanocomposite was synthesized by co-precipitation method. XRD analysis showed the crystalline nature of nanocomposite. The formation of sheet like structure of LDH was confirmed by TEM analysis. The results of TEM was strongly supported by AFM. The BET surface area, the pore volume and pore diameter was estimated to be 1.216 m^2/g, 9.3 mm^3/g and 22.7 nm, respectively. The equilibrium was achieved in 10 min for Y^{3+}, La^{3+} and Ce^{3+}. Also, the kinetic data fitted well to pseudo second order kinetic model. From the results of intra-particle diffusion model and Boyd model, film diffusion was found to be the rate controlling step in adsorption process. At optimum pH 7, CL-Zn/Al LDH exhibits the maximum Y^{3+}, La^{3+} and Ce^{3+} adsorption of 102.25, 92.51 and 96.25 mg/g, respectively, according to Langmuir model. Thermodynamic parameters (ΔH^0, ΔS^0, ΔG^0) showed that the process of adsorption is spontaneous and endothermic in nature. Regeneration studies revealed the good potential of CL-Zn/Al LDH for reuse and showed a slight decrease in adsorption after 5 cycles. The decrease of up to 10% in overall uptake of Y^{3+}, La^{3+} and Ce^{3+} on CL-Zn/Al LDH was observed when present in a same system. However, in the presence of competing ions a slight decrease in uptake of Y^{3+}, La^{3+} and Ce^{3+} was observed because of the presence of Al^{3+}. The intra-series adsorption behavior of REEs on CL-Zn/Al LDH was different. Thus, the CL-Zn/Al LDH nanocomposite has a great potential to be used as an adsorbent for the abatement of Y^{3+}, La^{3+} or Ce^{3+} from effluent.

Appendix A. Supplementary data

Supplementary data associated with this article can be found, in the online version, at http://dx.doi.org/10.1016/j.cej.2016.10.028.

References

[1] D. Sadovsky, A. Brenner, B. Astrachan, B. Asaf, R. Gonen, Biosorption potential of cerium ions using Spirulina biomass, J. Rare Earths 34 (2016) 644–652.
[2] K. Vijayaraghavan, R. Balasubramanian, Single and binary biosorption of cerium and europium onto crab shell particles, Chem. Eng. J. 163 (2010) 337–343.
[3] J. Ponou, L.P. Wang, G. Dodbiba, K. Okaya, T. Fujita, K. Mitsuhashi, T. Atarashi, G. Satoh, M. Noda, Recovery of rare earth elements from aqueous solution obtained from Vietnamese clay minerals using dried and carbonized parachlorella, J. Environ. Chem. Eng. 2 (2014) 1070–1081.
[4] F. Zhao, E. Repo, Y. Meng, X. Wang, D. Yin, M. Sillanpää, An EDTA-β-cyclodextrin material for the adsorption of rare earth elements and its application in preconcentration of rare earth elements in seawater, J. Colloid Interface Sci. 465 (2016) 215–224.
[5] M. Humphries, Rare earth elements: the global supply chain, Congressional Res. Serv. 2012 (2011) 7–5700.
[6] M. Humphries, Rare Earth Elements: The Global Supply Chain, DIANE Publishing, 2010.
[7] M. Roohani, Y. Habibi, N.M. Belgacem, G. Ebrahim, A.N. Karimi, A. Dufresne, Cellulose whiskers reinforced polyvinyl alcohol copolymers nanocomposites, Eur. Polymer J. 44 (2008) 2489–2498.
[8] M.-G. Ma, F. Deng, K. Yao, Manganese-containing cellulose nanocomposites: the restrain effect of cellulose treated with NaOH/urea aqueous solutions, Carbohydr. Polym. 111 (2014) 230–235.
[9] Y. Zhou, X. Hu, M. Zhang, X. Zhuo, J. Niu, Preparation and characterization of modified cellulose for adsorption of Cd (II), Hg (II), and acid fuchsin from aqueous solutions, Ind. Eng. Chem. Res. 52 (2013) 876–884.
[10] Y. Zhu, W. Wang, Y. Zheng, F. Wang, A. Wang, Rapid enrichment of rare-earth metals by carboxymethyl cellulose-based open-cellular hydrogel adsorbent from HIPEs template, Carbohydr. Polym. 140 (2016) 51–58.
[11] R. Rojas, M.R. Perez, E.M. Erro, P.I. Ortiz, M.A. Ulibarri, C.E. Giacomelli, EDTA modified LDHs as Cu^{2+} scavengers: removal kinetics and sorbent stability, J. Colloid Interface Sci. 331 (2009) 425–431.
[12] M. Park, C.L. Choi, Y.J. Seo, S.K. Yeo, J. Choi, S. Komarneni, J.H. Lee, Reactions of Cu^{2+} and Pb^{2+} with Mg/Al layered double hydroxide, Appl. Clay Sci. 37 (2007) 143–148.
[13] M. Darder, M. López-Blanco, P. Aranda, F. Leroux, E. Ruiz-Hitzky, Bio-nanocomposites based on layered double hydroxides, Chem. Mater. 17 (2005) 1969–1977.
[14] M.R. Awual, T. Yaita, H. Shiwaku, Design a novel optical adsorbent for simultaneous ultra-trace cerium (III) detection, sorption and recovery, Chem. Eng. J. 228 (2013) 327–335.
[15] M.R. Awual, T. Kobayashi, H. Shiwaku, Y. Miyazaki, R. Motokawa, S. Suzuki, Y. Okamoto, T. Yaita, Evaluation of lanthanide sorption and their coordination mechanism by EXAFS measurement using novel hybrid adsorbent, Chem. Eng. J. 225 (2013) 558–566.
[16] M.R. Awual, T. Kobayashi, Y. Miyazaki, R. Motokawa, H. Shiwaku, S. Suzuki, Y. Okamoto, T. Yaita, Selective lanthanide sorption and mechanism using novel hybrid Lewis base (N-methyl-N-phenyl-1, 10-phenanthroline-2-carboxamide) ligand modified adsorbent, J. Hazard. Mater. 252 (2013) 313–320.

[17] V. Srivastava, Y. Sharma, M. Sillanpää, Green synthesis of magnesium oxide nanoflower and its application for the removal of divalent metallic species from synthetic wastewater, Ceram. Int. 41 (2015) 6702–6709.
[18] Y. Seida, Y. Nakano, Removal of humic substances by layered double hydroxide containing iron, Water Res. 34 (2000) 1487–1494.
[19] D. Wu, P.R. Chang, X. Ma, Preparation and properties of layered double hydroxide–carboxymethylcellulose sodium/glycerol plasticized starch nanocomposites, Carbohydr. Polym. 86 (2011) 877–882.
[20] J.I. Langford, A. Wilson, Scherrer after sixty years: a survey and some new results in the determination of crystallite size, J. Appl. Crystallogr. 11 (1978) 102–113.
[21] M.R. Awual, M.M. Hasan, M.A. Khaleque, M.C. Sheikh, Treatment of copper (II) containing wastewater by a newly developed ligand based facial conjugate materials, Chem. Eng. J. 288 (2016) 368–376.
[22] M.R. Awual, New type mesoporous conjugate material for selective optical copper (II) ions monitoring & removal from polluted waters, Chem. Eng. J. 307 (2017) 85–94.
[23] M.R. Awual, Solid phase sensitive palladium (II) ions detection and recovery using ligand based efficient conjugate nanomaterials, Chem. Eng. J. 300 (2016) 264–272.
[24] M.R. Awual, Assessing of lead (III) capturing from contaminated wastewater using ligand doped conjugate adsorbent, Chem. Eng. J. 289 (2016) 65–73.
[25] M.R. Awual, Ring size dependent crown ether based mesoporous adsorbent for high cesium adsorption from wastewater, Chem. Eng. J. (2016).
[26] T. Türk, I. Alp, H. Deveci, Adsorption of As (V) from water using Mg–Fe-based hydrotalcite (FeHT), J. Hazard. Mater. 171 (2009) 665–670.
[27] D. Zhao, G. Sheng, J. Hu, C. Chen, X. Wang, The adsorption of Pb (II) on Mg 2 Al layered double hydroxide, Chem. Eng. J. 171 (2011) 167–174.
[28] Y. You, G.F. Vance, H. Zhao, Selenium adsorption on Mg–Al and Zn–Al layered double hydroxides, Appl. Clay Sci. 20 (2001) 13–25.
[29] S. Lagergren, About the theory of so-called adsorption of soluble substances, 1898.
[30] Y.-S. Ho, G. McKay, Pseudo-second order model for sorption processes, Process Biochem. 34 (1999) 451–465.
[31] Y.-S. Ho, Review of second-order models for adsorption systems, J. Hazard. Mater. 136 (2006) 681–689.
[32] Y.R. Smith, D. Bhattacharyya, T. Willhard, M. Misra, Adsorption of aqueous rare earth elements using carbon black derived from recycled tires, Chem. Eng. J. 296 (2016) 102–111.
[33] H.M. Marwani, H.M. Albishri, T.A. Jalal, E.M. Soliman, Study of isotherm and kinetic models of lanthanum adsorption on activated carbon loaded with recently synthesized Schiff's base, Arabian J. Chem. (2013).
[34] C. Qing, Study on the adsorption of lanthanum (III) from aqueous solution by bamboo charcoal, J. Rare Earths 28 (2010) 125–131.
[35] Q. Yuan, N. Li, Y. Chi, W. Geng, W. Yan, Y. Zhao, X. Li, B. Dong, Effect of large pore size of multifunctional mesoporous microsphere on removal of heavy metal ions, J. Hazard. Mater. 254 (2013) 157–165.
[36] Y. Chen, J. Hu, J. Wang, Kinetics and thermodynamics of Cu (II) biosorption on to a novel magnetic chitosan composite bead, Environ. Technol. 33 (2012) 2345–2351.
[37] S. Duan, R. Tang, Z. Xue, X. Zhang, Y. Zhao, W. Zhang, J. Zhang, B. Wang, S. Zeng, D. Sun, Effective removal of Pb (II) using magnetic $Co_{0.6}Fe_{2.4}O_4$ micro-particles as the adsorbent: synthesis and study on the kinetic and thermodynamic behaviors for its adsorption, Colloids Surf. A 469 (2015) 211–223.
[38] X. Yanfei, L. Huang, L. Zhiqi, F. Zongyu, W. Liangshi, Adsorption ability of rare earth elements on clay minerals and its practical performance, J. Rare Earths 34 (2016) 543–548.
[39] M. Mushtaq, H.N. Bhatti, M. Iqbal, S. Noreen, Eriobotrya japonica seed biocomposite efficiency for copper adsorption: isotherms, kinetics, thermodynamic and desorption studies, J. Environ. Manage. 176 (2016) 21–33.
[40] Y. Zhu, Y. Zheng, A. Wang, Preparation of granular hydrogel composite by the redox couple for efficient and fast adsorption of La (III) and Ce (III), J. Environ. Chem. Eng. 3 (2015) 1416–1425.
[41] A. Tadjarodi, V. Jalalat, R. Zare-Dorabei, Adsorption of La (III) in aqueous systems by N-(2-hydroxyethyl) salicylaldimine-functionalized mesoporous silica, Mater. Res. Bull. 61 (2015) 113–119.
[42] S.S. Hussien, O.A. Desouky, Biosorption studies on yttrium using low cost pretreated biomass of pleurotus ostreatus, 4th International Conference on Radiation Sciences and ApplicationsTaba, Egypt, 2014, pp. 139–150.
[43] N. Ünlü, M. Ersoz, Adsorption characteristics of heavy metal ions onto a low cost biopolymeric sorbent from aqueous solutions, J. Hazard. Mater. 136 (2006) 272–280.
[44] Ş. Sert, C. Kütahyali, S. İnan, Z. Talip, B. Çetinkaya, M. Eral, Biosorption of lanthanum and cerium from aqueous solutions by *Platanus orientalis* leaf powder, Hydrometallurgy 90 (2008) 13–18.
[45] S. Zhou, X. Li, Y. Shi, A. Alshameri, C. Yan, Preparation, characterization, and Ce (III) adsorption performance of poly (allylamine)/silica composite, Desalin. Water Treat. 56 (2015) 1321–1334.

Publication II

Iftekhar, S., Srivastava, V., and Sillanpää, M.
Enrichment of lanthanides in aqueous system by cellulose based silica nanocomposite

Reprinted with permission from
Chemical Engineering Journal
Vol. 320, pp. 151-159, 2017

Chemical Engineering Journal 320 (2017) 151–159

Contents lists available at ScienceDirect

Chemical Engineering Journal

journal homepage: www.elsevier.com/locate/cej

Enrichment of lanthanides in aqueous system by cellulose based silica nanocomposite

Sidra Iftekhar [a,*], Varsha Srivastava [a], Mika Sillanpää [a,b]

[a] Laboratory of Green Chemistry, School of Engineering Science, Lappeenranta University of Technology, Sammonkatu 12, FI-50130 Mikkeli, Finland
[b] Department of Civil and Environmental Engineering, Florida International University, Miami, FL 33174, USA

HIGHLIGHTS

- Cellulose based silica nanocomposites were synthesized.
- CLx/SiO_2 was used to investigate the adsorption behavior of lanthanides.
- The surface modification highly effect the surface area of CLx/SiO_2.
- CLCA/SiO_2 exhibits compact particle packing and low surface area.
- CLN/SiO_2 seems to be a relatively effective adsorbent for lanthanides.

GRAPHICAL ABSTRACT

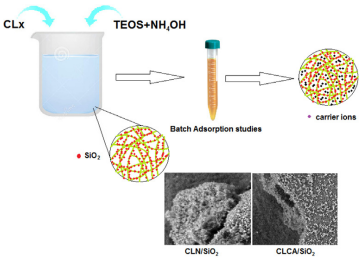

ARTICLE INFO

Article history:
Received 20 January 2017
Received in revised form 13 March 2017
Accepted 14 March 2017
Available online 16 March 2017

Keywords:
Cellulose
Nanocomposite
Lanthanides
Adsorption

ABSTRACT

Synthesis of cellulose based silica (CLx/SiO_2) nanocomposite was successfully carried out and employed for the removal of Eu(III), La(III) and Sc(III). Nanocomposite was characterized by TEM, AFM, SEM, XRD, FTIR and BET. TEM analysis indicated that the particle diameter of nanocomposite was in the range of 9–15 nm and silica particles was uniformly distributed throughout the nanocomposites. The presence of mixed phases of cellulose and SiO_2 was observed by FTIR and XRD. Experimental results showed that CLx/SiO_2 nanocomposite produced by sulfuric acid modification possess higher surface area than that of citric acid modified. Various parameters including contact time, pH, nanocomposite dosage, initial concentration, and temperature were optimized to achieve maximum adsorption capacity. The kinetics results revealed that the surface chemical sorption for Eu(III) and La(III) and physisorption for Sc(III). Also, the film diffusion was the rate-determining step of the adsorption process. Importantly, the isotherms fitted better to Langmuir for Eu(III) and La(III) than Freundlich. The positive values of ΔH^0 indicates that the adsorption process was endothermic and negative value of ΔG^0 indicates the feasibility of Eu(III), La(III) and Sc(III) removal by adsorption on CLN/SiO_2 nanocomposite and suggests the spontaneous nature of adsorption on nanocomposite. Desorption of adsorbate loaded on nanocomposite during adsorption process was easily carried out up to three cycles. The results indicate that the nanocomposite is an efficient adsorbent with good adsorption capacity for Eu(III), La(III) and Sc(III).

1. Introduction

In modern societies, the application of lanthanides is increasing due to the unique physical and chemical properties of rare earth

* Corresponding author.
E-mail addresses: sidra_iftekhar@yahoo.com, sidra.iftekhar@lut.fi (S. Iftekhar).

http://dx.doi.org/10.1016/j.cej.2017.03.051
1385-8947/

elements (REEs) [1]. REEs are employed extensively in chemical engineering, metallurgy, electronics, medicine, lasers, storage batteries etc. [1–4]. Numerous techniques have been used for the determination of REEs including atomic adsorption spectroscopy (AAS) [5], UV-vis spectroscopy [6,7], inductively coupled plasma-mass spectrometry (ICP-MS) and inductively coupled plasma optical emission spectroscopy (ICP-OES) [5,8]. Similarly, several techniques have been applied for the uptake of REEs from aqueous systems such as solvent extraction, ion exchange, solid-phase extraction, ion-selective electrodes [2–4] and adsorption [9–14]. But these methods are not preferred because of several disadvantages such as high consumption of reagent and energy, low selectivity, high operational cost and generation of secondary metabolites; in addition, these methods are also time consuming and labor-intensive [12]. However, adsorption method is the best technique because of cost, simplicity of design and operation [15]. Therefore, many researchers have started developing a cost effective and eco-friendly method to recover rare earth metals from aqueous environment [12]. The general class of nanocomposite inorganic/organic materials is a fast-growing area of research [16–18]. Hybrid organic–inorganic materials may be produced by nanoparticle deposition on the fiber surface [19]. Significant effort is focused on the ability to obtain control of the nanoscale structures via innovative synthetic approaches. The properties of nanocomposite materials depend not only on the properties of their individual components but also on their morphological and interfacial characteristics. This rapidly expanding field is generating many exciting new materials with novel properties [19].

The nanocomposite combine the most abundant natural polymer cellulose [14,16,20] with the inorganic nanoparticles of silica [21]. Cellulose being one of the world's most abundant natural polymer; the unique morphological properties of natural fibers given by the hierarchical self-assembly of the polymer chains have not seen in many synthetic fibers [14]. On the other hand, silica particles have wide application in industries related to the production of pigments, pharmaceuticals, ceramics and catalysts [21]. Furthermore, silica based adsorbent materials have industrial application for the removal of heavy metals and lanthanides [13,22,23]. Also, to improve the adsorptive properties a variety of functional groups grafted on the surface of mesoporous silica were also reported by several researchers [13,22–24].

In the present study, we synthesized two different acid modified cellulose based silica nanocomposite which were further characterized by using TEM, AFM, SEM, XRD, FTIR and BET. The nanocomposites were applied for the uptake of lanthanides from aqueous medium. The effects of important factors viz. contact time, pH, nanocomposite dosage, initial concentration and temperature on Eu(III), La(III) and Sc(III) adsorption onto cellulose based silica nanocomposites were studied. The aim of this work was to study the adsorption kinetics, equilibrium and thermodynamics employing different models along with the recovery of Eu(III), La(III) and Sc(III).

2. Materials and methods

2.1. Chemicals

Cotton linters cellulose (CL), tetraethyl orthosilicate (TEOS), ammonium hydroxide (NH_4OH), citric acid monohydrate ($C_6H_8O_7$. H_2O), sulfuric acid (H_2SO_4) and analytical grade acetone were purchased from Sigma Aldrich and used as received. Chlorides of europium(III), lanthanum(III) and scandium(III) (Sigma Aldrich) were used for the preparation of stock solutions (1000 mg/L). The working solutions containing different concentrations of Eu(III), La(III) and Sc(III) were prepared by stepwise dilution of the stock solution.

2.2. Preparation of CLx

Acid hydrolysis was done by using 15% H_2SO_4 and citric acid with a solid liquid ratio of 1:20. Briefly, 5 g of CL was added separately to 15% H_2SO_4 and citric acid under constant stirring (200 rpm) at 45 °C for 4 h. The suspension was diluted with cold water and cooled down to room temperature. The cellulose particles were separated by centrifugation (EPPENDORF 5810) at 4000 rpm for 10 min and dialyzed with water down to neutral pH; dried in oven (TERMAKS) at 60 °C for 12 h and ground to get fine powder by Tube mill (IKA Tube mill control). In text and figures, CLx was replaced by CLN or CLCA indicating H_2SO_4 and citric acid modified cellulose, respectively.

2.3. Synthesis of CLx/SiO_2 nanocomposites

1 g of CLx was added in 50 ml of deionized water and sonicated (BRANSON 2510) for 30 min. 2 ml of NH_4OH and 5 ml of TEOS was added in CLx suspension and stirred at 40 °C for 16 h. The suspensions were precipitated by adding 250 ml of acetone, filtered, washed with water several times, dried in oven at 60 °C for 12 h and ground to get fine powder.

2.4. Characterization

Particle size of nanocomposite was determined by using transmission electron microscopy (TEM, Model: Hitachi H-7600). For TEM analysis, synthesized nanocomposite was dispersed in ethanol and sonicated for 15 min and a drop of suspension was placed on carbon coated Cu grid. To study the surface morphology Park Systems NX10 was used for Atomic force microscopy (AFM) analysis with commercial NCHR tip. The scanner was calibrated in the XY directions using a 5 μm grafting and in the Z direction using several conventional height standards. The measurement was performed in air at ambient pressure and humidity and the image was stored as 256 × 256 point arrays. Morphological characteristics of the nanocomposites were evaluated by SEM in a Hitachi S-4800 microscope operating at 10 kV. XRD patterns of nanocomposites were recorded on a PANalytical X-ray diffractometer using Co Kα radiation (λ = 1.790307 Å) in the 2Θ range of 15–120^0 operated at 40 kV and 40 mA. Fourier transform infrared spectroscopy of the CLN/SiO_2 and CLCA/SiO_2 was done by ATR-FTIR, Bruker Vertex 70 model, in a spectral range of 400–4000 cm^{-1}. The surface area and pore size of the synthesized CLN/SiO_2 and CLCA/SiO_2 nanocomposites were calculated using BET and BJH model at 77 K on Tristar® II Plus system. pH_{zpc} of CLN/SiO_2 and CLCA/SiO_2 was calculated by method reported earlier [11]. 0.2 g of CLN/SiO_2 and CLCA/SiO_2 was added in a solution of 0.01 M NaCl and pH was adjusted from 2 to 12 by addition of NaOH and HCl. After 48 h the final pH of solutions was measured and the point of intersection of pH_{final} vs $pH_{initial}$ was noted as pH_{zpc} of nanocomposites.

2.5. Adsorption studies

The adsorption studies were conducted by mixing 30 mg adsorbent with 10 mL of Eu(III), La(III) and Sc(III) solution at desired concentration (25 mg/L). The mixtures were shaken in an orbital shaker (IKA KS 4000 ic control) with a constant speed of 200 rpm and temperature of 298 K for a given time, and then the adsorbents were separated by using 0.45 μm PTFE membrane filter. After that, the concentration of Eu(III), La(III) or Sc(III) in the residual solution was measured by ICP-OES (Thermo iCAP 6300 series). The adsorp-

tion capacity of the nanocomposites was calculated from the following equation:

$$q_e = \frac{(C_0 - C_f)V}{M} \quad (1)$$

where q_e is the adsorption capacity in mg/g, V is the volume of solution (L), M is the mass of nanocomposite (g). C_o and C_f is the initial and equilibrium concentrations of Eu(III), La(III) or Sc(III) in solution (mg/L), respectively.

To optimize the adsorption conditions, batch adsorption experiments were carried out. During the experiments to maintain pH value at the desirable range, the initial pH was adjusted by using 0.1 mol/L NaOH or HCl solution. The pH was tested in a range of 2 –6 to avoid precipitation of Eu(III), La(III) and Sc(III) during adsorption. For adsorption kinetic studies, a series of adsorbents were immersed into 25 mg/L solutions of Eu(III), La(III) and Sc (III) solution at 298 K, and were separated from the solution at predetermined intervals of time. The sorption isotherms for metal ions were established as follows: 30 mg adsorbent was added into 10 mL of Eu(III), La(III) and Sc(III) solution with various initial concentration, and shaken at 298 K until adsorption saturation. After filtration, all the supernatant was left for further analysis to obtain the corresponding adsorption capacity.

2.6. Desorption studies

Desorption experiments were performed in the same way as adsorption tests except, in this case, experiments were started with Eu(III), La(III) or Sc(III) loaded CLN/SiO_2 nanocomposite which was separated by centrifugation, washed with deionized water and desorbed with different concentrations of HCl and NaOH. The solution was filtered and desorbed concentration of Eu(III), La(III) or Sc (III) was estimated. The process was repeated several times and efficiency of nanocomposite for Eu(III), La(III) or Sc(III) uptake was investigated.

3. Results and discussion

3.1. Characterization of CLN/SiO_2 and CLCA/SiO_2 nanocomposites

The TEM images (Fig. 1(a) and (b)) of CLN/SiO_2 and CLCA/SiO_2 nanocomposites confirms the formation of small spherical silica particles, which are uniformly distributed throughout the nanocomposites. Also, it can be seen from TEM images of both nanocomposites that particles almost have same morphologies and the particle diameter of nanocomposites was in a range of 9–15 nm. Fig. 1(c) and (d) shows the AFM images of both the nanocomposites. The peak height of particles shown in Fig. 1 (c) and (d) is up to 10 nm and agglomeration of particles also occurred at some places. Also, SEM images of nanocomposites (Fig. 1(e) and (f)) show the deposition of SiO_2 nanoparticles on the CLx surface, which indicates that the SiO_2 nanoparticles are well dispersed. The smaller silica particles tend to agglomerate at the surface of CLx yielding compact coatings. It can be seen from AFM, TEM and SEM images that CLCA/SiO_2 in contrast to CLN/SiO_2 appears to have more compact particles packing.

The XRD diffraction peaks for cotton linter cellulose lies at 2Θ = 14.8° (1 1 0), 22.6° (0 2 0) and 34.5° (0 4 0) [14,25]. However, the shift in peaks was observed after modification of CL using sulfuric acid and citric acid as shown in Fig. S1. The peaks in case of CLN appeared at 2Θ = 18.62°, 26.36° and 40.79° whereas the peaks obtained for CLCA are indexed at 2Θ = 17.66°, 26.2° and 40.32°, 49.09°, 52.92° Furthermore, it can also be seen from Fig. S1 that the intensity of peaks are more in case of CLCA compare to CLN which indicates the structure of cellulose was destroyed when modified with sulfuric acid. Fig. 2 represents the XRD curves of CLN/SiO_2 and CLCA/SiO_2 nanocomposites. SiO_2 remains amorphous for both nanocomposites and is indexed by broad diffraction peak located in a range of 23–27°. One can see that the sample consisted of the mixed phases of cellulose and SiO_2 (marked with ∗ in Fig. 2).

To identify the functional groups of CLN, CLCA, CLN/SiO_2 and CLCA/SiO_2 nanocomposites FTIR analysis was used. The FTIR spectra of CLN and CLCA is shown Fig. S1 shows the peaks at 3336, 2901, 1636, 1429 and 1370 cm^{-1} corresponds to –OH stretching, C–H stretching, –OH bending, –CH_2 bending and C–H bending, respectively. All these peaks are characteristic adsorption bands of cotton linters cellulose [26,27]. Furthermore, the peaks at 1412, 1043 and 896 cm^{-1} (CLN) which emerged at 1427, 1029 cm^{-1} and 876 cm^{-1} in CLCA corresponds to CH_2 symmetric scissoring, skeletal vibrations of C-O-C ring and the β-glycosidic linkages, respectively [25,28]. The additional peak observed at 1160 cm^{-1} in case of CLCA attributed to antisymmetric bridge stretching of C-O group [25]. The crystal absorption peak of cellulose at 1105 cm^{-1} disappeared in CLN spectra indicates the crystal structure of cellulose was destroyed. Fig. 2 represents the FTIR spectra of CLN/SiO_2 and CLCA/SiO_2 nanocomposites. Along with the characteristic bands of cellulose, the presence of overlapping peak in a region near 1058 cm^{-1} attributed to Si–O–C [16] which strongly confirms the formation of chemical bonding between cellulose and silica. The peaks around 798 cm^{-1} and 465 cm^{-1} are attributed to symmetric stretching and bending vibrations of Si–O–Si, respectively [29].

The N_2 adsorption–desorption isotherms of CLN/SiO_2 and CLCA/SiO_2 are shown in Fig. 3. However, CLN/SiO_2 nanocomposite showed high surface areas, large pore size distributions and high pore volumes. A typical IV-type (for mesoporous materials) with broad H2 hysteresis loop was observed in both CLN/SiO_2 and CLCA/SiO_2 nanocomposites. The specific surface areas, pore volume and pore diameter were calculated to be 169.74 m^2/g, 0.478 cm^3/g and 11.2 nm for CLN/SiO_2 and 110.29 m^2/g, 0.144 cm^3/g and 9.7 nm for CLCA/SiO_2, respectively. The surface area of the CLN/SiO_2 was higher than CLCA/SiO_2 due to the fact that surface area reached minimum when silica was produced in the presence of citric acid [30].

Although a clear difference was observed from XRD and FTIR after modification of CL by sulfuric acid and citric acid. However, no prominent change was noticed in final nanocomposites except surface area. The change in surface area indicates that the presence of acidic groups on CL surface mainly effects the generation of SiO_2 and overall surface area of nanocomposites.pH_{zpc} plot for CLN/SiO_2 and CLCA/SiO_2 nanocomposites is shown in Fig. 3. pH_{zpc} plot for CLN/SiO_2 and CLCA/SiO_2 were found to be 7.06 and 7.58, respectively.

3.2. Preliminary investigation using CLN/SiO_2 and CLCA/SiO_2 nanocomposites for uptake of Eu(III), La(III) and Sc(III)

To investigate the overall removal, both the nanocomposites was agitated (200 rpm) with the solutions of Eu(III), La(III) or Sc (III) for different time intervals and nanocomposite dosage with initial concentration of 25 mg/L at 298 K. It could be seen from Fig. S3 that the removal percentage of Eu(III), La(III) and Sc(III) in case of CLN/SiO_2 was far higher than CLCA/SiO_2 which might be due to higher surface area of CLN/SiO_2. Thus, preliminary study showed that among the two tested nanocomposites, CLN/SiO_2 was more efficient in removal of Eu(III), La(III) and Sc(III) which was then used for further studies.

Furthermore, it can also be seen from Fig. S3 that the removal trend for Eu(III), La(III) and Sc(III) on CLN/SiO_2 is different. In case La(III) and Sc(III), the removal increases by increasing the nanocomposite dose. On the contrary, 97% removal was observed

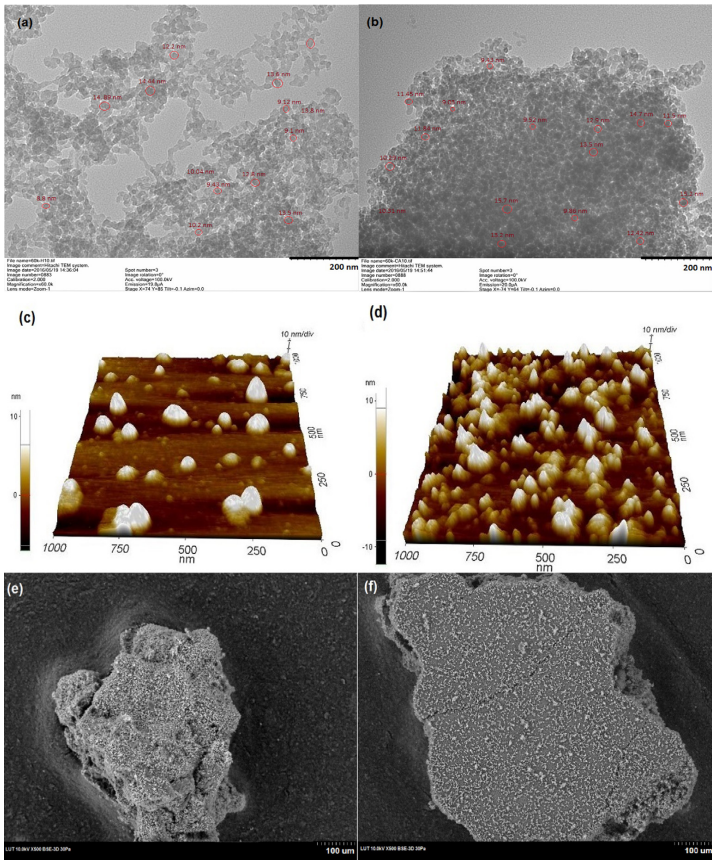

Fig. 1. TEM, AFM, SEM, of CLN/SiO_2 (a, c, e) and CLCA/SiO_2 (b, d, f).

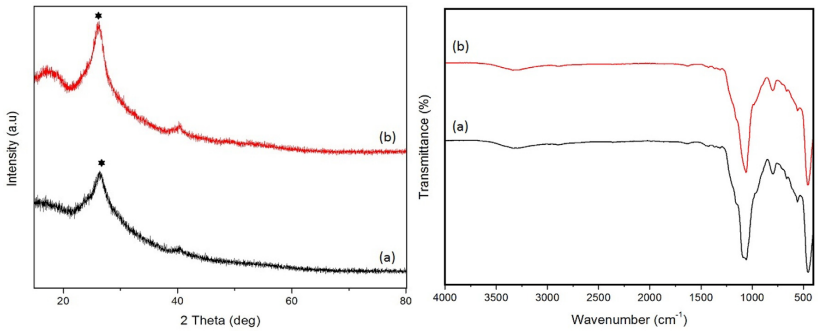

Fig. 2. XRD and FTIR plots of CLN/SiO_2 (a) and CLCA/SiO_2 (b).

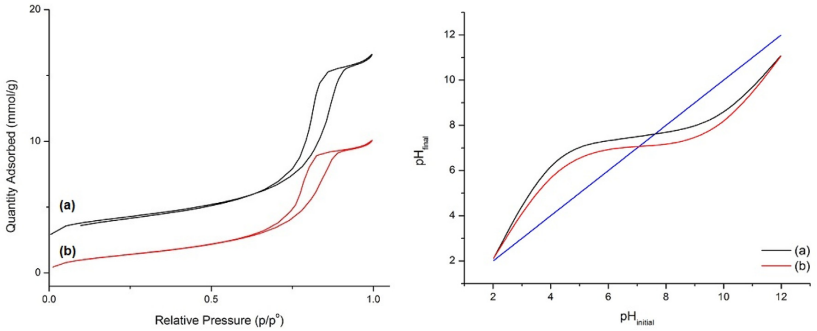

Fig. 3. BET and pH_{zpc} p.lot for CLN/SiO_2 (a) and $CLCA/SiO_2$ (b)

at 20 mg/10 mL nanocomposite dose and further increase in dose resulted in the slight increase in removal of Eu(III) which might be because of lesser amount of Eu(III) left in solution.

3.3. Effect of adsorbate-absorbent contact time

To determine optimum contact time CLN/SiO_2 nanocomposites was agitated with the solutions of Eu(III), La(III) or Sc(III) for different time intervals. In case of CLN/SiO_2, faster removal was observed within 30 min after that there was only slight increase in the removal of Eu(III), La(III) or Sc(III). However, as shown in Fig. S4 (a), at 50 min the removal of Sc(III) increased from 81% to 93%.

At the initial stages, the removal of carrier ions is faster due to the availability of free adsorbent sites and the removal becomes slower after certain time as the available adsorbents sites are not enough for the leftover carrier ions. Therefore, 50 min time was sufficient to remove Eu(III), La(III) and Sc(III) effectively in case of CLN/SiO_2.

3.4. Effect of solution pH

The pH of solution is an effective parameter, which decides the surface nature of adsorbent and adsorbate in aqueous solution as well as the degree of ionization. The uptake study of Eu(III), La (III) and Sc(III) were carried out in pH range of 2–6. The adsorption at pH higher than 6 was not considered as the precipitation started above this, resulting in the formation of insoluble metal hydroxides [31,32]. It is obvious from Fig. S4(b), that the removal of Eu (III), La(III) and Sc(III) is pH-dependent. The removal of Eu(III), La (III) and Sc(III) increases considerably from pH 2–6. The low absorption at low pH values is related to protonation of the lone pair of electrons on functional groups, resulting in a decrease in the adsorption of metal ions [1]. In strong acidic medium, the nanocomposites showed low adsorption capacity, probably due to the competitive adsorption between H^+ and REE ions. Aqueous H^+ ions with higher concentration and smaller ionic radii are easier to be adsorbed than REE ions. Thus, with increasing pH, the concentration of aqueous H^+ decreases slowly and REE ions coordinated with the nanocomposites more easily. The strong dependency of adsorption on the pH shows that metal ion complexes are formed with functional groups that is in agreement with the surface complexation model [1]. The maximum adsorption of Eu(III), La(III) and Sc(III) was observed at pH 6. Therefore, further experiments were performed at pH 6 with CLN/SiO_2 nanocomposite.

3.5. Effect of nanocomposite dosage

To explain the effect of CLN/SiO_2 nanocomposite dosage for removal of Eu(III), La(III) or Sc(III), adsorption was conducted at different dosages from 5 to 30 mg/10 mL. The trend of removal of Eu (III), La(III) and Sc(III) is shown in Fig. S4(c). Increased removal of Eu(III), La(III) and Sc(III) with increasing CLN/SiO_2 dose is obvious as higher CLN/SiO_2 dose facilitate more adsorbent sites for Eu(III), La(III) and Sc(III) removal. The removal percentage of Eu(III) increased by increasing the dose from 5 to 20 mg/10 mL after which there is not an obvious increase in removal. However, for La(III) and Sc(III) the removal keeps on increasing and was maximum at 30 mg/10 mL. Thus, a CLN/SiO_2 dose of 30 mg/10 mL was selected for all other adsorption experiments.

3.6. Effect of initial concentration of Eu(III), La(III) and Sc(III)

To investigate the effect of initial concentration of Eu(III), La(III) and Sc(III) on CLN/SiO_2, initial concentration was varied from 20 to 150 mg/L. It was observed from Fig. S5(a) that on increasing initial concentration, the adsorbed amount of Eu(III), La(III) and Sc(III) increased because at lower concentration most of the adsorbent sites were left unoccupied while number of occupied adsorbent sites increased by increasing initial concentration, resulting in increased adsorption capacity.

3.7. Effect of temperature

To study the effect of temperature on the adsorption of Eu(III), La(III) and Sc(III) four different temperatures were taken under consideration. The removal of Eu(III), La(III) and Sc(III) was found to increase slightly with the increase in temperature which suggests that the interaction between Eu(III), La(III) and Sc(III) on CLN/SiO_2 nanocomposite was higher at higher temperatures (Fig. S5(b)). The increase in removal of Eu(III), La(III) and Sc(III) on CLN/SiO_2 nanocomposite may be due to the pore size enlargement which provides new adsorbent sites for the interaction which were not available at lower temperature [33].

3.8. Kinetics

To study the adsorption process, kinetic study is useful in order to understand the adsorption mechanism [10]. Experiments were performed at 298 K with the Eu(III), La(III) and Sc(III) concentration of 25 mg/L. Pseudo first-order [10,34] and pseudo second-order

kinetic [35] models were used on adsorption data to determine the rate constants.

$$\log(q_e - q_t) = \log q_e - \frac{k_1}{2.303}t \quad (2)$$

$$\frac{t}{q_t} = \frac{1}{k_2 q_e^2} + \frac{1}{q_e}t \quad (3)$$

where t is time (min); q_e and q_t are adsorption capacity at equilibrium and at time t (mg/g), respectively; k_1 (min^{-1}) and k_2 (g/mg. min^{-1}) are rate constants for pseudo first order and second order, respectively.

The correlation coefficient R^2 and the parameters for pseudo first order and pseudo second order kinetic model are listed in Table S2. The adsorption of Eu(III) and La(III) on CLN/SiO_2 followed pseudo second order kinetics with a higher value of R^2, whereas, the R^2 value obtained from pseudo first rate equation (Eq. (2)) was higher for Sc(III) compared to pseudo second order kinetics. Similarly, the adsorption capacity of Eu(III) and La(III) at equilibrium estimated from pseudo second order rate equation (Eq. (3)) agreed with the experimental data and vice versa for Sc(III). It could be stated that the adsorption of Eu(III) and La(III) on CLN/SiO_2 supports the assumption of chemisorption and physisorption for Sc(III) [36].

Furthermore, intra-particle diffusion model and Boyd model was used to investigate the contribution of various steps involved in the adsorption process viz intra-particle diffusion and film diffusion. Following Weber–Morris equation [37] (Eq. (4)) for intra-particle diffusion was applied on the kinetic data:

$$q_t = k_i t^{1/2} + C \quad (4)$$

where q_t is the adsorption capacity at time t (mg/g), k_i is the intra-particle diffusion rate constant and C is a constant which is related to the boundary layer effects. The linear fitting of experimental data to (Eq. (4)) indicates that the adsorption process is only controlled by intra-particle diffusion. However, in case of adsorption of Eu (III), La(III) and Sc(III) on CLN/SiO_2 (Fig. 4(c)) the linear plot did not pass through the origin indicating that the intra-particle diffusion is not the only rate governing step.

The Boyd model is mainly used to distinguish between intra-particle diffusion and film diffusion; expressed as (Eq. (5)). Therefore, the kinetic data were also analyzed by Boyd model [38] (liquid film diffusion model) in order to determine the actual rate controlling step involved in the adsorption process.

$$\ln\left(1 - \frac{q_t}{q_e}\right) = k_f t \quad (5)$$

where k_f is the film diffusion rate constant. If the straight line does not pass through the origin, the adsorption process is governed by film diffusion, otherwise, it is governed by intra-particle diffusion process. It can be seen from Fig. 4(d); film diffusion control the adsorption of Eu(III), La(III) and Sc(III) on CLN/SiO_2 as the linear plot does not passes through the origin.

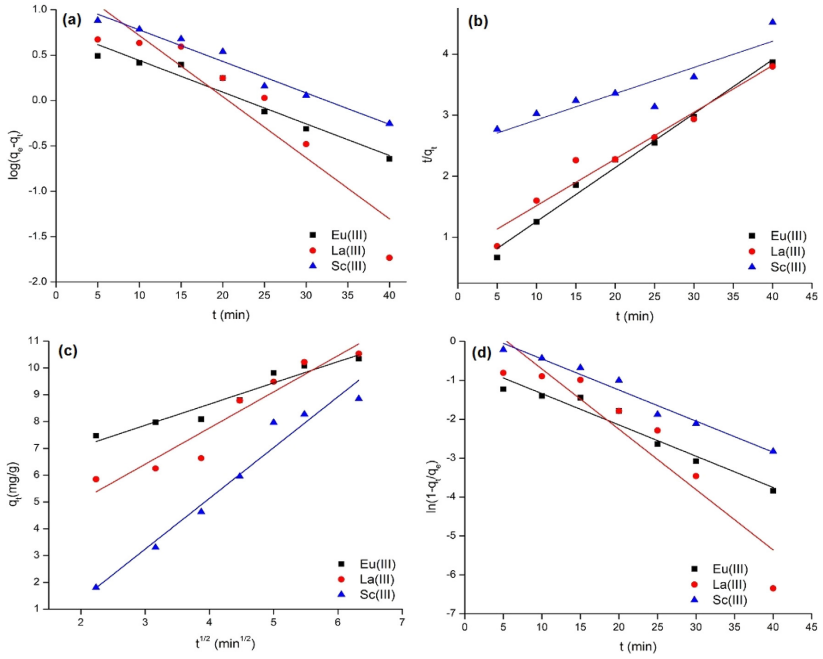

Fig. 4. Plot of pseudo first order model (a), pseudo second order model (b), intra-particle diffusion model (c) and Boyd model (d) for adsorption of Eu(III), La(III) and Sc(III) on CLN/SiO_2.

3.9. Isotherms

The adsorption isotherm is helpful in the designing of any adsorption system [10]. The equilibrium data was analyzed by Langmuir, Freundlich and Tempkin isotherm model. The four different linearized forms of Langmuir isotherm are as follows [10,39]:

$$\text{Langmuir I } \frac{C_e}{q_e} = \frac{1}{K_L Q_0} + \frac{C_e}{Q_0} \quad (6)$$

$$\text{Langmuir II } \frac{1}{q_e} = \left(\frac{1}{K_L Q_0}\right)\frac{1}{C_e} + \frac{1}{Q_0} \quad (7)$$

$$\text{Langmuir III } q_e = Q_0 - \left(\frac{1}{K_L}\right)\frac{q_e}{C_e} \quad (8)$$

$$\text{Langmuir IV } \frac{q_e}{C_e} = K_L Q_0 - K_L qe \quad (9)$$

where q_e and Q_0 are the equilibrium adsorption capacity and the maximum adsorption capacity (mg/g), respectively; C_e is equilibrium concentration of metal ions (mg/L); K_L is Langmuir constant related to energy of adsorption. The equilibrium data was analyzed by all the four linearized forms of Langmuir isotherm to calculate the maximum Langmuir adsorption capacity.

The Freundlich isotherm gives following expression on linearization [38,40]:

$$\ln q_e = \ln K_f + \frac{1}{n}\ln C_e \quad (10)$$

where K_f represents the Freundlich adsorption capacity while n is the term used for the heterogeneity factor related to adsorption intensity. In order to determine the maximum adsorption capacity, it is necessary to operate with constant initial concentration C_0 and variable weights of adsorbent; thus $\ln q_e$ is the extrapolated value of lnq for $C_e = C_0$ [41].

The linearized equations for Tempkin isotherm is given below [9,10]:

$$q_e = B\log(A) + B\log(C_e) \quad (11)$$

where $B = RT/b$ is a constant related to heat of sorption (J/mol), A is Tempkin constant at equilibrium (L/g), R is the gas constant (J/mol K), T is temperature in kelvin (K) and b is Tempkin constant related to heat of sorption.

The different isotherm parameters of Langmuir, Freundlich and Tempkin isotherm are summarized in Table 1 and the obtained straight lines are shown in Fig. S6(a–f). Best fit isotherm model for experimental data can be determined by correlation coefficient (R^2) values. Among different type of Langmuir isotherms, type I was found to be suitable for describing isotherm data for Eu(III) and La(III) with a higher correlation coefficient (R^2) values compared to Freundlich isotherm model. It was also observed that for Eu(III) and La(III) Langmuir type I had good R^2 values and higher adsorption capacities in comparison to Langmuir type II, III and IV. However, high correlation coefficient (R^2) value derived by fitting the experimental data fitted well to Freundlich model for adsorption of Sc(III). The results also strongly supported the validity of kinetic study [42]. The following trend was observed for different isotherm models: Langmuir I > Freundlich > Tempkin (for Eu and La); Freundlich > Langmuir II > Tempkin (for Sc).

Table 2 summarizes the maximum adsorption capacities and regeneration cycles on CLN/SiO_2 and some previously reported adsorbents. The higher adsorption capacity values of CLN/SiO_2 than those of the most of the reported sorbents except CL-Zn/Al LDH, suggested that CLN/SiO_2 is a relatively efficient adsorbent for removal of Eu(III), La(III) and Sc(III). The extraordinarily high adsorption capacity of La(III) by CL-Zn/Al LDH was attributed due to the surface properties of LDH layer [9].

Table 1
Langmuir, Freundlich and Tempkin isotherm model parameters for adsorption of Eu (III), La(III) and Sc(III) onto CLN/SiO_2.

Kinetic models	Model parameters	Eu(III)	La(III)	Sc(III)
Langmuir I	Q_o	24.47	29.48	93.54
	K_L (L/mg)	0.085	0.072	0.014
	R^2_{L1}	0.955	0.964	0.632
Langmuir II	Q_o	18.05	19.96	41.56
	K_L (L/mg)	1.8	1.24	0.056
	R^2_{L2}	0.573	0.509	0.884
Langmuir III	Q_o	18.79	21.4	49.63
	K_L (L/mg)	1.58	1.05	0.044
	R^2_{L3}	0.330	0.281	0.393
Langmuir IV	Q_o	20.55	24.31	78.42
	K_L (L/mg)	0.60	0.35	0.019
	R^2_{L4}	0.330	0.281	0.393
Freundlich	K_f (L/g)	9.57	8.58	2.70
	n	5.82	4.24	1.48
	R^2_F	0.849	0.862	0.965
Tempkin	A (L/g)	25.65	5.27	0.25
	B (J/mol)	2.66	3.96	14.55
	R^2_T	0.757	0.774	0.837

3.10. Thermodynamics study

To explain spontaneity of process, randomness of adsorbate-adsorbent system and endothermic/exothermic nature of adsorption process investigation of thermodynamic parameters viz. changes of Gibbs free energy (ΔG^0), enthalpy (ΔH^0), and entropy (ΔS^0) is very important. Following equations were used for the calculation of thermodynamic parameters;

$$\ln K_C = \frac{\Delta S^0}{R} - \frac{\Delta H^0}{RT} \quad (12)$$

$$\Delta G^0 = -RT\ln K_C \quad (13)$$

where K_c is thermodynamic equilibrium constant (L/g), R is universal gas constant (8.314 J/mol/K), T is temperature (K), ΔG^0 is Gibbs free energy (kJ/mol), ΔS^0 is entropy (J/mol/K) and ΔH^0 is enthalpy (kJ/mol) [43]. The values of ΔG^0, ΔH^0 and ΔS°Calculated using Eqs. (12) and (13) are shown in Table S3. Negative value of ΔG^0 indicates the feasibility of Eu(III), La(III) and Sc(III) removal by adsorption on CLN/SiO_2 nanocomposite and suggests the spontaneous nature of adsorption on nanocomposite. The positive values of ΔH^0 indicates the adsorption process was endothermic. The enthalpy values obtained also suggests the chemisorption process for Eu(III) and La(III) ($\Delta H^0 > 50$ kJ/mol) and physisorption for Sc (III) ($\Delta H^0 < 50$ kJ/mol) [31]. It was also observed that Sc(III) showed different behavior towards the nanocomposite compared to Eu(III) and La(III) which might be due to the phenomenon of lanthanide contraction and stabilization of the repulsion energy between f-electrons [44]. In addition, positive values of the entropy change (ΔS^0) suggests about the randomness at the solid-liquid interface which increases during the adsorption of Eu(III), La(III) and Sc(III) on CLN/SiO_2.

3.11. Desorption study

As different concentrations of HCl and NaOH were investigated to find out better desorbing medium and desorption study showed that among all tested eluents 0.5 mol/L HCl was highly efficient to desorb the maximum amount of Eu(III), La(III) and Sc(III) from CLN/SiO_2. So, 0.5 mol/L HCl was selected as desorbing medium for desorption of Eu(III), La(III) and Sc(III) and regeneration of CLN/SiO_2 for further adsorption–desorption cycles. Regenerated adsorbent was

Table 2
Maximum adsorption capacities of Eu(III), La(III) and Sc(III) on different adsorbents.

Adsorbent	Adsorption capacity (mg/g)			Regeneration cycles	Refs.
	Eu(III)	La(III)	Sc(III)		
CLN/SiO_2	24.27	29.48	23.76[a]	3	This study
CL-Zn/Al LDH	–	92.15	–	5	Iftekhar et al. (2017)
Kaolin	–	1.73	–	–	Yanfei et al. (2016)
GMZ bentonite	26.1	18.4	–	3	Wu et al. (2012)
Hydroxyapatite	0.94	0.25	–	–	Granados-Correa et al. (2012)
SiO_2-A336	12.61[b]	–	2.518[b]	6	Turanov et al. (2016)
Amberite	–	4.27	–	–	El-Sofany (2008)

[a] Calculated from freundlich isotherm.
[b] Converted from the original unit of mmol/g presented in the literatures.

rather efficient for the removal of Eu(III), La(III) and Sc(III) up to three adsorption–desorption cycles (Fig. S7). However, in third cycle removal of Eu(III), La(III) and Sc(III) decreased to 59.9%, 57.6% and 49.9%, respectively. Thus, further cycles were not investigated.

3.12. Effect of competing ions

The Eu(III), La(III) and Sc(III) can be substituted by other cations due to similar ionic radius and effect the adsorption of Eu(III), La (III) and Sc(III) on CLN/SiO_2 [9,13,23,45]. Therefore it is important to check the competing ion effect on the adsorption of Eu(III), La (III) and Sc(III) on CLN/SiO_2. The experiments was performed in a multicomponent system with competing ions. The decrease of 8–10% in overall uptake of Eu(III), La(III) and Sc(III) on CLN/SiO_2 was observed in presence of 10-fold concentration of Na^+, K^+, Ca^{2+}, Mg^{2+}, Al^{3+} was observed (Fig. S8). This was probably because of Al^{3+} with similar ionic charge as that of Eu(III), La(III) and Sc(III) [46]. However, when present in a same system, considerable decrease in overall removal of Eu(III), La(III) and Sc(III) was noticed which might be due to the presence of the same ionic charge in the system [9].

4. Conclusion

In this paper, two different cellulose based silica (CLx/SiO_2) nanocomposite was synthesized and characterized by various techniques viz. TEM, AFM, SEM, XRD, FTIR and BET in order to determine its characteristics. TEM analysis indicated that the particle diameter of nanocomposite was in the range of 9–15 nm and silica particles was uniformly distributed throughout the nanocomposites. The presence of mixed phases of cellulose and SiO_2 was also observed by XRD and FTIR. Experimental results showed that CLx/SiO_2 produced when CL was modified with sulfuric acid possess higher surface area than that of citric acid modified. The adsorption rate was relatively fast that it could reach the equilibrium within 50 min. The results revealed the surface chemical sorption for Eu(III) and La(III) and physisorption for Sc (III). Present study suggests that CLN/SiO_2 nanocomposite could be explored as a promising adsorbent for Eu(III), La(III) and Sc(III) and can be utilized for the preconcentration of REEs from the diluted aqueous streams.

Acknowledgement

The authors are thankful to Mr. Toni Väkiparta from LUT School for Engineering Science for the SEM analysis.

Appendix A. Supplementary data

Supplementary data associated with this article can be found, in the online version, at http://dx.doi.org/10.1016/j.cej.2017.03.051.

References

[1] A. Tadjarodi, V. Jalalat, R. Zare-Dorabei, Adsorption of La (III) in aqueous systems by N-(2-hydroxyethyl) salicylaldimine-functionalized mesoporous silica, Mater. Res. Bull. 61 (2015) 113–119.
[2] J. Ponou, L.P. Wang, G. Dodbiba, K. Okaya, T. Fujita, K. Mitsuhashi, T. Atarashi, G. Satoh, M. Noda, Recovery of rare earth elements from aqueous solution obtained from Vietnamese clay minerals using dried and carbonized parachlorella, J. Environ. Chem. Eng. 2 (2014) 1070–1081.
[3] D. Sadovsky, A. Brenner, B. Astrachan, B. Asaf, R. Gonen, Biosorption potential of cerium ions using Spirulina biomass, J. Rare Earths 34 (2016) 644–652.
[4] F. Zhao, E. Repo, Y. Meng, X. Wang, D. Yin, M. Sillanpää, An EDTA-β-cyclodextrin material for the adsorption of rare earth elements and its application in preconcentration of rare earth elements in seawater, J. Colloid Interface Sci. 465 (2016) 215–224.
[5] M.R. Ganjali, V.K. Gupta, F. Faridbod, P. Norouzi, Lanthanides Series Determination by Various Analytical Methods, Elsevier, 2016.
[6] A.L. El-Ansary, N.S. Abdel-Kader, Synthesis, characterization of La (III), Nd (III), and Er (III) complexes with Schiff bases derived from Benzopyran-4-one and their fluorescence study, Int. J. Inorganic Chem. 2012 (2012).
[7] O.A. Burghard, S. Chatterjee, Z. Wang, S.A. Bryan, Spectroscopic properties of lanthanide (III) compounds in aqueous and ionic media, 2011.
[8] A. Premadas, P. Srivastava, Inductively coupled plasma atomic emission spectrometric determination of lanthanides and Y in various uranium hydrometallurgical products, J. Radioanal. Nucl. Chem. 251 (2002) 233–239.
[9] S. Iftekhar, V. Srivastava, M. Sillanpää, Synthesis and application of LDH intercalated cellulose nanocomposite for separation of rare earth elements (REEs), Chem. Eng. J. 309 (2017) 130–139.
[10] V. Srivastava, M. Sillanpää, Synthesis of malachite@ clay nanocomposite for rapid scavenging of cationic and anionic dyes from synthetic wastewater, J. Environ. Sci. 51 (2017) 97–110.
[11] V. Srivastava, Y. Sharma, M. Sillanpää, Green synthesis of magnesium oxide nanoflower and its application for the removal of divalent metallic species from synthetic wastewater, Ceram. Int. 41 (2015) 6702–6709.
[12] D. Das, C.J.S. Varshini, N. Das, Recovery of lanthanum (III) from aqueous solution using biosorbents of plant and animal origin: Batch and column studies, Miner. Eng. 69 (2014) 40–56.
[13] M.R. Awual, T. Yaita, H. Shiwaku, Design a novel optical adsorbent for simultaneous ultra-trace cerium (III) detection, sorption and recovery, Chem. Eng. J. 228 (2013) 327–335.
[14] Y. Zhu, W. Wang, Y. Zheng, F. Wang, A. Wang, Rapid enrichment of rare-earth metals by carboxymethyl cellulose-based open-cellular hydrogel adsorbent from HIPEs template, Carbohydr. Polym. 140 (2016) 51–58.
[15] N. Das, D. Das, Recovery of rare earth metals through biosorption: an overview, J. Rare Earths 31 (2013) 933–943.
[16] J. Raabe, A. de Souza Fonseca, L. Bufalino, C. Ribeiro, M.A. Martins, J.M. Marconcini, G.H.D. Tonoli, Evaluation of reaction factors for deposition of silica (SiO_2) nanoparticles on cellulose fibers, Carbohydr. Polym. 114 (2014) 424–431.
[17] F. Zhao, W.Z. Tang, D. Zhao, Y. Meng, D. Yin, M. Sillanpää, Adsorption kinetics, isotherms and mechanisms of Cd (II), Pb (II), Co (II) and Ni (II) by a modified magnetic polyacrylamide microcomposite adsorbent, J. Water Process Eng. 4 (2014) 47–57.
[18] F. Zhao, E. Repo, M. Sillanpää, Y. Meng, D. Yin, W.Z. Tang, Green synthesis of magnetic EDTA-and/or DTPA-cross-linked chitosan adsorbents for highly efficient removal of metals, Ind. Eng. Chem. Res. 54 (2015) 1271–1281.
[19] R.J. Pinto, P.A. Marques, A.M. Barros-Timmons, T. Trindade, C.P. Neto, Novel SiO_2/cellulose nanocomposites obtained by in situ synthesis and via polyelectrolytes assembly, Compos. Sci. Technol. 68 (2008) 1088–1093.
[20] S. Hokkanen, A. Bhatnagar, E. Repo, S. Lou, M. Sillanpää, Calcium hydroxyapatite microfibrillated cellulose composite as a potential adsorbent for the removal of Cr (VI) from aqueous solution, Chem. Eng. J. 283 (2016) 445–452.
[21] K. Nozawa, H. Gailhanou, L. Raison, P. Panizza, H. Ushiki, E. Sellier, J. Delville, M. Delville, Smart control of monodisperse Stöber silica particles: effect of reactant addition rate on growth process, Langmuir 21 (2005) 1516–1523.
[22] M.R. Awual, New type mesoporous conjugate material for selective optical copper (II) ions monitoring & removal from polluted waters, Chem. Eng. J. 307 (2017) 85–94.

[23] M.R. Awual, T. Kobayashi, Y. Miyazaki, R. Motokawa, H. Shiwaku, S. Suzuki, Y. Okamoto, T. Yaita, Selective lanthanide sorption and mechanism using novel hybrid Lewis base (N-methyl-N-phenyl-1, 10-phenanthroline-2-carboxamide) ligand modified adsorbent, J. Hazard. Mater. 252 (2013) 313–320.
[24] D.L. Ramasamy, E. Repo, V. Srivastava, M. Sillanpää, Chemically immobilized and physically adsorbed PAN/acetylacetone modified mesoporous silica for the recovery of rare earth elements from the waste water-comparative and optimization study, Water Res. 114 (2017) 264–276.
[25] X. Yu, S. Tong, M. Ge, J. Zuo, Removal of fluoride from drinking water by cellulose@ hydroxyapatite nanocomposites, Carbohydr. Polym. 92 (2013) 269–275.
[26] C. Liu, A. Zhang, W. Li, F. Yue, R. Sun, Succinoylation of cellulose catalyzed with iodine in ionic liquid, Ind. Crops Prod. 31 (2010) 363–369.
[27] Y. Tian, M. Wu, R. Liu, D. Wang, X. Lin, W. Liu, L. Ma, Y. Li, Y. Huang, Modified native cellulose fibers—a novel efficient adsorbent for both fluoride and arsenic, J. Hazard. Mater. 185 (2011) 93–100.
[28] Y. Zhou, X. Hu, M. Zhang, X. Zhuo, J. Niu, Preparation and characterization of modified cellulose for adsorption of Cd (II), Hg (II), and acid fuchsin from aqueous solutions, Ind. Eng. Chem. Res. 52 (2013) 876–884.
[29] R. Sivakami, P. Thiyagarajan, The effect of citric acid on morphology and photoluminescence properties of white light emitting ZnO–SiO 2 nanocomposites, Photonics Nanostruct.-Fundam. Appl. 20 (2016) 31–40.
[30] T.-H. Liou, C.-C. Yang, Synthesis and surface characteristics of nanosilica produced from alkali-extracted rice husk ash, Mater. Sci. Eng., B 176 (2011) 521–529.
[31] Ş. Sert, C. Kütahyali, S. İnan, Z. Talip, B. Çetinkaya, M. Eral, Biosorption of lanthanum and cerium from aqueous solutions by Platanus orientalis leaf powder, Hydrometallurgy 90 (2008) 13–18.
[32] K. Vijayaraghavan, R. Balasubramanian, Single and binary biosorption of cerium and europium onto crab shell particles, Chem. Eng. J. 163 (2010) 337–343.
[33] B. Yan, Z. Chen, L. Cai, Z. Chen, J. Fu, Q. Xu, Fabrication of polyaniline hydrogel: synthesis, characterization and adsorption of methylene blue, Appl. Surf. Sci. 356 (2015) 39–47.
[34] S. Lagergren, About the theory of so-called adsorption of soluble substances, 1898.
[35] Y.-S. Ho, G. McKay, Pseudo-second order model for sorption processes, Process Biochem. 34 (1999) 451–465.
[36] Y.-S. Ho, Review of second-order models for adsorption systems, J. Hazard. Mater. 136 (2006) 681–689.
[37] P. Wang, M. Cao, C. Wang, Y. Ao, J. Hou, J. Qian, Kinetics and thermodynamics of adsorption of methylene blue by a magnetic graphene-carbon nanotube composite, Appl. Surf. Sci. 290 (2014) 116–124.
[38] S. Duan, R. Tang, Z. Xue, X. Zhang, Y. Zhao, W. Zhang, J. Zhang, B. Wang, S. Zeng, D. Sun, Effective removal of Pb (II) using magnetic $Co_{0.6}Fe_{2.4}O_4$ micro-particles as the adsorbent: Synthesis and study on the kinetic and thermodynamic behaviors for its adsorption, Colloids Surf., A 469 (2015) 211–223.
[39] I. Langmuir, The adsorption of gases on plane surfaces of glass, mica and platinum, J. Am. Chem. Soc. 40 (1918) 1361–1403.
[40] H. Freundlich, Over the adsorption in solution, J. Phys. Chem. 57 (1906) 1100–1107.
[41] O. Hamdaoui, E. Naffrechoux, Modeling of adsorption isotherms of phenol and chlorophenols onto granular activated carbon: Part I. Two-parameter models and equations allowing determination of thermodynamic parameters, J. Hazard. Mater. 147 (2007) 381–394.
[42] H.M. Marwani, H.M. Albishri, T.A. Jalal, E.M. Soliman, Study of isotherm and kinetic models of lanthanum adsorption on activated carbon loaded with recently synthesized Schiff's base, Arab. J. Chem. 10 (2013) S1032–S1040.
[43] X. Yanfei, L. Huang, L. Zhiqi, F. Zongyu, W. Liangshi, Adsorption ability of rare earth elements on clay minerals and its practical performance, J. Rare Earths 34 (2016) 543–548.
[44] A.N. Turanov, V.K. Karandashev, N.S. Sukhinina, V.M. Masalov, G.A. Emelchenko, Adsorption of lanthanides and scandium ions by silica sol-gel material doped with novel bifunctional ionic liquid, trioctylmethylammonium 1-phenyl-3-methyl-4-benzoyl-5-onate, J. Environ. Chem. Eng. 4 (2016) 3788–3796.
[45] S. Zhou, X. Li, Y. Shi, A. Alshameri, C. Yan, Preparation, characterization, and Ce (III) adsorption performance of poly (allylamine)/silica composite, Desalination Water Treat. 56 (2015) 1321–1334.
[46] M.R. Awual, T. Kobayashi, H. Shiwaku, Y. Miyazaki, R. Motokawa, S. Suzuki, Y. Okamoto, T. Yaita, Evaluation of lanthanide sorption and their coordination mechanism by EXAFS measurement using novel hybrid adsorbent, Chem. Eng. J. 225 (2013) 558–566.

Publication III

Iftekhar, S., Srivastava, V., Casas, A., and Sillanpää, M.
Synthesis of novel GA-g-PAM/SiO_2 nanocomposite for the recovery of rare earth elements (REE) ions from aqueous solution

Reprinted with permission from
Journal of Cleaner Production
Vol. 170, pp. 251-259, 2018

Journal of Cleaner Production 170 (2018) 251–259

Contents lists available at ScienceDirect

Journal of Cleaner Production

journal homepage: www.elsevier.com/locate/jclepro

Synthesis of novel GA-g-PAM/SiO_2 nanocomposite for the recovery of rare earth elements (REE) ions from aqueous solution

Sidra Iftekhar [a, *], Varsha Srivastava [a], Alba Casas [b], Mika Sillanpää [a, c]

[a] Laboratory of Green Chemistry, School of Engineering Science, Lappeenranta University of Technology, Sammonkatu 12, FI-50130 Mikkeli, Finland
[b] IES Enrique Florez, Department of Chemistry, C/Madrid 20, 09002 Burgos, Spain
[c] Department of Civil and Environmental Engineering, Florida International University, Miami, FL 33174, USA

ARTICLE INFO

Article history:
Received 4 May 2017
Received in revised form
16 September 2017
Accepted 16 September 2017
Available online 18 September 2017

Keywords:
Adsorption
EPR spin trapping
Lanthanides
Nanocomposite

ABSTRACT

The study highlights the preparation of novel Gum Arabic (GA) grafted polyacrylamide based silica nanocomposite using in-situ radial graft copolymerization method. The presence of radicals involved in synthesis of GA-g-PAM was detected using DMPO as a spin trapping agent by Electron paramagnetic resonance (EPR) analysis and the possible reaction pathway was proposed. The novel GA-g-PAM/SiO_2 nanocomposite was characterized by Elemental analyzer (CHNS/O), Fourier transform infrared spectroscopy (FTIR), X-ray diffraction (XRD), Transmission electron microscopy (TEM), Atomic force microscopy (AFM), Brunauer Emmett and Teller (BET) and zeta potential (ZP) to study the chemical, structural and textural properties of nanocomposite. The successful incorporation of silica in grafted copolymer matrix was confirmed by FTIR and XRD analysis. The results indicated that surface area increased significantly after formation of GA-g-PAM/SiO_2 compared to parental polymer (GA) matrix and 273.55 m^2/g surface area was determined for GA-g-PAM/SiO_2 nanocomposite. The recovery of rare earth elements (REE) from aqueous solution was also investigated using GA-g-PAM/SiO_2 nanocomposite. The optimum conditions for REEs adsorption were determined from the batch adsorption experiments. The adsorption kinetics for REEs were well described by pseudo first order model. The adsorption equilibrium data fitted well with Langmuir isotherm except for Sc ions. The thermodynamic studies confirm that the adsorption is spontaneous and endothermic. Desorption studies affirmed the regenerative efficiency of loaded REEs up to three cycles.

1. Introduction

In modern societies, the application of rare earth elements (REEs) is increasing due to their unique physical and chemical properties (Iftekhar et al., 2017a, b). Several techniques have been applied for the uptake/recovery of REEs from aqueous systems such as solvent extraction, ion exchange, solid-phase extraction, ion-selective electrodes (Ponou et al., 2014; Sadovsky et al., 2016; Zhao et al., 2016) and adsorption (Awual et al., 2013; Das et al., 2014; Iftekhar et al., 2017a; Srivastava et al., 2015; Srivastava and Sillanpää, 2017; Zhu et al., 2016); owing to their low concentration in waste sources. Adsorption method is the best technique because of cost, simplicity of design and operation (Das and Das, 2013). Therefore, many researchers have started developing a cost effective and eco-friendly materials to recover rare earth metals from aqueous environment (Das et al., 2014).

Nowadays technologies demand the materials to be modified precisely by varying the several parameters during synthesis, i.e. tailored materials are required. Under this category lies grafted polymers, as the properties of these materials can be tailored by controlling the grafting percentage (Sen et al., 2009; Sen and Pal, 2009). The combination of both natural and synthetics polymers resulted in new materials with unique properties (Sen et al., 2009). However, the major drawback of synthetic polymers being used for modifying the natural polymers is shear degradability (Ghosh et al., 2010). The most common and efficient method of modifying structural and functional properties of natural polymers is chemical grafting (Ghorai et al., 2012; Sen et al., 2009). Graft copolymerization of natural polysaccharides is becoming an important resource for developing advanced materials as it can improve the functional properties of natural polysaccharides. The grafting results in combining the properties of both polymers because of the

* Corresponding author.
E-mail addresses: sidra.iftekhar@lut.fi, sidra_iftekhar@yahoo.com (S. Iftekhar).

https://doi.org/10.1016/j.jclepro.2017.09.166
0959-6526/

attachment of synthetic polymeric chains on backbone of natural polymers (polysaccharides); they have reasonable shear stability and biodegradability to some level (Sen et al., 2009). Highly customizable matrices resulted by grafting on polysaccharides by synthetic polymers (Sen and Pal, 2009). Grafted polymers synthesis mainly involves free radical mechanism (Sen and Pal, 2009). These free radicals can be generated by various methods including use of free radical initiator (Chen et al., 2009; Ghosh et al., 2010; Sen et al., 2009; Singh et al., 2007a), high energy radiations for instance ɣ-rays (Wang et al., 2008) or by microwave irradiation (Rahul et al., 2014; Sen and Pal, 2009). Furthermore, silicate based polymer composites often reveal notable improvement in mechanical, thermal, and physicochemical properties when compared with pure polymers and their conventional grafted composites (micro-composites) due to the nano-level interactions with the polymer matrix (Singh et al., 2007a).

Natural polymer hybridization via synthetic polymers by addition of nano-level silica is of great interest due to their wider application in several fields viz. controlled drug release (Sen et al., 2009; Sen and Pal, 2009), flocculants (Ghosh et al., 2010; Rahul et al., 2014; Sen et al., 2009; Wang et al., 2008), adsorbent (Ghorai et al., 2012; Pal et al., 2012; Sen and Pal, 2009). It has also been noticed that by grafting of polyacrylamide (PAM) chains onto polysaccharides make it is possible to develop efficient adsorbent materials for the treatment of industrial effluents and wastewaters (Ghosh et al., 2010). The main advantages of using gum polysaccharide-based nanocomposites for the treatment of wastewater is their easy availability, low toxicity, low cost and environmentally friendly nature (Mittal et al., 2016). Adsorbents/nanocomposites based on gum polysaccharides such as gum ghatti (Mittal and Mishra, 2014), gum guar (Singh et al., 2007a), gum karaya (Mittal et al., 2016), gum xanthan (Ghorai et al., 2012; Mittal et al., 2014), tamarind kernel (Ghosh et al., 2010) are less reported in literature. However, some polysaccharides like chitosan (Wang et al., 2008), cellulose (Zhu et al., 2016) and carboxymethyl starch (Sen et al., 2009; Sen and Pal, 2009; Wu et al., 2011) are extensively studied, which have shown potential in the removal of various pollutants from contaminated water.

Among these all, naturally occurring polysaccharides Gum Arabic (GA) is a class of polysaccharides extracted from the trunks and barks of acacia tree (Quintanilha et al., 2014). GA is also the most abundant and important gum used as emulsifiers and stabilizers (Banerjee and Chen, 2007). GA is chemically defined as a blend of branched polymers and oligomers containing arabinose, galactose, rhamnose and uronic acids as monosaccharide components that can be associated with some proteins (Fauconnier et al., 2000; Quintanilha et al., 2014). To the best of our knowledge, there are no studies reported in the literature on the synthesis of tailored materials (GA-g-PAM/SiO_2 nanocomposite) and its application for REEs removal. Further, spin trap of radicals during synthesis of GA-g-PAM/SiO_2 and their determination by EPR analysis is not yet well explored.

In this study, we investigated the mechanism of synthesis of GA-g-PAM from free radicals using EPR spin trapping technique and possible reaction pathway was proposed. The synthesized nanocomposite was characterized by various techniques viz. CHNS/O, FTIR, XRD, TEM, AFM, BET surface area and ZP. Furthermore, GA-g-PAM/SiO_2 was utilized for the removal of REEs viz. Eu, La, Nd and Sc from aqueous solutions. The operating parameters affecting the adsorption performance were investigated for the optimization of removal process. In addition, adsorption kinetics, equilibrium and thermodynamic data were processed to understand the adsorption mechanism.

Table 1
Langmuir, Freundlich and Tempkin isotherm model parameters for adsorption of Ln (III) on GA-g-PAM/SiO_2 nanocomposite.

Models	Model Parameters	Eu	La	Nd	Sc
Langmuir	Q_o	10.11	7.90	12.24	35.22
	K_L (L/mg)	0.21	0.17	0.07	0.02
	R_L^2	0.994	0.986	0.981	0.810
Freundlich	K_f (L/g)	4.98	3.07	2.37	1.56
	n	6.73	4.96	2.92	1.64
	R_F^2	0.855	0.756	0.867	0.987
Tempkin	A (L/g)	63.81	7.09	0.84	0.25
	B (J/mol)	1.11	1.17	2.49	6.74
	R_T^2	0.829	0.763	0.899	0.892
Elovich	Q_o	0.79	0.75	0.29	0.06
	K_e (L/mg)	1121.86	86.72	103.35	11.52
	R_E^2	0.772	0.635	0.759	0.765

2. Methods

2.1. Materials and reagents

Gum Arabic (GA), polyacrylamide (AA), potassium persulphate (KPS), tetraethylorthosilicate (98% TEOS), ammonium hydroxide (NH_4OH), ethanol (99.9% pure), 5,5-Dimethyl-1-pyrroline N-oxide (DMPO) and chloride salts of REEs were purchased from Sigma−Aldrich. All the chemicals were used as received without further purification.

2.2. Synthesis of GA-g-PAM

The polyacrylamide grafted gum arabic was synthesized by radical polymerization technique in nitrogen atmosphere using KPS as initiator. One gram of GA was slowly dissolved into 100 mL of distilled water with constant stirring (400 rpm) at 70 °C for 1 h. Afterwards, required amount of AA (listed in Table 1) was added to the GA solution and stirred for 30 min at the same temperature (70 °C) with constant stirring (400 rpm). Afterwards, KPS of required concentration (Table S1) was added and reaction was continued for another 1 h. The reaction mixture was cooled to room temperature (23 ± 2 °C) and dispersed in acetone. The product was finally washed with 250 mL of acetone, filtered and then dried in a hot air oven at 50 °C for 12 h, ground to fine powder by Tubemill (IKA Tube mill control). The synthesis parameters are reported in Table S1. % Grafting and % Efficiency of graft copolymer was calculated by Eq. (1) and Eq. (2) (Singh et al., 2007a)

$$\%Grafting(\%G) = \frac{W_1 - W_0}{W_0} \times 100 \quad (1)$$

$$\%Efficiency(\%E) = \frac{W_1 - W_0}{W_2} \times 100 \quad (2)$$

where W_0, W_1 and W_2 are the weight of GA, weight of GA-g-PAM and weight of monomer, respectively.

2.3. Synthesis of GA-g-PAM/SiO_2

For synthesis of GA-g-PAM/SiO_2, 0.5 g of GA-g-PAM was dissolved in 50 mL distilled water with constant stirring (400 rpm) at 50 °C. Required amount of 2.5 mL TEOS was dissolved in 2.5 mL ethanol and 2 mL of NH_4OH (12 N) was also prepared separately. Then, the three solutions were rapidly mixed into a reaction glass vessel and kept under continuous stirring (400 rpm) at 50 °C. The reaction was allowed to continue for 18 h to grow monodisperse SiO_2 particles, within the modified biopolymer medium and then precipitated by adding 250 mL of acetone. The obtained hybrid

nanocomposite was then dried at 50 °C, pulverized by Tubemill and sieved through a 150 μm sieve.

2.4. Electron paramagnetic resonance (EPR) studies

The presence of radicals generated during synthesis of GA-g-PAM was identified by EPR using 5,5-dimethyl-1-pyrroline-N-oxide (DMPO) as the spin-trapping agent. The concentration of DMPO used was 100 mM. The EPR spectra were obtained at room temperature using an ADANI CMS-8400 with a microwave frequency of 9.43 GHz, modulation frequency of 100 kHz, modulation amplitude of 100 μT, sweep width of 25 mT, time constant of 80 s.

2.5. Characterization

C, H, N analysis was performed using an Elemental Analyzer (Thermo scientific, CHNS/O analyzer Flash 2000). The nanocomposite was also characterized by FTIR (Model: Bruker Vertex 70) and XRD (Model: PANalytical X-ray diffractometer) to identify the surface groups and phase identification. Morphological characterization was done by using TEM (Model: Hitachi H-7600) and AFM (Model: Park Systems NX10). The surface area and pore size of the nanocomposites were calculated using BET (Model: Tristar® II Plus). To perform isoelectric point titration, Malvern Zeta potential Nano ZEN3500 was used.

2.6. Adsorption and desorption experiments

Synthesized GA-g-PAM/SiO_2 nanocomposite was used for the treatment of REEs (Eu, La, Nd, Sc) from aqueous solution. Aqueous solution (25 mg/L) was prepared by the addition of required amount of salt of chosen REEs in deionized water. 2 g/L of GA-g-PAM/SiO_2 nanocomposite was added in REEs solutions (10 mL) and agitated in a temperature control shaker (25 ± 2 °C) at 200 rpm. Afterwards, the adsorbents were separated by using 0.45 μm PTFE membrane filter and the residual concentration of REE ions was measured by ICP-OES (Thermo iCAP 6300 series). All the tests were conducted in duplicate. Kinetic experiments were performed in the same way as discussed above except samples were collected at different time intervals. The adsorption capacity of the nanocomposites was calculated from the following equation:

$$q_e = \frac{\left(C_0 - C_f\right)V}{M} \tag{3}$$

where q_e is the adsorption capacity in mg/g, V is the volume of solution (L), M is the mass of nanocomposite (g), C_o and C_f is the initial and equilibrium concentrations of REEs in solution (mg/L).

For desorption study, experiments were started with REEs loaded GA-g-PAM/SiO_2 nanocomposite which was separated by centrifugation, washed with deionized water and desorbed with different concentrations of HCl and NaOH. The process was repeated several times and efficiency of nanocomposite for REEs uptake for different adsorption-desorption cycle was investigated.

2.7. Models to fit kinetic, isotherm and thermodynamics

The adsorption kinetics was analyzed by pseudo first order and pseudo second order kinetic model, which can be expressed as:

Pseudo first order model (Lagergren, 1898):

$$\log(q_e - q_t) = \log q_e - \frac{k_1}{2.303}t \tag{4}$$

Pseudo second order model (Ho and McKay, 1999):

$$\frac{t}{q_t} = \frac{1}{k_2 q_e^2} + \frac{1}{q_e}t \tag{5}$$

where t is time (min); q_e and q_t are adsorption capacity of REEs over GA-g-PAM/SiO_2 at equilibrium and at time t (mg/g), respectively; k_1 (min^{-1}) and k_2 (g mg^{-1} min^{-1}) are rate constants for pseudo first order and second order, respectively.

For further understanding of adsorption process, intra-particle diffusion model and Boyd model was used to analyze the kinetic behavior of adsorption process, which can be expressed as:

Intra-particle diffusion model (Chen et al., 2012; Yuan et al., 2013):

$$q_t = k_i t^{1/2} + C \tag{6}$$

Boyd Model (Duan et al., 2015):

$$\ln\left(1 - \frac{q_t}{q_e}\right) = k_f t \tag{7}$$

where C is a constant, k_i and k_f is the intra-particle diffusion rate constant and film diffusion rate constant, respectively. The linear fitting of experimental data to (Eq. (6)) indicates that the adsorption process is only controlled by intra-particle diffusion. However, in case of deviation, the process is composed by two or three steps. Similarly, if the straight line (Eq. (7)) does not pass through the origin the adsorption process is governed by film diffusion, otherwise, it is governed by intra-particle diffusion process.

To elucidate the adsorption performance of GA-g-PAM/SiO_2, four different equilibrium isotherm models were employed.

Langmuir model (Langmuir, 1918):

$$\frac{C_e}{q_e} = \frac{1}{K_L Q_0} + \frac{C_e}{Q_0} \tag{8}$$

Freundlich model (Freundlich, 1906):

$$\ln q_e = \ln K_f + \frac{1}{n}\ln C_e \tag{9}$$

Tempkin model (Dada et al., 2012):

$$q_e = B\ln(A) + B\ln(C_e) \tag{10}$$

Elovich model (Elovich and Larinov, 1962):

$$\ln\frac{q_e}{C_e} = \ln(K_e Q_0) - \frac{q_e}{Q_0} \tag{11}$$

where q_e and Q_0 are the equilibrium and maximum REEs uptake (mg/g), respectively; C_e is equilibrium REEs concentration (mg/L); K_L, K_f and K_e are Langmuir, Freundlich and Elovich isotherm constants; n is the heterogeneity factor related to adsorption intensity; B = RT is a constant related to heat of sorption (J/mol); A is Tempkin constant at equilibrium (L/g), R is the gas constant (J/mol K), T is temperature in Kelvin and b is Tempkin constant related to heat of sorption.

Thermodynamic parameters (i.e. ΔH^0, ΔS^0, ΔG^0) were calculated using following equations;

$$\ln K_C = \frac{\Delta S^0}{R} - \frac{\Delta H^0}{RT} \tag{12}$$

$$\Delta G^0 = -RT\ln K_C \tag{13}$$

where; K_c is thermodynamic equilibrium constant (L/g), R is universal gas constant (8.314 J/mol/K), T is temperature (K), ΔG^0 is

Gibbs free energy (kJ/mol), ΔS^0 is entropy (J/mol/K) and ΔH^0 is enthalpy (kJ/mol) (Yanfei et al., 2016).

3. Results and discussion

3.1. Mechanism of GA-g-PAM synthesis

EPR technique was used to study the mechanism of different radicals generated during synthesis of GA-g-PAM. DMPO was selected as the spin trapping agent in EPR experiments (Fontmorin et al., 2016). As seen in Fig. 1, when GA was tested with the addition of DMPO no peaks were identified indicating that no spins were present due to absence of any radicals. However, after the addition of KPS, samples were taken at different time intervals from 1 to 30 min and tested by adding DMPO (100 mM). At 1 min, the presence of $SO_4^{\cdot}$ (Fig. 1b) was noticed. Generated $SO_4^{\cdot-}$ radical attacked the GA backbone and resulted in the generation of oxygen-centered radical sites (Fig. 1c–e). These oxygen-centered radicals trapped then combined with the AA chains resulting in the successful formation of GA-g-PAM. It was also noticed that as the reaction propagated, the intensity of oxygen-centered radical decreased as it combined with AA chains. After 30 min, only OH radicals were found to be present in the system and no peaks for the $SO_4^{\cdot-}$ was found due to the fast transformation of $SO_4^{\cdot}$ to OH (Carlsson et al., 2010). KPS dissociates and generates sulfate radicals ($SO_4^{\cdot}$) which in turns attacks GA backbone to create free radical sites which then reacts with AA (monomer) to form graft polymer. A possible mechanism of radial graft copolymerization is explained in Fig S1.

Potassium persulfate (KPS) was used as a source for generation of free radical in the synthesis of GA-g-PAM. Table S1 represents some parameters varied for the synthesis of various grades of grafted copolymer. A series of nine (9) graft copolymer have been synthesized. For the first four grades the concentration of monomer (AA) was varied and for others free radical initiator (KPS) was altered. By increasing the AA (monomer) concertation from 0.14 to 0.21 M the % grafting increased which might be due to extra monomer availability for grafting on GA backbone. Similarly, increasing the KPS concentration from 15 to 30 mM resulting in generation of more radical sites on GA and thus the overall grafting percentage increases. However, at concentration of 0.28 M and 40 mM of AA and KPS, respectively, the decrease in grafting percentage was observed. This may be due to the fact that all the GA sites which have a possibility to react with AA due to radical generation are already converted to graft copolymer and no more sites are available thus resulting in the formation of homomer through side reaction. The GA-g-PAM/SiO_2 nanocomposite was produced by in-situ polymerization of TEOS in the presence of GA-g-PAM. NH_4OH is used to provide the catalytic effects in order to facilitate the crosslinking of silica particles in the formation of GA-g-PAM/SiO_2 nanocomposite. The sol–gel process occurs via hydrolysis of the precursor used for silica followed by condensation of the formed monomers (silanols). The mechanism through which the GA-g-PAM/SiO_2 nanocomposite is formed is depicted in Fig S1.

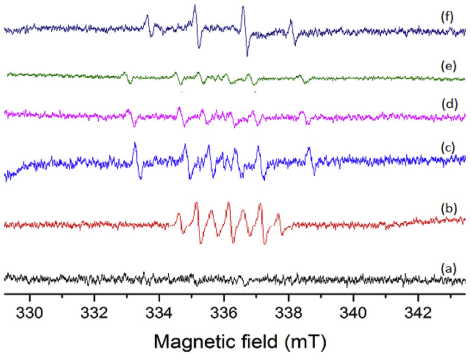

Fig. 1. EPR signals at different time intervals; (a) GA, (b) at t = 1 min DMPO- $SO_4^{\cdot-}$, (c–e) at t = 5, 10, 20 min, respectively DMPO-oxygen centered radicals, (f) at t = 30 min DMPO-oxygen centered radicals DMPO-OH.

3.2. Characterization

The results obtained from elemental analysis for GA, GA-g-PAM and GA-g-PAM/SiO_2 are listed in Table S2. The presence of considerable amount of nitrogen in grafted polymer sample indicates the grafting of PAM chains on backbone of GA. However, the amount decreased in composite sample (GA-g-PAM/SiO_2) which is due to the conversion of grafted copolymer ($-CONH_2$ to $-COO^-$) groups because of hydrolysis resulting in release of ammonia gas. Furthermore, due to the presence of silanol –OH groups, the % O increased in GA-g-PAM/SiO_2 compared to grafted polymer.

A board spectral peak (Fig. 2a) in a region of 3200–3500 cm^{-1} is due to the stretching vibrations of O–H (Singh et al., 2007a) and a small peak at 2927 cm^{-1} in GA-g-PAM samples is due to stretching vibrations of C–H (Singh et al., 2007b) which disappeared in GA-g-PAM/SiO_2. The bands at 1658 cm^{-1} and 1414 cm^{-1} are assigned to COO^- groups, which has been produced as a result of hydrolysis of PAM chains on GA backbone. The bands at 1607 cm^{-1} and 1390 cm^{-1} are the representative of N–H stretching vibrations and C–N stretching vibrations. Furthermore, CH_2 twisting and CH_2 scissoring bands appears at 1319 cm^{-1} and 1448 cm^{-1}, respectively. Additionally, the peak at 1120 cm^{-1} is attributed to the C–O stretching of ester group in GA-g-PAM provided substantial evidence of PAM grafting on GA. In GA-g-PAM/SiO_2 nanocomposite, the intense peak at 1080 cm^{-1} is assigned to the asymmetric stretching vibration of the Si–O bonds of Si–O–Si bridges. Similarly, the peaks at 792 cm^{-1} and 450 cm^{-1} are attributed to the symmetric stretching and bending vibrations of Si–O–Si bonds (Singh et al., 2007a; Sivakami and Thiyagarajan, 2016). The peak at 966 cm^{-1} is due to Si–O bonds of Si–OH groups (Singh et al., 2007a).

XRD patterns of nanocomposites were recorded using Co Kα radiation (λ = 1.790307 Å) in the 2Θ range of 15–120° operated at 40 kV and 40 mA. Fig. 2b represents the X-Ray diffraction pattern of GA-g-PAM and GA-g-PAM/SiO_2. The diffraction peaks for GA-g-PAM at 2Θ = 24.98°, 27.92°, 34.94°, 36°, 42.04°, 42.08°, 43.58°, 44.33°, 47.45°, 47.97°, 51.08°, 56.63° and 64.85° indicates the presence of PAM grafts on GA. However, the crystalline peaks diminish in GA-g-PAM/SiO_2 significantly and show just a single hump of amorphous SiO_2 in a range of 23–27° (Iftekhar et al., 2017a).

For TEM analysis, synthesized nanocomposite was dispersed in ethanol and sonicated for 15 min and a drop of suspension was placed on carbon coated Cu grid. The presence of small particles in TEM images of GA-g-PAM/SiO_2 (Fig. 3a) indicated the evenly distribution of silica particles all over the matrix. However, in both TEM and AFM (Fig. 3a–b) images aggregation of silica along with grafted polymer was also observed. The particle size is in a range of 25–60 nm. The peak height of particles shown in Fig. 3b is 15 nm.

A N_2 adsorption–desorption isotherms of GA-g-PAM/SiO_2 nanocomposites was also obtained. The nanocomposite shows typical type-IV (for mesoporous materials) with broad H2

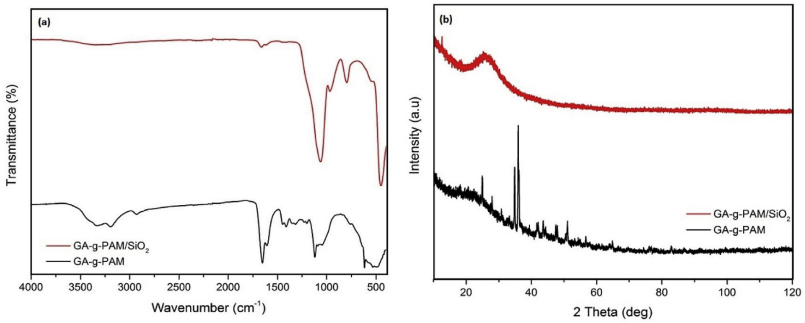

Fig. 2. XRD (a) and FTIR (b) plots of GA-g-PAM and GA-g-PAM/SiO_2.

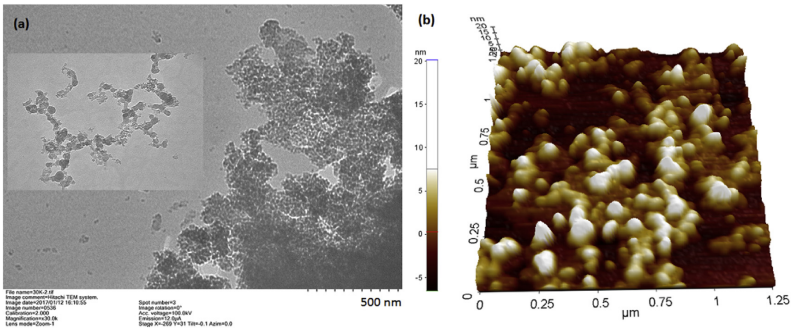

Fig. 3. TEM (a) and AFM (b) of GA-g-PAM/SiO_2.

hysteresis loop (Fig. 4a) (Sing, 1985). The specific surface areas, pore volume and pore diameter of GA-g-PAM/SiO_2 was calculated to be 273.55 m^2/g, 0.428 cm^3/g and 6.26 nm, respectively. The isoelectric point was determined by zeta potential measurement and found to be at a pH value of 3.18 (Fig. 4b).

3.3. *Effect of pH*

The pH of solution is an effective parameter, which decides the surface nature of adsorbent and adsorbate in aqueous solution as well as the degree of ionization (Srivastava and Sillanpää, 2017).

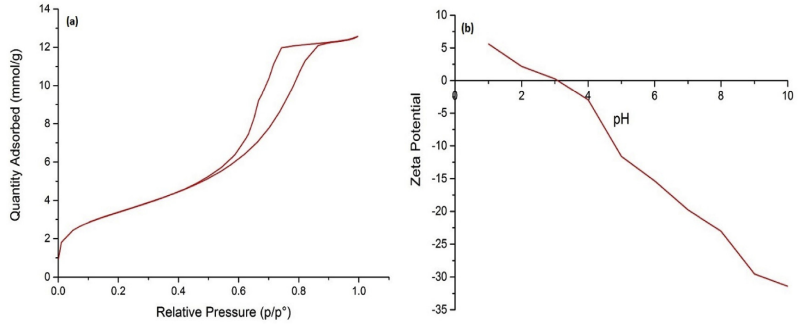

Fig. 4. BET (a) and zeta potential (b) plot for GA-g-PAM/SiO_2.

The uptake study of REEs were carried out at a pH range of 2–6. The adsorption at pH higher than 6 was not considered as the precipitation started above this, resulting in the formation of insoluble metal hydroxides (Iftekhar et al., 2017a; Sert et al., 2008; Vijayaraghavan and Balasubramanian, 2010). It is obvious from Fig. 5a that the removal of REEs is highly pH-dependent. The removal of REEs was very low up to pH 3 and then it increased significantly.

The removal of metal with changing pH is mainly associated with the zeta potential of the adsorbent (Ramasamy et al., 2017). When the solution pH is less than pH_{zpc}, the surface of GA-g-PAM/SiO_2 carries positive charge hence, the electrostatic repulsion is the driving factor between surface positive charge and REE ions. Therefore, under acidic conditions, the GA-g-PAM/SiO_2 showed low adsorption capacity, due to the competitive adsorption between H^+ and REE ions. Furthermore, increasing the pH resulted in the deprotonation of adsorbent surface and thus more active sites are available to positively charged REE ions because of electrostatic attraction with increase in pH. In case of REEs, the maximum removal was observed at pH 6. Therefore, further experiments were performed at pH 6 for REEs with GA-g-PAM/SiO_2 nanocomposite.

3.4. Effect of dosage

To explain the effect of GA-g-PAM/SiO_2 nanocomposite dose for the removal of REEs, adsorption was conducted at different dosages ranging from 0.5 to 4 g/L. The trend of removal of REEs is shown in Fig. 5b. Increased removal of REEs with increasing GA-g-PAM/SiO_2 dose is obvious as higher GA-g-PAM/SiO_2 dose facilitate more adsorbent sites for interaction of REE ions. The removal percentage of REEs increased by varying the dose from 0.5 to 3.5 g/L after which there is not an obvious increase in removal. Thus, a GA-g-PAM/SiO_2 dose of 3.5 g/L was selected for all other adsorption experiments.

3.5. Isotherm

Experiments were performed to estimate the saturation capacity of GA-g-PAM/SiO_2 (Fig S2) and several adsorption isotherms viz. Langmuir, Freundlich, Tempkin and Elovich isotherms were used to model the experiment data. The different isotherm parameters of Langmuir, Freundlich, Tempkin and Elovich isotherm are summarized in Table 1 and the obtained straight lines are shown in Fig S2(a-d). Best fit isotherm model for experimental data can be determined by correlation coefficient (R^2) values.

Among different isotherms used, Langmuir isotherms was found to be suitable for describing isotherm data for Eu, La and Nd with a higher correlation coefficient (R^2) values compared to Freundlich isotherm model. However, high correlation coefficient (R^2) value were obtained for Freundlich model in case of Sc. Also, the adsorption capacities (Q_0) was obtained by fitting the experimental data to Langmuir isotherm for Eu, La and Nd and for Sc calculated from Freundlich isotherm. The adsorption capacities reported for Eu, La, Nd and Sc was 10.11, 7.9, 12.24 and 11.05 mg/g, respectively. The adsorption capacities observed for REEs in the present study

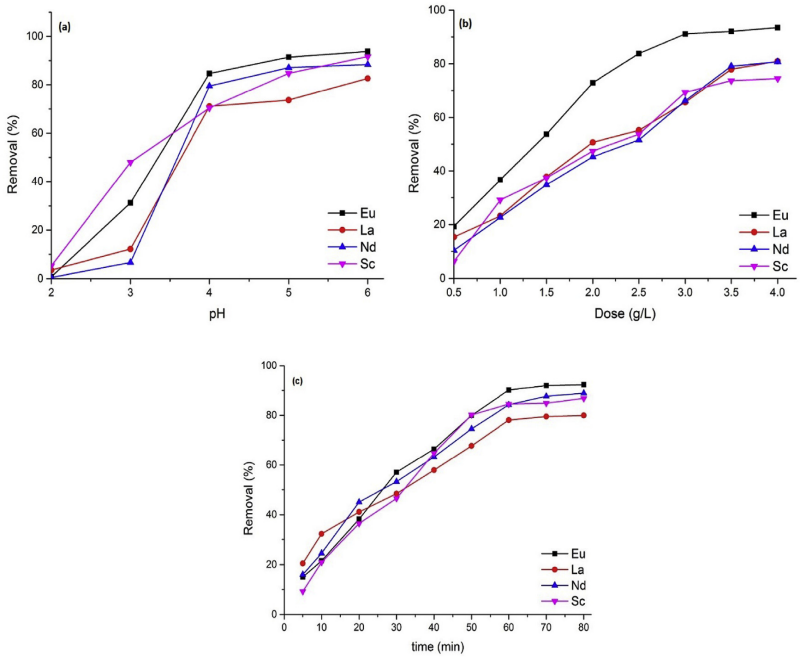

Fig. 5. Adsorption of Ln (III) as a function of pH (a), dose (b) and time (c) on GA-g-PAM/SiO_2 nanocomposite.

Table 2
Kinetics model parameters for adsorption of Ln (III) on GA-g-PAM/SiO_2 nanocomposite.

Models	Model Parameters	Eu	La	Nd	Sc
Pseudo first order	$q_{e,exp}$ (mg/g)	5.77	5.64	7.30	5.17
	$q_{e,cal}$ (mg/g)	6.87	5.09	7.51	7.90
	k_1 (min^{-1})	4.23×10^{-3}	3.27×10^{-3}	3.57×10^{-3}	5.64×10^{-3}
	R^2	0.942	0.947	0.968	0.821
Pseudo second order	$q_{e,exp}$ (mg/g)	5.77	5.64	7.30	5.17
	$q_{e,cal}$ (mg/g)	11.47	6.21	10.57	20.81
	k_2 (g mg^{-1} min^{-1})	1.32×10^{-3}	8.4×10^{-3}	2.47×10^{-3}	2.83×10^{-4}
	R^2	0.815	0.944	0.958	0.555
Intra-Particle	K_i	0.88	0.75	1.00	0.87
	C	−1.25	−1.18	−0.96	−1.52
	R^2	0.984	0.978	0.992	0.974

were higher compared to the results reported in literature. The kaolin (Yanfei et al., 2016) and SiO_2-A336 (Turanov et al., 2016) exhibited 1.73 mg/g and 2.518 mg/g for La and Sc, respectively. Similarly, in another study hydroxyapatite (Granados-Correa et al., 2012) exhibited 0.94 mg/g and 0.25 mg/g for Eu and La compared to 10.11 mg/g and 7.09 mg/g, respectively.

3.6. Kinetics

Fig. 5c illustrates the removal of REEs onto GA-g-PAM/SiO_2 as a function of time. From Fig. 5c, it is revealed that removal of Eu, La, Sc and Nd is 90%, 78%, 85% and 84%, respectively, in 60 min. The initial quick phase was followed by slow attainment and there is no prominent increase in the removal afterwards.

The experimental kinetic data was modelled using pseudo first order and pseudo second order kinetics. The correlation coefficient R^2 and the parameters for pseudo first order and pseudo second order kinetic model are presented in Table 2. The adsorption of REEs on GA-g-PAM/SiO_2 followed pseudo first order kinetics with a higher value of R^2 compared to pseudo second order kinetics. Similarly, the adsorption capacity of REEs at equilibrium estimated from pseudo first order rate equation (Eq. (4)) agreed with the experimental data. It could be stated that the adsorption of REEs on GA-g-PAM/SiO_2 supports the assumption of physisorption (Ho, 2006)

Furthermore, intra-particle diffusion model (Eq. (6)) and Boyd model (Eq. (7)) was used to investigate the contribution of various steps involved in the adsorption process viz intra-particle diffusion

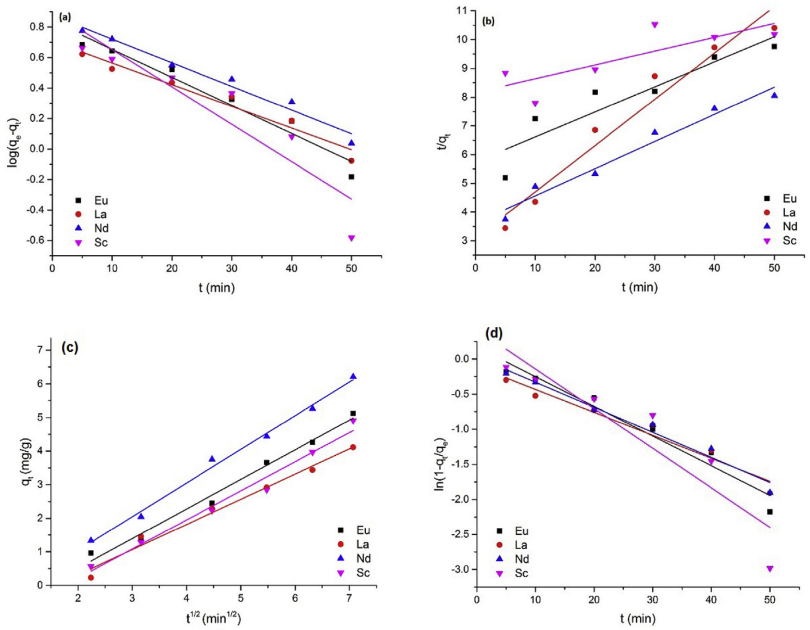

Fig. 6. Plot of pseudo first order model (a), pseudo second order model (b), intra-particle diffusion model (c) and Boyd model (d) for adsorption of Ln (III) on GA-g-PAM/SiO_2 nanocomposite.

Table 3
Thermodynamic parameters for Ln (III) adsorption onto GA-g-PAM/SiO_2.

Model Parameters		Eu	La	Nd	Sc
ΔH^0 (kJ/mol)		12.55	32.57	41.33	46.37
ΔS^0 (J/mol/K)		54.92	110.14	138.51	157.47
ΔG^0 (kJ/mol)	298 K	−3.98	−0.15	−0.13	−1.10
	308 K	−4.29	−1.35	−0.86	−1.41
	318 K	−4.53	−2.82	−3.15	−3.36
	328 K	−5.77	−3.31	−3.99	−5.79

and film diffusion. However, in case of adsorption of all four REEs reported in this study on GA-g-PAM/SiO_2 (Fig. 6c) the linear plot did not pass through the origin indicating that the intra-particle diffusion is not the only rate governing step. The results of intra-particle model were further validated by Boyd model. It can be seen from Fig. 6d; the linear plot does not pass through the origin indicating the film diffusion control the adsorption of REEs on GA-g-PAM/SiO_2.

3.7. Thermodynamics

The values of ΔG^0, ΔH^0 and ΔS^0 thermodynamic parameters were calculated using Eq. (12) and Eq. (13) are shown in Table 3. Negative values of ΔG^0 indicates the feasibility of REEs removal by adsorption on GA-g-PAM/SiO_2 nanocomposite and suggests the spontaneous nature of adsorption on nanocomposite. The positive values of the entropy change (ΔS^0) suggests about the randomness at the solid-liquid interface which increases during the adsorption of REEs on GA-g-PAM/SiO_2. In addition, positive values of ΔH^0 indicates the adsorption process was endothermic. Furthermore, the enthalpy values obtained also suggests the physisorption process for REEs ($\Delta H^0 < 50$ kJ/mol) (Iftekhar et al., 2017a; Sert et al., 2008). The results are also in agreement with the kinetic study for REEs on GA-g-PAM/SiO_2

3.8. Desorption

Desorption study showed that among all tested eluents, 0.1 mol/L HCl was highly efficient to desorb the maximum amount of REEs from GA-g-PAM/SiO_2. So, 0.1 mol/L HCl was selected as desorbing medium for desorption of REEs and regeneration of GA-g-PAM/SiO_2 for further adsorption–desorption cycles. Regenerated adsorbent was rather efficient for the removal of REEs up to three adsorption–desorption cycles (Fig. 7). However, in third cycle removal of REEs decreased to 50–55%, respectively. Thus, further cycles were not investigated.

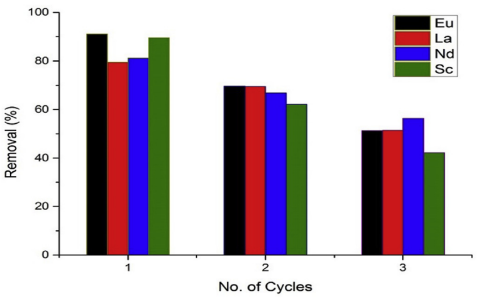

Fig. 7. Adsorption-desorption cycles for Ln (III).

4. Conclusion

A novel nanocomposite has been synthesized based on in-situ radial graft copolymerization method. The presence of free radicals involved in the synthesis of GA-g-PAM from GA was detected using DMPO as a spin trapping agent by EPR spin trapping technique and the possible reaction pathway was proposed for the better illustration of mechanism of synthesis. FTIR and XRD confirmed the successful incorporation of silica in grafted copolymer. Compared to GA and GA-g-PAM, the surface area of GA-g-PAM/SiO_2 was significantly higher. The adsorption kinetics for REEs were best described by pseudo first order model. Also, the adsorption equilibrium data for REEs fitted well with Langmuir isotherm except Sc. The thermodynamic studies confirm that the adsorption is spontaneous and endothermic. Furthermore, the results obtained suggests the physisorption process for REEs adsorption on GA-g-PAM/SiO_2. Desorption studies affirmed the regenerative efficiency of loaded REEs up to three cycles. Present study revealed that GA-g-PAM/SiO_2 nanocomposite could be utilized for the adsorption and recovery of REEs from aqueous streams.

Appendix A. Supplementary data

Supplementary data related to this article can be found at https://doi.org/10.1016/j.jclepro.2017.09.166.

References

Awual, M.R., Yaita, T., Shiwaku, H., 2013. Design a novel optical adsorbent for simultaneous ultra-trace cerium (III) detection, sorption and recovery. Chem. Eng. J. 228, 327–335.
Banerjee, S.S., Chen, D.-H., 2007. Fast removal of copper ions by gum Arabic modified magnetic nano-adsorbent. J. Hazard. Mater. 147 (3), 792–799.
Carlsson, L., Rose, S., Hourdet, D., Marcellan, A., 2010. Nano-hybrid self-crosslinked PDMA/silica hydrogels. Soft Matter 6 (15), 3619–3631.
Chen, G., Dufresne, A., Huang, J., Chang, P.R., 2009. A novel thermoformable bio-nanocomposite based on cellulose nanocrystal-graft-poly (ε-caprolactone). Macromol. Mater. Eng. 294 (1), 59–67.
Chen, Y., Hu, J., Wang, J., 2012. Kinetics and thermodynamics of Cu (II) biosorption on to a novel magnetic chitosan composite bead. Environ. Technol. 33 (20), 2345–2351.
Dada, A., Olalekan, A., Olatunya, A., Dada, O., 2012. Langmuir, Freundlich, Temkin and Dubinin–Radushkevich isotherms studies of equilibrium sorption of Zn2+ unto phosphoric acid modified rice husk. IOSR J. Appl. Chem. 3 (1), 38–45.
Das, N., Das, D., 2013. Recovery of rare earth metals through biosorption: an overview. J. Rare Earths 31 (10), 933–943.
Das, D., Varshini, C.J.S., Das, N., 2014. Recovery of lanthanum (III) from aqueous solution using biosorbents of plant and animal origin: batch and column studies. Miner. Eng. 69, 40–56.
Duan, S., Tang, R., Xue, Z., Zhang, X., Zhao, Y., Zhang, W., Zhang, J., Wang, B., Zeng, S., Sun, D., 2015. Effective removal of Pb (II) using magnetic Co 0.6 Fe 2.4 O 4 micro-particles as the adsorbent: synthesis and study on the kinetic and thermodynamic behaviors for its adsorption. Colloids Surf. A Physicochem. Eng. Aspect. 469, 211–223.
Elovich, S.Y., Larinov, O., 1962. Theory of adsorption from solutions of non electrolytes on solid (I) equation adsorption from solutions and the analysis of its simplest form, (II) verification of the equation of adsorption isotherm from solutions. Izv. Akad. Nauk. SSSR Otd. Khim. Nauk. 2 (2), 209–216.
Fauconnier, M.-L., Blecker, C., Groyne, J., Razafindralambo, H., Vanzeveren, E., Marlier, M., Paquot, M., 2000. Characterization of two Acacia gums and their fractions using a Langmuir film balance. J. Agric. Food Chem. 48 (7), 2709–2712.

Fontmorin, J., Castillo, R.B., Tang, W., Sillanpää, M., 2016. Stability of 5, 5-dimethyl-1-pyrroline-N-oxide as a spin-trap for quantification of hydroxyl radicals in processes based on Fenton reaction. Water Res. 99, 24–32.
Freundlich, H., 1906. Over the adsorption in solution. J. Phys. Chem. 57, 1100–1107, 385471.
Ghorai, S., Sinhamahpatra, A., Sarkar, A., Panda, A.B., Pal, S., 2012. Novel biodegradable nanocomposite based on XG-g-PAM/SiO 2: application of an efficient adsorbent for Pb 2+ ions from aqueous solution. Bioresour. Technol. 119, 181–190.
Ghosh, S., Sen, G., Jha, U., Pal, S., 2010. Novel biodegradable polymeric flocculant based on polyacrylamide-grafted tamarind kernel polysaccharide. Bioresour. Technol. 101 (24), 9638–9644.
Granados-Correa, F., Vilchis-Granados, J., Jiménez-Reyes, M., Quiroz-Granados, L., 2012. Adsorption behaviour of La (III) and Eu (III) ions from aqueous solutions by hydroxyapatite: kinetic, isotherm, and thermodynamic studies. J. Chem. 2013.
Ho, Y.-S., 2006. Review of second-order models for adsorption systems. J. Hazard. Mater. 136 (3), 681–689.
Ho, Y.-S., McKay, G., 1999. Pseudo-second order model for sorption processes. Process Biochem. 34 (5), 451–465.
Iftekhar, S., Srivastava, V., Sillanpää, M., 2017a. Enrichment of lanthanides in aqueous system by cellulose based silica nanocomposite. Chem. Eng. J. 320, 151–159.
Iftekhar, S., Srivastava, V., Sillanpää, M., 2017b. Synthesis and application of LDH intercalated cellulose nanocomposite for separation of rare earth elements (REEs). Chem. Eng. J. 309, 130–139.
Lagergren, S., 1898. About the theory of so-called adsorption of soluble substances.
Langmuir, I., 1918. The adsorption of gases on plane surfaces of glass, mica and platinum. J. Am. Chem. Soc. 40 (9), 1361–1403.
Mittal, H., Mishra, S.B., 2014. Gum ghatti and Fe 3 O 4 magnetic nanoparticles based nanocomposites for the effective adsorption of rhodamine B. Carbohydr. Polym. 101, 1255–1264.
Mittal, H., Parashar, V., Mishra, S., Mishra, A., 2014. Fe 3 O 4 MNPs and gum xanthan based hydrogels nanocomposites for the efficient capture of malachite green from aqueous solution. Chem. Eng. J. 255, 471–482.
Mittal, H., Maity, A., Ray, S.S., 2016. Gum karaya based hydrogel nanocomposites for the effective removal of cationic dyes from aqueous solutions. Appl. Surf. Sci. 364, 917–930.
Pal, S., Ghorai, S., Das, C., Samrat, S., Ghosh, A., Panda, A.B., 2012. Carboxymethyl tamarind-g-poly (acrylamide)/silica: a high performance hybrid nanocomposite for adsorption of methylene blue dye. Ind. Eng. Chem. Res. 51 (48), 15546–15556.
Ponou, J., Wang, L.P., Dodbiba, G., Okaya, K., Fujita, T., Mitsuhashi, K., Atarashi, T., Satoh, G., Noda, M., 2014. Recovery of rare earth elements from aqueous solution obtained from Vietnamese clay minerals using dried and carbonized parachlorella. J. Environ. Chem. Eng. 2 (2), 1070–1081.
Quintanilha, R.C., Orth, E.S., Grein-Iankovski, A., Riegel-Vidotti, I.C., Vidotti, M., 2014. The use of gum Arabic as “Green” stabilizer of poly (aniline) nanocomposites: a comprehensive study of spectroscopic, morphological and electrochemical properties. J. Colloid Interface Sci. 434, 18–27.
Rahul, R., Jha, U., Sen, G., Mishra, S., 2014. A novel polymeric flocculant based on polyacrylamide grafted inulin: aqueous microwave assisted synthesis. Carbohydr. Polym. 99, 11–21.
Ramasamy, D.L., Repo, E., Srivastava, V., Sillanpää, M., 2017. Chemically immobilized and physically adsorbed PAN/acetylacetone modified mesoporous silica for the recovery of rare earth elements from the waste water-comparative and optimization study. Water Res. 114, 264–276.
Sadovsky, D., Brenner, A., Astrachan, B., Asaf, B., Gonen, R., 2016. Biosorption potential of cerium ions using Spirulina biomass. J. Rare Earths 34 (6), 644–652.
Sen, G., Pal, S., 2009. Microwave initiated synthesis of polyacrylamide grafted carboxymethylstarch (CMS-g-PAM): application as a novel matrix for sustained drug release. Int. J. Biol. Macromol. 45 (1), 48–55.
Sen, G., Kumar, R., Ghosh, S., Pal, S., 2009. A novel polymeric flocculant based on polyacrylamide grafted carboxymethylstarch. Carbohydr. Polym. 77 (4), 822–831.
Sert, Ş., Kütahyali, C., İnan, S., Talip, Z., Çetinkaya, B., Eral, M., 2008. Biosorption of lanthanum and cerium from aqueous solutions by Platanus orientalis leaf powder. Hydrometallurgy 90 (1), 13–18.
Sing, K.S., 1985. Reporting physisorption data for gas/solid systems with special reference to the determination of surface area and porosity (Recommendations 1984). Pure Appl. Chem. 57 (4), 603–619.
Singh, V., Tiwari, A., Pandey, S., Singh, S.K., Sanghi, R., 2007a. Synthesis and characterization of novel saponified guar-graft-poly (acrylonitrile)/silica nanocomposite materials. J. Appl. Polym. Sci. 104 (1), 536–544.
Singh, V., Tiwari, S., Sharma, A.K., Sanghi, R., 2007b. Removal of lead from aqueous solutions using Cassia grandis seed gum-graft-poly (methylmethacrylate). J. Colloid Interface Sci. 316 (2), 224–232.
Sivakami, R., Thiyagarajan, P., 2016. The effect of citric acid on morphology and photoluminescence properties of white light emitting ZnO–SiO 2 nanocomposites. Photonics Nanostruct. Fund. Appl. 20, 31–40.
Srivastava, V., Sillanpää, M., 2017. Synthesis of malachite@ clay nanocomposite for rapid scavenging of cationic and anionic dyes from synthetic wastewater. J. Environ. Sci. 51, 97–110.
Srivastava, V., Sharma, Y., Sillanpää, M., 2015. Green synthesis of magnesium oxide nanoflower and its application for the removal of divalent metallic species from synthetic wastewater. Ceram. Int. 41 (5), 6702–6709.
Turanov, A.N., Karandashev, V.K., Sukhinina, N.S., Masalov, V.M., Emelchenko, G.A., 2016. Adsorption of lanthanides and scandium ions by silica sol-gel material doped with novel bifunctional ionic liquid, trioctylmethylammonium 1-phenyl-3-methyl-4-benzoyl-5-onate. J. Environ. Chem. Eng. 4 (4), 3788–3796.
Vijayaraghavan, K., Balasubramanian, R., 2010. Single and binary biosorption of cerium and europium onto crab shell particles. Chem. Eng. J. 163 (3), 337–343.
Wang, J.-P., Chen, Y.-Z., Zhang, S.-J., Yu, H.-Q., 2008. A chitosan-based flocculant prepared with gamma-irradiation-induced grafting. Bioresour. Technol. 99 (9), 3397–3402.
Wu, D., Chang, P.R., Ma, X., 2011. Preparation and properties of layered double hydroxide–carboxymethylcellulose sodium/glycerol plasticized starch nanocomposites. Carbohydr. Polym. 86 (2), 877–882.
Yanfei, X., Huang, L., Zhiqi, L., Zongyu, F., Liangshi, W., 2016. Adsorption ability of rare earth elements on clay minerals and its practical performance. J. Rare Earths 34 (5), 543–548.
Yuan, Q., Li, N., Chi, Y., Geng, W., Yan, W., Zhao, Y., Li, X., Dong, B., 2013. Effect of large pore size of multifunctional mesoporous microsphere on removal of heavy metal ions. J. Hazard. Mater. 254, 157–165.
Zhao, F., Repo, E., Meng, Y., Wang, X., Yin, D., Sillanpää, M., 2016. An EDTA-β-cyclodextrin material for the adsorption of rare earth elements and its application in preconcentration of rare earth elements in seawater. J. Colloid Interface Sci. 465, 215–224.
Zhu, Y., Wang, W., Zheng, Y., Wang, F., Wang, A., 2016. Rapid enrichment of rare-earth metals by carboxymethyl cellulose-based open-cellular hydrogel adsorbent from HIPEs template. Carbohydr. Polym. 140, 51–58.

Publication IV

Iftekhar, S., Srivastava, V., Ramasamy, D. L., Naseer, W. A., and Sillanpää, M.
A novel approach for synthesis of exfoliated biopolymeric-LDH hybrid nanocomposites via in-stiu coprecipitation with gum Arabic: Application towards REEs recovery

Reprinted with permission from
Chemical Engineering Journal
Vol. 347, pp. 398-406, 2018

Chemical Engineering Journal 347 (2018) 398–406

Contents lists available at ScienceDirect

Chemical Engineering Journal

journal homepage: www.elsevier.com/locate/cej

A novel approach for synthesis of exfoliated biopolymeric-LDH hybrid nanocomposites via in-stiu coprecipitation with gum Arabic: Application towards REEs recovery

Sidra Iftekhar[a,*], Varsha Srivastava[a], Deepika Lakshmi Ramasamy[a], Waqar Ahmad Naseer[a], Mika Sillanpää[a,b]

[a] Department of Green Chemistry, School of Engineering Science, Lappeenranta University of Technology, Sammonkatu 12, FI-50130 Mikkeli, Finland
[b] Department of Civil and Environmental Engineering, Florida International University, Miami, FL 33174, USA

HIGHLIGHTS

- LDH-exfoliation was possibly by in-situ coprecipitaion in biopolymeric matrix.
- The divalent ions of LDH affects the morphology and characteristics of GAnXA.
- The GA5MA showed superior adsorption and reusability for REEs compared to others.
- All GAnXA were highly selective for Sc and HREEs removal favorable over LREEs.

GRAPHICAL ABSTRACT

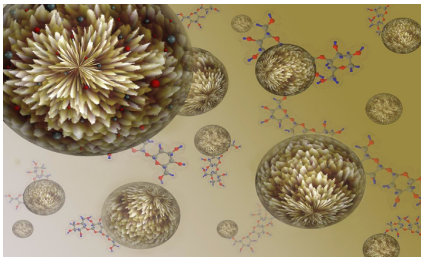

ARTICLE INFO

Keywords:
Gum Arabic
Layered double hydroxide
Exfoliation
Rare earth elements

ABSTRACT

Delamination and exfoliation of layered double hydroxides (LDH) is an interesting way for the synthesis of novel nanocomposites. Herein, we report the synthesis of various exfoliated biopolymeric-LDH nanocomposites via in-situ coprecipitation method with gum Arabic (GA). The influence of various divalent ions on the morphological characteristics of GAnXA (n = wt% of GA and X = Mg, Ca, Ba, Sr) was explored Transmission Electron Microscopy (TEM), Atomic Force Microscopy (AFM), and Scanning Electron Microscopy (SEM). X-ray diffraction pattern was used for the determination of phase composition of synthesized nanocomposites. The surface functional groups of GAnXA were investigated by Fourier Transform Spectroscopy (FTIR). Furthermore, the surface charge characteristics was explored by zeta potential analysis. Specific surface area of GAnXA was determined by BET analysis. The overall adsorption of REEs decreased with an increase in ionic size of divalent ions and the noticeable difference in the morphologies of exfoliated GAnXA was observed. In a single component system, the REEs adsorption capacities followed the order: Sc > Y > Nd > Ce > Eu > La, whereas, in multicomponent system, adsorption seems to be competitive and presence of competing ions affect the overall REEs removal. Moreover, HREEs removal superseded over LREEs and the nanocomposites (GA5CA, GA5SA, GA5BA) were highly selective for Sc recovery. The post-adsorption FTIR and SEM results revealed the importance of surface hydroxyl and carboxyl functional groups enacting as the principal REE binding sites. Overall,

* Corresponding author.
E-mail address: sidra.iftekhar@lut.fi (S. Iftekhar).

https://doi.org/10.1016/j.cej.2018.04.126
Received 8 March 2018; Received in revised form 18 April 2018; Accepted 19 April 2018
Available online 22 April 2018

ability to extract REEs at pH 4 (slightly acidic) presented a facile route for the recovery and separation of REEs from aqueous medium and enhances the possibility of its use in many industrial applications.

1. Introduction

REEs consists of group of 17 elements with 15 lanthanides and two pseudo lanthanides (Sc,Y) with same electron configuration. These are then further categorized as LREEs (light rare earth elements: La-Eu) and HREEs (heavy rare earth elements: Gd-Lu) based on their atomic numbers, where Sc is categorized as LREEs and Y as HREEs [1–5]. The application of REEs in various modern applications resulted in escalation in their demand [6,7]. On the other hand, the gap between the world's demand and supply is increasing [6] which serves as a motivation for the search of new methods to recover REEs from secondary sources for instance industrial residues [1]. Several existent methods for the recovery of REEs are: ion exchange, membrane separation, chemical precipitation, solvent extraction, adsorption, etc. [8–13]. Compared to the conventional methods, adsorption was found as one of the most cost efficient, eco-friendly and economical method for the recovery of REEs.

Gum Arabic (GA) also known as Gum Acacia, a natural biopolymer, exudated from the trunks and barks of Acacia tree and consists of amino acids linked to short arabinose side chain [14,15]. GA is found to be a suitable biomaterial for several technological applications due to its biological, chemical and physical properties. GA has already been employed for the synthesis of various new hybrid materials of technological interest due to its non-toxic nature, high solubility, low viscosity and good emulsifying characteristics [14,16]. Several studies reported GA based nanocomposites viz. GA-Fe_3O_4 [14], GA loaded MgO nanoflower [17], GA-AgNPs [15], GA-g-PAM/SiO_2 [5] etc. The novel production of hybrid organic-inorganic materials synthesized at nanoscale interface displays new properties based on the synergic effect of both organic and inorganic part. For the preparation of such hybrids layered double hydroxides (LDH) have been considered as a favorable host.

LDH often termed as anionic clays are compounds composed of positively charge brucite like layers [18]. LDH (bi-dimensional solids) mainly consists of divalent and trivalent cations and various inorganic or organic anions are introduced between the layers to compensate the positive charge [4]. LDH has been widely used as adsorbents [4,19,20], catalysts [21], cement additives [22] and as drug delivery host [23]. Delamination and exfoliation of LDH is an interesting way for the synthesis of novel inorganic-inorganic or organic-inorganic nanocomposites [24]. Nevertheless, the exfoliated LDH are of more interest compared to intercalated nanocomposites due to better dispersion in polymer matrix [25], whereas, exfoliation of LDH is quite difficult compared to cationic clays like montmorillonite [26]. The possible ways to synthesize the exfoliated polymeric-LDH nanocomposites are: (a) intercalation of the monomer molecules and in situ polymerization, (b) direct intercalation of extended polymer chains, (c) pre-exfoliation and followed by mixing with polymer. Researchers in past used the above mentioned methods for preparing exfoliated polymer/LDH nanocomposite by using variety of polymers such as polyacrylate [27], polyimide [28], polymethyl-methacrylate [29], polycaprolactone [30], polystyrene [31], polyvinyl alcohol [32], etc. The intercalation of various biopolymers in LDH has been reported [4] by either reconstitution, anion exchange or coprecipitation method [33], however, no evidence in literature was found towards the synthesis and application of exfoliated biopolymer-LDH nanocomposites.

Therefore, this work provides a novel and efficient strategy for synthesis of exfoliated biopolymeric-LDH (GAnXA) by in-situ coprecipitation method. The change in shape, size and morphology of exfoliated GAnXA was investigated by exchanging divalent cations (Mg, Ca, Sr, Ba) of LDH matrix and wt% of GA. The application of exfoliated GAnXA nanocomposites towards recovery of REEs was investigated in detail. Moreover, the studies had been carried out in single and multicomponent system, with or without competing ions and for the REEs trend on GAnXA nanocomposites.

2. Materials and methods

2.1. Chemicals

Gum Arabic (GA) from acacia tree, sodium hydroxide (NaOH), hydrochloric acid (HCl), magnesium nitrate hexahydrate (Mg$(NO_3)_2{\cdot}6H_2O$), calcium nitrate tetrahydrate ($Ca(NO_3)_2{\cdot}4H_2O$) were obtained from Sigma Aldrich. Barium nitrate ($Ba(NO_3)_2$), and aluminum nitrate nonahydrate ($Al(NO_3)_3{\cdot}9H_2O$) were supplied by Acros Organics and strontium nitrate ($Sr(NO_3)_2$) was procured from Alfa Aesar. pH adjustment was done using 0.1 M NaOH/HCl solution. All the chemicals are of reagent grade and used without further purification.

2.2. Synthesis of GAnXA

The exfoliated GA-LDH was prepared by in-situ coprecipitation method (Scheme 1). Briefly, 2 g of GA (2 wt%) was dissolved in 100 mL of distilled water with constant stirring (300 rpm) at 70 °C for 1 h. Thereafter, 0.75 M $Mg(NO_3)_2{\cdot}6H_2O$ and 0.25 M $Al(NO_3)_3{\cdot}9H_2O$ (Mg:Al = 3:1) was added in GA solution and stirred for 2 h. The pH of solution was adjusted to 10 by slow addition of NaOH. The resulting GA-LDH precipitates were aged for 18 h, separated by centrifugation (EPPENDORF 5810) and washed with water several times. Then, the final product obtained was freeze dried (CHRIST Alpha 2-4 LD-Plus) and ground to get fine powder by IKA Tube mill control. The GA-LDH nanocomposites with $Ca(NO_3)_2{\cdot}4H_2O$, $Sr(NO_3)_2$, $Ba(NO_3)_2$ were also prepared using the same method. Moreover, same synthesis conditions were employed for each composition of the materials containing 5 wt%

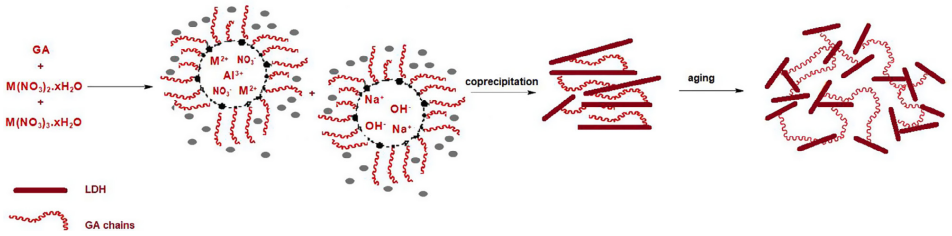

Scheme 1. Schematic illustration of GAnXA via in-situ coprecipitation method.

of GA. The products obtained were labelled as GAnXA (where n = wt% of GA and X = Mg, Ca, Sr and Ba denoted as M, C, S and B, respectively).

2.3. Method of characterization

Phase compositions and particles sizes of the GAnXA were determined by XRD using a Co-Kα (λ = 1.7809 Å) radiation source in a PANalytical X-ray diffractometer. FTIR of the GAnXA was done by Bruker Vertex 70 model, in a spectral range of 400–4000 cm^{-1}. Particle size of nanocomposite was determined by TEM using Hitachi HT-7700. To study the surface morphology, Park Systems NX10 was used for AFM analysis with commercial NCHR tip. Microstructure and morphology of the GAnXA was carried out using SEM in a Hitachi S-4800 microscope operating at 10 kV. N_2 adsorption-desorption isotherms were used for determination of BET surface area and pore size with Tristar® II Plus instrument. Malvern Zetasizer Nano ZEN3500 was employed to measure the zeta-potential (ζ) in a pH range of 2–12.

2.4. Adsorption and regeneration procedure

Six REEs including Sc, Y, La, Ce, Eu, Nd were selected as target ions to evaluate the adsorption performance of GAnXA and the adsorption experiments were conducted as follows: 10 mg of nanocomposite were added into a 15 mL PPE tube with 10 mL REE solution (50 mg/L), and placed in an orbital shaker (IKA KS 4000 ic control) at a constant speed (200 rpm) and temperature (25 °C) for a given time. The suspension was then filtered by using a 0.45 μm PTFE syringe filter, REEs concentration in solution was determined by ICP-OES (Agilent ICP-OES 5110) and the adsorption capacity of REEs is calculated by the following equation:

$$Q = \frac{(C_0 - C_f)V}{M} \quad (1)$$

where Q is the adsorption capacity in mg/g, V is the volume of solution (L), M is the mass of nanocomposite (g), C_o and C_f is the initial and equilibrium concentrations of REEs in solution (mg/L).

For desorption and regeneration process, the separated REE saturated nanocomposite was desorbed in HNO_3 (0.1 M) solution and filtered. The material was then washed with distilled water to neutralize and used for the next cycle, where the dosage was maintained at 1 g/L by taking account of the weight loss at each cycle.

2.5. Analysis method

The isotherm, kinetic and thermodynamic equations used for analysis of experimental data are presented in Section S1 (Supplementary Material).

3. Results and discussion

3.1. Structure and morphology of exfoliated GAnXA

The structure of GAnXA synthesized by in-situ coprecipitation was identified by XRD pattern illustrated in Fig. 1a. The entire exfoliation of LDH in GA matrix can be seen in XRD patterns of all the samples. The diffraction peak at 2θ = 7.6° (0 0 3) in case of GA2MA and GA5MA, reveals that the interlayer spacing increase to 2.01 nm and 2.15 nm, respectively. The enlargement in basal spacing is due to intercalation of GA into LDH galleries which could possibly form a structure where brucite layers can either lay or tilt to some angle resulting in exfoliation [34]. The board peaks also suggests that the interlayer galleries are not uniform. However, the plane (0 0 3) shifted to larger angle in GA2CA and GA5CA samples and the peak intensity is very weak. Moreover, a sharp diffraction peak corresponding to plane (0 0 9) in GA2CA shows that a part of LDH is still present in crystalline form because polymeric matrix is not enough for complete exfoliation of LDH. The reflection peaks of LDH are barely observed in GA5SA except the bump, which corresponds to exfoliation of LDH structure during loading or intercalation of GA on the surface. Also, the peaks forming planes (1 1 0) and (1 1 3) appeared in Mg and Ca based GA-LDH, whereas, the planes are unobvious in Sr and Ba based samples demonstrating either the absence or disturbance in brucite-like layered structure. The absence of basal planes was already reported in previous studies on the exfoliation of LDH corroborating the structural damage [35].

In FTIR spectrum (Fig. 1b), the adsorption bands in a region of 3700–3200 cm^{-1} are attributed to O–H stretching vibrations. Additionally, the bands below 800 cm^{-1} are ascribed to the lattice vibrations of M-O and O-M-O (where M = Mg, Ca, Sr, Ba, Al). The bands at 3000–2800 cm^{-1}, ~1750 cm^{-1}, ~1635 cm^{-1}, 1200–1050 cm^{-1}, ~1410 cm^{-1} and ~ 1350 cm^{-1} corresponds to C—H (CH_2 and CH_3) stretching vibrations, C—O stretching vibrations, C═O stretching vibrations of carbonyl groups, stretching vibrations of C—O—C aliphatic ether, bending vibrations of CH_2 and CH, respectively [29,30,36–39]. The band ~1750 cm^{-1} was missing in Sr and Ba based LDH possibly due to GA coverage onto LDH surface. The presence of these bands demonstrate the successful modifications of LDH by GA via in-situ co-precipitation method.

The microscopic investigation of GAnXA nanocomposites is needed for complete morphological characterization to visualize the morphology, size, dispersion of LDH in GA matrix and spatial distribution. Fig. 2 shows the TEM micrographs of various GAnXA nanocomposites. The micrographs reveals the uniform distribution of LDH in GA matrix, however, the LDH layers are partially exfoliated with 2 wt% GA matrix and degree of exfoliation increases with increase of wt% of GA. The previous study also stated that polymeric loading mainly affect the LDH

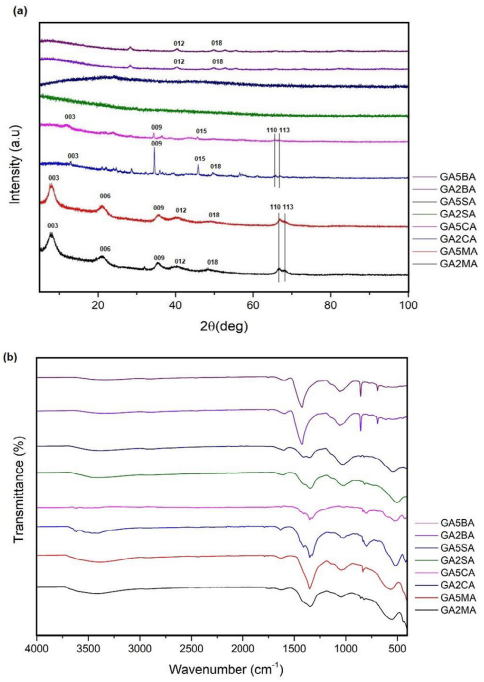

Fig. 1. XRD patterns (a) and FTIR spectra (b) of various GAnXA nanocomposites.

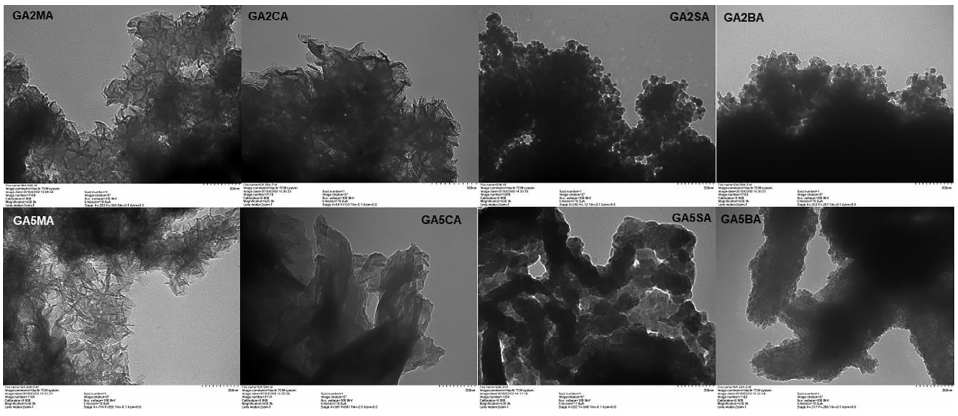

Fig. 2. TEM micrographs of various GAnXA nanocomposites (Scale bar: 200 nm).

orientation in polymer matrix [38]. The irregular shaped fibrous morphology of LDH sheets can be seen in GA2MA, GA5MA, GA2CA and GA5CA nanocomposites. Moreover, the fibers are more slanted with respect to cutting section in case of Mg based GA-LDH (5–11 nm) compared to Ca based (13–25 nm), which might be due to smaller ionic radii of Mg leading to the formation of true brucite-like layers [40]. On the other hand, TEM micrographs of GA-LDH synthesized using Sr and Ba (Fig. 2) are completely different from those of Mg and Ca based GA-LDH. The images of GA2SA, GA5SA, GA2BA and GA5BA exhibits disc like shape where the platelets seems to be lying on the substrate and some of them are overlapping on the edge. Additionally, the settling of multiple disc (Fig. 2) suggests that platelets might stacked together due to loading and intercalation of GA. Though, divalent cations with ionic radii greater than 0.8 Å seems to be incompatible in forming brucite-like layered structure [40], conversely, Sranko et al. [41,42] testified the formation of Ba/Fe LDH under alkaline conditions with similar morphologies.

The AFM images exhibits the same morphologies as seen in TEM images. Fig. 3 shows the topographic images of LDH platelets decorated with GA. It is worth noting that Mg and Ca based GA-LDH has well-developed sheet like morphology where the sheet thickness is half for Mg (6–8 nm) compared to the that of Ca (15–18 nm) samples. The appearance of sheets (GA2MA and GA5MA) in all dimensions indicates that the crystals are monolithic and the aggregates of small particles. The height of the disc like particles as seen in case of Sr and Ba based GA-LDH is more than 3 nm indicating the particles consists of multiple LDH layers. Based on AFM observations, it can be proposed that GA form a flexible shell around the LDH layers, which makes the particles thicker. Additionally, as seen in SEM images (Fig. 4), the nanocomposites lost their topotactical properties where LDH sheets have random orientation and unorderly stacked with non-uniform size platelets dispersed in GA matrix. The exfoliated morphology observed here by TEM, AFM and SEM is in good agreement with the XRD and FTIR results.

3.2. Screening of nanocomposites

As mentioned in Section 3.1, various nanocomposites were synthesized and all the prepared GAnXA nanocomposites were investigated for selected REEs (Sc, Y, La, Ce, Nd and Eu) removal. The results are shown in Fig. SF1 (Supplementary Material). Among all prepared nanocomposites, GA-LDH prepared with 5 wt% of GA presented better results for REEs. However, the surface area (Table ST1-Supplementary

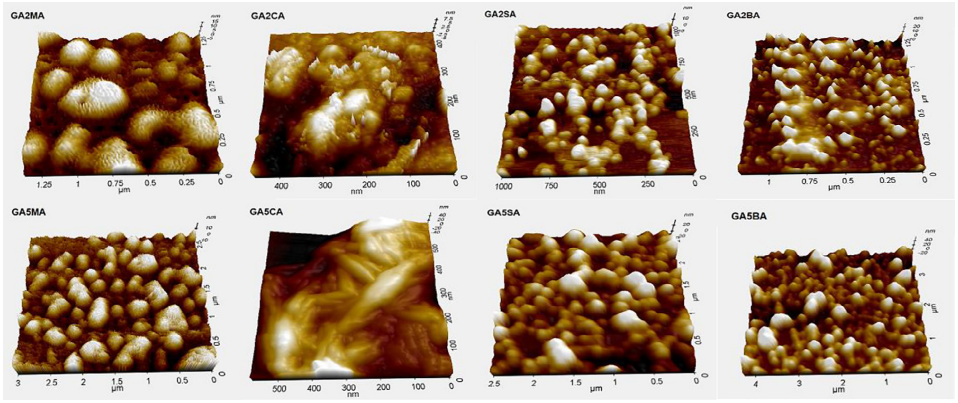

Fig. 3. 3D AFM images of all GAnXA nanocomposites.

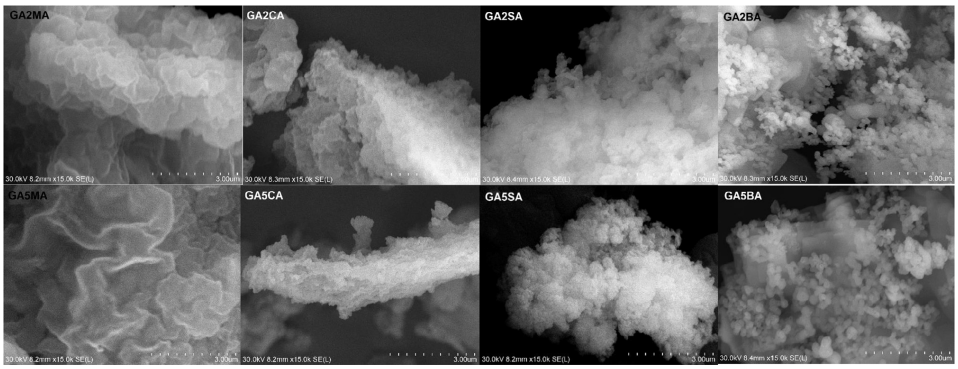

Fig. 4. SEM images of GAnXA nanocomposites.

Material) presented by GA5XA is less than GA2XA, conversely, revealed better adsorption of REEs over the nanocomposites being scrutinized. It is noteworthy, that ionic size of divalent ions (Mg, Ca, Sr, Ba) used in the synthesis of brucite layer GA-LDH is also of key importance in terms of their adsorptive ability toward REEs. Noticeably, GA5MA offered the highest removal for REEs due to smaller ionic radii of Mg (0.65 Å) [40] and were hence considered for further assessments.

3.3. Adsorption performance of GA5MA

3.3.1. Effect of pH

The pH is a key factor to influence the adsorption performance, which decides the surface nature of adsorbent and adsorbate in solution [43]. The influence of initial pH on adsorption of REEs was investigated in a pH range of 2–7 in view of fact that REEs would precipitate to corresponding insoluble metal hydroxides above pH 7 [44]. As shown in Fig. 5a, the adsorption of REEs increases significantly with the increase in pH and reaches maximum at pH 7 indicating the higher pH

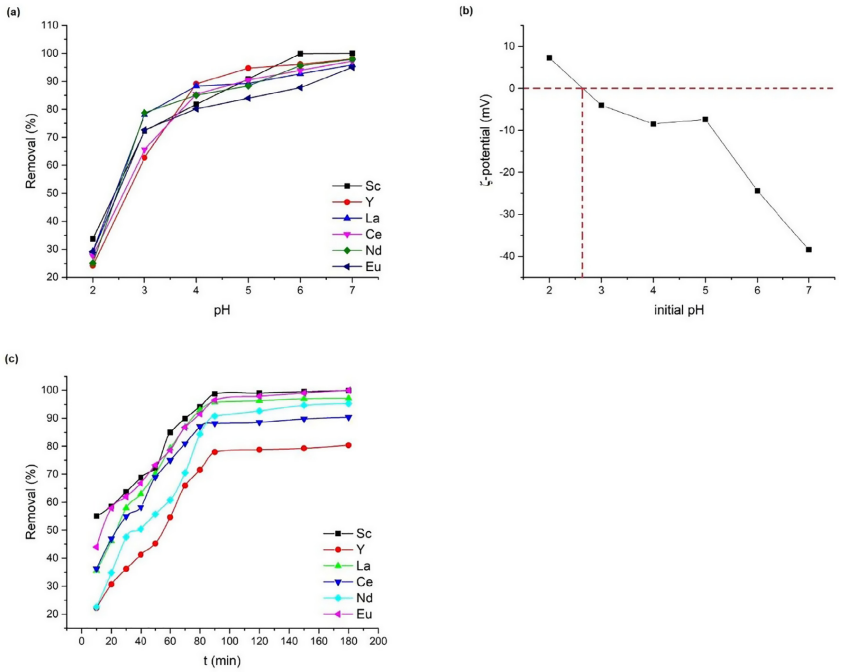

Fig. 5. Effect of pH on the REEs removal by GA5MA (a); the zeta potential at different pH (b); effect of contact time on REEs removal by GA5MA (c).

would lead to better adsorption. To explain this phenomena, surface ζ-potential graph of GA5MA at different pH is shown in Fig. 5b and ζ-potential point appeared at pH_{zpc} 2.65. Though the pH_{zpc} 7.41 was reported for pristine Mg/Al-LDH [45] and possible decrees in pH_{zpc} value might be due to exfoliation of LDH and presence of free carboxyl groups of GA [16]. When the pH < pH_{zpc}, adsorption of REEs was adversely affected because of electrostatic repulsion due to protonation of surface hydroxyl group of GA5MA (surface positive charge). Meanwhile the occurrence of excess H^+ will also compete for adsorption sites. Nevertheless the surface carries negative charge with the rise in pH resulting in deprotonation of GA5MA surface and escalation in electrostatic attraction of REEs towards active sites of GA5MA. Notably, a leaping rise in removal of REEs occurred from pH 4. Therefore, the most optimal pH for adsorption of REEs on GA5MA used in following experiments was pH 4.

3.3.2. Equilibrium adsorption isotherms

According to Fig. SF2a (Supplementary Material), the amount of REE adsorbed per gram of GA5MA increases with the increase in REEs concentration. This might be explained by the fact that at lower concentration of REEs, large number of adsorption sites on GA5MA could not be exhausted and increasing the REEs concentration resulted in an increase of adsorption capacity by saturating the adsorbents surface. Fig. SF2b-d (Supplementary Material) shows the fitting plots of isotherm models used and the obtained parameters and correlation coefficients (R^2) values are listed in Table 1. By comparing the R^2 values of isotherms used, it was found that Langmuir model is better in describing the data satisfactorily for all targeted REEs except Sc. This further indicates that adsorption of Y, La, Ce, Nd and Eu on GA5MA is regarded as monolayer adsorption. Whereas, Freundlich model was found to be suitable for describing isotherm data for Sc with higher R^2 value. Furthermore, the n value obtained for Sc was higher than unity indicating that Sc adsorption on GA5MA surface was heterogeneous. Notably, the maximum adsorption capacities of examined REEs followed the order: Sc > Y > Nd > Ce > Eu > La; elucidated by the fact that smaller ionic radii has the better adsorbing capacity [46]. This result also complement the findings of previous studies [2,47]. In addition, a comparative study of different previously reported adsorbents is performed in Table 2. It is evident that GA5MA have better adsorption capacity compared to others.

3.3.3. Adsorption kinetics

Fig. 5c reveals the influence of contact time on adsorption of REEs (Sc, Y, La, Ce, Nd and Eu) on GA5MA. It is noticed that REEs adsorption show a sheer increase during first 90 min and then the adsorption process slow down until it attains equilibrium. This might be because of carboxyl groups of GA, which are abundantly assessable leading to an efficient interaction of REEs with GA5MA. Other researchers reported the same phenomena in case of Ce adsorption on PSD-g-PAA and PGS-g-PMAA [48,49]. After the saturation of external surface active sites, REEs diffuses in the inner pores of GA5MA, which would take comparatively more time. Fig. SF3a-b (Supplementary Material) shows the fitting plots of PS1 and PS2 models used and the obtained parameters and correlation coefficients (R^2) values are listed in Table 1. The results depict that PS2 in describing the kinetic data with higher R^2 values for all REEs (Sc, Y, La, Ce, Nd, Ce). Additionally, the calculated q_e values of PS2 model are closer to the experimental values, which also favors the suitability of PS2 model. This also suggests that chemisorption is the rate limiting step in the REEs adsorption over GA5MA.

The Weber-Morris intra-particle diffusion model and Boyd model revealed film diffusion as actual rate limiting step in the adsorption process. From Fig. SF3c (Supplementary Material), the three linear regions observed in case of Nd and Eu attributed that diffusion occurred by three steps viz. external film or boundary layer diffusion, macropore and micropore diffusion. On the other hand, the absence of second linear region in the plots of Sc, Y, La and Ce signifies that macropore diffusion is practically negligible. Thus, based on results of kinetic modeling, it was concluded that both chemisorption and diffusion affected the REEs adsorption by GA5MA.

3.3.4. Adsorption thermodynamics

Fig. SF4 (Supplementary Material) represents the linear dependency of $\ln K_c$ vs 1/T related to the adsorption of REEs onto GA5MA and calculated values of thermodynamic parameters viz. ΔG^0, ΔH^0, ΔS^0 are summarized in Table ST2 (Supplementary Material). Analyzing these parameters, it can be concluded that the adsorption of REEs on GA5MA is spontaneous processes as ΔG^o has negative values in all cases. Subsequently ΔH^o has positive values indicating the adsorption of REEs is endothermic process. Moreover, the absolute value of ΔH^o is above 50 kJ/mol illustrating the adsorption process is chemical adsorption and elucidated the fact that the adsorption capacity improved with rise in temperature [50–52]. The REE adsorption onto PEI-CNC [2], hydroxyapatite [53], Fe_3O_4/chitosan nanocomposite [54,55] and CLN/SiO_2 [3] was also found to be endothermic in nature. In addition, positive values ΔS^o suggests an increased disorder at the solid-liquid interface during the adsorption process.

3.3.5. Desorption and reusability

The reusability of GA5MA is a significant factor towards its potential use. The HNO_3 solution was used for elution and eight (08) consecutive adsorption-desorption cycles were carried out to determine the reusability performance of GA5MA. It was observed that removal rate of REEs using GA5MA decreased in each successive cycle. Additionally, adsorption process of REEs on GA5MA seems to be reversible in the presence of H^+ by ion exchange [49] due to good desorption rate in each assay. However, the possible reason for decrease in removal of REEs after each cycle might be due to hydraulic shear force in adsorption process, which damage the GA5MA surface ultimately reducing the availability of adsorption sites. The incomplete desorption of REEs might be another reason. Nevertheless, compared to other adsorbents reported in literature the reusability of GA5MA toward REEs is quite satisfactory [3–5].

3.4. Adsorption mechanism

The possible binding mechanism of REEs over GA5MA might be due to electrostatic interaction, ion-exchange reactions and complexation/chelation of surface functional groups of GA [47,56]. Based on the

Table 1
Adsorption isotherm and kinetic constants for REEs adsorption onto GA5MA.

REEs	Langmuir			Freundlich			Temkin		
	Q_o	K_L (L/mg)	R_L^2	K_f (L/g)	n	R_F^2	A (L/g)	B (J/mol)	R_T^2
Isotherms									
Sc	145.14	0.023	0.91	10.1	2.01	0.94	0.30	28.46	0.88
Y	144.72	0.034	0.84	30.90	4.34	0.68	8.51	13.61	0.55
La	108.69	0.05	0.94	24.75	3.87	0.89	3.28	14.14	0.78
Ce	116.82	0.06	0.90	39.68	6.32	0.74	114.97	9.02	0.59
Nd	141.44	0.053	0.94	20.46	2.59	0.94	1.01	24.48	0.87
Eu	111.73	0.102	0.97	40.30	5.74	0.88	74.41	10.05	0.75

REEs	$q_{e,exp}$ (mg/g)	Pseudo first order			Pseudo second order		
		$q_{e,cal}$ (mg/g)	k_1 (min^{-1})	R^2	q_e (mg/g)	k_2 (g/mg. min^{-1})	R^2
Kinetic							
Sc	33.16	53.21	5.0×10^{-2}	0.68	38.77	1.23×10^{-3}	0.95
Y	19.15	47.59	4.21×10^{-2}	0.71	23.28	0.83×10^{-3}	0.77
La	21.45	41.98	5.14×10^{-2}	0.79	28.95	0.96×10^{-3}	0.96
Ce	24.47	49.30	5.53×10^{-2}	0.82	26.74	1.47×10^{-3}	0.96
Nd	24.33	40.51	3.78×10^{-2}	0.73	27.13	0.79×10^{-3}	0.84
Eu	26.89	31.60	3.82×10^{-2}	0.81	31.61	1.37×10^{-3}	0.96

Table 2
Comparison of maximum adsorption capacity of REEs on different adsorbents.

Adsorbents		Adsorption Capacity (mg/g)						Ref
		Sc	Y	La	Ce	Nd	Eu	
Cys@Fe_3O_4	C_0:5 mg/L, Dose: 2.5 g/L, pH: 7	–	11	16.7	–	14	–	[50]
CA@Fe_3O_4	C_0:5 mg/L, Dose:2.5 g/L, pH: 7	–	44	41.85	–	53	–	[50]
thiourea@cellulose	C_0:50 mg/L, Dose:4 g/L	–	–	–	–	32	73	[51]
Zr@XG-ZA	C_0:25 mg/L, Dose:3 g/L, pH: 4	76.40	–	–	–	38.42	–	[7]
PAN mobilized SEP	C_0:1 mg/L, Dose:1 g/L, pH: 4	42.39[b]	33.34[b]	115.01[b]	12.64[b]	–	88.29[b]	[9]
CL-Zn/Al LDH	C_0:50 mg/L, Dose:1 g/L, pH: 7	–	102.25	92.51	96.25	–	–	[4]
CLN/SiO_2	C_0:25 mg/L, Dose:3 g/L, pH: 6	23.76[a]	–	29.48	–	–	24.27	[3]
GA-g-PAM/SiO_2	C_0:25 mg/L, Dose:3.5 g/L, pH: 6	35.22	–	7.9	–	12.24	10.11	[5]
M-Pyr	C_0:10 mg/L, Dose:2 g/L, pH: 6	–	–	–	–	–	7.9	[52]
Palygorskite	C_0:10 mg/L, Dose: 1 g/L, pH: 7	–	–	–	–	–	16.37	[53]
GA5MA	C_0:50 mg/L, Dose:1 g/L, pH: 4	145.13	144.72	108.69	116.82	141.44	111.73	This study

[a] Calculated from freundlich isotherm.
[b] Converted from the original unit of mmol/g presented in the literatures.

results of ζ-potential and pH, electrostatic interaction might be considered as one of the adsorption process; when the surface of GA5MA becomes negative at pH > 2.65 manifested in electrostatic interaction toward REEs. The SEM images of REEs (Sc, Y, La, Ce, Nd and Eu) saturated GA5MA are illustrated in Fig. SF5 (Supplementary Material). It is clear that after adsorption of REEs, the surface morphology changes by annihilating the brucite structure. The adsorption process with the GA moieties occur possibly due to coordination/chelation mechanism with carboxyl groups of GA, which can be observed in post adsorption FTIR spectra (Fig. SF6-Supplementary Material) by disappearance of ~2900 cm^{-1} and ~1750 cm^{-1} bands and shifting of other GA bands to lower wavenumbers, stating that carboxyl functional groups act as active sites for REEs adsorption. Additionally, the O-M-O bridging species may also facilitates the reaction between REEs and surface hydroxyl groups via ion exchange. It can be concluded that both the processes occur simultaneously under the same given conditions implying none of them is exclusive.

3.5. Adsorption in multi-component system

The Fig. 6b depicts the influence on REE adsorption over GA5MA in a multi-component system with an initial concentration of 10 mg/L. Among the targeted REEs, adsorption of Sc was higher due to smaller ionic size while La adsorption was least. A similar findings was reported by Ramasamy et al. [9], where Sc adsorption was significant compared to La and Y in a multi-component system. Additionally, the values of

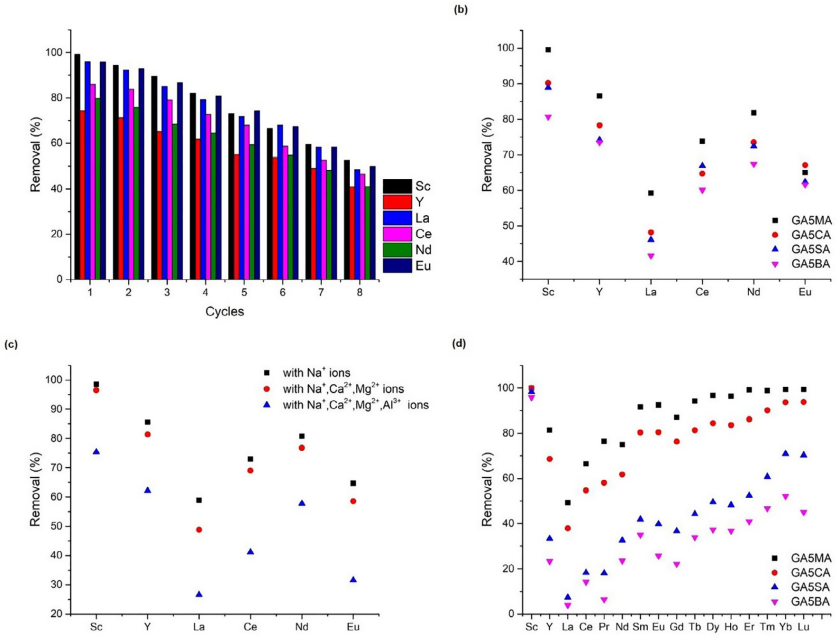

Fig. 6. Adsorption- desorption cycles for REEs on GA5MA (a); Adsorptive behavior of REEs on GA5MA, GA5CA, GA5SA and GA5BA in multi-component system (b); Adsorptive behavior of REEs on GA5MA in multi-component system with competing ions (Na^+, Ca^{2+}, Mg^{2+}, Al^{3+}) (c); Intra-series separation behavior of REEs.

q_{multi}/q_{single} calculated were less than 1, revealing that adsorption was barred by the presence of other REEs (i.e. competitive adsorption). The experiments were also performed at pH 4 with GA5CA, GA5SA and GA5BA nanocomposites as demonstrated in Fig. 6b. The REEs adsorption efficiencies were found to be in order of GA5MA > GA5CA > GA5SA > GA5BA complementing the fact that adsorption of REEs on GA-LDH depends upon the size of M^{2+} ions, smaller the ionic radii of divalent ions better will be the adsorption capacity.

The adsorption of REEs might be influenced by the occurrence of other cations due to similar ionic radius. The experiments was thus performed with 5-fold concentration of Na^+, Ca^{2+}, Mg^{2+} and Al^{3+} competing ions in a multi-component system. Fig. 6c illustrates the influence on the removal of REEs due to the presence of competing ions. The presence of Na^+ alone with REEs had negligible effect on removal, whereby, the existence of Ca^{2+} and Mg^{2+} ensued in slight decrease in efficacies of REEs due to competitive adsorption over nanocomposite. On the other hand, the presence of Al^{3+} ions hampered the adsorption of REEs significantly; might be due to similar ionic charge [57]. An additional revelation was the higher adsorption of Sc compared to other REEs in the presences of competing ions.

3.6. Intra-series REEs trend

To get a better insight into adsorption trend, the REE series was investigated to check their affinities of GA5MA, GA5CA, GA5SA and GA5BA nanocomposites towards LREEs and HREEs. The intra-series REEs adsorption trend over GA5MA, GA5CA, GA5SA and GA5BA nanocomposites is elucidated in Fig. 6d. At an initial REE concentration of 10 mg/L and pH 4, GA5MA record the superior adsorption of REEs. Meanwhile, in case of all four nanocomposites used, the increment in adsorption was observed by increasing atomic numbers with Sc exhibiting the highest adsorption and La the least. It could also be stated that nanocomposites are more selective towards HREEs except Y. This could be attributed to larger ionic size and different electronic configuration of Y in comparison to other HREEs. The similar trend was reported in literature where in multi-component system Sc displaying higher adsorption due to its smaller ionic size while adsorption of La and Y was insignificant [9,58]. Though the adsorption of REEs decrease as the size of interlayer divalent ions increases, yet, the nanocomposites (GA5CA, GA5SA, GA5BA) indicated higher adsorption of Sc. Notably, the zig zag pattern seen was possibly due to REE tetrad effect [59].

4. Conclusion

In a nutshell, the exfoliated GA5MA synthesized via in-situ coprecipitation with 5 wt% GA and Mg as a divalent ions exhibited better adsorption capacity toward REEs in comparison to other nanocomposites. The increase in basal spacing indicated the presence of GA in the interlayers of exfoliated LDH sheets. Likewise, prominent difference in the morphologies of exfoliated GAnXA was observed by changing the interlayer divalent ions. The sequence of REEs with respect to their adsorption capacities was Sc > Y > Nd > Ce > Eu > La. The adsorption behavior of GA5MA was good for REEs, experimented in multi-component system with or without competing ions. HREEs removal seems to be favorable over LREEs. Moreover, the nanocomposites (GA5CA, GA5SA, GA5BA) were highly selective for Sc recovery. The ability of GA5MA to extract REEs at pH 4 (slightly acidic) presented the possibility of its use towards REE recovery/separation via column studies and in many industrial applications viz. treatment of wastewater, recovery of REEs etc.

Conflicts of interest

There are no conflicts of interest to declare.

Acknowledgement

The authors are thankful to Nida Iftikhar for help with 3D-art work.

Appendix A. Supplementary data

Supplementary data associated with this article can be found, in the online version, at http://dx.doi.org/10.1016/j.cej.2018.04.126.

References

[1] D.L. Ramasamy, V. Puhakka, S. Iftekhar, A. Wojtuś, E. Repo, S.B. Hammouda, E. Iakovleva, M. Sillanpää, N-and O-ligand doped mesoporous silica-chitosan hybrid beads for the efficient, sustainable and selective recovery of rare earth elements (REE) from acid mine drainage (AMD): understanding the significance of physical modification and conditioning of the polymer, J. Hazard. Mater. 348 (2018) 84–91.
[2] F. Zhao, E. Repo, Y. Song, D. Yin, S.B. Hammouda, L. Chen, S. Kalliola, J. Tang, K.C. Tam, M. Sillanpää, Polyethylenimine-cross-linked cellulose nanocrystals for highly efficient recovery of rare earth elements from water and a mechanism study, Green Chem. 19 (2017) 4816–4828.
[3] S. Iftekhar, V. Srivastava, M. Sillanpää, Enrichment of lanthanides in aqueous system by cellulose based silica nanocomposite, Chem. Eng. J. 320 (2017) 151–159.
[4] S. Iftekhar, V. Srivastava, M. Sillanpää, Synthesis and application of LDH intercalated cellulose nanocomposite for separation of rare earth elements (REEs), Chem. Eng. J. 309 (2017) 130–139.
[5] S. Iftekhar, V. Srivastava, A. Casas, M. Sillanpää, Synthesis of novel GA-g-PAM/SiO_2 nanocomposite for the recovery of rare earth elements (REE) ions from aqueous solution, J. Clean. Prod. 170 (2017) 251–259.
[6] T. Feder, D. Kramer, Concern grows over China's dominance of rare-earth metals, Phys. Today 63 (2010) 22–28.
[7] S. Iftekhar, V. Srivastava, S.B. Hammouda, M. Sillanpää, Fabrication of novel metal ion imprinted xanthan gum-layered double hydroxide nanocomposite for adsorption of Rare Earth Elements, Carbohyd. Polym., 2018 (in press Accepted Manuscript).
[8] D.L. Ramasamy, E. Repo, V. Srivastava, M. Sillanpää, Chemically immobilized and physically adsorbed PAN/acetylacetone modified mesoporous silica for the recovery of rare earth elements from the waste water-comparative and optimization study, Water Res. 114 (2017) 264–276.
[9] D.L. Ramasamy, V. Puhakka, E. Repo, S. Khan, M. Sillanpää, Coordination and silica surface chemistry of lanthanides (III), scandium (III) and yttrium (III) sorption on 1-(2-pyridylazo)-2-napththol (PAN) and acetylacetone (acac) immobilized gels, Chem. Eng. J. 324 (2017) 104–112.
[10] D.L. Ramasamy, A. Wojtuś, E. Repo, S. Kalliola, V. Srivastava, M. Sillanpää, Ligand immobilized novel hybrid adsorbents for rare earth elements (REE) removal from waste water: Assessing the feasibility of using APTES functionalized silica in the hybridization process with chitosan, Chem. Eng. J. 330 (2017) 1370–1379.
[11] D.L. Ramasamy, S. Khan, E. Repo, M. Sillanpää, Synthesis of mesoporous and microporous amine and non-amine functionalized silica gels for the application of rare earth elements (REE) recovery from the waste water-understanding the role of pH, temperature, calcination and mechanism in Light REE and Heavy REE separation, Chem. Eng. J. 322 (2017) 56–65.
[12] S. Iftekhar, M.U. Farooq, M. Sillanpää, M.B. Asif, R. Habib, Removal of Ni (II) using multi-walled carbon nanotubes electrodes: relation between operating parameters and capacitive deionization performance, Arabian J. Sci. Eng. 42 (2017) 235–240.
[13] T. Yao, Y. Xiao, X. Wu, C. Guo, Y. Zhao, X. Chen, Adsorption of Eu (III) on sulfonated graphene oxide: combined macroscopic and modeling techniques, J. Mol. Liq. 215 (2016) 443–448.
[14] D. Bhakat, P. Barik, A. Bhattacharjee, Electrical conductivity behavior of Gum Arabic biopolymer-Fe3O4 nanocomposites, J. Phys. Chem. Solids 112 (2018) 73–79.
[15] M.M. Solomon, H. Gerengi, S.A. Umoren, N.B. Essien, U.B. Essien, E. Kaya, Gum Arabic-silver nanoparticles composite as a green anticorrosive formulation for steel corrosion in strong acid media, Carbohydr. Polym. 181 (2018) 43–55.
[16] R.M. Daoub, A.H. Elmubarak, M. Misran, E.A. Hassan, M.E. Osman, Characterization and functional properties of some natural Acacia gums, J. Saudi Soc. Agric. Sci. (2016).
[17] V. Srivastava, Y. Sharma, M. Sillanpää, Green synthesis of magnesium oxide nanoflower and its application for the removal of divalent metallic species from synthetic wastewater, Ceram. Int. 41 (2015) 6702–6709.
[18] R. Rojas, M.R. Perez, E.M. Erro, P.I. Ortiz, M.A. Ulibarri, C.E. Giacomelli, EDTA modified LDHs as Cu 2+ scavengers: removal kinetics and sorbent stability, J. Colloid Interface Sci. 331 (2009) 425–431.
[19] G. Carja, S. Ratoi, G. Ciobanu, I. Balasanian, Uptake of As (V) from aqueous solution by anionic clays type FeLDHs, Desalination 223 (2008) 243–248.
[20] R. Sadik, R. Lahkale, N. Hssaine, W. ElHatimi, M. Diouri, E. Sabbar, Sulfate removal from wastewater by mixed oxide-LDH: equilibrium, kinetic and thermodynamic studies, J. Mater. Environ. Sci. 6 (2015) 2895–2905.
[21] X. Xu, R. Lu, X. Zhao, S. Xu, X. Lei, F. Zhang, D.G. Evans, Fabrication and photocatalytic performance of a ZnxCd1−xS solid solution prepared by sulfuration of a single layered double hydroxide precursor, Appl. Catal. B 102 (2011) 147–156.
[22] J. Plank, D. Zhimin, H. Keller, F.V. Hössle, W. Seidl, Fundamental mechanisms for polycarboxylate intercalation into C3A hydrate phases and the role of sulfate

present in cement, Cem. Concr. Res. 40 (2010) 45–57.
[23] P. Aranda, M. Darder, E. Ruiz-Hitzky, Bionanocomposites based on alginate–zein/layered double hydroxide materials as drug delivery systems, J. Mater. Chem. 20 (2010) 9495–9504.
[24] A. Lukashin, A. Vyacheslavov, A. Vertegel, Y.D. Tret'yakov, Synthesis of PbS/LDH Nanocomposites with the Use of the Method of Reversible Delamination of LDHs, Doklady Chemistry, Springer, 2002, pp. 178–181.
[25] T. Kuila, H. Acharya, S. Srivastava, A. Bhowmick, Effect of vinyl acetate content on the mechanical and thermal properties of ethylene vinyl acetate/MgAl layered double hydroxide nanocomposites, J. Appl. Polym. Sci. 108 (2008) 1329–1335.
[26] Q. Wang, D. O'Hare, Recent advances in the synthesis and application of layered double hydroxide (LDH) nanosheets, Chem. Rev. 112 (2012) 4124–4155.
[27] M. Tanaka, I.Y. Park, K. Kuroda, C. Kato, Formation of hydrotalcite–acrylate intercalation compounds and their heat-treated products, Bull. Chem. Soc. Jpn. 62 (1989) 3442–3445.
[28] H.-B. Hsueh, C.-Y. Chen, Preparation and properties of LDHs/polyimide nanocomposites, Polymer 44 (2003) 1151–1161.
[29] Y. Ding, Z. Gui, J. Zhu, Y. Hu, Z. Wang, Exfoliated poly (methyl methacrylate)/MgFe-layered double hydroxide nanocomposites with small inorganic loading and enhanced properties, Mater. Res. Bull. 43 (2008) 3212–3220.
[30] H. Peng, Y. Han, T. Liu, W.C. Tjiu, C. He, Morphology and thermal degradation behavior of highly exfoliated CoAl-layered double hydroxide/polycaprolactone nanocomposites prepared by simple solution intercalation, Thermochim. Acta 502 (2010) 1–7.
[31] L. Qiu, W. Chen, B. Qu, Exfoliation of layered double hydroxide in polystyrene by in-situ atom transfer radical polymerization using initiator-modified precursor, Colloid Polym. Sci. 283 (2005) 1241–1245.
[32] B. Li, Y. Hu, J. Liu, Z. Chen, W. Fan, Preparation of poly (methyl methacrylate)/LDH nanocomposite by exfoliation-adsorption process, Colloid Polym. Sci. 281 (2003) 998–1001.
[33] S. Vial, V. Prevot, F. Leroux, C. Forano, Immobilization of urease in ZnAl layered double hydroxides by soft chemistry routes, Microporous Mesoporous Mater. 107 (2008) 190–201.
[34] M.-F. Chiang, T.-M. Wu, Synthesis and characterization of biodegradable poly (L-lactide)/layered double hydroxide nanocomposites, Compos. Sci. Technol. 70 (2010) 110–115.
[35] G. Hu, N. Wang, D. O'Hare, J. Davis, Synthesis of magnesium aluminium layered double hydroxides in reverse microemulsions, J. Mater. Chem. 17 (2007) 2257–2266.
[36] H. Chen, G. Qian, X. Ruan, R.L. Frost, Abatement of aqueous anionic contaminants by thermo-responsive nanocomposites:(Poly (N-isopropylacrylamide))-co-silylanized Magnesium/Aluminun layered double hydroxides, J. Colloid Interface Sci. 448 (2015) 65–72.
[37] B. Guo, Y. Zhao, Q. Huang, Q. Jiao, A new method to prepare exfoliated UV-cured polymer/LDH nanocomposites via nanoplatelet-like LDHs modified with N-Lauroyl-glutamate, Compos. Sci. Technol. 81 (2013) 37–41.
[38] V. Katiyar, N. Gerds, C.B. Koch, J. Risbo, H.C.B. Hansen, D. Plackett, Poly l-lactide-layered double hydroxide nanocomposites via in situ polymerization of l-lactide, Polym. Degrad. Stab. 95 (2010) 2563–2573.
[39] J. Teng, X. Zeng, X. Xu, J.-G. Yu, Assembly of a novel porous 3D graphene oxide-starch architecture by a facile hydrothermal method and its adsorption properties toward metal ions, Mater. Lett. 214 (2018) 31–33.
[40] V. Rives, Layered Double Hydroxides: Present and Future, Nova Publishers, 2001.
[41] D. Srankó, M. Sipiczki, É.G. Bajnóczi, M. Darányi, Á. Kukovecz, Z. Kónya, S.E. Canton, K. Norén, P. Sipos, I. Pálinkó, A SEM, EDX and XAS characterization of Ba (II) Fe (III) layered double hydroxides, J. Mol. Struct. 993 (2011) 62–66.
[42] Á. Kukovecz, Z. Kónya, P. Sipos, I. Pálinkó, Synthesis and properties of novel Ba (II) Fe (III) layered double hydroxides, Appl. Clay Sci. 48 (2010) 214–217.
[43] V. Srivastava, M. Sillanpää, Synthesis of malachite@ clay nanocomposite for rapid scavenging of cationic and anionic dyes from synthetic wastewater, J. Environ. Sci. 51 (2017) 97–110.
[44] Y. Zhu, W. Wang, Y. Zheng, F. Wang, A. Wang, Rapid enrichment of rare-earth metals by carboxymethyl cellulose-based open-cellular hydrogel adsorbent from HIPEs template, Carbohydr. Polym. 140 (2016) 51–58.
[45] K. Yang, L.-G. Yan, Y.-M. Yang, S.-J. Yu, R.-R. Shan, H.-Q. Yu, B.-C. Zhu, B. Du, Adsorptive removal of phosphate by Mg–Al and Zn–Al layered double hydroxides: kinetics, isotherms and mechanisms, Sep. Purif. Technol. 124 (2014) 36–42.
[46] G.A. Moldoveanu, V.G. Papangelakis, Recovery of rare earth elements adsorbed on clay minerals: I. Desorption mechanism, Hydrometallurgy 117 (2012) 71–78.
[47] F. Zhao, E. Repo, Y. Meng, X. Wang, D. Yin, M. Sillanpää, An EDTA-β-cyclodextrin material for the adsorption of rare earth elements and its application in pre-concentration of rare earth elements in seawater, J. Colloid Interface Sci. 465 (2016) 215–224.
[48] J. Chen, W. Luo, A. Guo, T. Luo, C. Lin, H. Li, L. Jing, Preparation of a novel carboxylate-rich palygorskite as an adsorbent for Ce^{3+} from aqueous solution, J. Colloid Interface Sci. 512 (2018) 657–664.
[49] S. Gao, T. Luo, W. Luo, A novel and efficient method on the recovery of nanosized CeO_2 in Ce^{3+} wastewater remediation using modified sawdust as adsorbent, J. Colloid Interface Sci. 512 (2018) 629–637.
[50] N. Ünlü, M. Ersoz, Adsorption characteristics of heavy metal ions onto a low cost biopolymeric sorbent from aqueous solutions, J. Hazard. Mater. 136 (2006) 272–280.
[51] Y.R. Smith, D. Bhattacharyya, T. Willhard, M. Misra, Adsorption of aqueous rare earth elements using carbon black derived from recycled tires, Chem. Eng. J. 296 (2016) 102–111.
[52] Ş. Sert, C. Kütahyali, S. İnan, Z. Talip, B. Çetinkaya, M. Eral, Biosorption of lanthanum and cerium from aqueous solutions by *Platanus orientalis* leaf powder, Hydrometallurgy 90 (2008) 13–18.
[53] F. Granados-Correa, J. Vilchis-Granados, M. Jiménez-Reyes, L. Quiroz-Granados, Adsorption behaviour of La (III) and Eu (III) ions from aqueous solutions by hydroxyapatite: kinetic, isotherm, and thermodynamic studies, J. Chem. 2013 (2012).
[54] A.A. Galhoum, M.G. Mafhouz, S.T. Abdel-Rehem, N.A. Gomaa, A.A. Atia, T. Vincent, E. Guibal, Cysteine-functionalized chitosan magnetic nano-based particles for the recovery of light and heavy rare earth metals: uptake kinetics and sorption isotherms, Nanomaterials 5 (2015) 154–179.
[55] R.M. Ashour, A.F. Abdel-Magied, A.A. Abdel-Khalek, O. Helaly, M. Ali, Preparation and characterization of magnetic iron oxide nanoparticles functionalized by l-cysteine: adsorption and desorption behavior for rare earth metal ions, J. Environ. Chem. Eng. 4 (2016) 3114–3121.
[56] S. Iftekhar, D.L. Ramasamy, V. Srivastava, M.B. Asif, M. Sillanpää, Understanding the factors affecting the adsorption of Lanthanum using different adsorbents: a critical review, Chemosphere, 2018 (in press accepted manuscript).
[57] M.R. Awual, T. Kobayashi, H. Shiwaku, Y. Miyazaki, R. Motokawa, S. Suzuki, Y. Okamoto, T. Yaita, Evaluation of lanthanide sorption and their coordination mechanism by EXAFS measurement using novel hybrid adsorbent, Chem. Eng. J. 225 (2013) 558–566.
[58] D.L. Ramasamy, V. Puhakka, E. Repo, S.B. Hammouda, M. Sillanpää, Two-stage selective recovery process of scandium from the group of rare earth elements in aqueous systems using activated carbon and silica composites: dual applications by tailoring the ligand grafting approach, Chem. Eng. J. 341 (2018) 351–360.
[59] T. Monecke, U. Kempe, J. Monecke, M. Sala, D. Wolf, Tetrad effect in rare earth element distribution patterns: a method of quantification with application to rock and mineral samples from granite-related rare metal deposits, Geochim. Cosmochim. Acta 66 (2002) 1185–1196.

Publication V

Iftekhar, S., Srivastava, V., Hammouda, S. B., and Sillanpää, M.

Fabrication of novel metal ion imprinted xanthan gum-layered double hydroxide nanocomposite for adsorption of rare earth elements

Reprinted with permission from
Carbohydrate Polymers
Vol. 194, pp. 274-284, 2018

Carbohydrate Polymers 194 (2018) 274–284

Contents lists available at ScienceDirect

Carbohydrate Polymers

journal homepage: www.elsevier.com/locate/carbpol

Fabrication of novel metal ion imprinted xanthan gum-layered double hydroxide nanocomposite for adsorption of rare earth elements

Sidra Iftekhar[a,*], Varsha Srivastava[a], Samia Ben Hammouda[a], Mika Sillanpää[a,b]

[a] Laboratory of Green Chemistry, School of Engineering Science, Lappeenranta University of Technology, Sammonkatu 12, FI-50130 Mikkeli, Finland
[b] Department of Civil and Environmental Engineering, Florida International University, Miami, FL 33174, USA

ARTICLE INFO

Keywords:
Adsorption
Gum xanthan
Nanocomposite
Photocatalyst
Rare earth elements

ABSTRACT

The work focus to enhance the properties of xanthan gum (XG) by anchoring metal ions (Fe, Zr) and encapsulating inorganic matrix (M@XG-ZA). The fabricated nanocomposite was characterized by Transmission Electron Microscopy (TEM), Scanning Electron Microscopy (SEM), Energy-dispersive X-ray spectroscopy (EDX), Fourier Transform Infrared Spectroscopy (FTIR), surface area (BET) and zeta potential analysis. The adsorption of Sc, Nd, Tm and Yb was investigated after screening of synthesized materials in detail to understand the influence of pH, contact time, temperature and initial REE (rare earth element) concentration both in single and multicomponent system via batch adsorption. The adsorption mechanism was verified by FTIR, SEM and elemental mapping. The SEM images of Zr@XG-ZA demonstrate scutes structure, which disappeared after adsorption of REEs. The maximum adsorption capacities were 132.30, 14.01, 18.15 and 25.73 mg/g for Sc, Nd, Tm and Yb, respectively. The adsorption efficiency over Zr@XG-ZA in multicomponent system was higher than single system and the REEs followed the order: Sc > Yb > Tm > Nd. The Zr@XG-ZA demonstrate good adsorption behavior for REEs up to five cycles and then it can be used as photocatalyst for the degradation of tetracycline. Thus, the work adds a new insight to design and preparation of efficient bifunctional adsorbents from sustainable materials for water purification.

1. Introduction

Rare earth elements (REEs) have been employed in many technological and advanced industries for instance, in batteries, engine turbines, supermagnets, fluorescent lamps etc. (Bonificio & Clarke, 2016; Kim et al., 2015; Ramasamy, Puhakka, Repo, Khan, & Sillanpää, 2017; Ramasamy, Repo, Srivastava, & Sillanpää, 2017). REEs are generally the by-product of mining and China supplies more than 85% of the worldwide production of REEs (Li et al., 2016; Moriwaki et al., 2016; Park et al., 2016). In 2010, the world demand for REEs was 136,000 t per year and it was expected to upsurge to at least 160,000 t annually by 2016 (Humphries, 2010, 2012). In another report published in 2012, only 1% of REEs was estimated to be recycled (Sadovsky, Brenner, Astrachan, Asaf, & Gonen, 2016). Thus, in 2013 the Critical Materials Institute launched by U.S. Department of Energy, to find alternatives for REEs or recycling of REEs from waste (Fujita et al., 2015) due to dependence of many technologies on REEs. Moreover, there is a necessity to recover REEs in eco-friendly way since they are toxic for living organisms if accumulated in food chain (Ramasamy, Puhakka, Iftekhar et al. 2018; Ramasamy, Wojtuś et al., 2017; Vijayaraghavan & Balasubramanian, 2010). Numerous methods have been used for the removal and recovery of REEs viz. electrochemical (Maes, Zhuang, Rabaey, Alvarez-Cohen, & Hennebel, 2017), ion exchange (Hong et al., 2015), chemical precipitation (Dupont & Binnemans, 2015), solvent extraction (Kim et al., 2015), adsorption (Ramasamy, Khan, Repo, & Sillanpää, 2017; Ramasamy, Puhakka, Repo, & Sillanpää, 2018). Adsorption is one of the most cost efficient, eco-friendly and economical method for the treatment and recovery of REEs compared to the conventional methods, which are costly, environmentally hazardous and inefficient at low concentration of REEs (Kim et al., 2015).

Anionic clays or layered double hydroxides (LDH) are bi-dimensional solids having brucite like layer structure (Rojas et al., 2009). They are well-known to act as host matrices for the synthesis of hybrid organic-inorganic nanocomposites by intercalating the organic polymers (Leroux & Besse, 2001). When calcined at moderated temperatures (300–500 °C) LDH show a special trait to yield corresponding mixed oxides which can be recovered to original layer structure by contacting with solution containing anionic species. This property is useful in interaction of LDH with organic species (Darder, López-Blanco, Aranda, Leroux, & Ruiz-Hitzky, 2005; Latterini, Elisei, Aloisi,

* Corresponding author.
E-mail address: sidra.iftekhar@lut.fi (S. Iftekhar).

https://doi.org/10.1016/j.carbpol.2018.04.054
Received 17 January 2018; Received in revised form 13 April 2018; Accepted 13 April 2018
Available online 17 April 2018
0144-8617/

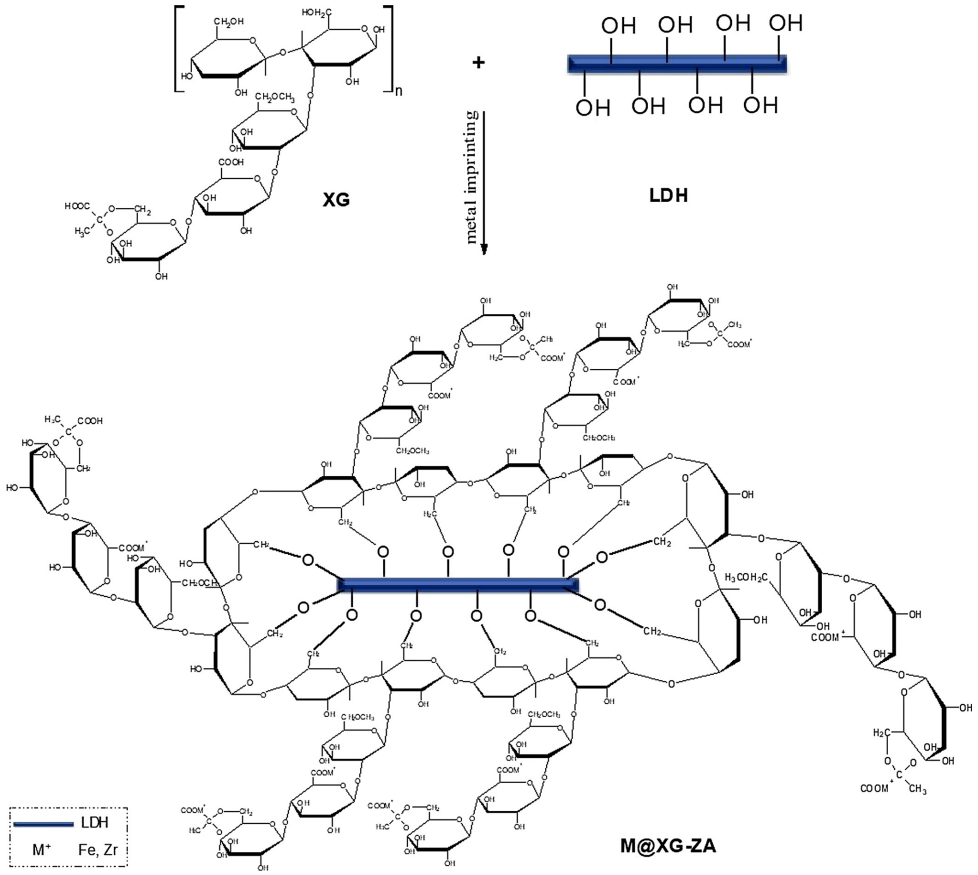

Scheme 1. Schematic illustration of synthesis process of M@XG-ZA.

Costantino, & Nocchetti, 2002; Rives, 2002; Sharma, Kumar et al., 2017). Xanthan gum (XG; Fig. S1), with anionic character is a polysaccharide consisting of cellulose like backbone with a trisaccharide (β-D-mannose β-D-glucuronic acid-α-D-mannose) side chain attached to alternate D-glucose units of the main chain (Katzbauer, 1998). The anionic character of XG is due to the presence of glucuronic acid and pyruvic acid groups in the side chain. Due to ease of manufacturing, biocompatibility, biodegradability safety and cost effectiveness, XG have found various applications in drug delivery, hydrogels, nanoparticles, microspheres, coatings, films and matrix tablets (Shalviri, Liu, Abdekhodaie, & Wu, 2010). This non-toxic biopolymer have drawn significant interests as eco-friendly adsorbent due to presence of abundant hydroxyl groups, however, its solubility in water limits its use (Zhang et al., 2013). XG based nanocomposites and hydrogel were utilized for the treatment of contaminated water as the major advantage of using biopolymers is their biodegradable nature and can be used repeatedly (Crini & Badot, 2008).

Besides these advantages, biopolymers also have some serious limitations, such as poor thermal stability, low surface area, poor mechanical strength and solubility in water limits Xanthan gum applications in water treatment. These drawbacks of XG can be overcome by incorporations of inorganic fillers. Numerous XG-inorganic based adsorbents were reported in literature (Bueno, Bentini, Catalani, Barbosa, & Petri, 2014; Ghorai, Sinhamahpatra, Sarkar, Panda, & Pal, 2012; Mittal, Parashar, Mishra, & Mishra, 2014; Sharma, Thakur et al., 2017). LDHs are suitable candidate for the improvement of XG as LDHs act as host matrices for the synthesis of hybrid organic-inorganic nanocomposites by intercalating the organic polymers. The unique combination of LDH encapsulated in XG has not been reported for REE recovery. So the author decided to explore the LDH encapsulated in XG by different metal imprinting to overcome the limits of XG as well as its application for REEs recovery from single and multi-component system.

The primary objective of the present study was thus to investigate the REE adsorption efficiency using metal ion anchored xanthan gum capsuling LDH nanocomposite. The adsorption process was focused and studied for targeted REEs including Sc, Nd, Tm, and Yb (i.e. scandium, neodymium, thulium and ytterbium). The adsorption process was studied in single as well as in multi-component system and influence of various parameters were investigated. The adsorption mechanism and the regeneration were also investigated. Furthermore, to get better

insight characterization of synthesized material was performed before and after adsorption. Finally, a special attention was devoted to the reusability of nanocomposite and the REE loaded nanocomposite as a photocatalyst.

2. Experimental methods

2.1. Reagents

Xanthan gum (XG) from Xanthomonas campestris (Section S1), urea (CH_4N_2O), sodium hydroxide (NaOH), nitric acid (HNO_3), zinc chloride ($ZnCl_2$), aluminum chloride hexahydrate ($AlCl_3{\cdot}6H_2O$) were purchased from Sigma Aldrich. The nitrate salts of the REEs were utilized for the preparation of solutions of desired concentrations. All the chemicals are of reagent grade and used as received without further purification.

2.2. Synthesis ZA LDH

The synthesis of Zn-Al (ZA) LDH was prepared by urea hydrolysis method as reported with slight modifications (Iftekhar, Srivastava, & Sillanpää, 2017b). In a typical synthesis, a solution with appropriate moles of the corresponding metal chloride ions with Zn:Al ratio of 3 was added dropwise in 1 M urea solution under constant stirring at 300 rpm. The pH was then adjusted to 10 by addition of NaOH and precipitates were aged for 18 h at 70 °C. The resultant material was subsequently washed with deionized water and oven-dried (TERMAKS) at 50 °C for overnight followed by calcination at 500 °C for 4 h.

2.3. Synthesis of metal anchored @XG-ZA

2% XG solution (w/v) was prepared in 50 mL of DI water at 60 °C. Meanwhile, about 3 g of ZA was dispersed in water (50 mL) and sonicated for 30 min. The dispersion was then added into the XG solution. The mixture (XG-ZA) was maintained at the same temperature (60 °C) and vigorously stirred for 24 h.

For synthesizing M@XG-ZA, the XG-ZA emulsion was added slowly in 3% $FeCl_3$ and $ZrOCl_2{\cdot}8H_2O$ solution (w/v) and kept for 4 h. The synthesized hydrogel type nanocomposites were filtered, washed thoroughly with DI water and freeze-dried (CHRIST Alpha 2-4LDplus). The dried nanocomposites (M@XG-ZA; where M = Zr or Fe) were then subjected to REE sorption studies. The schematic illustration of synthesis process is shown in Scheme 1.

2.4. Characterization

Hitachi H-7600 transmission electron microscopy (TEM) was employed for the determination of particle size of nanocomposite. Microstructure and morphology of the M@XG-ZA was carried out using Hitachi S-4800 scanning electron microscope (SEM) operating at 10 kV. The elemental composition of M@XG-ZA was determined using Energy Dispersive X-ray Spectrometer (EDX). Fourier transform infrared spectroscopy (FTIR) of the M@XG-ZA was conducted by Bruker Vertex 70 model, in a spectral range of 400–4000 cm^{-1}. N_2 adsorption-desorption isotherms were used for the determination of surface area and pore size with Tristar® II Plus instrument.

2.5. REE uptake experiments

All the adsorption experiments were performed by agitating 3 g/L of M@XG-ZA with 10 mL of REE solution at chosen initial concentration. The effect of pH and contact time was investigated at initial concentration of 25 mg/L in pH range of 2–6. After each assay, the nanocomposite was separated from solution using 0.45 µm PTFE syringe filters. The amount of REE adsorbed by M@XG-ZA was calculated by using Eq. (1):

$$q_e = \frac{(C_o - C_f)V}{M} \quad (1)$$

Where q_e is the adsorption capacity (mg/g), C_o and C_f is the initial and equilibrium concentrations of REE in solution (mg/L), V is solution volume (L), M is the mass of M@XG-ZA nanocomposite (g).

Due to similar chemical properties, the separation of REE is difficult (Zhao et al., 2017). Thus, the adsorption of REE in multicomponent system on M@XG-ZA was investigated. To carry out the experiments in multicomponent system parameter including pH, contact time, temperature and initial concentration was varied.

2.6. Regeneration and reusability studies

For desorption and regeneration process, the separated REE saturated M@XG-ZA was desorbed in different concentration of HNO_3 (0.1 M, 0.5 M and 1 M). Briefly, 10 mL of 25 mg/L of REE were mixed with M@XG-ZA for specific time. The material was then separated by centrifugation, washed with distilled water to neutralize and used in succeeding cycles for REE enrichment.

The leftover nanocomposite was then collected and used as a photocatalyst for the degradation of tetracycline (TC). The experiment was conducted in batch mode by adding required amount of nanocomposite in 100 mL of 20 mg/L TC solution. Afterwards, required amount of H_2O_2 and PMS (peroxymonosulfate or oxone) was used in separate systems to initiate and accelerate the reaction. The TC sample of 1 mL was withdrawn after set interval and filtered through 0.45 µm membrane filter. The TC concentration in samples were measured by using High performance liquid chromatography with UV detector (Shimadzu HPLC-UV).

3. Results and discussion

3.1. Characterization and properties of M@XG-ZA

The synthesized M@XG-ZA nanocomposite exhibits different nanostructures and morphologies. According to TEM images (Fig. 1a, d), the organic cluster appeared to be bigger in size in case of Zr@XG-ZA compare to Fe@XG-ZA. In Fe@XG-ZA (Fig. 1a), the organic cluster is more dense, however the presence of small particles toward the edges of cluster can also be seen. It is also clear from the images that XG is encapsulating ZA and no free ZA structure was observed in TEM images, which show the formation of binary nanocomposite. The SEM images of Fe@XG-ZA and Zr@XG-ZA (Fig. 1b, e) look like scutes and cycloids scales, respectively. Additionally, the outer wall in both cases is buildup of XG anchored with Fe or Zr, which changes the whole morphology of nanocomposites. The EDX spectra results of M@XG-ZA are given in Fig. 1c, f and the results of elemental analysis (wt.%) are summarized in Table S1. The amount of Fe loaded on the surface is quite high compare to Zr loading. The decree in wt.% of O was observed in case of Fe@XG-ZA, which might be due to binding of Fe by replacing the −OH groups of LDH.

The FTIR spectra of XG, Fe@XG-ZA and Zr@XG-ZA are shown in Fig. 2a. The FTIR spectra of Zr@XG-ZA showed peaks at 3345, 1706, 1620, 1407 and 1022 cm^{-1}, which are attributed to the stretching of O—H, C=O stretching, COO− (asymmetric), COO− (symmetric) and O—H band of XG, respectively (Darzi, Larimi, & Darzi, 2012; Mittal et al., 2014; Pongjanyakul & Puttipipatkhachorn, 2007). Similar, in Fe@XG-ZA the bands appeared with a slight shift at 3352, 1602, 1404 and 1021 cm^{-1} because of different metal being anchored on XG-ZA, which obviously provided a shift to wavenumbers and in the intensities of peaks. This result is in a good agreement with previous study (Pongjanyakul & Puttipipatkhachorn, 2007). It is also noticed that several characteristic peaks of XG disappeared in M@XG-ZA, might be due to formation of ionic bond of XG with metal ions. The peaks in a region of 400–800 cm^{-1} corresponds to M—OH vibrations and O—M—O

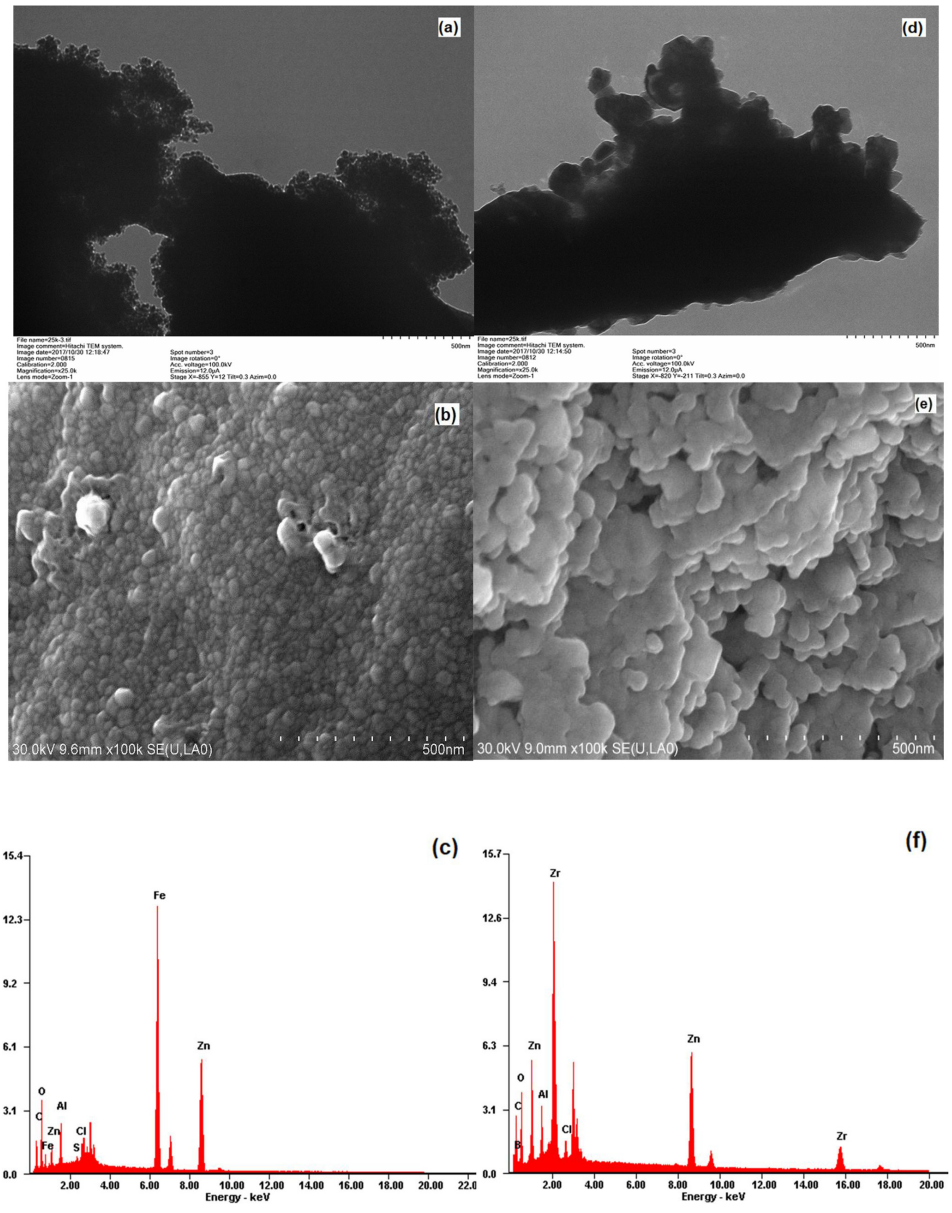

Fig. 1. TEM, SEM images and EDX spectra of Fe@XG-ZA (a–c) and Zr@XG-ZA (d–f), respectively (scale bar of TEM and SEM images is 500 nm).

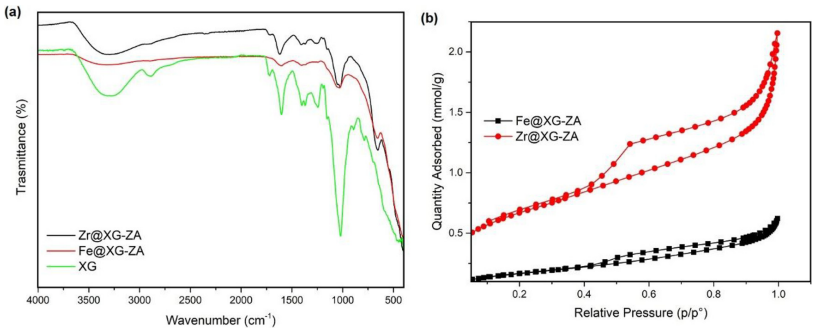

Fig. 2. FTIR spectra (a) and BET (b) of Fe@XG-ZA and Zr@XG-ZA.

stretching (where M = Zn and Al). The presence of these peaks confirm that the inorganic matrix of ZA was encapsulated in XG and resulted in successful formation of M@XG-ZA nanocomposite. BET studies were carried out to observe the effect of metal anchoring on surface area, pore volume and pore diameter of nanocomposites. The BET surface area, pore volume and pore diameter of Fe@XG-ZA is 13.09 m^2/g, 17.69 mm3/g, 4.79 nm, whereas, for Zr@XG-ZA is 21.49 m^2/g, 40.49 mm3/g, 7.29 nm, respectively. The lower surface area of Fe@XG-ZA is due to high Fe binding, which is evident by the disappearance of FTIR peaks at 1706 and 1250 cm^{-1}. The presence of these peaks might act as active sites for the targeted REEs and thus Fe@XG-ZA will possibly have lower removal rate compare to Zr@XG-ZA nanocomposite.

3.2. Screening of nanocomposites-preliminary test

As mentioned in Section 2.1, Fe and Zr anchored XG-ZA was synthesized and both nanocomposites were tested for Sc, Nd, Tm and Yb. The initial concentration of REEs was 25 mg/L and experiments were performed at room temperature for 3 h. The results illustrated in Fig. 3a show that the adsorption of REEs on Fe@XG-ZA was almost negligible compare to Zr@XG-ZA. This was probably due to similar ionic charge of REEs and Fe. Another possible reason is the extensive Fe bridging on XG-ZA, which occupied all the possible locations where REEs could get adsorbed. Fe and Zr bridging can also be seen clearly in microscopic images (Fig. S2a, b) and percentage loading calculated by measuring the concentration of Fe and Zr in solution before and after loading on XG-ZA was 99.99% and 90.62%, respectively. Thus, Zr@XG-ZA was used in further experiments.

3.3. Effect of pH

At the solid-liquid interface, pH of the solution plays a vital role in physiochemical reaction. It determines the interaction between adsorbent and adsorbate in aqueous medium (Srivastava & Sillanpää, 2017). As presented in Fig. 3b, the dependency on pH followed the trend as reported for APTES/APTMS modified silica gels with PAN and Acac (Ramasamy, Repo et al., 2017), CL-Zn/Al LDH (Iftekhar, Srivastava, & Sillanpää, 2017b) and GA-g-PAM/SiO_2 (Iftekhar, Srivastava, Casas, & Sillanpää, 2017) toward REEs. The adsorption at pH above 6 was not studied due to the precipitation of REEs as hydroxides. The adsorption efficiency was lowest at pH 2 (Fig. 3b), due to competition of H^+ ions with REEs (Sc, Nd, Tm, Yb) over the Zr@XG-ZA reducing the adsorption. This behavior may instigate the regeneration approach of used Zr@XG-ZA by using acidic media. In addition, the removal of REEs with pH is related with the zeta potential of Zr@XG-ZA. When the solution pH is less than pH_{zpc}, the surface of Zr@XG-ZA carries positive charge and vice versa. The pH_{zpc} value for Zr@XG-ZA is 3.2 (Fig. 3c). Zr@XG-ZA showed increase in removal with increasing pH of solution due to the negative surface potential, which enhances the electrostatic interaction between positively charged REEs and surface of adsorbent. In case of Nd and Yb, the removal efficiency reaches the maximum at pH 4 attaining the maximum adsorption while for Sc and Tm the removal keeps on increasing upto pH 6.

3.4. Effect of temperature

The effect of temperature was studied from 25 to 55 °C (Fig. 3d). It is shown that with increase in temperature, the removal of Sc, Nd, Tm, Yb increases significantly, suggesting the process of adsorption on Zr@XG-ZA is endothermic (Zhao et al., 2017). The most influential response of rise in temperature was observed in case of Nd where the removal efficiency increased from 61% to 91%. On the other hand, Sc seems to be the least affected among others. Ramasamy, Khan et al. (2017) reported similar results (Ramasamy, Repo et al., 2017). Acceleration of sorption process, formation of new active or binding sites and transport against concentration gradient or diffusion across the energy barrier might be the phenomena responsible for increase in sorption capacity with increasing temperature (Saeed, Saeed, Ahmed, & Ahmed, 2005).

To explain spontaneity of process, randomness of adsorbate-adsorbent system and endothermic/exothermic nature of adsorption process investigation of thermodynamic parameters viz. changes of Gibbs free energy (ΔG^0), enthalpy (ΔH^0), and entropy (ΔS^0) is very important. The thermodynamic parameters can be calculated from following equations;

$$\ln\ K_C = \frac{\Delta S^0}{R} - \frac{\Delta H^0}{RT} \tag{2}$$

$$\Delta G^0 = -RT \ln\ K_C \tag{3}$$

Where; K_c is thermodynamic equilibrium constant (L/g), R is universal gas constant (8.314 J/mol/K), T is temperature (K), ΔG^0 is Gibbs free energy (kJ/mol), ΔS^0 is entropy (J/mol/K) and ΔH^0 is enthalpy (kJ/mol) (Naushad, Vasudevan, Sharma, Kumar, & ALOthman, 2016; Yanfei, Huang, Zhiqi, Zongyu, & Liangshi, 2016). The values of ΔG^0, ΔH^0 and ΔS^0 thermodynamic parameters are shown in Table S2. Negative values of ΔG^0 indicates the feasibility of Sc, Nd, Tm, Yb removal and suggests the spontaneous nature of adsorption on Zr@XG-ZA. The positive values of the entropy change (ΔS^0) suggests about the randomness at the solid-liquid interface which increases during the adsorption of Sc, Nd, Tm, Yb on Zr@XG-ZA. Additionally, positive values of ΔH^0 indicates that the adsorption process was endothermic. The REE adsorption onto PEI-CNC (Zhao et al., 2017), hydroxyapatite (Granados-Correa, Vilchis-Granados, Jiménez-Reyes, & Quiroz-Granados, 2012), Fe_3O_4/chitosan nanocomposite (Ashour, Abdel-

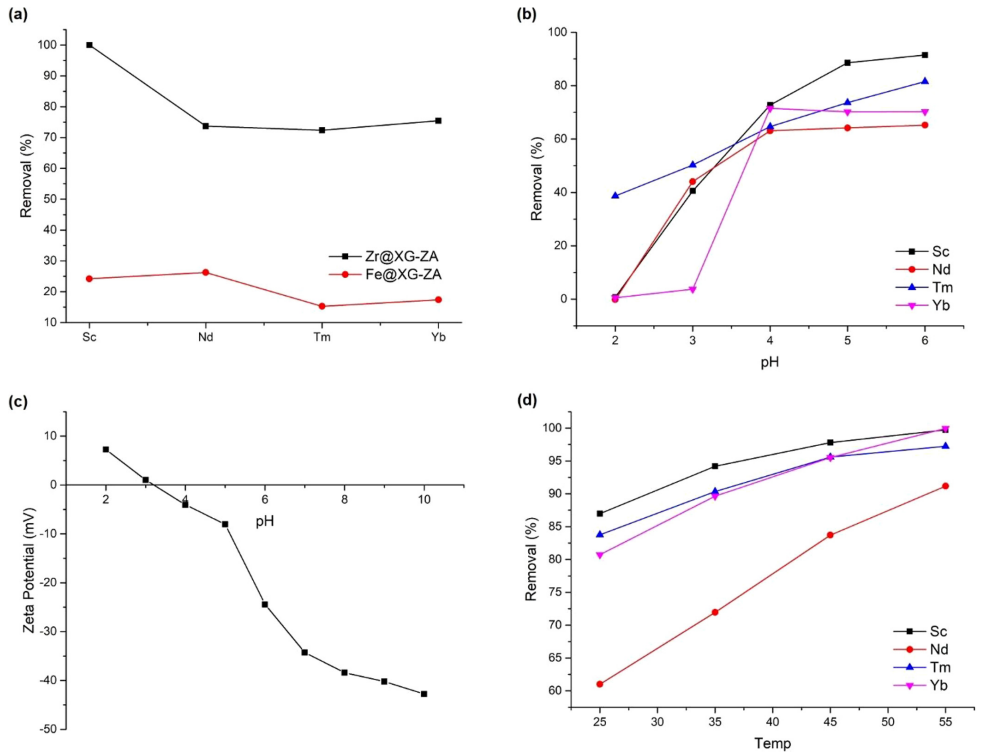

Fig. 3. (a) Adsorptive behavior of Fe@XG-ZA and Zr@XG-ZA for Sc, Nd, Tm, Yb; (b) Adsorptive behavior of Sc, Nd, Tm, Yb as a function of pH on Zr@XG-ZA (Experimental conditions: conc. of REEs = 25 mg/L, dosage = 3 g/L, contact time = 3 h, working volume = 10 mL); (c) Zeta potential of Zr@XG-ZA; (d) as a function of temperature on Zr@XG-ZA.

Table 1
Kinetics model parameters for adsorption of Sc, Nd, Tm, Yb on Zr@XG-ZA.

Models	Model Parameters	Sc	Nd	Tm	Yb
Pseudo first order	$q_{e,exp}$ (mg/g)	9.18	7.37	8.89	7.41
	$q_{e,cal}$ (mg/g)	9.15	7.07	8.85	7.40
	k_1 (min^{-1})	0.13	0.08	0.14	0.11
	R^2	0.98	0.97	0.99	0.98
Pseudo second order	$q_{e,exp}$ (mg/g)	9.18	7.37	8.89	7.41
	$q_{e,cal}$ (mg/g)	4.29	4.11	3.94	3.79
	k_2 ($g\,mg^{-1}\,min^{-1}$)	1.94×10^{-2}	1.23×10^{-2}	2.18×10^{-2}	1.59×10^{-2}
	R^2	0.96	0.94	0.96	0.95

Magied, Abdel-Khalek, Helaly, & Ali, 2016; Galhoum et al., 2015) and CLN/SiO_2 (Iftekhar et al., 2017a) was also found to be endothermic in nature.

3.5. Adsorption kinetics

The influence of contact time on Sc, Nd, Tm and Yb over Zr@XG-ZA was studied according to the experimental conditions illustrated earlier. As known, the rate of adsorption at very initial stages was higher due to availability of greater number of adsorption sites. The behavior of Sc, Nd, Tm, Yb on Zr@XG-ZA followed the same trend. It can be seen from Fig. S5a that Sc has the higher adsorption efficiency. A removal of 87% was recorded in 30 min of contact time for Sc. The smaller atomic radius might be responsible for rapid adsorption as reported earlier (Pniok et al., 2014; Ramasamy, Repo et al., 2017). Nd depicts the increase in adsorption over time and equilibrium was attained in 80 min. Moreover, to elucidate the adsorption rate and rate limiting steps; the pseudo first-order (PS1) (Hammouda et al., 2017; Lagergren, 1898; Srivastava & Sillanpää, 2017), pseudo second-order (PS2) (Ho & McKay, 1999) and intra particle diffusion models (Wang et al., 2014; Weber & Morris, 1963) were used to fit the kinetic data. The kinetic models used are given by:

$$q_t = q_e(1 - \exp(-k_1 t)) \quad (4)$$

$$q_t = \frac{(t.\ k_2.\ q_e^2)}{(1 + (t.\ k_2.\ q_e))} \quad (5)$$

where t is time (min); q_e and q_t are adsorption capacity at equilibrium and at time t (mg/g), respectively; k_1 (min^{-1}) and k_2 (g/mg min^{-1}) are rate constants for pseudo first order and second order, respectively. The correlation coefficient R^2 and the parameters of kinetic models are presented in Table 1. The fitting results of REEs adsorption on Zr@XG-ZA followed PS1 with a higher value of correlation coefficient (R^2) compared to PS2. Similarly, the adsorption capacity of REEs at equilibrium estimated from PS1 equation (Eq. (4)) agreed with the experimental data.

Furthermore, intra-particle diffusion model was used to investigate the contribution of steps involved in the adsorption process viz intra-particle diffusion and film diffusion. Following Weber–Morris equation (Wang et al., 2014; Weber & Morris, 1963) (Eq. (6)) for intra-particle diffusion was applied on the kinetic data:

$$q_t = k_i t^{1/2} + C \quad (6)$$

where q_t is the adsorption capacity at time t (mg/g), k_i is the intra-particle diffusion rate constant and C is a constant which is related to the boundary layer effects. The linear fitting of experimental data to (Eq. (6)) indicates that the adsorption process is only controlled by intra-particle diffusion. As shown in Fig. S5c, the three linear regions attributed that diffusion of Nd occurred by three steps viz. external film or boundary layer diffusion, macropore and micropore diffusion. On the other hand, the absence of second linear region in the plots of Sc, Tm and Yb signifies that macropore diffusion is practically negligible. In addition, as the linear plots does not pass through origin indicating that film diffusion is the rate limiting step. Thus, based on results of kinetic modeling, it was concluded that diffusion affected the REE adsorption by Zr@XG-ZA.

3.6. Adsorption isotherms

To elucidate the adsorption performance of Zr@XG-ZA Langmuir and Freundlich models were employed (Iftekhar, Farooq, Sillanpää, Asif, & Habib, 2017; Mushtaq, Bhatti, Iqbal, & Noreen, 2016; Yanfei et al., 2016; Zhu, Wang, Zheng, Wang, & Wang, 2016). The equations are given below;

$$q_e = \frac{K_L Q_0 C_e}{1 + K_L C_e} \quad (7)$$

$$q_e = K_f C_e^{\frac{1}{n}} \quad (8)$$

Where q_e and Q_0 are the equilibrium adsorption capacity and the maximum adsorption capacity (mg/g), respectively; C_e is equilibrium concentration of REE ions (mg/L); K_L, K_f and 1/n are empirical constants. The different isotherm constants of Langmuir and Freundlich isotherm are summarized in Table 2 and the obtained straight lines are shown in Fig. S5d. Among two mentioned isotherm models used, Freundlich model was found to be suitable for describing isotherm data for Sc, Nd, Tm, Yb onto Zr@XG-ZA with higher correlation coefficient value (R^2 = 0.98–0.99) than the Langmuir model (0.57–0.96). Further, the n values obtained was higher than unity indicating that the REEs adsorption on Zr@XG-ZA surface was heterogeneous. This is in agreement with the experimental results for adsorbent having different functional groups on the surface. Notably, the maximum adsorption capacities of examined REEs followed the order: Sc > Yb > Tm > Nd. This could be elucidated that ionic radii follows the order Nd (0.995 Å) > Tm (0.869 Å) > Yb (0.858 Å) > Sc (0.745 Å) (Wu et al., 2012); where smaller ionic radii has better adsorbing capacity (Moldoveanu & Papangelakis, 2012). For the same reason, in another work La exhibited much lower loading amount in comparison with the Eu and Er in this study, due to its higher ionic radii (1.06 Å) (Zhao et al., 2017).

Table 2
Langmuir and Freundlich isotherm constants for adsorption of Sc, Nd, Tm, Yb on Zr@XG-ZA (Experimental conditions: Dosage = 3 g/L, pH = 4 for -Nd,Yb and 6 for Sc, Tm, contact time = 80 min).

Models	Model Parameters	Sc	Nd	Tm	Yb
Langmuir	Q_0	76.4	38.42	31.98	41.25
	K_L	0.48	1.21	1.51	2.66
	R^2	0.96	0.58	0.75	0.71
Freundlich	n	1.93	1.63	2.47	2.29
	K_F	24.96	1.94	4.93	6.31
	R^2	0.99	0.98	0.99	0.99

Table S3 summarizes the maximum adsorption capacities on Zr@XG-ZA and some previously reported adsorbents. The higher adsorption capacity values of Zr@XG-ZA than those of the most of the reported sorbents except DETA-functionalized chitosan magnetic nano-based particles, suggested that Zr@XG-ZA is a relatively efficient adsorbent for removal of REEs.

3.7. Adsorption of REEs in multicomponent system

The Fig. 4a depicts the influence of pH on REE adsorption over Zr@XG-ZA, executed at an initial pH of 2, 4 and 6 with an initial concentration of 10 mg/L for 60 min. In general, increase in pH increases the adsorption efficiency for all REEs under consideration. At pH 2, poor adsorption was observed for all REEs, however, due to competitive adsorption between REEs the adsorption efficiency was slightly higher compared to the single component system. The adsorption in acidic pH regime might be due to xanthan units. Sc demonstrate higher adsorption at pH 4 and 6 compared to Nd, Tm and Yb. Further, it was noticed that in multicomponent system the overall removal of REEs on Zr@XG-ZA is higher than single system and the REEs followed the order: Sc > Yb > Tm > Nd which also complement steric hindrance effect that smaller ionic radii show better adsorbing power exhibiting stronger electrostatic interaction (Moldoveanu & Papangelakis, 2012). The same fact was also observed when influence of contact time on REEs in multicomponent system was investigated as shown in Fig. 4b. In addition, 60 min of contact time seems to be sufficient to have almost 100% removal for REEs.

To study the effect of temperature in multicomponent system, the experiments were conducted from 25 to 55 °C and the observations are plotted in Fig. 4c. Sc appears to be least sensitive with almost negligible impact with rise in temperature conversely; at room temperature, the removal was higher than other REEs. Ramasamy, Puhakka et al. (2017) reported the same in work (Ramasamy, Puhakka et al., 2017). However, an increase in temperature has positive impact on REE removal especially for Nd. At 25 °C, Tm and Yb has higher removal, whereas the affinity shifted towards Nd at 35 °C with higher adsorption compare to Tm and Yb. It can be clearly seen that the adsorption of Nd improves significantly with the increase in temperature.

The REE adsorption was conducted at 25 °C for 30 min to understand the effect of initial concentration, the results of which are illustrated in Fig. 4d. At the concentration of 1 mg/L, Sc and Nd showed greater affinity than Tm and Yb. However, with the increase in concentration to 2.5 mg/L there is an increment in removal Tm and Yb and is only slightly higher in % than Nd removal. With further increase in concentration to 5 and 10 mg/L, the trend shifted towards Tm and Yb. This result also complement the findings of previous study performed on SEP and SEA for LREEs and HREEs (Ramasamy, Puhakka et al., 2017). As the adsorption experiments were carried out in aqueous system comprising same concentrations of Sc, Nd, Tm, Yb, hence, for REE adsorption in multicomponent system, three possible cases may occur:

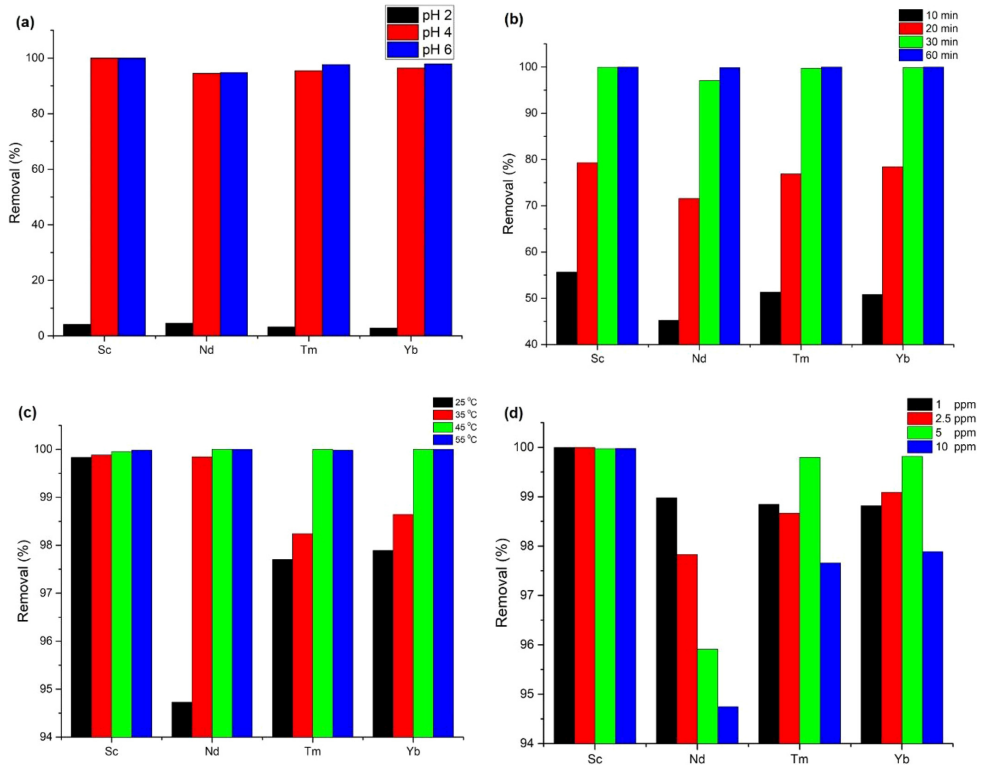

Fig. 4. Adsorption efficiency of REE adsorbed on Zr@XG-ZA as a function of (a) pH, (b) contact time, (c) temperature, (d) concentration in a multi-component system.

Case I	$\frac{q_{mult.}}{q_{single}} > 1$	Synergistic effect, enhanced in the presence of other REEs
Case II	$\frac{q_{mult.}}{q_{single}} = 1$	No interaction in the presence of other REEs
Case III	$\frac{q_{mult.}}{q_{single}} < 1$	Competitive effect, inhibited in the presence of other REEs

In this study, the values of q_{multi}/q_{single} calculated were less than 1, revealing that adsorption of Sc, Nd, Tm and Yb was barred by the presence of other REEs. Among them, the value of Sc (0.21) was lower than that of Nd (0.27), Tm (0.28) and Yb (0.28) indicating a more significant competitive effect on Sc in a multi-component mixture. This can be explained by the fact that metals from the same class has strongest ionic competition (Pearson law) (Pearson, 1963) where the REEs under consideration are classified as hard metals (Zhao et al., 2015).

3.8. Adsorption mechanism

The mechanism that might involve in the adsorption process are: (a) electrostatic interactions between carboxylic, hydroxyl groups and REE ions at higher pH (b) ion exchange and (c) complexation/coordination mechanism between O− groups and REE cations. Based on the results of isoelectric point, pH, FTIR (Fig. S6a), SEM and EDS (Fig. S6b–i), a proposed schematic representation of the adsorption mechanisms is shown in Scheme 2. The electrostatic interaction might be considered as one of the adsorption process when the surface of Zr@XG-ZA becomes negative at pH > 3.2 resulting in electrostatic interaction toward REEs. The band at 1706 cm^{-1} (carboxylate) disappeared indicating that the particular functional groups act as active sites for REEs adsorption. Additionally, in all the four cases the peaks shifted toward lower wave number. This can be attributed to the electrostatic attraction with $-COO^-$ or −OH groups and surface complexation/chelation of the adjacent −OH groups with REE ions. The mechanism of chelation of REEs with the hydrous oxide surfaces involves an ion exchange process in which the adsorbed cations replace bound protons (Swain, Mishra, & Devi, 2017) as shown in Scheme 2. The Zr@XG-ZA loaded SEM images of Sc, Nd, Tm and Yb illustrated that after adsorption of Sc, Nd, Tm and Yb, the surface morphology changes by vanishing the scute structure. The appearance of REE peaks in EDX spectra further confirms the adsorption onto Zr@XG-ZA. Moreover, the colorful elemental mapping (Fig. S7a–d) illustrates the uniform distribution of REEs on fabricated nanocomposite.

3.9. Regeneration and reusability

To investigate the reusability of nanocomposite, REE loaded Zr@XG-ZA was regenerated using 0.1 mol/L HNO_3. The regeneration efficiency was highest during the first cycle and decreased upto 50% after

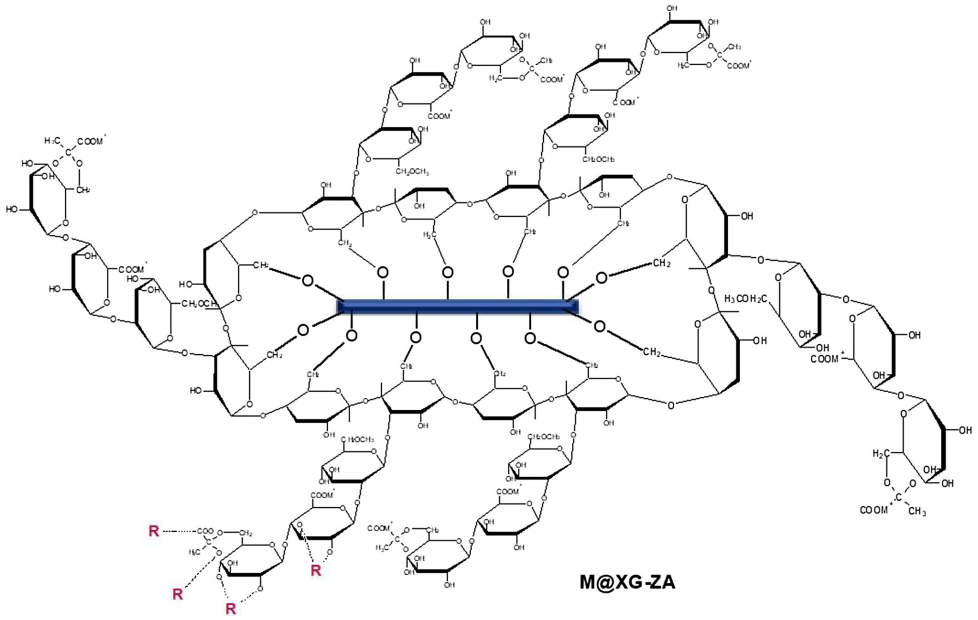

Scheme 2. Binding mechanism of REEs with Zr@XG-ZA.

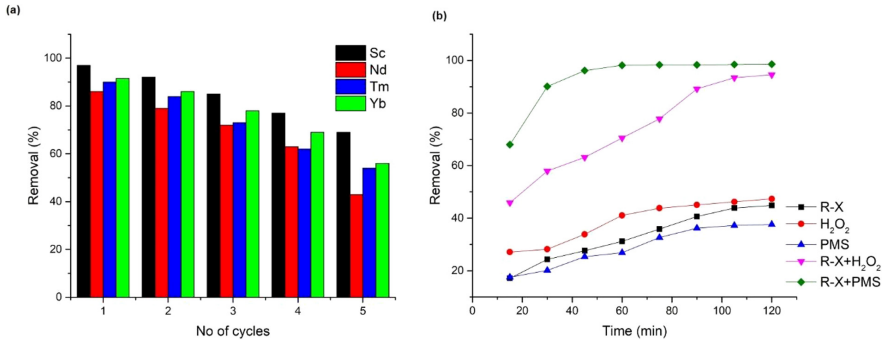

Fig. 5. Adsorption-desorption cycles of Sc, Nd, Tm, Yb onto Zr@XG-ZA (a); Reusability of R-X as a photocatalyst for the of TC (b) (Experimental conditions: R-X dose = 0.1 g/L, natural pH, working volume = 100 mL, [H_2O_2] = 20 mM, [PMS] = 1 mM, [TC] = 20 mg/L).

fifth cycle. The possible reason for decrease in removal of REEs after each cycle might be due to hydraulic shear force in adsorption process, which damage the Zr@XG-ZA surface ultimately reducing the availability of adsorption sites. It was also noticed that during desorption dissociation of LDH occurred in form of Zn leaching and therefore the adsorption decreases in each cycle (Table S4). After five cycles, a part of REEs was still present on surface of nanocomposite, which play a role to enhance the catalytic activity of nanocomposites. Thus, the leftover Zr@XG-ZA nanocomposite denoted by R-X (REE-loaded-nanocomposite) was collected and used as a photocatalyst for degradation of tetracycline. Without pH adjustment, experiments were also performed without addition of oxidants to check the possibility of adsorption of TC on R-X. The adsorption affinity of TC over R-X is very low and addition of oxidant enhances the removal of TC (Fig. 5b). Thus, after using the fabricated Zr@XG-ZA for REEs removal, the material can further used as photocatalyst for the degradation of tetracycline.

4. Conclusion

A novel and environmentally friendly bifunctional nanocomposite was synthesized by encapsulating ZA (inorganic matrix) in XG anchored by Fe and Zr. The Zr@XG-ZA exhibited good absorptivity toward Sc, Nd, Tm and Yb and the maximum adsorption capacities were 132.30, 14.01, 18.15 and 25,73 mg/g, respectively. The adsorption was found

to be heterogeneous and endothermic in nature. Both chemisorption and diffusion affected the REE adsorption by Zr@XG-ZA. In multi-component system, the overall removal of REEs on Zr@XG-ZA is higher than single system and the REEs followed the order: Sc > Yb > Tm > Nd. The SEM image of Zr@XG-ZA demonstrate scutes structure, which disappeared after adsorption of REEs. In addition, absence of carboxylate and nitrile functional group act as active sites for adsorption of REEs. Additionally, the nanocomposite showed promising results in degradations of tetracycline as a photocatalyst. It is believed that synthesis of hybrid nanocomposite by incorporation of organic-inorganic matrices can be widened to synthesize a wide variety of bifunctional materials for several applications.

Acknowledgement

The authors are grateful to Nida Iftikhar for assistance with some figures.

Appendix A. Supplementary data

Supplementary data associated with this article can be found, in the online version, at https://doi.org/10.1016/j.carbpol.2018.04.054.

References

Ashour, R. M., Abdel-Magied, A. F., Abdel-Khalek, A. A., Helaly, O., & Ali, M. (2016). Preparation and characterization of magnetic iron oxide nanoparticles functionalized by l-cysteine: Adsorption and desorption behavior for rare earth metal ions. *Journal of Environmental Chemical Engineering, 4*(3), 3114–3121.

Bonificio, W. D., & Clarke, D. R. (2016). Rare-earth separation using bacteria. *Environmental Science & Technology Letters, 3*(4), 180–184.

Bueno, V. B., Bentini, R., Catalani, L. H., Barbosa, L. R., & Petri, D. F. S. (2014). Synthesis and characterization of xanthan–hydroxyapatite nanocomposites for cellular uptake. *Materials Science and Engineering: C, 37*, 195–203.

Crini, G., & Badot, P.-M. (2008). Application of chitosan, a natural aminopolysaccharide, for dye removal from aqueous solutions by adsorption processes using batch studies: A review of recent literature. *Progress in Polymer Science, 33*(4), 399–447.

Darder, M., López-Blanco, M., Aranda, P., Leroux, F., & Ruiz-Hitzky, E. (2005). Bio-nanocomposites based on layered double hydroxides. *Chemistry of Materials, 17*(8), 1969–1977.

Darzi, H. H., Larimi, S. G., & Darzi, G. N. (2012). Synthesis, characterization and physical properties of a novel xanthan gum/polypyrrole nanocomposite. *Synthetic Metals, 162*(1), 236–239.

Dupont, D., & Binnemans, K. (2015). Rare-earth recycling using a functionalized ionic liquid for the selective dissolution and revalorization of Y 2 O 3: Eu 3+ from lamp phosphor waste. *Green Chemistry, 17*(2), 856–868.

Fujita, Y., Barnes, J., Eslamimanesh, A., Lencka, M. M., Anderko, A., Riman, R. E., & Navrotsky, A. (2015). Effects of simulated rare earth recycling wastewaters on biological nitrification. *Environmental Science & Technology, 49*(16), 9460–9468.

Galhoum, A. A., Mafhouz, M. G., Abdel-Rehem, S. T., Gomaa, N. A., Atia, A. A., Vincent, T., & Guibal, E. (2015). Cysteine-functionalized chitosan magnetic nano-based particles for the recovery of light and heavy rare earth metals: Uptake kinetics and sorption isotherms. *Nanomaterials, 5*(1), 154–179.

Ghorai, S., Sinhamahpatra, A., Sarkar, A., Panda, A. B., & Pal, S. (2012). Novel biodegradable nanocomposite based on XG-g-PAM/SiO 2: Application of an efficient adsorbent for Pb 2+ ions from aqueous solution. *Bioresource Technology, 119*, 181–190.

Granados-Correa, F., Vilchis-Granados, J., Jiménez-Reyes, M., & Quiroz-Granados, L. (2012). Adsorption behaviour of La (III) and Eu (III) ions from aqueous solutions by hydroxyapatite: Kinetic, isotherm, and thermodynamic studies. *Journal of Chemistry, 2013*.

Hammouda, S. B., Zhao, F., Safaei, Z., Srivastava, V., LakshmiRamasamy, D., Iftekhar, S., & Sillanpää, M. (2017). Degradation and mineralization of phenol in aqueous medium by heterogeneous monopersulfate activation on nanostructured cobalt based-perovskite catalysts ACoO 3 (A = La, Ba, Sr and Ce): Characterization, kinetics and mechanism study. *Applied Catalysis B: Environmental, 215*, 60–73.

Ho, Y.-S., & McKay, G. (1999). Pseudo-second order model for sorption processes. *Process Biochemistry, 34*(5), 451–465.

Hong, G., Wang, M., Li, X., Shen, L., Wang, X., Zhu, M., & Hsiao, B. S. (2015). Micro-nano structure nanofibrous p-sulfonatocalix [8] arene complex membranes for highly efficient and selective adsorption of lanthanum (III) ions in aqueous solution. *RSC Advances, 5*(27), 21178–21188.

Humphries, M. (2010). *Rare earth elements: The global supply chain.* DIANE Publishing.

Humphries, M. (2012). *Rare earth elements: The global supply chain.* Congressional Research Service7–5700 2011.

Iftekhar, S., Farooq, M. U., Sillanpää, M., Asif, M. B., & Habib, R. (2017). Removal of Ni (II) using multi-walled carbon nanotubes electrodes: Relation between operating parameters and capacitive deionization performance. *Arabian Journal for Science and Engineering, 42*(1), 235–240.

Iftekhar, S., Srivastava, V., Casas, A., & Sillanpää, M. (2017). Synthesis of novel GA-g-PAM/SiO 2 nanocomposite for the recovery of rare earth elements (REE) IONS from aqueous solution. *Journal of Cleaner Production*.

Iftekhar, S., Srivastava, V., & Sillanpää, M. (2017a). Enrichment of lanthanides in aqueous system by cellulose based silica nanocomposite. *Chemical Engineering Journal, 320*, 151–159.

Iftekhar, S., Srivastava, V., & Sillanpää, M. (2017b). Synthesis and application of LDH intercalated cellulose nanocomposite for separation of rare earth elements (REEs). *Chemical Engineering Journal, 309*, 130–139.

Katzbauer, B. (1998). Properties and applications of xanthan gum. *Polymer Degradation and Stability, 59*(1–3), 81–84.

Kim, D., Powell, L. E., Delmau, L. H., Peterson, E. S., Herchenroeder, J., & Bhave, R. R. (2015). Selective extraction of rare earth elements from permanent magnet scraps with membrane solvent extraction. *Environmental Science & Technology, 49*(16), 9452–9459.

Lagergren, S. (1898). *About the theory of so-called adsorption of soluble substances*.

Latterini, L., Elisei, F., Aloisi, G., Costantino, U., & Nocchetti, M. (2002). Space-resolved fluorescence properties of phenolphthalein-hydrotalcite nanocomposites. *Physical Chemistry Chemical Physics, 4*(12), 2792–2798.

Leroux, F., & Besse, J.-P. (2001). Polymer interleaved layered double hydroxide: A new emerging class of nanocomposites. *Chemistry of Materials, 13*(10), 3507–3515.

Li, H., Shan, C., Zhang, Y., Cai, J., Zhang, W., & Pan, B. (2016). Arsenate adsorption by hydrous ferric oxide nanoparticles embedded in cross-linked anion exchanger: Effect of the host pore structure. *ACS Applied Materials & Interfaces, 8*(5), 3012–3020.

Maes, S., Zhuang, W.-Q., Rabaey, K., Alvarez-Cohen, L., & Hennebel, T. (2017). Concomitant leaching and electrochemical extraction of rare earth elements from monazite. *Environmental Science & Technology, 51*(3), 1654–1661.

Mittal, H., Parashar, V., Mishra, S., & Mishra, A. (2014). Fe 3 O 4 MNPs and gum xanthan based hydrogels nanocomposites for the efficient capture of malachite green from aqueous solution. *Chemical Engineering Journal, 255*, 471–482.

Moldoveanu, G. A., & Papangelakis, V. G. (2012). Recovery of rare earth elements adsorbed on clay minerals: I. Desorption mechanism. *Hydrometallurgy, 117*, 71–78.

Moriwaki, H., Masuda, R., Yamazaki, Y., Horiuchi, K., Miyashita, M., Kasahara, J., ... Yamamoto, H. (2016). Application of freeze-dried powders of genetically engineered microbial strains as adsorbents for rare earth metal ions. *ACS Applied Materials & Interfaces, 8*(40), 26524–26531.

Mushtaq, M., Bhatti, H. N., Iqbal, M., & Noreen, S. (2016). Eriobotrya japonica seed biocomposite efficiency for copper adsorption: Isotherms, kinetics, thermodynamic and desorption studies. *Journal of Environmental Management, 176*, 21–33.

Naushad, M., Vasudevan, S., Sharma, G., Kumar, A., & ALOthman, Z. (2016). Adsorption kinetics, isotherms, and thermodynamic studies for Hg2+ adsorption from aqueous medium using alizarin red-S-loaded amberlite IRA-400 resin. *Desalination and Water Treatment, 57*(39), 18551–18559.

Park, D. M., Reed, D. W., Yung, M. C., Eslamimanesh, A., Lencka, M. M., Anderko, A., ... Jiao, Y. (2016). Bioadsorption of rare earth elements through cell surface display of lanthanide binding tags. *Environmental Science & Technology, 50*(5), 2735–2742.

Pearson, R. G. (1963). Hard and soft acids and bases. *Journal of the American Chemical Society, 85*(22), 3533–3539.

Pniok, M., Kubíček, V., Havlíčková, J., Kotek, J., Sabatie-Gogová, A., Plutnar, J., ... Hermann, P. (2014). Thermodynamic and kinetic study of scandium (III) complexes of DTPA and DOTA: A step toward scandium radiopharmaceuticals. *Chemistry-A European Journal, 20*(26), 7944–7955.

Pongjanyakul, T., & Puttipipatkhachorn, S. (2007). Xanthan–alginate composite gel beads: Molecular interaction and in vitro characterization. *International Journal of Pharmaceutics, 331*(1), 61–71.

Ramasamy, D. L., Khan, S., Repo, E., & Sillanpää, M. (2017). Synthesis of mesoporous and microporous amine and non-amine functionalized silica gels for the application of rare earth elements (REE) recovery from the waste water-understanding the role of pH, temperature, calcination and mechanism in Light REE and Heavy REE separation. *Chemical Engineering Journal, 322*, 56–65.

Ramasamy, D. L., Puhakka, V., Repo, E., Khan, S., & Sillanpää, M. (2017). Coordination and silica surface chemistry of lanthanides (III), scandium (III) and yttrium (III) sorption on 1-(2-pyridylazo)-2-napththol (PAN) and acetylacetone (acac) immobilized gels. *Chemical Engineering Journal, 324*, 104–112.

Ramasamy, D. L., Puhakka, V., Iftekhar, S., Wojtuś, A., Repo, E., Hammouda, S. B., ... Sillanpää, M. (2018). N-and O-ligand doped mesoporous silica-chitosan hybrid beads for the efficient, sustainable and selective recovery of rare earth elements (REE) from acid mine drainage (AMD): Understanding the significance of physical modification and conditioning of the polymer. *Journal of Hazardous Materials, 348*, 84–91.

Ramasamy, D. L., Puhakka, V., Repo, E., & Sillanpää, M. (2018). Selective separation of scandium from iron, aluminium and gold rich wastewater using various amino and non-amino functionalized silica gels–A comparative study. *Journal of Cleaner Production, 170*, 890–901.

Ramasamy, D. L., Repo, E., Srivastava, V., & Sillanpää, M. (2017). Chemically immobilized and physically adsorbed PAN/acetylacetone modified mesoporous silica for the recovery of rare earth elements from the waste water-comparative and optimization study. *Water Research, 114*, 264–276.

Ramasamy, D. L., Wojtuś, A., Repo, E., Kalliola, S., Srivastava, V., & Sillanpää, M. (2017). Ligand immobilized novel hybrid adsorbents for rare earth elements (REE) removal from waste water: Assessing the feasibility of using APTES functionalized silica in the hybridization process with chitosan. *Chemical Engineering Journal, 330*, 1370–1379.

Rives, V. (2002). Characterisation of layered double hydroxides and their decomposition products. *Materials Chemistry and Physics, 75*(1), 19–25.

Rojas, R., Perez, M. R., Erro, E. M., Ortiz, P. I., Ulibarri, M. A., & Giacomelli, C. E. (2009). EDTA modified LDHs as Cu 2+ scavengers: Removal kinetics and sorbent stability. *Journal of Colloid and Interface Science, 331*(2), 425–431.

Sadovsky, D., Brenner, A., Astrachan, B., Asaf, B., & Gonen, R. (2016). Biosorption potential of cerium ions using Spirulina biomass. *Journal of Rare Earths, 34*(6), 644–652.
Saeed, M., Saeed, M., Ahmed, R., & Ahmed, R. (2005). Temperature effected sorption of europium (III) onto 1-(2-pyridylazo)-2-naphthol impregnated polyurethane foam. *Journal of Radioanalytical and Nuclear Chemistry, 267*(1), 147–153.
Shalviri, A., Liu, Q., Abdekhodaie, M. J., & Wu, X. Y. (2010). Novel modified starch–xanthan gum hydrogels for controlled drug delivery: Synthesis and characterization. *Carbohydrate Polymers, 79*(4), 898–907.
Sharma, G., Kumar, D., Kumar, A., Ala'a, H., Pathania, D., Naushad, M., & Mola, G. T. (2017). Revolution from monometallic to trimetallic nanoparticle composites, various synthesis methods and their applications: A review. *Materials Science and Engineering: C, 71*, 1216–1230.
Sharma, G., Thakur, B., Naushad, M., Kumar, A., Stadler, F. J., Alfadul, S. M., & Mola, G. T. (2017). Applications of nanocomposite hydrogels for biomedical engineering and environmental protection. *Environmental Chemistry Letters,* 1–34.
Srivastava, V., & Sillanpää, M. (2017). Synthesis of malachite@ clay nanocomposite for rapid scavenging of cationic and anionic dyes from synthetic wastewater. *Journal of Environmental Sciences, 51*, 97–110.
Swain, K. K., Mishra, P. M., & Devi, A. P. (2017). Biosorption of Praseodymium (III) using Terminalia arjuna bark powder in batch systems: Isotherm and kinetic studies. *Water Science and Technology* wst2017589.
Vijayaraghavan, K., & Balasubramanian, R. (2010). Single and binary biosorption of cerium and europium onto crab shell particles. *Chemical Engineering Journal, 163*(3), 337–343.
Wang, P., Cao, M., Wang, C., Ao, Y., Hou, J., & Qian, J. (2014). Kinetics and thermodynamics of adsorption of methylene blue by a magnetic graphene-carbon nanotube composite. *Applied Surface Science, 290*, 116–124.
Weber, W. J., & Morris, J. C. (1963). Kinetics of adsorption on carbon from solution. *Journal of the Sanitary Engineering Division, 89*(2), 31–60.
Wu, D., Zhu, C., Chen, Y., Zhu, B., Yang, Y., Wang, Q., & Ye, W. (2012). Preparation, characterization and adsorptive study of rare earth ions using magnetic GMZ bentonite. *Applied Clay Science, 62*, 87–93.
Yanfei, X., Huang, L., Zhiqi, L., Zongyu, F., & Liangshi, W. (2016). Adsorption ability of rare earth elements on clay minerals and its practical performance. *Journal of Rare Earths, 34*(5), 543–548.
Zhang, S., Xu, F., Wang, Y., Zhang, W., Peng, X., & Pepe, F. (2013). Silica modified calcium alginate–xanthan gum hybrid bead composites for the removal and recovery of Pb (II) from aqueous solution. *Chemical Engineering Journal, 234*, 33–42.
Zhao, F., Repo, E., Sillanpää, M., Meng, Y., Yin, D., & Tang, W. Z. (2015). Green synthesis of magnetic EDTA-and/or DTPA-cross-linked chitosan adsorbents for highly efficient removal of metals. *Industrial & Engineering Chemistry Research, 54*(4), 1271–1281.
Zhao, F., Repo, E., Song, Y., Yin, D., Hammouda, S. B., Chen, L., ... Sillanpää, M. (2017). Polyethylenimine-cross-linked cellulose nanocrystals for highly efficient recovery of rare earth elements from water and a mechanism study. *Green Chemistry, 19*(20), 4816–4828.
Zhu, Y., Wang, W., Zheng, Y., Wang, F., & Wang, A. (2016). Rapid enrichment of rare-earth metals by carboxymethyl cellulose-based open-cellular hydrogel adsorbent from HIPEs template. *Carbohydrate Polymers, 140*, 51–58.

Publication VI

Iftekhar, S., Ramasamy, D. L., Srivastava, V., Asif, M. B., and Sillanpää, M.

Understanding the factors affecting the adsorption of Lanthanum using different adsorbents: A critical review

Reprinted with permission from
Chemosphere
Vol. 204, pp. 413-430, 2018

Chemosphere 204 (2018) 413–430

Contents lists available at ScienceDirect

Chemosphere

journal homepage: www.elsevier.com/locate/chemosphere

Review

Understanding the factors affecting the adsorption of Lanthanum using different adsorbents: A critical review

Sidra Iftekhar [a, *], Deepika Lakshmi Ramasamy [a], Varsha Srivastava [a], Muhammad Bilal Asif [b], Mika Sillanpää [a, c]

[a] Department of Green Chemistry, School of Engineering Science, Lappeenranta University of Technology, Sammonkatu 12, FI-50130 Mikkeli, Finland
[b] Strategic Water Infrastructure Laboratory, School of Civil, Mining and Environmental Engineering, University of Wollongong, Wollongong NSW 2522, Australia
[c] Department of Civil and Environmental Engineering, Florida International University, Miami, FL 33174, USA

HIGHLIGHTS

- Highlights of process parameters using conventional batch assays for La.
- Statistical analysis of process parameters for La adsorption by various adsorbents.
- Knowledge of adsorption isotherm, kinetics and thermodynamics and desorption for La.
- Mechanism for hydroxyl, carboxyl, amine and phosphoryl groups was proposed.

ARTICLE INFO

Article history:
Received 6 March 2018
Received in revised form
8 April 2018
Accepted 10 April 2018
Available online 12 April 2018

Handling Editor: Y. Yeomin Yoon

Keywords:
Lanthanum
Adsorption kinetics
Isotherm
Thermodynamics
Adsorption mechanism
Operating parameters

ABSTRACT

Over the past few decades, removal and recovery of Lanthanum (La) have received great attention due to its significance in different industrial processes. In this review, the application of various adsorbents viz. biosorbents, commercial and hybrid materials, nanoparticles, nanocomposites etc. have been summarized in terms of the removal and recovery of La. The influence of various operating parameters including pH, dosage, contact time, temperature, coexisting ions, adsorption kinetics, isotherm and thermodynamics were investigated. Statistical analysis of the obtained data revealed that 60% and 70% of the authors reported an optimum pH of 4–6 and a dose of 1–2 g/L, respectively. It can be concluded on the basis of an extensive literature survey that the adsorbent materials (especially hybrids nanocomposites) containing carboxyl, hydroxyl and amine groups offered efficient La removal over a wide range of pH with higher adsorption capacity as compared to other adsorbents (e.g., biosorbents and magnetic adsorbents). Also, in most cases, equilibrium and kinetics were followed by Langmuir and pseudo second-order model and adsorption was endothermic in nature. To evaluate the adsorption efficiency of several adsorbents towards La, desorption and regeneration of adsorbents should be given due consideration. The main objective of the review is to provide an insight into the important factors that may affect the recovery of La using various adsorbents.

Contents

* Corresponding author.
E-mail addresses: sidra.iftekhar@lut.fi, sidra_iftekhar@yahoo.com (S. Iftekhar).

https://doi.org/10.1016/j.chemosphere.2018.04.053
0045-6535/

1. Introduction

Rare earth elements (REEs) consist of 17 elements with 15 lanthanides and two pseudo lanthanides (Sc and Y) (Vijayaraghavan and Balasubramanian, 2010; Sadovsky et al., 2016; Iftekhar et al., 2017d; c; Jacinto et al., 2018). Based on their atomic number, REEs can be further sub-divided into: (i) light rare earth elements (LREEs) such as La, Ce, Pr, Nd, Pm, Sm, Eu and Gd; and (ii) heavy rare earth elements (HREEs) such as Tb, Dy, Ho, Er, Tm Yb, Lu and Y. The application of REEs, particularly lanthanides, is increasing due to their unique catalytic, magnetic, optical and chemical properties (Tadjarodi et al., 2015; Rahman et al., 2017; Negrea et al., 2018). They are often termed as the "seeds of technology" or "industrial vitamin" due to their extensive use in different fields such as chemical engineering, electronics, metallurgy and medicine (Iftekhar et al., 2017b; Xu et al., 2018). Currently, China, Australia and USA are the leading producers of REEs, with China holding 90–95% of global REE production (Feder and Kramer, 2010; Das and Das, 2013; Anastopoulos et al., 2016; El-Magied et al., 2017). In 2015, the global demand of REEs was 119,650 metric tons per year and is likely to escalate by 5% until 2020 (Zhou et al., 2017). Despite their extensive use, the extent of REE recycling/reuse has been reported to be only 1% in 2011 (Binnemans et al., 2013; Sadovsky et al., 2016; Jacinto et al., 2018). Notably, many countries, which import REEs for manufacturing, have already started looking for an alternative source of these metals, because their availability is prone to become a major concern in near future (Das and Das, 2013; Shaver, 2015). On the other hand, some countries and companies, including Toyota, are trying to secure the mines in Australia, South Africa and Greenland to meet their future demands (Feder and Kramer, 2010; Anastopoulos et al., 2016).

Among REEs, lanthanum (La), a very copious and reactive element has gained special attention due to its unique physico-chemical properties (Das et al., 2014). La is found in the minerals of rare earths such as allanite, monazite, cerite and bastnasite (Awwad et al., 2010). The principle ores consisting of 25% and 38% of La are monazite and bastnasite, respectively. Mischmetals are used in making lighter flints that contains approximately 25% of La (Marwani et al., 2013). Lanthanum is used either in pure form or in combination with other elements for the production of super alloys, catalysts, batteries and ceramics (Tadjarodi et al., 2015; Jacinto et al., 2018). The effluent discharge of these industries (specially from mining activity and ore processing) often contains high concentration of La, which can contaminate the environment and endanger human health being carcinogenic and geno-toxic towards human peripheral blood lymphocytes (Wang et al., 2016b). In addition, due to the accumulation of La in aquatic biota and its toxicity (Chen et al., 2018; Li et al., 2018), scientific community feels the need to develop an effective and economical method for the separation and pre-concentration of La from waste streams. Several methods have been developed for the treatment of La such as membrane separation, ion exchange, chemical precipitation, solvent extraction and adsorption (Ponou et al., 2014; Sadovsky et al., 2016; Zhao et al., 2016a,b; Iftekhar et al., 2017a; Gao et al., 2018). Among these separation methods, adsorption has been reported to be the most efficient, eco-friendly and economical technique for the treatment and recovery of La (Sadovsky et al., 2016). To date, various materials including raw and modified biosorbents (Diniz and Volesky, 2005a; b), nanocomposites (Wu et al., 2013), hybrids (Pal et al., 2012; Zhang et al., 2013), silica-based materials (Tadjarodi et al., 2015), magnetic, inorganic (Rahman et al., 2014) and carbon-based commercial materials (Koochaki-Mohammadpour et al., 2014) have been studied for the recovery of La from the aqueous medium. Excellent reviews on REEs adsorption by different materials have been published in last five years (Das and Das, 2013; Anastopoulos et al., 2016). However, the influence of operating parameters on adsorption along with mechanism of removal has not been comprehensively reviewed. In addition, there is a need to focus on specific REE (e.g., La). Due to its commercial significance, performance of a wide range of adsorbents for the removal of La should be critically analyzed. To date, no other review is available, discussing the removal of La by different adsorbents as a function of various operating parameters.

Therefore, the review mainly consists of four aspects. The main goal of this review is to provide highlights of process parameters that can affect La adsorption. In addition, adsorption isotherm, kinetics and thermodynamics are critically discussed. The third section of the article outline adsorption mechanism of La. Finally, dynamic adsorption of La is reviewed and discussed.

2. Statistical trend of adsorbents

The statistical trends based on the Scopus database of numerous adsorbents studied extensively in the previous years for removal/recovery of REEs and La are illustrated in Fig. 1. This implies that more research is being conducted for the removal/recovery of REEs after 2010, more than half of which is for La. Additionally, a continual increment in the application of nanocomposites and

hybrid materials mostly by improving the properties of naturally occurring biopolymers either by incorporating inorganic matrix or by grafting method is observed in recent years.

3. Insight into the materials for La adsorption

3.1. Biosorbents

Applications of biosorbent for the uptake of La have been studied by many research groups. Majority of the authors studied the potential of biosorbents including *Sargassum fluitans* (Palmieri et al., 2002), brown marine (Vijayaraghavan et al., 2011), fresh water algae (Birungi and Chirwa, 2014), *Pinus brutia* (Kütahyali et al., 2010), *Platanus orientalis* (Sert et al., 2008), leaf powder (Sert et al., 2008; Kütahyali et al., 2010), neem sawdust (Das et al., 2014), fish scale (Das et al., 2014) and peels (Torab-Mostaedi, 2013; Torab-Mostaedi et al., 2015) without any prior treatment. Nevertheless, chemically modified biosorbents were also investigated and were reported to achieve improved La adsorption. For example, *Sargassum polycystum* (Diniz and Volesky, 2005b) and *Sargassum* biomass (Diniz and Volesky, 2005a) were modified with $CaNO_3$, while *agrobacterium sp.* (Shuxia et al., 2011) was chemically modified by HCl and NaOH. In addition, carb shells (Vijayaraghavan et al., 2009) and bamboo charcoal (Qing, 2010) were pretreated with HCl and HNO_3, respectively. AC was prepared from RH (precursor) using one step chemical activation by H_3PO_4 (Awwad et al., 2010). Since biochars appear to be good substitutes of AC, Wang et al. (2016b) investigated the adsorption of La by using pyrolyzing biomass following its modification with ammonium citrate. The ammonium citrate modification resulted in an increase in the surface area of biochar from 1.51 to 76.1 m^2/g (Wang et al., 2016b).

3.2. Hybrids, magnetic, silica based, inorganic nano/composites

Application of hybrid material has gained importance in last few years. The novel production of hybrids materials including organic-organic, organic-inorganic and inorganic-inorganic that have been synthesized at nanoscale interface displays new properties based on the synergic effect of both matrices (Roy et al., 2009). For the preparation of organic-organic hybrids, common methods used are crosslinking and grafting of a monomer on a polymer backbone.

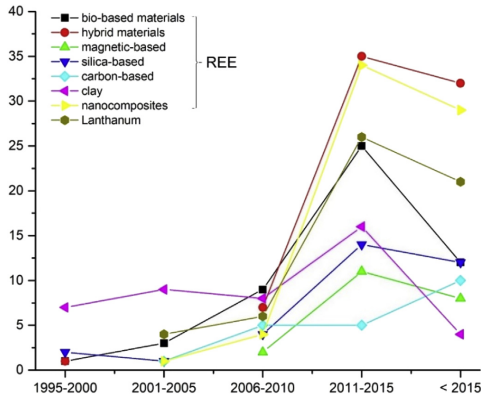

Fig. 1. Annual publication data extracted from Scopus using the keywords: rare earth element, lanthanum, adsorption.

Although the reactivity of some functional groups of polymers (e.g., amines of chitosan) to La following the crosslinking or grafting decreased, it can be compensated by the functional groups of cross linker or grafted monomer (Roy et al., 2009). Hence, the selection of a cross linker or monomer is vital for an effective La adsorption process. Among the literature studied, it was found that authors mainly used "grafting from" approach in which growth of the monomer chain occurred by initiating sites on the polymer backbone. The general mechanism of monomer grafting on polymer backbone by radical generation is shown in Scheme 1. *N,N*-methylenebisacrylamide (MBA) as a monomer was grafted on the cellulose backbone by using ammonium persulfate (APS) and Fenton reagents (ammonium iron sulfate hexahydrate and H_2O_2) as radical initiators (Zhu et al., 2015b, 2016). A combination of ascorbic acid and H_2O_2 was used for the grafting of MBA on the surface of chitosan (Zhu et al., 2015a). Cerium ammonium nitrate was also used as an initiator (Rahman et al., 2017). In addition to the grafting technique, cellulose was cross-linked by using tetraethylenepentaamine (TEPA) and polyethylenimine (PEI) to study its efficacy for La sorption (Tolba et al., 2017; Zhao et al., 2017). The common surface functional groups after crosslinking or grafting were amines (primary, secondary), carboxyl and hydroxyl. Although, the most abundantly occurring biopolymer (*i.e.* cellulose and chitosan) were studied extensively, in one study Gum Arabic (GA) was grafted with polyacrylamide using radical polymerization technique followed by the fusion of silica into grafted copolymers to make it water insoluble (Iftekhar et al., 2017b).

Silica is another common inorganic matrix used for hybridization with organic matrix. The incorporation of SiO_2 in acid (e.g., sulfuric and citric acid) modified cellulose demonstrated different surface area, whereas the particle size was same in both cases (*i.e.*, 9–15 nm) (Iftekhar et al., 2017c). This was attributed to the breakdown of main cellulose chain into many fragments due to sulfuric acid modification, thereby providing more sites to silanes for attachment (Scheme 2). For La recovery and uptake, application of functionalized silica was widely investigated using several ligands including diethylenetriaminepentaacetic dianhydride (DTPADA), phosphonoacetic acid (PAA), *N,N*-bis(phosphonomethyl)gylcine (BPG), 1- (2-Pyridylazo) 2-naphthol (PAN) and acetyl acetone (Acac), polyacrylic acid (PAA), 2-acrylamido 2-methyl propane sulfonic acid (AMPS) and *N*-(2-hydroxyrthyl) salicylaldimine (Borai et al., 2015; Tadjarodi et al., 2015; Ramasamy et al., 2017c; Callura et al., 2018). On the other hand, chemical immobilization and physically adsorbed amine (*N*–) and non-amine (O–) ligand groups were used for functionalization of silica. Ramasamy et al. (2017b) estimated that the cost of modified silica based adsorbents (900–1200 €/kg) was closer to commercially available adsorbents. In another study, silica-chitosan hybrids were prepared by encapsulation of functionalized silica into chitosan as well as by the functionalization of bare silica encapsulated in chitosan with ligands (Ramasamy et al., 2018a). In a study by Wu et al. (2013), the application of magnetic-silica nanocomposite grafted by 2-ethylexyl phosphoric acid was reported, and the hybrid material exhibited exceptional La adsorption due to the presence of phosphoryl groups on the surface.

Magnetic nanoparticles is another most frequently used inorganic matrix for the synthesis of hybrids by either functionalization or capsuling in some polymer matrix. The major advantage of using magnetic adsorbents over others is their easy separation using external magnets. L-cysteine (Cys) and citric acid (CA) functionalized magnetic nanoparticles were employed for La adsorption by Ashour et al. (2017b). Similarly, nanoparticles were encapsulated in calcium alginate, alginate-chitosan and chitosan polymeric matrix for making the gel bead magnetic nanoparticles (Wu et al., 2010, 2011; Haldorai et al., 2015). In another research, instead of

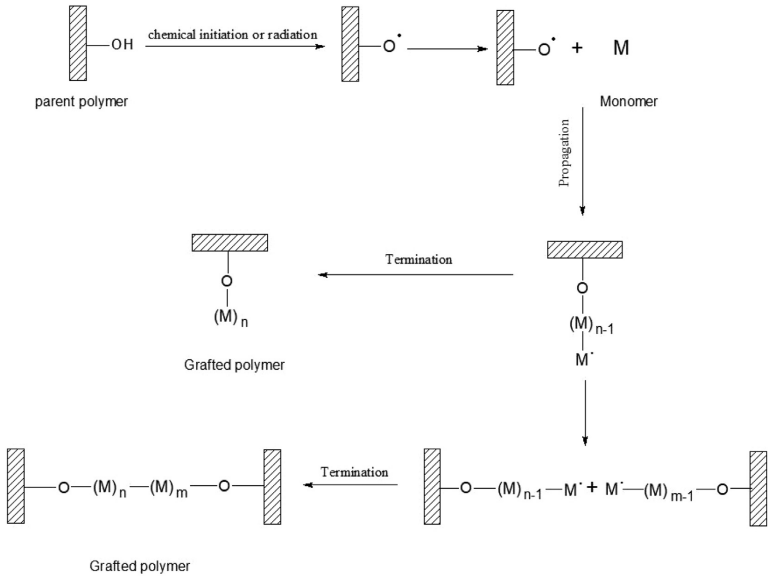

Scheme 1. General mechanism of monomer grafting on polymer backbone by radical generation.

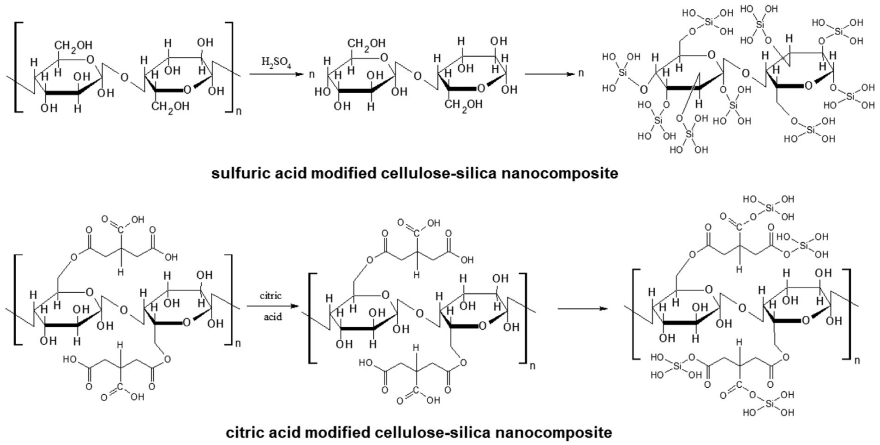

Scheme 2. Proposed schematic diagram for synthesis of sulfuric acid and citric acid modified cellulose-silica nanocomposites.

encapsulation, one-pot co-precipitation method was used for synthesis of chitosan-magnetic nanoparticles, and cysteine was used for cross-linking (Galhoum et al., 2015). Likewise, same method was used for preparation of Zn–Al LDH intercalated cellulose (Iftekhar et al., 2017d), while EDTA (ethylene-diamine-tetra-acetate) intercalated Cu–Al LDH was synthesized by LDH reconstruction method (Kameda et al., 2011). A few inorganic nanocomposite *viz* hydroxyapatite (Granados-Correa et al., 2012), SnO_2–TiO_2 (Rahman et al., 2014) and Mg–Fe LDH (Gasser and Aly, 2013) was examined for La adsorption and achieved promising results.

3.3. Commercially available adsorbents

Commercially available adsorbents including MWCNTs (Koochaki-Mohammadpour et al., 2014), graphene oxide (Ashour et al., 2017a), activated carbon (Marwani et al., 2013) and tailored activated carbon-silica composite have demonstrated great potential for La recovery. Although commercially available adsorbents offer high surface area, the major drawback of using commercially available adsorbents is their high cost as compared to locally available biosorbents or other low cost hybrid materials.

4. Factors of operating conditions on La adsorption by various materials

A wide range of materials including naturally occurring, synthetic and hybrid adsorbents has been investigated for La separation under different operating conditions such as pH, adsorbent dose and contact time (Table 1). However, efforts are required to systematically analyze the wealth of studies to estimate operating conditions to achieve efficient La adsorption. In this section, the influence of operating conditions on La adsorption process by different materials is elucidated based on the data presented in Table 1.

4.1. Effect of pH

pH is one of the most important process variables that can directly affect the uptake of La by adsorbents because it can affect the extent of La ionization as well as the surface characteristics of an adsorbent. In order to understand La behavior in solution, the chemical equilibrium for the estimation of La speciation over a pH range of 1–12 was carried out by Visual MINTEQ (ver. 3.0). Up to pH 6, La is the dominant species in solution, while it converts to $LaOH^{3+}$ by increasing the pH of the solution beyond 6 (Fig. 2).

A number of biosorbents have been studied for La adsorption. These biosorbents include *Sargassum polycystum* (Diniz and Volesky, 2005b), *Sargassum fluitans* (Palmieri et al., 2002), *Sargassum* biomass (Diniz and Volesky, 2005a), *Grobacterium* sp. (Shuxia et al., 2011), marine algae (Vijayaraghavan et al., 2011), crab shell (Vijayaraghavan et al., 2009), fish scale (Das et al., 2014), peels (Torab-Mostaedi, 2013; Torab-Mostaedi et al., 2015) and leave powders (Sert et al., 2008; Kütahyali et al., 2010), modified and unmodified biochar (Wang et al., 2016b). These biosorbents have been reported to show pH-dependent La adsorption. For example, Palmieri et al. (2002) observed ten-fold increase in La uptake by *S. fluitans* when pH of the process was changed from 2 to 5. In another study by Diniz and Volesky (2005a), a rapid increase in La adsorption on *Sargassum* biomass was observed following an increase in pH. Similarly, by increasing the pH to 6.8, La adsorption rate on *Agrobacterium* sp. was also improved (Shuxia et al., 2011).

Based on the comprehensive literature survey in this study, it seems that the mechanism of La removal by adsorbents can change from adsorption to precipitation, depending on the pH of the reaction media. For example, Vijayaraghavan et al. (2009) studied the efficacy of pre-treated crab shells (PCSP) for La adsorption. They observed that PCSP can act as a nonspecific chelator and forms weak hydrogen bonds with La due to the presence of chitin in PCSP. In addition, an increase in the pH of the reaction media from 5 to 9.6 was also observed during La adsorption by PCSP, which can be attributed to dissolution of carbonate groups available on PSCP surface (Vijayaraghavan et al., 2009). Notably, due to change in the pH of the reaction media, the dominant mechanism of La removal was changed from adsorption to precipitation in the form of $LaCO_3^+$ and $La(CO_3)_2^-$ (Vijayaraghavan et al., 2009). Although pH is reported as the most important performance governing factor, Wang et al. (2016b) observed that La adsorption by ammonium-citrate-modified biochar was not affected by solution pH. Although the author did not elucidate the reason, it can be seen from proposed structure of adsorbent shown in Scheme 3 that adsorbent surface contains various functional groups including carboxyl, hydroxyl and, providing an opportunity for the optimization of adsorbent dose. Another possible explanation might be that after modification of biochar with ammonium citrate, the zero point charge of surface lies around pH 3.5–4. Thus, the adsorbent is efficient enough to adsorb La at pH 4 (slight acidic) due to presence of different functional groups and in acidic region (*i.e.* pH 3) due to electrostatic repulsion between surface functional groups and H^+ ions.

In addition to different biosorbents, a variety of other adsorbent materials have been employed for La removal. These adsorbents include organic-inorganic hybrid nanocomposites, while some are modified silica-based materials (Table 1). Among these organic-inorganic hybrid materials (Table 1), the application of magnetic nanoparticles in the organic matrix is widely used. Due to the presence of organic matrix, La adsorption occurs by complexation of surface functional groups with La at a certain pH (Wu et al., 2010). A similar observation was made when Cysteine functionalized chitosan magnetic nanocomposite (Cys@CHI-magnetic) were assessed for La adsorption at pH 5 (Galhoum et al., 2015). Notably, the formation of La-organic complexes did not change the solution pH, and this was attributed to the buffering capacity of Cys@CHI-magnetic nanocomposite (Galhoum et al., 2015). Other adsorbents exhibiting buffering capacity against pH change include Layered double hydroxides (LDH) based materials (Kameda et al., 2011; Granados-Correa et al., 2012; Iftekhar et al., 2017d). However, it is important to note that not all adsorbents can act as a buffer. For example, Ashour et al. (2016) reported that Cys@Fe_3O_4 nanoparticles did not seem to have the buffering capacity, despite having amine and carboxylic functional groups.

Some organic grafted materials achieved promising results for La adsorption. These materials include CTS-g-PAA/APT (Zhu et al., 2015a), HPC-g-PAA/APT (Zhu et al., 2015b) and DGA-g-PAA (Zhou et al., 2016). The optimum pH for these materials ranged from 5 to 7 (Table 1). A large number of silica-based adsorbents reported in the literature were proved to be quite effective for La adsorption. In a study by Tadjarodi et al. (2015), HESI-SBA-15 achieved effective La adsorption (96%) at pH 7. In recent studies, various modified silica gels such as amine-functionalized silica (Ramasamy et al., 2017c), hybridized silica-chitosan (Ramasamy et al., 2017d) and silica-carbon composites (Ramasamy et al., 2018b) were subjected to the investigation of REEs uptake including La. These adsorbents when grafted with silanes and ligands, exuded an enormous potential for the recovery of La in the acidic pH regime. The interesting observation made during one of these studies was that when the ligands, 1- (2-pyridylazo)-2-naphthol (PAN) and acetylacetone (Acac), were chemically immobilized onto the silica surface by means of a coupling agent, such as 3-aminopropyltriethoxy silane (APTES) and 3-aminopropyltrimethoxy silane (APTMS), resulted in a supreme La adsorption from a lower pH regime of 4 and 5. On the other hand, the same ligands, when grafted via physical loading process without any coupling agent resulted in shifting the optimum adsorption pH to 7 (Ramasamy et al., 2017a). Similarly, when the chitosan units containing pH-responsive functional groups were hybridized with amine-functionalized silica, caused the adsorption of La to occur from the acidic pH range of 2–3 (Ramasamy et al., 2017d, 2018a).

Commercially available MWCNTs and GO have also been used for La adsorption. MWCNTs becomes negatively charged at $3 < pH < 6$, thus La adsorption may increase in this range (Koochaki-Mohammadpour et al., 2014). GO sheets seem to be highly negatively charged due to the presence of oxygen functional

Table 1
Parameter for the removal of La from different adsorbents.

Adsorbent	pH	Dose (g/L)	Contact time (min)	Temp(K)	Conc. Range (mg/L)	Conc.(mg/L)	pH_{zpc}	BET (m^2/g)	Separation Method	Ref
Sargassum polycystum	5	2	–	298	100–500	100	–	–	–	(Diniz and Volesky, 2005b)
S. fluitans	5	2.5	25	303	–	140	–	–	–	(Palmieri et al., 2002)
Sargassum biomass	5	2	24[a]	–	0.4–7.2 [b]	–	–	–	–	(Diniz and Volesky, 2005a)
Agrobacterium sp.	6.8	0.3	120	303	5–30	15	–	–	CF[d]	(Shuxia et al., 2011)
Gracilaria gracilis	–	0.45	48[a]	–	–	0.5	–	–	0.45 μm MF[c]	(Jacinto et al., 2018)
Brown marine algae	5	2	240	–	0.7–2.8 [b]	0.7 [b]	–	–	0.45 μm MF[c]	(Vijayaraghavan et al., 2011)
Crab shell	5	5	100	297	350–3500	1000	–	–	0.45 μm MF[c]	(Vijayaraghavan et al., 2009)
Fish scale	6	0.3	240	293	50–350	300	–	–	F[e]	(Das et al., 2014)
Neem sawdust	6	0.2	180	293	50–350	250	–	–	F[e]	(Das et al., 2014)
Pinus brutia leaf powder	5	4	30	303	25–300	25	–	–	FP[f]	(Kütahyali et al., 2010)
Plantanus orientalis leaf powder	4	4	60	303	25–300	100	–	–	FP[f]	(Sert et al., 2008)
Grapefruit peel	5	0.25	60	298	10–200	50	–	–	FP[f]	(Torab-Mostaedi et al., 2015)
Tangerine peel	5	2	60	–	10–200	20	–	–	FP[f]	(Torab-Mostaedi, 2013)
AC from RH	4	3	60	298	50–300	50	–	451.82	CF[d]	(Awwad et al., 2010)
Bamboo Charcoal	7.2	0.6	480	298	1.5–3	2.7	–	–	–	(Qing, 2010)
Biochar	7	1	60	293	25–500	50	–	1.51	0.22 μm MF[c]	(Wang et al., 2016b)
ammonium citrate-modified biochar	7	1	60	293	25–500	50	–	76.1	0.22 μm MF[c]	(Wang et al., 2016b)
PEI-CNC	5.4	1	6[a]	303	0.5–2[b]	1.4 [b]	1.9	–	0.45 μm MF[c]	(Zhao et al., 2017)
CST-g-PAA/APT20/1, 1/0, 6/1	6	1	40	303	50–500	400	–	–	F[e]	(Zhu et al., 2015a)
HPC-g-APT/PAA	6	1	40	303	50–500	300	–	–	F[e]	(Zhu et al., 2015b)
DGA-g-PAA	7	0.5	120	298	20–100	100	1	–	–	(Zhou et al., 2016)
CMC-g-PAA	neutral	0.8	30	–	100–800	200	–	–	–	(Zhu et al., 2016)
KCL-g-PAM/HA	6	1.5	180	298	5–1400	10	–	–	–	(Rahman et al., 2017)
CL	5	0.2	180	300	25–200	100	–	–	F[e]	(Tolba et al., 2017)
PAC	5	0.2	180	300	25–200	100	–	–	F[e]	(Tolba et al., 2017)
PCMC	5	0.2	180	300	25–200	100	–	–	F[e]	(Tolba et al., 2017)
EDTA-β-CD	3	2	45	–	0.05–2[b]	1.33[b]	–	–	0.45 μm MF[c]	(Zhao et al., 2016a,b)
Kaolinite	6.9	2.5	24[a]	295	–	0.13	4.5	–	–	(Coppin et al., 2002)
CNS	3	2	60	–	–	0.035 [b]	–	–	–	(Zhao et al., 2016b)
oxidized-MWCNTs	5	0.8	120	303	10–200	20	–	151.7	0.45 μm MF[c]	(Koochaki-Mohammadpour et al., 2014)
GO nanosheets	6	1	30	298	5–50	5	10.8	–	CF[d]	(Ashour et al., 2017a,b)
GO-CZ		0.25	150	298	10–80	50	–	223.45	–	(Xu et al., 2018)
AC-DETADHBA	6	0.025	60	298	10–400	5	2	–	F[e]	(Marwani et al., 2013)
SnO_2–TiO_2 NC	5	1	60	298	0–150	125	–	88.51	F[e]	(Rahman et al., 2014)
Hydroxyapatite	5.7	10	20	293	3.3×10^{-5}-3.6×10^{-4} [b]	5.7×10^{-5}	–	59.7	CF[d]	(Granados-Correa et al., 2012)
EDTA intercalated Cu–Al LDH	6	–	120	303	–	1 [b]	–	–	0.45 μm MF[c]	(Kameda et al., 2011)
MgFe-LDH-Cyanex272	1	10	120	298	5000–10000		–	–	–	(Gasser and Aly, 2013)
Magnetic GMZ bentonite	6.5	1	60	298	0.015–2.5[b]	27.5	6.5	26.4	EM[g]	(Wu et al., 2012)
Cys@CHI-magnetic	5	2.5	240	300	25–300	100	–	43	EM[g]	(Galhoum et al., 2015)
Fe_3O_4/CHI NC	11	0.65	50	313	100–1000	100	–	–	CF[d]	(Haldorai et al., 2015)
Fe_3O_4@Ca-Alg beads	5	2	28[a]	298	–	1 [b]	–	–	EM[g]	(Wu et al., 2010)
Fe_3O_4@Alg-CHI beads	2.8	1	10[a]	298	0.1–2[b]	1 [b]	–	–	EM[g]	(Wu et al., 2011)
Cys@Fe_3O_4	6	0.25	15	298	200–1000	200	5.1	53.95	EM[g]	(Ashour et al., 2016)
Cys@Fe_3O_4	7	0.25	–	298	5–50	5	5.1	53.95	EM[g]	(Ashour et al., 2017a,b)
CA@Fe_3O_4	7	0.25		298	5–50	5	–	94.65	EM[g]	(Ashour et al., 2017a,b)
CL-Zn/Al lDH	7	1	10	298	50–150	50	9.1	1.216	0.45 μm MF[c]	(Iftekhar et al., 2017c)
CLN/SiO_2	6	3	60	298	20–150	25	7.06	169.74	0.45 μm MF[c]	(Iftekhar et al., 2017b)
GA-g-PAM/SiO_2	6	2	60	298	20–150	25	3.18	273.55	0.45 μm MF[c]	(Iftekhar et al., 2017a)
PAA-S-HNFs	6	0.1	180	298	25–400	250	–	–	–	(Wang et al., 2016a)
APTES/PAN	4	1	60	298	5–200	25	–	118.06	0.45 μm MF[c]	(Ramasamy et al., 2017c)
APTES/Acac	4	1	60	298	5–200	25	–	90.09	0.45 μm MF[c]	(Ramasamy et al., 2017c)
APTMS/PAN	4	1	60	298	5–200	25	–	161.64	0.45 μm MF[c]	(Ramasamy et al., 2017c)
APTMS/Acac	4	1	60	298	5–200	25	–	131.89	0.45 μm MF[c]	(Ramasamy et al., 2017c)
PAN modified	4	1	60	298	5–200	25	–	352.25	0.45 μm MF[c]	(Ramasamy et al., 2017c)
Acac modified	4	1	60	298	5–200	25	–	335.83	0.45 μm MF[c]	(Ramasamy et al., 2017c)
SEP	5	1	240	296	1–100	10	–	–	0.45 μm MF[c]	(Ramasamy et al., 2017b)
SEA	6	1	20[a]	296	1–100	10	–	–	0.45 μm MF[c]	(Ramasamy et al., 2017b)
APTES	4	1	24[a]	296	–	20	7	174.19	0.45 μm MF[c]	(Ramasamy et al., 2017a)
APTMS	4	1	24[a]	296	–	20	5.3	176.79	0.45 μm MF[c]	(Ramasamy et al., 2017a)
MTM	7	1	24[a]	296	–	20	3	306.07	0.45 μm MF[c]	(Ramasamy et al., 2017a)
TMCS	7	1	24[a]	296	–	20	5	345.63	0.45 μm MF[c]	(Ramasamy et al., 2017a)
APTES-C3-PAN	4	1	90	296	1–250	25	5.8	71.89	0.45 μm MF[c]	(Ramasamy et al., 2017d)
APTES-C3-Acac	4	1	90	296	1–250	25	5.8	56.8	0.45 μm MF[c]	(Ramasamy et al., 2017d)
MTM-C3-PAN	4	1	90	296	1–250	25	5.8	133.96	0.45 μm MF[c]	(Ramasamy et al., 2017d)
MTM-C3-Acac	4	1	90	296	1–250	25	5.8	160.09	0.45 μm MF[c]	(Ramasamy et al., 2017d)
B4P	4	1	60	296	5–10	5	5	–	0.45 μm MF[c]	(Ramasamy et al., 2018a)
B6P	4	1	60	296	5–10	5	5	–	0.45 μm MF[c]	(Ramasamy et al., 2018a)
SIL	4	1	30	296	–	25		71.01	0.45 μm MF[c]	(Ramasamy et al., 2018b)
AC-SIL	4	1	30	296	–	25		250.85	0.45 μm MF[c]	(Ramasamy et al., 2018b)

Table 1 (*continued*)

Adsorbent	pH	Dose (g/L)	Contact time (min)	Temp(K)	Conc. Range (mg/L)	Conc.(mg/L)	pH_{zpc}	BET (m^2/g)	Separation Method	Ref
1SILP	4	1	30	296	–	25		128.71	0.45 μm MF[c]	(Ramasamy et al., 2018b)
1AC-SILP	4	1	30	296	–	25		134.06	0.45 μm MF[c]	(Ramasamy et al., 2018b)
1AC-P	4	1	30	296	–	25		185.99	0.45 μm MF[c]	(Ramasamy et al., 2018b)
2SILP	4	1	30	296	–	25		109.21	0.45 μm MF[c]	(Ramasamy et al., 2018b)
2AC-SILP	4	1	30	296	–	25		21.28	0.45 μm MF[c]	(Ramasamy et al., 2018b)
1AC-P	4	1	30	296	–	25		466.39	0.45 μm MF[c]	(Ramasamy et al., 2018b)
P507 magnetic silica NC	5.5	1	6u0	298	10–150	35	–	–	EM[g]	(Wu et al., 2013)
P(VP-AMPS)	5	5	24[a]	298	25–2000	100	–	–	0.45 μm MF[c]	(Borai et al., 2015)
P(VP-AMPS-SiO_2)	5	5	24[a]	298	25–2000	100	–	–	0.45 μm MF[c]	(Borai et al., 2015)
HESI-SBA15	7	2.33	45	–	10–200	20	–	234	CF[d] + F[e]	(Tadjarodi et al., 2015)

The units for dosage, contact time, concentration, BET surface area are g/L, min, mg/L, m^2/g, respectively unless otherwise stated.
[a] Contact time in h.
[b] Concentration in mmol/L.
[c] Membrane filter.
[d] Centrifugation.
[e] Filtration.
[f] Filter paper (Whatman No. 41).
[g] External magnetic.

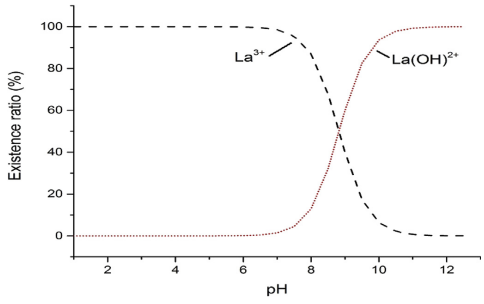

Fig. 2. La speciation for pH 1-12.

groups. The degree of GO deprotonation was greatly influenced by pH, and adsorption was observed to be efficient at pH > 7 (Ashour et al., 2017a). Researchers have also reported effective La adsorption at a very low pH. For example, Gasser and Aly (2013) reported efficient La adsorption (>90%) by MgFe-LDH-Cyanex272 at pH = 1. However, the reason for >90% La adsorption by MgFe-LDH-Cyanex272 at strong acidic pH was not explained (Gasser and Aly, 2013).

Based on the discussion above and data presented in Table 1, it is clear that La adsorption has been investigated over a wide range of pH (*i.e.*, 1–11). The maximum removal potential was achieved in the pH range of 4–6, as supported by the histogram and cumulative distribution function graphs (Fig. 3a). The solution pH is important because it can influence the mechanism of La adsorption. La removal can be attributed to adsorption at the pH range of 4–6, while precipitation of La due to the formation of $La(OH)_3$ via hydrolysis at alkaline pH (particularly beyond pH 7) is the dominant removal mechanism (Haldorai et al., 2015; Iftekhar et al., 2017c).

4.2. Effect of adsorbent dose

In general, the extent of adsorption of a solute increases with the increase in the concentration of an adsorbent because the increase in adsorbent concentration translates into increased active exchangeable adsorption sites. However, the overall solute adsorption per unit weight of an adsorbent can decrease following the increase in adsorbent concentration due to interference caused by the interaction of active sites of an adsorbent (Esposito et al., 2001; Das and Das, 2013; Xie et al., 2015). In a study by Wu et al. (2010), increasing the dosage of Fe_3O_4@Ca-Alg beads from 0.1 to 0.3 g/50 mL did not improve the extent of La adsorption. Moreover, neem sawdust (Das et al., 2014) and *S. fluitans* (Palmieri et al., 2002) achieved effective La adsorption (>90%) at a dose of 0.2 and 2.5 g/L, respectively. Likewise, Kütahyali et al. (2010) varied the dose of a biosorbent (*i.e., Pinus brutia* leaf) from 0.05 to 0.45 g, and found that removal increased with increase in dose. In contrast, Torab-Mostaedi et al. (2015) found that after certain increase of dosage, the removal decreases due to binding of all the La ions with adsorbent. Therefore, it is vital to optimize the dose of an adsorbent for achieving effective La removal.

Investigating the influence of dose along with its optimization is the mandatory component of La adsorption studies. From Fig. 3b and Table 1, it can be seen that the optimum adsorbent dose usually varies from 1 to 2 g/L for La adsorption, despite the difference in adsorbent materials and types. The optimum adsorbent dose is mainly related to availability of active site, which is interrelated to the presence of surface functional groups. However, the highest adsorption dose of 10 g/L was reported to be the optimum for La adsorption when MgFe-LDH-Cyanex72 (Gasser and Aly, 2013) and hydroxyapatite (Granados-Correa et al., 2012) were assessed as adsorbents. This is probably because La concentration was too high (*i.e.*, 5000–10000 mg/L) as compared to other studies presented in Table 1. This also indicates that optimum dose is directly linked with the concentration of adsorbate used.

4.3. Effect of contact time

The contact time significantly affects the adsorption process. Also, contact time can influence the economic efficiency of the process as well as the adsorption kinetics. Therefore, contact time is another performance governing factor in adsorption process (Srivastava et al., 2015).

Adsorption of La on Fe_3O_4/chitosan nanocomposite was investigated by Haldorai et al. (2015), they achieved 86% La removal after a contact time of 60 min. Notably, La removal reduced by increasing the contact time from 60 to 150 min. The reduced La removal was attributed to the desorption of La (Haldorai et al., 2015). In another study, La adsorption on DGA-g-PAA reached saturation in 120 min (Zhou et al., 2016). Adsorption of La on Cys@Fe_3O_4 and CA@Fe_3O_4 was observed to increase after a contact time of 5 and 15 min, while reached at equilibrium in 15 and 30 min, respectively (Ashour et al.,

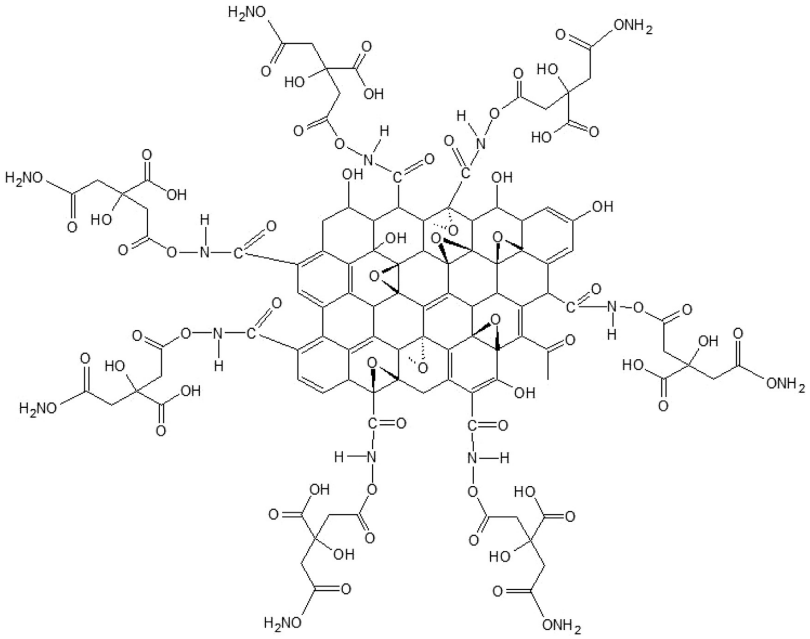

Scheme 3. Proposed structure of ammonium citrate modified biochar.

2017b). In other studies, La adsorption on tangerine peel (Torab-Mostaedi, 2013) and *Plantanus orientalis* leaf (Sert et al., 2008) was explored as a function of contact time. It was observed that La removal increased up to 60 min, and no further increase was noted afterward. Qing (2010) observed that La adsorption by modified bamboo charcoal increased linearly by increasing the contact time from 0 to 480 min (Qing, 2010). Among all the adsorbents, it can be seen from Table 1 that CL-Zn/Al LDH nanocomposites displayed 99% removal of La within 10 min (Iftekhar et al., 2017d). In another study, it was reported that the hybridized silica-chitosan beads exhibited instant La adsorption within 1–5 min, while the hybridized silica-chitosan flakes of similar modifications demanded a longer contact time of more than 2 h due to the diffusion restrictions in the flake form with its increased particle size (Ramasamy et al., 2017d). The statistical analysis of the data presented in Table 1 indicates that optimum contact time for La removal by different adsorption materials is highly variable with a mean contact time of 329 min (Fig. 3c).

4.4. Effect of temperature

The temperature of the solution mainly affects the enlargement nature of adsorbents, mobility of La ions and solid/liquid interface (Iftekhar et al., 2017c). It can be seen from Fig. 2d that 298 K has the highest frequency of occurrence, indicating that majority of studies (Table 1) were conducted at room temperature.

Along with temperature, thermodynamic parameters were used to determine the nature of adsorption process *viz* exothermic or endothermic, spontaneity and randomness and also to determine whether the temperature is favorable for the process or not. The important thermodynamic parameters are ΔG^0, ΔH^0 and ΔS^0 representing the change in Gibbs free energy, enthalpy and entropy. The negative values of ΔG^0 are associated with the adsorption process being spontaneous. Similarly, the positive values of ΔH^0 indicate that the process is endothermic. Also, the magnitude of ΔH^0 seems to be related with the type of sorption viz. physisorption ($\Delta H^0 < 50$ kJ/mol) and chemisorption ($\Delta H^0 > 50$ kJ/mol) (Iftekhar et al., 2017c; d). Moreover, the positive values of ΔS^0 could be explained as that increase in entropy occurred due to the exchange of metal ions by more mobile ions during adsorption process (Iftekhar et al., 2017c). Therefore, many researchers studied the effect of temperature on La adsorption by various adsorbents and related works are summarized in Table 2.

From Table 2, it can be concluded that La adsorption on most of the adsorbents reported was endothermic with few exceptions. The adsorption process of La on SnO_2–TiO_2 nanocomposite (Rahman et al., 2014), MWCNTs (Koochaki-Mohammadpour et al., 2014), Fe_3O_4@Alg-CHI (Wu et al., 2011) and Fe_3O_4@Ca-Alg beads (Wu et al., 2010) was observed to be exothermic as suggested by the negative value of ΔH^0. In addition, adsorption process seems to be spontaneous and favorable due to negative ΔG^0 along with positive ΔS^0. In a study carried out by Rahman et al. (2014) on SnO_2–TiO_2 nanocomposite; the negative values of ΔG^0 increased (−27.7 to −30.62 kJ/mol) with temperature from 278 to 338 K indicating adsorption was favorable at a higher temperature (Rahman et al., 2014). The same was observed by Mohammadpour et al. (2014) in

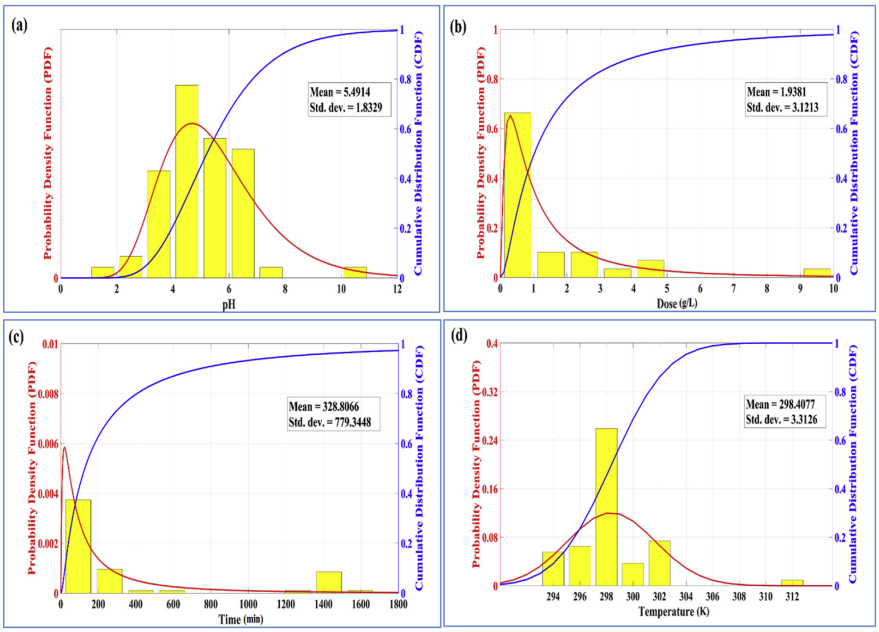

Fig. 3. Histogram and cumulative plot for La adsorption as a function of pH (a), dose (b), time (c) and temperature (d).

a temperature range of 303–333 K (Koochaki-Mohammadpour et al., 2014).

Apart from a few instances, the majority of investigators reported the process of La was endothermic in nature. For example, Ramasamy et al. (2017c) in their work investigated the effect of temperature from 25 to 60 °C. The rise in temperature positively impacted the adsorption process and the La removal efficiency was significantly increased in case of Acac modified silica gel. In addition to this, it was also evident from the authors' works that the temperature largely impacted the HREE adsorption process in comparison to LREE (e.g., La) adsorption process (Ramasamy et al., 2017c, 2018a, 2018b). The increase in adsorption with the rise in temperature might be due to the formation of new exchangeable sites, pore enlargement, diffusion across energy barrier, increased rate of sorption and transport against energy barrier (Hashemian et al., 2013). Likewise, the enthalpy values obtained for CL-Zn/Al LDH and CLN/SiO_2 nanocomposites suggests the chemisorption process for La(III) (Iftekhar et al., 2017d; c). The results also suggest that the randomness at the solid-liquid interface increased during the adsorption of La(III) on CLN/SiO_2 (Iftekhar et al., 2017c).

4.5. Effect of competing ions

The removal efficiency of La is greatly influenced by the presence of co-existing ions in solution leading to competitive adsorption on the adsorbent surface (Zhang et al., 2016). In recent years, many research groups reported the effect of co-existing ions on La adsorption. For example, Iftekhar et al. (2017d) investigated that the presence of 10 fold concentration of Na^+, K^+, Ca^{2+}, Mg^{2+}, Al^{3+} resulted in a decrease of 10% La adsorption on CL-Zn/Al LDH (Iftekhar et al., 2017d). Similarly, La adsorption on CLN/SiO_2 decreased considerably when present in the same system along with Na^+, K^+, Ca^{2+}, Mg^{2+}, Al^{3+}, probably due to same ionic charge of Al^{3+} (Iftekhar et al., 2017c). The influence on La adsorption on P507 magnetic silica nanocomposite was studied by Wu et al. (2013) in the presence of alkali metal ions viz. Na^+, K^+, Li^+, Ca^{2+}, Mg^{2+}, Ni^{2+}, Co^{2+}. The removal of La was not affected by the monovalent ions, however, a slight decrease was observed due to divalent ions which were attributed to high ionic strength (Wu et al., 2013). Similar observations were made with activated carbon-silica composites where the removal of La was not inhibited in the presence of high water salinity (Na^+) but in the presence of water hardness ions (Ca^{2+} and Mg^{2+}) and organic/oil compound (e.g., heptane) (Ramasamy et al., 2018b). In another study, the presence of monovalent and divalent cations and anions was studied and results showed a high selectivity of AC-DETADHBA towards La along with competing ions (Wang et al., 2016a). Similar results had been reported by Tadjarodi et al. (2015) and Wang et al. (2016b) as well.

It was reported in the literature that the hindrance of competing ions with regards to La adsorption could be largely influenced by the process pH. For instance, recovery of La from the acidic solutions posed challenges from the competing ions such as Fe^{3+}, quite common in industrial waste waters or mine waters (Ramasamy et al., 2018c). At lower pHs, besides Fe^{3+}, interference from noble elements and palladium group elements such as Au^{3+}, Pd^{3+} and Pt^{3+}, could be fairly excessive. On the other hand, at higher pH, ions such as Mn^{2+}, Al^{3+}, Cd^{2+}, Cu^{2+}, Co^{2+} and Zn^{2+} could deter the adsorption process of La (Ramasamy et al., 2017a, 2018a). It should also be mentioned that poor La adsorption was commonly recorded

Table 2
Nature and Regeneration of La adsorption on different adsorbents.

Adsorbent	Nature of adsorption	ΔH^0	ΔS^0	Regeneration Cycles	Desorbing Eluents	Ref
Fish scale	endo	13.04	38	6	0.1 M HCl	(Das et al., 2014)
Marine algae	–	–	–	3	0.05 M HCl	(Vijayaraghavan et al., 2011)
Neem sawdust	endo	13.75	40	–	–	(Das et al., 2014)
Grapefruit peel	endo	36.57	192.71	–	–	(Torab-Mostaedi et al., 2015)
Tangerine peel	endo	28.57	170.85	–	–	(Torab-Mostaedi, 2013)
Pleurotus ostreatus basidiocarps	endo	6.65	39	–	–	(Hussien, 2014)
Pinus brutia leaf powder	endo	5.65	77	–	0.5 M HNO_3	(Kütahyali et al., 2010)
Plantanus orientalis leaf powder	endo	5.076	81	–	0.5 M HNO_3	(Sert et al., 2008)
AC from RH	endo	3.37	–	–	–	(Awwad et al., 2010)
Bamboo Charcoal	endo	6.61	84.6	–	–	(Qing, 2010)
ammonium citrate-modified biochar	–	–	-	6	0.2 M HCl	(Wang et al., 2016b)
PEI-CNC	endo	–	-	3	HNO_3	(Zhao et al., 2017)
CST-g-PAA/APT20/1, 1/0, 6/1	–	–	-	5	0.5 M HCl	(Zhu et al., 2015a)
HPC-g-APT/PAA	–	–	–	5	0.5 M HCl	(Zhu et al., 2015b)
DGA-g-PAA	–	–	–	8	0.2 M HCl	(Zhou et al., 2016)
CMC-g-PAA	–	–	–	5	0.5 M HCl	(Zhu et al., 2016)
KCL-g-PAM/HA	–	–	–	10	2 M HCl	(Rahman et al., 2017)
CL	endo	3.18	88.4	5	0.5 M HNO_3	(Tolba et al., 2017)
PAC	endo	3.94	92.7	5	0.5 M HNO_3	(Tolba et al., 2017)
PCMC	endo	3.07	92.9	5	0.5 M HNO_3	(Tolba et al., 2017)
EDTA-β-CD	–	–	–	5	1 M HNO_3	(Zhao et al., 2016a,b)
AC-DETADHBA	exo	−55.44	−92.05	–	0.15 M HCl	(Marwani et al., 2013)
Oxidized-MWCNTs	exo	−17.23	94	–	HNO_3	(Koochaki-Mohammadpour et al., 2014)
GO nanosheets	endo	2.93	18	–	0.1 M HNO_3	(Ashour et al., 2017a,b)
SnO_2–TiO_2 NC	exo	−14.43	48.59	–	–	(Rahman et al., 2014)
Hydroxyapatite	endo	5.9	80			(Granados-Correa et al., 2012)
MgFe-LDH-Cyanex272	–	–	–	7	0.01 M HCl	(Gasser and Aly, 2013)
GMZ bentonite	–	–	–	3	0.5 M NaCl	(Wu et al., 2012)
Cys@CHI-magnetic	endo	7.85	103	4	0.5 M thiourea	(Galhoum et al., 2015)
Fe_3O_4/CHI NC	endo	41.8	152	–	–	(Haldorai et al., 2015)
Fe_3O_4@Ca-Alg	exo	−7.93	–	3	0.05 M $CaCl_2$	(Wu et al., 2010)
Fe_3O_4@Alg-CHI beads	exo	−15.45	−50.7	3	0.1 M HCl	(Wu et al., 2011)
Cys@Fe_3O_4	endo	0.403	12.7	–	0.1 M HNO_3	(Ashour et al., 2016)
Cys@Fe_3O_4	endo	41.85	165	–	0.5 M HNO_3	(Ashour et al., 2017a,b)
CA@Fe_3O_4	endo	16.7	87	–	0.5 M HNO_3	(Ashour et al., 2017a,b)
CL-Zn/Al lDH	endo	50.73	276.81	5	0.1 M HCl	(Iftekhar et al., 2017c)
CLN/SiO_2	endo	188.95	644.96	3	0.5 M HCl	(Iftekhar et al., 2017b)
GA-g-PAM/SiO_2	endo	32.57	110.14	3	0.1 M HCl	(Iftekhar et al., 2017a)
PAA-S-HNFs	–	–	–	4	0.5 M HCl	(Wang et al., 2016a)
APTES/PAN	endo	124.5	431.58	–	1 M HNO_3	(Ramasamy et al., 2017c)
APTES/Acac	endo	144.93	444.32	–	1 M HNO_3	(Ramasamy et al., 2017c)
APTMS/PAN	endo	22.56	93.35	–	1 M HNO_3	(Ramasamy et al., 2017c)
APTMS/Acac	endo	134.74	416.24	–	1 M HNO_3	(Ramasamy et al., 2017c)
PAN modified	endo	7.67	2.76	–	1 M HNO_3	(Ramasamy et al., 2017c)
Acac modified	endo	−37.92	−157.29	–	1 M HNO_3	(Ramasamy et al., 2017c)
P507 magnetic silica NC	–	–	–	10	0.1 M HCl	(Wu et al., 2013)
HESI-SBA15	–	–	–	4	0.1 M HCl	(Tadjarodi et al., 2015)

in multicomponent systems, which showed a higher affinity towards HREE and Sc, possessing lower ionic radii, in comparison to LREE (such as La). Lanthanide contraction effect plays a significant role in which the ionic radii of lanthanides decreases steadily with the increase in atomic number owing to the imperfect electron shielding within the same sub-shell (Ramasamy et al., 2017b). Besides, in the same work by Ramasamy et al. (2017b), the affinity towards LREE over HREE was recorded at lower pH, temperature and initial adsorbate concentration under real water conditions whereas the affinity shifted towards to HREE with the increase in pH, temperature and concentration.

5. Adsorption equilibrium and kinetic

5.1. Adsorption equilibrium

The information on adsorption equilibrium is one of the vital factors required for proper analysis and design of the adsorbent-adsorbate system (Zhang et al., 2016). Over the years, various models have been employed to explain the adsorption equilibrium, including two and three parameters isotherm models. These isotherm models provide useful evidence about adsorbing property of adsorption system and information about the distribution of exchangeable sites on the surface of the adsorbent. The list of the various models used by different authors is presented in Table 3. Also, the summary of best-fit isotherm for La adsorption on different adsorbent materials is shown in Table 4. In comparison with other models, Langmuir and Freundlich model had been widely used by the researchers to describe equilibrium adsorption.

It is evident from Table 4 that with the exception of a few adsorbent materials, the rest followed Langmuir model for adsorption of La. The adsorption of La onto neem sawdust (Das et al., 2014), Fe_3O_4/chitosan nanocomposite (Haldorai et al., 2015), hydroxyapatite (Granados-Correa et al., 2012) and bamboo charcoal (Qing, 2010) followed Freundlich assuming a heterogeneous surface with a non-uniform distribution of heat of sorption. Meanwhile, Zhao et al. (2017) applied three isotherms including Langmuir, Freundlich and Sips to elucidate the equilibrium data on PEI-CNC and found that experimental data fitted well to Sips model compared to the others. In addition to Freundlich, the Langmuir

Table 3
List of common models used for adsorption of La.

	Nonlinear equation	Linear equation	Ref
Isotherm model			
Langmuir	$q_e = \frac{K_L Q_0 C_e}{1+K_L C_e}$	$\frac{C_e}{q_e} = \frac{1}{K_L Q_0} + \frac{C_e}{Q_0}$	(Langmuir, 1918)
Freundlich	$q_e = K_F C_e^{1/n}$	$\ln q_e = \ln K_f + \frac{1}{n} \ln C_e$	(Freundlich, 1906)
Temkin	$q_e = B(\ln A)C_e$	$q_e = B\log(A) + B\log(C_e)$	(Iftekhar et al., 2017c)
Dubin-Radushkevich	$q_e = (q_s)\exp(-\beta\varepsilon^2)$	$\ln q_e = \ln q_s - \beta\varepsilon^2$	(Dada et al., 2012)
Redlich-Peterson	$q_e = \frac{k_{RP}C_e}{1+a_R C_e^{\beta_{RP}}}$	$\ln k_{RP}\frac{C_e}{q_e} - 1 = \beta_{RP} \ln C_e + \ln a_{RP}$	(Redlich and Peterson, 1959)
Sips	$q_e = \frac{k_s C_e^{\beta_s}}{1+a_s C_e^{\beta_s}}$	$\beta_s \ln C_e = \ln\left(\frac{k_s}{q_e}\right) + \ln a_s$	(Sips, 1948)
Toth	$q_e = \frac{k_T C_e}{(a_T + C_e)^{1/t}}$	$\ln\frac{q_e}{k_t} = \ln C_e - \frac{1}{t}\ln(a_T + C_e)$	(Toth, 1971)
Kinetic model			
Pseudo first order	$\frac{dq_t}{dt} = k_1(q_e - q_t)$	$\log(q_e - q_t) = \log q_e - \frac{k_1}{2.303}t$	(Lagergren, 1898)
Pseudo second order	$\frac{dq_t}{dt} = k_2(q_e - q_t)^2$	$\frac{t}{q_t} = \frac{1}{k_2 q_e^2} + \frac{1}{q_e}t$	(Ho and McKay, 1999)
Intra-particle diffusion	$q_t = k_i t^{1/2} + C$		(Iftekhar et al., 2017c)
Boyd	$-k_b t = \ln(1-F); F = \frac{q_t}{q_e}$		(Boyd and AW, 1947)
Elovich	$\frac{dq_t}{dt} = \alpha\exp(-\beta q_t)$	$q_t = (1/\beta)\ln(\alpha\beta) + (1/\beta)\ln t$	(Elovich and Larinov, 1962)
Mass transfer model	$q_t = k_t t^{1/2} + q_{max}$		(Weber and Morris, 1963)
Dynamic Adsorption models			
Thomas model	$\frac{C_e}{C_o} = \frac{1}{1+\exp[K_T(Q_m - C_e V)/\theta]}$	$\ln\left(\frac{C_e}{C_o} - 1\right) = \frac{K_T Q_m}{\theta} - \frac{K_T C_e}{\theta}V$	(Qing, 2010; Das et al., 2014)
Bed Depth Service Time model (BDST)	$\ln\left(\frac{C_o}{C_b - 1}\right) = \ln(e^{K_a N_o Z/v} - 1) - K_a C_o t$	$t = \frac{N_o Z}{C_o v} - \frac{1}{K_a C_o}\ln\left(\frac{C_o}{C_b - 1}\right)$	(Das et al., 2014) (Wu et al., 2010)

isotherm was found to be followed by most of the adsorbent material for La adsorption. The La adsorption performance on GA-g-PAM/SiO_2 was elucidated by employing four equilibrium models (Langmuir, Freundlich, Tempkin and Elovich), however, the higher values of R^2 indicated that the process was explained well by Langmuir (Iftekhar et al., 2017b) with maximum adsorption capacity of 7.9 mg/g. Notably, the adsorption capacity of CLN/SiO_2 (Iftekhar et al., 2017c), GA-g-PAM/SiO_2 (Iftekhar et al., 2017b) and HESI-SBA15 (Tadjarodi et al., 2015) was lesser than other silica-based materials for instance, ligand grafted silica gels (SEP) (Ramasamy et al., 2017b), functionalized silica-chitosan immobilized with PAN (APTES-C3-PAN) (Ramasamy et al., 2018a) and activated carbon and silica grafted PAN (2AC-SLIP) (Ramasamy et al., 2018b). Similarly, GA-g-PAM/SiO_2, which is a PAM grafted-silica hybrid nanocomposite, showed poor adsorption capacity in comparison to other grafted materials (Fig. 4). The maximum adsorption capacities for La found in literature were 480.8, 362.32, 342.46 and 333.33 mg/g over MgFe-LDH-Cyanex272 (Gasser and Aly, 2013), ammonium citrate-modified biochar (Wang et al., 2016b), Fe_3O_4/chitosan nanocomposite (Haldorai et al., 2015) and CST-g-PAA/APT (Zhu et al., 2015a), respectively.

5.2. Adsorption kinetics

In order to understand the mechanism of adsorption and the rate limiting steps; kinetics is of utmost importance. Also, the knowledge about kinetics is required for the selection of optimum conditions for the design of full-scale batch process (Zhang et al., 2016). In the past few year, research groups have been used different kinetic models for La adsorption viz. pseudo-first-order-model (PS1), pseudo-second-order-model (PS2), and intra-particle diffusion model (IPD). Along with these three most widely used models, some other kinetic models reported are Boyd model (BM), Elovich model (EM) and Mass Transfer model (MTM). The linear and non-linear form of all the models mentioned above are listed in Table 3.

Table 4 summarizes the best fit model and it can be seen that in almost all cases, PS2 model fit the experimental data well indicating the chemisorption adsorption of La over all adsorbents reported in this review. Das et al. (2014) applied PS1, PS2, IBP and BM models for fitting the kinetic data for La adsorption on fish scale and neem sawdust. The results demonstrated that the experimental data fitted well to the PS2 equation and apart from intra-particle diffusion, film diffusion also takes part in case of neem sawdust (Das et al., 2014). Wang et al.(2016a,b) found that the adsorption of La on PAA-S HNFs followed PS2, and the IPD plots exhibit two linear portions revealing that the process is controlled by both film and intra-particle diffusion (Wang et al., 2016a). Similarly, Awwad et al. (2010) reported that $q_{e,cal}$ was closer to $q_{e,exp}$ calculated from the PS2 equation and the plot of IPD did not pass through the origin indicating the intra-particle diffusion is not the only rate controlling step (Awwad et al., 2010). In a study by Koochaki-Mohammadpour et al. (2014), adsorption process onto oxidized-MWCNTs was controlled by ion exchange external diffusion and to some extent by intra-particle diffusion. Zhao et al. (2017) stated the appropriateness of PS2 order model suggesting that both chemisorption and diffusion affected the adsorption due to binding with surface ligands of PEI-CNC. A similar conclusion was drawn in another study where the author discovered that rate limiting step for adsorption of La on EDTA-β-CD was chemical sorption and mass transfer was not involved in the adsorption mechanism (Zhao et al., 2016a,b). However, PS1 showed a better fit compared to PS2 in case of CL, PAC and PCMC. Though the R^2 values were close enough, conversely, the rate coefficient for PS2 decreased as a result of grafting of CL which contradicted the fact that hydration and mass transfer should enhance with a decrease in crystallinity (Tolba et al., 2017). Likewise (Iftekhar et al., 2017b), found that adsorption of La along with other REEs supported the assumption of physio-sorption as the kinetic data fitted well to PS1 instead of PS2 model and film diffusion control the adsorption process over GA-g-PAM/SiO_2.

The La adsorption performance among different material is compared (Fig. 4). In case of biosorbents, ammonium citrate-modified biochar exhibited the highest adsorption capacity and less kinetic time. On the other hand, the hybrid materials prepared by grafting, *i.e.*, CST-g-PAA/APT, achieved equilibrium in less time, and the adsorption capacity is close to ammonium citrate-modified biochar. Importantly, LDH based hybrid with biopolymer in the

Table 4
Comparison of maximum adsorption capacity of La on different adsorbents.

Adsorbent	Isotherm	Kinetic	Adsorption capacity	Ref
Sargassum polycystum	L	–	69.4	(Diniz and Volesky, 2005b)
Crab shell	F	–	90.9	(Butnariu et al., 2015)
Crab shell	L	PS2	140.1	(Vijayaraghavan et al., 2009)
Fish scale	L	PS1	200	(Das et al., 2014)
Neem sawdust	F	PS2	160.2	(Das et al., 2014)
Pinus brutia leaf powder	L	PS2	22.94	(Kütahyali et al., 2010)
Plantanus orientalis leaf powder	L	PS2	28.65	(Sert et al., 2008)
Grapefruit peel	L	PS2	171.2	(Torab-Mostaedi et al., 2015)
Tangerine peel	L	PS2	154.86	(Torab-Mostaedi, 2013)
Pleurotus ostreatus basidiocarps	L	–	54.54	(Hussien, 2014)
Orange peel	F	–	125	(Butnariu et al., 2015)
Pineapple crown	F	–	100	(Butnariu et al., 2015)
Corn style	F	–	76.9	(Butnariu et al., 2015)
Egg shell	F	–	100	(Butnariu et al., 2015)
Prawn carapace	F	–	200	(Butnariu et al., 2015)
Bone powder	L	–	8.7	(Varshini and Das, 2014)
Stichococcus bacillaris	L	PS2	51.02	(Birungi and Chirwa, 2014)
Desmodesmus multivariabilis	L	PS2	100	(Birungi and Chirwa, 2014)
Chloroidium saccharophilum	L	PS2	129.87	(Birungi and Chirwa, 2014)
Chlamydomonas reinhardtii	L	PS2	142.86	(Birungi and Chirwa, 2014)
Scenedesmus acuminutus	L	PS2	111.1	(Birungi and Chirwa, 2014)
Chlorella vulgaris	L	PS2	74.6	(Birungi and Chirwa, 2014)
AC from RH	L	PS2	175.4	(Awwad et al., 2010)
Bamboo Charcoal	F	PS2	215	(Qing, 2010)
Ammonium citrate-modified biochar	L	PS2	362.32	(Wang et al., 2016b)
Biochar	L	PS2	275.48	(Wang et al., 2016b)
PEI-CNC	S	PS2	84.63[a]	(Zhao et al., 2017)
CST-g-PAA/APT20/11/06/1	L	PS2	333.33 322.58 303.03	(Zhu et al., 2015a)
HPC-g-APT/PAA	L	PS2	269.37	(Zhu et al., 2015b)
CMC-g-PAA	L	PS2	241.72	(Zhu et al., 2016)
KCL-g-PAM/HA	L	PS2	260	(Rahman et al., 2017)
CL	L	PS1	38.4	(Tolba et al., 2017)
PAC	L	PS1	101.3	(Tolba et al., 2017)
PCMC	L	PS1	170.2	(Tolba et al., 2017)
EDTA-β-CD	L	PS2	47.26[a]	(Zhao et al., 2016a,b)
AC-DETADHBA	L	PS2	144.8	(Marwani et al., 2013)
oxidized-MWCNTs	L	PS2	99.01	(Koochaki-Mohammadpour et al., 2014)
GO nanosheets	L	PS2	85.67	(Ashour et al., 2017a,b)
GO-CZ	–	–	17.29	(Xu et al., 2018)
SnO_2–TiO_2 NC	L	PS2	67.73	(Rahman et al., 2014)
Hydroxyapatite	F	PS2	0.25	(Granados-Correa et al., 2012)
MgFe-LDH-Cyanex272	L	–	480.8	(Gasser and Aly, 2013)
GMZ bentonite	L	PS2	18.4	(Wu et al., 2012)
Cys@CHI-magnetic	L	PS2	17.9	(Galhoum et al., 2015)
Fe_3O_4/CHI NC	F	PS2	342.46	(Haldorai et al., 2015)
Fe_3O_4@Ca-Alg beads	L	PS2	123.5	(Wu et al., 2010)
Fe_3O_4@Alg-CHI beads	L	PS2	97.1	(Wu et al., 2011)
Cys@Fe_3O_4	L	PS2	71.5	(Ashour et al., 2016)
Cys@Fe_3O_4	L	PS2	32.5	(Ashour et al., 2017a,b)
CA@Fe_3O_4	L	PS2	41.8516	(Ashour et al., 2017a,b)
CL-Zn/Al lDH	L	PS2	92.15	(Iftekhar et al., 2017c)
CLN/SiO_2	L	PS2	29.48	(Iftekhar et al., 2017b)
GA-g-PAM/SiO_2	L	PS1	7.9	(Iftekhar et al., 2017a)
PAA-S-HNFs	L	PS2	232.6	(Wang et al., 2016a)
SEP	L	–	115.01[a]	(Ramasamy et al., 2017b)
APTES-C3-PAN	L	PS2	120.7	(Ramasamy et al., 2017d)
2AC-SILP	–	–	103.5	(Ramasamy et al., 2018b)
P507 magnetic silica NC	L	PS2	55.9	(Wu et al., 2013)
HESI-SBA15	–	PS2	8.32	(Tadjarodi et al., 2015)

L is for Langmuir; F for Freundlich; PS1 for pseudo first order; PS2 for pseudo second order model.
[a] Converted from the original unit of mmol/g presented in the literatures.

interlayer (CL-Zn/Al LDH) achieved equilibrium in only 10 min and exhibits better capacity when compared to materials with longer kinetic time such as PEI-CNC and Fe_3O_4-Alg-CHI beads.

6. Desorption and reusability

The recovery of La from various adsorbents has following advantages: (a) reusability of adsorbent material, (b) recovery of La, and (c) reduction in sludge and process cost. Only few researchers have focused on the recovery of La. The selection of an efficient and effective eluent for desorption and regeneration is of utmost importance. Several eluents with different concentrations have been used for desorption and regeneration, for example, HNO_3, HCl, NaCl, thiourea and $CaCl_2$. Birungi and Chirwa (2014) used numerous

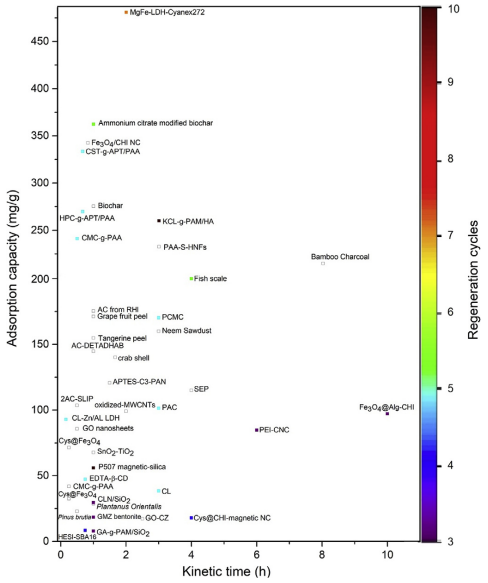

Fig. 4. Comparison between different adsorbents based on adsorption capacity, equilibrium time and regeneration cycles (□ indicates that regeneration data is not available).

types of freshwater algae. 0.1 M HNO_3 showed the highest desorption (99.63%) of La from Deemodesmus multivariabili, however, Stichococcus bacillaris showed the least (Birungi and Chirwa, 2014). In case of oxidized-MWCNTs, 65% desorption of La was achieved by varying pH values, whereas at pH 5, no recovery was noticed (Koochaki-Mohammadpour et al., 2014). This is because modified or functionalized MWCNTs has such a strong adsorbing power that they could not release the metal ions easily (Wan et al., 2017). Similarly, the experiments carried out by Hussien (2014) on pleurotus ostreatus basidiocarps showed that 0.1 M HNO_3 is enough to achieve 96.89% desorption. 0.5 M HCl was used as a desorbing agent and the desorption efficiency was almost 95% up to five cycles (Zhu et al., 2015a). It was also noticed that adsorption capacity increased in the second and third cycle due to the generation of new active sites after desorption. The same was observed by Zhu et al. (2015b) as well. The KCL-g-PAM/HA and P507 magnetic silica nanocomposite exhibited maximum regeneration up to ten cycles (Wu et al., 2013; Rahman et al., 2017).

A comparison on the basis of experimental maximum adsorption capacities, equilibrium times and regeneration cycles among different materials studied for La was illustrate in Fig. 4. Among the grafted hybrids, KCL-g-PAM/HA showed a potential to be used for up to 10 cycles, however the equilibrium time is on the higher side as compared to other hybrids. Similarly, MgFe-LDH-Cyanex272 seems to be even better than many commercially available materials studied for La adsorption due to its high adsorption capacity, lesser kinetic time and good reusability. Additionally, the regeneration is not good for GMZ bentonite, CLN/SiO_2, P507 magnetic silica nanocomposite, PEI-CNC and Fe_3O_4-Alg-CHI beads. Thus, it can be concluded that LDH based materials and grafted hybrids demonstrate better reusability and adsorbing capacity compared to silica based and commercially available materials.

7. Mechanism of adsorption

Though it's complicated to understand the adsorption mechanism of La on different adsorbents, it's crucial (Zhang et al., 2016). To date, only a handful of researchers have tried to explain La adsorption onto following adsorbents: brown marine algae (Vijayaraghavan et al., 2011), crab shell (Vijayaraghavan et al., 2009), grapefruit peel (Torab-Mostaedi et al., 2015), AC-DETADHBA (Marwani et al., 2013), P507 magnetic silica nanocomposite (Wu et al., 2013), PAA-S HNFs (Wang et al., 2016a), DGA-g-PAA (Zhou et al., 2016), HPC-g-PAA/APT (Zhu et al., 2015b), PEI-CNC (Zhao et al., 2017), PAN/Acac modified silica (Ramasamy et al., 2017b). FTIR, SEM and XPS techniques are most widely used, whereas, in some studies XRD and elemental analysis were also employed to understand the mechanism of adsorption. An attempt has been made to elucidate the adsorption mechanism by various functional groups as illustrated in Scheme 4.

Usually, the hydroxyl, carboxyl, amine functional groups and in some cases phosphoryl groups seems to be the major routes for the adsorption of La. The adsorption of La can occur mostly by either electrostatic interaction or surface complexation with the mentioned functional groups. The involvement of these groups could be attributed by shift of FTIR, XRD or XPS peaks.

The adsorption of La by hydroxyl groups (alone) mostly occur in case of LDH (or hydrotalcite) based materials, which consist of excess of hydroxyl groups on the surface. Though, the author did not explain the mechanism of REE removal by hydroxyapatite nanocomposite (Kameda et al., 2011). It was assumed that the possibly route of adsorption would be likely to occur by electrostatic interaction and surface complexation with hydroxyl groups besides ion exchanges as presented in Scheme 4a. On the other hand, adsorption on MgFe-LDH-Cyanex272 (Gasser and Aly, 2013) and EDTA intercalated Cu–Al LDH (Granados-Correa et al., 2012) was not only due to hydroxyl groups. Other functional groups viz. carboxyl and amine took part in adsorption due to presence of polymers in LDH interlayers. The involvement of carboxyl groups was found to be responsible in case of La adsorption over PAA-S-HNFs (Wang et al., 2016a), HPC-g-PAA/APT (Zhu et al., 2015b) and DGA-g-PAA (Zhou et al., 2016) by formation of bidentate bonds between La and carboxyl groups. Notably, HPC-g-PAA/APT (Zhu et al., 2015b) was synthesized by grafting of acrylates consisting of amine groups; which were not found to be involved in adsorption process. The possible reason might be that in some cases modification with polymers containing amine groups resulted in blockage of channels (Sun et al., 2009). The comparable singularity was observed when carbon shells was grafted by dopamine and carboxyl groups serves as the only active sites for La adsorption (Xiaoqi et al., 2016).

There are three kinds of amine groups namely primary, secondary and tertiary amines and possibility of their binding is shown in Scheme 4c. The occurrence of secondary amines are normally observed along with primary in case of grafting with PMA or other ligand groups viz. CMC-g-PAA (Zhu et al., 2016), P(VP-AMPS-SiO_2) (Borai et al., 2015). Nonetheless, tertiary amines rarely show involvement in adsorption process indicating that the primary and secondary groups are most important sites for adsorption. The above hypothesis was in agreement with the findings of Zhao et al. (2017), where the mechanism of REEs adsorption (including La) with primary and secondary amino groups was proposed. Conversely, earlier studies also reported that either coordination is possible with primary or secondary amine groups and remaining were occupied by H_2O molecules (Juang et al., 1999).

The combination of functional groups (like carboxyl-amine,

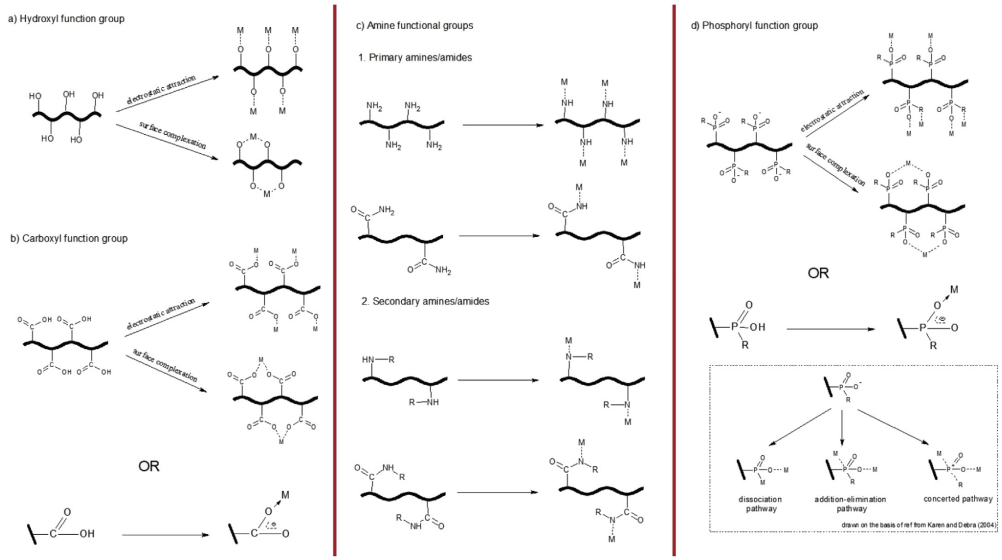

Scheme 4. Proposed schematic illustration of adsorption by hydroxyl, carboxyl, amine and phosphoryl functional group (where M = carrier ions; R = other groups).

hydroxyl-amine, hydroxyl-carboxyl-amine etc.) resulted in enhanced adsorption of La. Like, carboxyl and hydroxyl functional groups participate in La removal on grapefruit peel (Torab-Mostaedi et al., 2015). Similarly, adsorption of La on PAN/Acac modified silica gels occur mainly due to the following mechanisms: (a) electrostatic interactions between OH groups and La ions at higher pHs (b) ion exchange between the protonated cations on silica units and La ions and (c) chelation/coordination mechanism between *N*–/O- silica groups and REE cations. In addition, La being electropositive, it primarily attributes to ionic bonding instead of covalent interactions (Ramasamy et al., 2017b). In another work, the post-adsorption FTIR results of biosorbents from plant and animal origin demonstrated that surface functional groups i.e. amines, alkynes took part is adsorption process (Das et al., 2014; Varshini and Das, 2014). In case of P507 magnetic silica nanocomposites, P=O of phosphoryl groups were found to be involved in La adsorption (Wu et al., 2013), which is possible as proposed in Scheme 4d. Some studies also reported that the adsorption process occurred through ion exchange or precipitation. For instance, La ions may replace some of the monovalent and divalent ions from the cell wall via ion exchange when adsorbed on brown marine algae (Vijayaraghavan et al., 2011). Similarly, EDX spectrum of La-loaded PCSP confirmed the precipitation of $La_2(CO_3)_3$ on the surface of PCSP (Vijayaraghavan et al., 2009).

8. Dynamic adsorption

Literature on dynamic adsorption for La is rarely available. During the literature survey for adsorption of La, only three studies were found to be on dynamic adsorption. Though, towards practical application; the behavior of adsorbate-adsorbent system could be well explained by dynamic adsorption on the column system (Zhang et al., 2016). To explain the dynamic performance for the process of La adsorption and predicting the breakthrough; Qing (2010), Wu et al. (2010) and Das et al. (2014) employed the Thomas model and Bed Depth Service Time model (BDST). Along with these two models, the influence of process parameters *viz.* eluent dilutions, bed height and flow rates were also investigated. The recovery of La on fish scale was studied by Das et al. (2014). The results depicted that when the bed depth and flow rate were 12 cm and 1 mL/min, respectively, the maximum adsorption of 88.5% was achieved. In addition, the uptake of La on fish scale was found to be inversely related to the flow rate. Furthermore, the plot of La adsorption on fish scale was fitted well by BDST model with a correlation coefficient value of unity ($R^2 = 1$). To evaluate the column breakthrough, Thomas model was employed, and it exhibited a good fit. Also, with an increase in dilution (*i.e.* 0–50%), the rate constant (K_{TH}) was observed to increase from 1.6×10^{-5} to 1.9×10^{-5} (Das et al., 2014). Qing (2010) also reported that the experimental data fitted well to Thomas model ($R^2 = 0.98$) using bamboo charcoal and the Q_{exp} was close to Q_{cal}. However, in the case of Fe_3O_4@Ca-Alg beads at higher flow rates, the breakthrough seems to occur faster. The results suggested that La adsorption on Fe_3O_4@Ca-Alg were more pronounced at low flow rates (Wu et al., 2010).

9. Conclusion and future perspectives

La gained considerable attention in recent years, owing to the need of its removal and recovery. To enhance the adsorption efficiency, a wide range of adsorbents has been studied for the recovery of La from the aqueous medium. Some of those are biosorbents, inorganic sorbents, hybrid organic-inorganic nanocomposites, raw and modified silica-based adsorbents, magnetic adsorbents and also some commercially available AC, oxidized-MWCNTs. Adsorption was found to be influenced by several

operating parameters viz. pH, contact time, dosage, temperature. Langmuir isotherm and pseudo-second-order model were found to be fitting well to experimental data in the majority of the cases. Also, the thermodynamic studies revealed the process of La adsorption is predominantly endothermic and spontaneous in nature.

Despite the existence of imminent literature in the field of adsorption, it still serves as a primary option owing to the affordable process costs. The merit of this domain when coupled to a search for an efficient option to recover La from secondary wastes such as industrial stockpiles, mine tailings, and process water stream, exudes an immense potential for exploration in the coming years. In the meantime, it is of prime importance to address the existing technical challenges in the research area along with environmental issues. For instance, studies need to be focused toward the application of these adsorbent materials for the removal and recovery of La from real wastewater. Furthermore, column studies should be accompanied with batch studies for better understanding of adsorption mechanism as well as for understating the interaction of an adsorbent with an adsorbate. It is also highly essential that the developed materials can successfully extract or remove La selectively in the presence of common industrial metal contaminants such as Fe, Al, Na, K, Mg, Ca and S, and other groups of REEs. As the REEs are very similar in their physicochemical properties, they occur together in natural state and are difficult to separate from each other. Research must be driven towards the selective separation of La from the other REEs by studying and tailoring the process parameters such as pH and temperature. Besides customizing the material properties for selective separation of La by means of coordination ligands is also forthcoming in the recent years.

Even though the adsorption process is prevalent and well-established for many decades, the prospects of the design of advanced and sustainable green materials with greater selectivity and stability at lower costs are still promising and appealing to a great extent. The challenges stemming from the translation of research from lab scale adsorption process to pilot and industrial scale processes such as economic constraints, extensive regeneration of the adsorbents and over-utilization of chemicals must be addressed in the coming years. Besides, the exploitation of these selective adsorbents and resins in other technologies such as capacitive deionization and electrodeionization processes further supports the claim of this ever growing and flourishing domain with immense potential in the years to come.

Acknowledgement

The authors are thankful to Nida Iftikhar for help with some figures.

Appendix A. Abbreviations

1AC-P	Activated carbon
1AC-SILP	PAN impregnated activated carbon and silica gel with APTES
2AC-SILP	PAN grafted activated carbon and silica gel with APTES
AC	Activated charcoal
Acac modified	Silica gel chemically immobilized by acetylacetone
AC-DETADHBA	activated carbon modified diethylenetriamine and 3,4-dihydroxybenzaldehyde
AC-SIL	Activated carbon with silica
APTES	3-aminopropyltriethoxy silane
APTES/Acac	Silica gel chemically immobilized by acetylacetone with 3-aminopropyltriethoxy silane coupling agent
APTES-C3-PAN	APTES functionalized silica gel-chitosan (higher molecular weight) hybrid adsorbent with PAN modification
APTES-C3-Acac	APTES functionalized silica gel-chitosan (higher molecular weight) hybrid adsorbent with Acac modification
APTES/PAN	Silica gel chemically immobilized by 1-(2-pyridylazo)-2-naphthol with 3-aminopropyltriethoxy silane coupling agent
APTMS	3-aminopropyltrimethoxy silane
APTMS/Acac	Silica gel chemically immobilized by acetylacetone with 3-aminopropyltrimethoxy silane coupling agent
APTMS/PAN	silica gel chemically immobilized by 1-(2-pyridylazo)-2-naphthol with 3-aminopropyltrimethoxy silane coupling agent
B4P	APTES functionalized silica-chitosan beads
B6P	MMT functionalized silica-chitosan beads
CA@Fe_3O_4	Citric acid functionalized magnetic nanoparticles
CL	Cellulose
CLN/SiO2	Sulfuric acid modified cellulose based silica nanocomposites
CL-Zn/Al lDH	Cellulose intercalated zinc-aluminium layered double hydroxide
CMC-g-PAA	Carboxymethyl cellulose grafted polyacrylic acid
CNS	Carbonized polydopamine nano Carbon shells
CTS-g-PAA/APT	Chitosan grafted acrylic acid with attapulgite
Cys@CHI-magnetic NC	Cysteine functionalized chitosan magnetic nanocomposite
Cys@Fe3O4	Cysteine functionalized magnetic nanoparticles
DGA-g-PAA	Carboxylic acid functionalized diatomite grafted polyacrylic acid
EDTA intercalated Cu–Al LDH	Ethylene diamine tetraacetic acid intercalated copper-aluminium layered double hydroxide
EDTA- β-CD	Ethylenediamine tetraacetic acid- β-cyclodextrin
Fe3O4@Alg-CHI beads	Magnetic alginate chitosan gel beads
Fe3O4@Ca-Alg beads	Iron oxide loaded calcium alginate beads
GO	Graphene oxide
GO-CZ	Graphene oxide-corn zein
GA-g-PAM/SiO_2	Gum Arabic grafted polyacrylamide based silica nanocomposite
HESI-SBA-15	SBA-15 with covalently bonded *N*-(2-hydroxyethyl) salicylaldimine as a ligand
HPC-g-PAA/APT	Hydroxypropyl cellulose grafted acrylic acid with attapulgite
KCL-g-PAM/HA	Poly (methyl) acrylate grafted kenaf cellulose with poly (hydroxamic acid) ligand
LDH	Layered double hydroxides
MMT	Silica gel functionalized with trimethoxymethylsilane
MMT-C3-PAN	MTM functionalized silica gel-chitosan (higher molecular weight) hybrid adsorbent with PAN modification

(*continued on next page*)

(*continued*)

1AC-P	Activated carbon
MMT-C3-Acac	MTM functionalized silica gel-chitosan (higher molecular weight) hybrid adsorbent with Acac modification
MTM	Mass transfer model
MWCNTs	Multi-walled carbon nanotubes
NP	Nanoparticles
P(VP-AMPS	2-acrylamido 2-methyl propane sulphonic acid monomer onto poly (vinyl pyrillidone hydrogel)
P(VP-AMPS-SiO2	2-acrylamido 2-methyl propane sulphonic acid monomer onto poly (vinyl pyrillidone)-silica composite
PAA-S-HNFs	Poly (acrylic acid)-silica hydrogel nanofibers
PAC	Poly (aminated) cellulose
PAN	1-(2-pyridylazo)-2-naphthol
PCMC	Poly (carbocymethyl) cellulose
PCSP	Pre-treated crab shells
PEI-CNC	Polyethylenimine-cross-linked cellulose nanocrystals
RH	Rice husk
SBA-15	Silica prepared by hdrothermal method using tetraethyl othrosilicate
SEA	Silica gel chemically immobilized by acetylacetone
SEP	Silica gel chemically immobilized by 1-(2-pyridylazo)-2-naphthol
SIL	Bare silica
1SILP	PAN impregnated silica gel with APTES coupling agent
2SILP	PAN grafted silica gel with APTES coupling agent
TMCS	Silica gel functionalized with chlorotrimethylsilane

Appendix B. Supplementary data

Supplementary data related to this article can be found at https://doi.org/10.1016/j.chemosphere.2018.04.053.

References

Anastopoulos, I., Bhatnagar, A., Lima, E.C., 2016. Adsorption of rare earth metals: a review of recent literature. J. Mol. Liq. 221, 954–962.

Ashour, R.M., Abdel-Magied, A.F., Abdel-Khalek, A.A., Helaly, O., Ali, M., 2016. Preparation and characterization of magnetic iron oxide nanoparticles functionalized by l-cysteine: adsorption and desorption behavior for rare earth metal ions. J.Environ. Chem. Eng. 4, 3114–3121.

Ashour, R.M., Abdelhamid, H.N., Abdel-Magied, A.F., Abdel-Khalek, A.A., Ali, M., Uheida, A., Muhammed, M., Zou, X., Dutta, J., 2017a. Rare earth ions adsorption onto graphene oxide nanosheets. Solvent Extr. Ion Exch. 35, 91–103,

Ashour, R.M., El-sayed, R., Abdel-Magied, A.F., Abdel-khalek, A.A., Ali, M., Forsberg, K., Uheida, A., Muhammed, M., Dutta, J., 2017b. Selective separation of rare earth ions from aqueous solution using functionalized magnetite nanoparticles: kinetic and thermodynamic studies. Chem. Eng. J. 327, 286–296.

Awwad, N., Gad, H., Ahmad, M., Aly, H., 2010. Sorption of lanthanum and erbium from aqueous solution by activated carbon prepared from rice husk. Colloids Surfaces B Biointerfaces 81, 593–599.

Binnemans, K., Jones, P.T., Blanpain, B., Van Gerven, T., Yang, Y., Walton, A., Buchert, M., 2013. Recycling of rare earths: a critical review. J. Clean. Prod. 51, 1–22.

Birungi, Z., Chirwa, E., 2014. The kinetics of uptake and recovery of lanthanum using freshwater algae as biosorbents: comparative analysis. Bioresour. Technol. 160, 43–51.

Borai, E., Hamed, M., El-Kamash, A., Siyam, T., El-Sayed, G., 2015. Template polymerization synthesis of hydrogel and silica composite for sorption of some rare earth elements. J. Colloid Interface Sci. 456, 228–240.

Boyd, G., AW, A., 1947. LS, Myers Exchange adsorption of ions by organic zeolites II. Kinetics J. Am. Chem. Soc. 69, 2836–2848.

Butnariu, M., Negrea, P., Lupa, L., Ciopec, M., Negrea, A., Pentea, M., Sarac, I., Samfira, I., 2015. Remediation of rare earth element pollutants by sorption process using organic natural sorbents. Int. J. Environ. Res. Publ. Health 12, 11278–11287.

Callura, J.C., Perkins, K., Noack, C.W., Washburn, N., Dzombak, D., Karamalidis, A., 2018. Selective adsorption of rare earth elements onto functionalized silica particles. Green Chem. 20, 1515–1526.

Chen, J., Luo, W., Guo, A., Luo, T., Lin, C., Li, H., Jing, L., 2018. Preparation of a novel carboxylate-rich palygorskite as an adsorbent for Ce^{3+} from aqueous solution. J. Colloid Interface Sci. 512, 657–664.

Coppin, F., Berger, G., Bauer, A., Castet, S., Loubet, M., 2002. Sorption of lanthanides on smectite and kaolinite. Chem. Geol. 182, 57–68.

Dada, A., Olalekan, A., Olatunya, A., Dada, O., 2012. Langmuir, Freundlich, Temkin and Dubinin–Radushkevich isotherms studies of equilibrium sorption of Zn2+ unto phosphoric acid modified rice husk. IOSR J. Appl. Chem. 3, 38–45.

Das, N., Das, D., 2013. Recovery of rare earth metals through biosorption: an overview. J. Rare Earths 31, 933–943.

Das, D., Varshini, C.J.S., Das, N., 2014. Recovery of lanthanum (III) from aqueous solution using biosorbents of plant and animal origin: batch and column studies. Miner. Eng. 69, 40–56.

Diniz, V., Volesky, B., 2005a. Biosorption of La, Eu and Yb using *sargassum* biomass. Water Res. 39, 239–247.

Diniz, V., Volesky, B., 2005b. Effect of counterions on lanthanum biosorption by *Sargassum polycystum*. Water Res. 39, 2229–2236.

El-Magied, M.O.A., Galhoum, A.A., Atia, A.A., Tolba, A.A., Maize, M.S., Vincent, T., Guibal, E., 2017. Cellulose and chitosan derivatives for enhanced sorption of erbium (III). Colloid. Surface. Physicochem. Eng. Aspect. 529, 580–593.

Elovich, S.Y., Larinov, O., 1962. Theory of adsorption from solutions of non electrolytes on solid (I) equation adsorption from solutions and the analysis of its simplest form, (II) verification of the equation of adsorption isotherm from solutions. Izv. Akad. Nauk. SSSR, Otd. Khim. Nauk 2, 209–216.

Esposito, A., Pagnanelli, F., Lodi, A., Solisio, C., Veglio, F., 2001. Biosorption of heavy metals by Sphaerotilus natans: an equilibrium study at different pH and biomass concentrations. Hydrometallurgy 60, 129–141.

Feder, T., Kramer, D., 2010. Concern grows over China's dominance of rare-earth metals. Phys. Today 63, 22–28.

Freundlich, H., 1906. Over the adsorption in solution. J. Phys. Chem. 57, 1100–1107.

Galhoum, A.A., Mafhouz, M.G., Abdel-Rehem, S.T., Gomaa, N.A., Atia, A.A., Vincent, T., Guibal, E., 2015. Cysteine-functionalized chitosan magnetic nano-based particles for the recovery of light and heavy rare earth metals: uptake kinetics and sorption isotherms. Nanomaterials 5, 154–179.

Gao, S., Luo, T., Luo, W., 2018. A novel and efficient method on the recovery of nanosized CeO_2 in Ce^{3+} wastewater remediation using modified sawdust as adsorbent. J. Colloid Interface Sci. 512, 629–637.

Gasser, M., Aly, M., 2013. Separation and recovery of rare earth elements from spent nickel–metal-hydride batteries using synthetic adsorbent. Int. J. Miner. Process. 121, 31–38.

Granados-Correa, F., Vilchis-Granados, J., Jiménez-Reyes, M., Quiroz-Granados, L., 2012. Adsorption behaviour of La (III) and Eu (III) ions from aqueous solutions by hydroxyapatite: kinetic, isotherm, and thermodynamic studies. J. Chem. 2013.

Haldorai, Y., Rengaraj, A., Ryu, T., Shin, J., Huh, Y.S., Han, Y.-K., 2015. Response surface methodology for the optimization of lanthanum removal from an aqueous solution using a Fe_3O_4/chitosan nanocomposite. Mater. Sci. Eng., B 195, 20–29.

Hashemian, S., Ardakani, M.K., Salehifar, H., 2013. Kinetics and thermodynamics of adsorption methylene blue onto tea waste/CuFe2O4 composite. Am. J. Anal. Chem. 4, 1–7.

Ho, Y.-S., McKay, G., 1999. Pseudo-second order model for sorption processes. Process Biochem. 34, 451–465.

Hussien, S.S., 2014. Biosorption of lanthanum on Pleurotus ostreatus basidiocarp. Int. J. Biomed. Res. 26–36.

Iftekhar, S., Farooq, M.U., Sillanpää, M., Asif, M.B., Habib, R., 2017a. Removal of Ni (ii) using multi-walled carbon nanotubes electrodes: relation between operating parameters and capacitive deionization performance. Arabian J. Sci. Eng. 42, 235–240.

Iftekhar, S., Srivastava, V., Casas, A., Sillanpää, M., 2017b. Synthesis of novel GA-g-PAM/SiO_2 nanocomposite for the recovery of rare earth elements (REE) ions from aqueous solution. J. Clean. Prod. 170, 251–259.

Iftekhar, S., Srivastava, V., Sillanpää, M., 2017c. Enrichment of lanthanides in aqueous system by cellulose based silica nanocomposite. Chem. Eng. J. 320, 151–159.

Iftekhar, S., Srivastava, V., Sillanpää, M., 2017d. Synthesis and application of LDH intercalated cellulose nanocomposite for separation of rare earth elements (REEs). Chem. Eng. J. 309, 130–139.

Jacinto, J., Henriques, B., Duarte, A., Vale, C., Pereira, E., 2018. Removal and recovery of Critical Rare Elements from contaminated waters by living *Gracilaria gracilis*. J. Hazard Mater. 344, 531–538.

Juang, R.-S., Wu, F.-C., Tseng, R.-L., 1999. Adsorption removal of copper (II) using

chitosan from simulated rinse solutions containing chelating agents. Water Res. 33, 2403–2409.
Kameda, T., Hoshi, K., Yoshioka, T., 2011. Uptake of Sc^{3+} and La^{3+} from aqueous solution using ethylenediaminetetraacetate-intercalated Cu–Al layered double hydroxide reconstructed from Cu–Al oxide. Solid State Sci. 13, 366–371.
Koochaki-Mohammadpour, S.M.A., Torab-Mostaedi, M., Talebizadeh-Rafsanjani, A., Naderi-Behdani, F., 2014. Adsorption isotherm, kinetic, thermodynamic, and desorption studies of lanthanum and dysprosium on oxidized multiwalled carbon nanotubes. J. Dispersion Sci. Technol. 35, 244–254.
Kütahyali, C., Sert, Ş., Cetinkaya, B., Inan, S., Eral, M., 2010. Factors affecting lanthanum and cerium biosorption on *Pinus brutia* leaf powder. Separ. Sci. Technol. 45, 1456–1462.
Lagergren, S., 1898. About the Theory of So-called Adsorption of Soluble Substances.
Langmuir, I., 1918. The adsorption of gases on plane surfaces of glass, mica and platinum. J. Am. Chem. Soc. 40, 1361–1403.
Li, X., Zhang, X., Yang, H., Zhou, Q., 2018. Atomic-layered Mn clusters deposited on palygorskite as powerful adsorbent for recovering valuable REEs from wastewater with superior regeneration stability. J. Colloid Interface Sci. 509, 395–405.
Marwani, H.M., Albishri, H.M., Jalal, T.A., Soliman, E.M., 2013. Study of isotherm and kinetic models of lanthanum adsorption on activated carbon loaded with recently synthesized Schiff's base. Arab. J. Chem. 10, S1032–S1040.
Negrea, A., Gabor, A., Davidescu, C.M., Ciopec, M., Negrea, P., Duteanu, N., Barbulescu, A., 2018. Rare earth elements removal from water using natural polymers. Sci. Rep. 8, 316.
Pal, S., Ghorai, S., Das, C., Samrat, S., Ghosh, A., Panda, A.B., 2012. Carboxymethyl tamarind-g-poly (acrylamide)/silica: a high performance hybrid nanocomposite for adsorption of methylene blue dye. Ind. Eng. Chem. Res. 51, 15546–15556.
Palmieri, M.C., Volesky, B., Garcia, O., 2002. Biosorption of lanthanum using *Sargassum fluitans* in batch system. Hydrometallurgy 67, 31–36.
Ponou, J., Wang, L.P., Dodbiba, G., Okaya, K., Fujita, T., Mitsuhashi, K., Atarashi, T., Satoh, G., Noda, M., 2014. Recovery of rare earth elements from aqueous solution obtained from Vietnamese clay minerals using dried and carbonized parachlorella. J.Environ. Chem. Eng. 2, 1070–1081.
Qing, C., 2010. Study on the adsorption of lanthanum (III) from aqueous solution by bamboo charcoal. J. Rare Earths 28, 125–131.
Rahman, M.M., Khan, S.B., Marwani, H.M., Asiri, A.M., 2014. SnO2–TiO2 nanocomposites as new adsorbent for efficient removal of La (III) ions from aqueous solutions. J. Taiwan Inst. Chem Eng. 45, 1964–1974.
Rahman, M.L., Biswas, T.K., Sarkar, S.M., Yusoff, M.M., Sarjadi, M.S., Arshad, S.E., Musta, B., 2017. Adsorption of rare earth metals from water using a kenaf cellulose-based poly (hydroxamic acid) ligand. J. Mol. Liq. 243, 616–623.
Ramasamy, D.L., Khan, S., Repo, E., Sillanpää, M., 2017a. Synthesis of mesoporous and microporous amine and non-amine functionalized silica gels for the application of rare earth elements (REE) recovery from the waste water-understanding the role of pH, temperature, calcination and mechanism in Light REE and Heavy REE separation. Chem. Eng. J. 322, 56–65.
Ramasamy, D.L., Puhakka, V., Repo, E., Khan, S., Sillanpää, M., 2017b. Coordination and silica surface chemistry of lanthanides (III), scandium (III) and yttrium (III) sorption on 1-(2-pyridylazo)-2-napththol (PAN) and acetylacetone (acac) immobilized gels. Chem. Eng. J. 324, 104–112.
Ramasamy, D.L., Repo, E., Srivastava, V., Sillanpää, M., 2017c. Chemically immobilized and physically adsorbed PAN/acetylacetone modified mesoporous silica for the recovery of rare earth elements from the waste water-comparative and optimization study. Water Res. 114, 264–276.
Ramasamy, D.L., Wojtuś, A., Repo, E., Kalliola, S., Srivastava, V., Sillanpää, M., 2017d. Ligand immobilized novel hybrid adsorbents for rare earth elements (REE) removal from waste water: assessing the feasibility of using APTES functionalized silica in the hybridization process with chitosan. Chem. Eng. J. 330, 1370–1379.
Ramasamy, D.L., Puhakka, V., Iftekhar, S., Wojtuś, A., Repo, E., Hammouda, S.B., Iakovleva, E., Sillanpää, M., 2018a. N-and O-ligand doped mesoporous silica-chitosan hybrid beads for the efficient, sustainable and selective recovery of rare earth elements (REE) from acid mine drainage (AMD): understanding the significance of physical modification and conditioning of the polymer. J. Hazard Mater. 348, 84–91.
Ramasamy, D.L., Puhakka, V., Repo, E., Hammouda, S.B., Sillanpää, M., 2018b. Two-stage selective recovery process of scandium from the group of rare earth elements in aqueous systems using activated carbon and silica composites: dual applications by tailoring the ligand grafting approach. Chem. Eng. J. 341, 351–360.
Ramasamy, D.L., Puhakka, V., Repo, E., Sillanpää, M., 2018c. Selective separation of scandium from iron, aluminium and gold rich wastewater using various amino and non-amino functionalized silica gels–A comparative study. J. Clean. Prod. 170, 890–901.
Redlich, O., Peterson, D.L., 1959. A useful adsorption isotherm. J. Phys. Chem. 63, 1024–1024.
Roy, D., Semsarilar, M., Guthrie, J.T., Perrier, S., 2009. Cellulose modification by polymer grafting: a review. Chem. Soc. Rev. 38, 2046–2064.
Sadovsky, D., Brenner, A., Astrachan, B., Asaf, B., Gonen, R., 2016. Biosorption potential of cerium ions using *Spirulina* biomass. J. Rare Earths 34, 644–652.
Sert, Ş., Kütahyali, C., İnan, S., Talip, Z., Çetinkaya, B., Eral, M., 2008. Biosorption of lanthanum and cerium from aqueous solutions by *Platanus orientalis* leaf powder. Hydrometallurgy 90, 13–18.
Shaver, J., 2015. Rare–the high-stakes race to satisfy our need for the scarcest metals on earth. Can. Field Nat. 129, 203–204. Keith Veronese. 2014.[book review].
Shuxia, X., Zhang, S., Ke, C., Jinfeng, H., Huashan, L., Kun, W., 2011. Biosorption of La^{3+} and Ce^{3+} by agrobacterium sp. HN1. J. Rare Earths 29, 265–270.
Sips, R., 1948. Combined form of Langmuir and Freundlich equations. J. Chem. Phys. 16, 490–495.
Srivastava, V., Sharma, Y., Sillanpää, M., 2015. Green synthesis of magnesium oxide nanoflower and its application for the removal of divalent metallic species from synthetic wastewater. Ceram. Int. 41, 6702–6709.
Sun, X., Peng, B., Ji, Y., Chen, J., Li, D., 2009. Chitosan (chitin)/cellulose composite biosorbents prepared using ionic liquid for heavy metal ions adsorption. AIChE J. 55, 2062–2069.
Tadjarodi, A., Jalalat, V., Zare-Dorabei, R., 2015. Adsorption of La (III) in aqueous systems by N-(2-hydroxyethyl) salicylaldimine-functionalized mesoporous silica. Mater. Res. Bull. 61, 113–119.
Tolba, A.A., Mohamady, S.I., Hussin, S.S., Akashi, T., Sakai, Y., Galhoum, A.A., Guibal, E., 2017. Synthesis and characterization of poly (carboxymethyl)-cellulose for enhanced La (III) sorption. Carbohydr. Polym. 157, 1809–1820.
Torab-Mostaedi, M., 2013. Biosorption of lanthanum and cerium from aqueous solutions using tangerine (Citrus reticulata) peel: equilibrium, kinetic and thermodynamic studies. Chem. Ind. Chem. Eng. Quart. 19, 79–88.
Torab-Mostaedi, M., Asadollahzadeh, M., Hemmati, A., Khosravi, A., 2015. Biosorption of lanthanum and cerium from aqueous solutions by grapefruit peel: equilibrium, kinetic and thermodynamic studies. Res. Chem. Intermed. 41, 559–573.
Toth, J., 1971. State equation of the solid-gas interface layers. Acta Chim. Hung. 69, 311–328.
Varshini, C.J.S., Das, N., 2014. Relevant approach to assess the performance of Biowaste materials for the recovery of lanthanum (III) from aqueous medium. Res. J. Pharm. Biol. Sci. 5, 88–94.
Vijayaraghavan, K., Balasubramanian, R., 2010. Single and binary biosorption of cerium and europium onto crab shell particles. Chem. Eng. J. 163, 337–343.
Vijayaraghavan, K., Mahadevan, A., Joshi, U.M., Balasubramanian, R., 2009. An examination of the uptake of lanthanum from aqueous solution by crab shell particles. Chem. Eng. J. 152, 116–121.
Vijayaraghavan, K., Sathishkumar, M., Balasubramanian, R., 2011. Interaction of rare earth elements with a brown marine alga in multi-component solutions. Desalination 265, 54–59.
Wan, S., Wang, S., Li, Y., Gao, B., 2017. Functionalizing biochar with Mg–Al and Mg–Fe layered double hydroxides for removal of phosphate from aqueous solutions. J. Ind. Eng. Chem. 47, 246–253.
Wang, M., Li, X., Hua, W., Shen, L., Yu, X., Wang, X., 2016a. Electrospun Poly (acrylic acid)/silica hydrogel nanofibers scaffold for highly efficient adsorption of Lanthanide ions and its photoluminescence performance. ACS Appl. Mater. Interfaces 8, 23995–24007.
Wang, Y.-Y., Lu, H.-H., Liu, Y.-X., Yang, S.-M., 2016b. Ammonium citrate-modified biochar: an adsorbent for La (III) ions from aqueous solution. Colloid. Surface. Physicochem. Eng. Aspect. 509, 550–563.
Weber, W.J., Morris, J.C., 1963. Kinetics of adsorption on carbon from solution. J. Sanit. Eng. Div. 89, 31–60.
Wu, D., Zhao, J., Zhang, L., Wu, Q., Yang, Y., 2010. Lanthanum adsorption using iron oxide loaded calcium alginate beads. Hydrometallurgy 101, 76–83.
Wu, D., Zhang, L., Wang, L., Zhu, B., Fan, L., 2011. Adsorption of lanthanum by magnetic alginate-chitosan gel beads. J. Chem. Technol. Biotechnol. 86, 345–352.
Wu, D., Zhu, C., Chen, Y., Zhu, B., Yang, Y., Wang, Q., Ye, W., 2012. Preparation, characterization and adsorptive study of rare earth ions using magnetic GMZ bentonite. Appl. Clay Sci. 62, 87–93.
Wu, D., Sun, Y., Wang, Q., 2013. Adsorption of lanthanum (III) from aqueous solution using 2-ethylhexyl phosphonic acid mono-2-ethylhexyl ester-grafted magnetic silica nanocomposites. J. Hazard Mater. 260, 409–419.
Xiaoqi, S., Huimin, L., Mahurin, S.M., Rui, L., Xisen, H., Sheng, D., 2016. Adsorption of rare earth ions using carbonized polydopamine nano carbon shells. J. Rare Earths 34, 77–82.
Xie, J., Lin, Y., Li, C., Wu, D., Kong, H., 2015. Removal and recovery of phosphate from water by activated aluminum oxide and lanthanum oxide. Powder Technol. 269, 351–357.
Xu, X., Jiang, X.-Y., Jiao, F.-P., Chen, X.-Q., Yu, J.-G., 2018. Tunable assembly of porous three-dimensional graphene oxide-corn zein composites with strong mechanical properties for adsorption of rare earth elements. J. Taiwan Inst. Chem Eng. 85, 106–114.
Zhang, S., Xu, F., Wang, Y., Zhang, W., Peng, X., Pepe, F., 2013. Silica modified calcium alginate–xanthan gum hybrid bead composites for the removal and recovery of Pb (II) from aqueous solution. Chem. Eng. J. 234, 33–42.
Zhang, L., Zeng, Y., Cheng, Z., 2016. Removal of heavy metal ions using chitosan and modified chitosan: a review. J. Mol. Liq. 214, 175–191.
Zhao, F., Repo, E., Meng, Y., Wang, X., Yin, D., Sillanpää, M., 2016a. An EDTA-β-cyclodextrin material for the adsorption of rare earth elements and its application in preconcentration of rare earth elements in seawater. J. Colloid Interface Sci. 465, 215–224.
Zhao, Z., Sun, X., Dong, Y., 2016b. Synergistic effect of doped functionalized ionic liquids in silica hybrid material for rare earth adsorption. Ind. Eng. Chem. Res. 55, 2221–2229.
Zhao, F., Repo, E., Song, Y., Yin, D., Hammouda, S.B., Chen, L., Kalliola, S., Tang, J., Tam, K.C., Sillanpää, M., 2017. Polyethylenimine-cross-linked cellulose

nanocrystals for highly efficient recovery of rare earth elements from water and a mechanism study. Green Chem. 19, 4816–4828.
Zhou, Q., Yang, H., Yan, C., Luo, W., Li, X., Zhao, J., 2016. Synthesis of carboxylic acid functionalized diatomite with a micro-villous surface via UV-induced graft polymerization and its adsorption properties for Lanthanum (III) ions. Colloid. Surface. Physicochem. Eng. Aspect. 501, 9–16.
Zhou, B., Li, Z., Chen, C., 2017. Global potential of rare earth resources and rare earth demand from clean technologies. Minerals 7, 203.
Zhu, Y., Zheng, Y., Wang, A., 2015a. Preparation of granular hydrogel composite by the redox couple for efficient and fast adsorption of La (III) and Ce (III). J.Environ. Chem. Eng. 3, 1416–1425.
Zhu, Y., Zheng, Y., Wang, A., 2015b. A simple approach to fabricate granular adsorbent for adsorption of rare elements. Int. J. Biol. Macromol. 72, 410–420.
Zhu, Y., Wang, W., Zheng, Y., Wang, F., Wang, A., 2016. Rapid enrichment of rare-earth metals by carboxymethyl cellulose-based open-cellular hydrogel adsorbent from HIPEs template. Carbohydr. Polym. 140, 51–58.

ACTA UNIVERSITATIS LAPPEENRANTAENSIS

818. VASILYEV, FEDOR. Model-based design and optimisation of hydrometallurgical liquid-liquid extraction processes. 2018. Diss.

819. DEMESA, ABAYNEH. Towards sustainable production of value-added chemicals and materials from lignocellulosic biomass: carboxylic acids and cellulose nanocrystals. 2018. Diss.

820. SIKANEN, EERIK. Dynamic analysis of rotating systems including contact and thermal-induced effects. 2018. Diss.

821. LIND, LOTTA. Identifying working capital models in value chains: Towards a generic framework. 2018. Diss.

822. IMMONEN, KIRSI. Ligno-cellulose fibre poly(lactic acid) interfaces in biocomposites. 2018. Diss.

823. YLÄ-KUJALA, ANTTI. Inter-organizational mediums: current state and underlying potential. 2018. Diss.

824. ZAFARI, SAHAR. Segmentation of partially overlapping convex objects in silhouette images. 2018. Diss.

825. MÄLKKI, HELENA. Identifying needs and ways to integrate sustainability into energy degree programmes. 2018. Diss.

826. JUNTUNEN, RAIMO. LCL filter designs for paraller-connected grid inverters. 2018. Diss.

827. RANAEI, SAMIRA. Quantitative approaches for detecting emerging technologies. 2018. Diss.

828. METSO, LASSE. Information-based industrial maintenance - an ecosystem perspective. 2018. Diss.

829. SAREN, ANDREY. Twin boundary dynamics in magnetic shape memory alloy Ni-Mn-Ga five-layered modulated martensite. 2018. Diss.

830. BELONOGOVA, NADEZDA. Active residential customer in a flexible energy system - a methodology to determine the customer behaviour in a multi-objective environment. 2018. Diss.

831. KALLIOLA, SIMO. Modified chitosan nanoparticles at liquid-liquid interface for applications in oil-spill treatment. 2018. Diss.

832. GEYDT, PAVEL. Atomic Force Microscopy of electrical, mechanical and piezo properties of nanowires. 2018. Diss.

833. KARELL, VILLE. Essays on stock market anomalies. 2018. Diss.

834. KURONEN, TONI. Moving object analysis and trajectory processing with applications in human-computer interaction and chemical processes. 2018. Diss.

835. UNT, ANNA. Fiber laser and hybrid welding of T-joint in structural steels. 2018. Diss.

836. KHAKUREL, JAYDEN. Enhancing the adoption of quantified self-tracking wearable devices. 2018. Diss.

837. SOININEN, HANNE. Improving the environmental safety of ash from bioenergy production plants. 2018. Diss.

838. GOLMAEI, SEYEDMOHAMMAD. Novel treatment methods for green liquor dregs and enhancing circular economy in kraft pulp mills. 2018. Diss.

839. GERAMI TEHRANI, MOHAMMAD. Mechanical design guidelines of an electric vehicle powertrain. 2019. Diss.

840. MUSIIENKO, DENYS. Ni-Mn-Ga magnetic shape memory alloy for precise high-speed actuation in micro-magneto-mechanical systems. 2019. Diss.

841. BELIAEVA, TATIANA. Complementarity and contextualization of firm-level strategic orientations. 2019. Diss.

842. EFIMOV-SOINI, NIKOLAI. Ideation stage in computer-aided design. 2019. Diss.

843. BUZUKU, SHQIPE. Enhancement of decision-making in complex organizations: A systems engineering approach. 2019. Diss.

844. SHCHERBACHEVA, ANNA. Agent-based modelling for epidemiological applications. 2019. Diss.

845. YLIJOKI, OSSI. Big data - towards data-driven business. 2019. Diss.

846. KOISTINEN, KATARIINA. Actors in sustainability transitions. 2019. Diss.

847. GRADOV, DMITRY. Experimentally validated numerical modelling of reacting multiphase flows in stirred tank reactors. 2019. Diss.

848. ALMPANOPOULOU, ARGYRO. Knowledge ecosystem formation: an institutional and organisational perspective. 2019. Diss.

849. AMELI, ALIREZA. Supercritical CO2 numerical modelling and turbomachinery design. 2019. Diss.

850. RENEV, IVAN. Automation of the conceptual design process in construction industry using ideas generation techniques. 2019. Diss.

851. AVRAMENKO, ANNA. CFD-based optimization for wind turbine locations in a wind park. 2019. Diss.

852. RISSANEN, TOMMI. Perspectives on business model experimentation in internationalizing high-tech companies. 2019. Diss.

853. HASSANZADEH, AIDIN. Advanced techniques for unsupervised classification of remote sensing hyperspectral images. 2019. Diss.

854. POPOVIC, TAMARA. Quantitative indicators of social sustainability applicable in process systems engineering. 2019. Diss.

855. RAMASAMY, DEEPIKA. Selective recovery of rare earth elements from diluted aqueous streams using N- and O –coordination ligand grafted organic-inorganic hybrid composites. 2019. Diss.

ISBN 978-952-335-378-7
ISBN 978-952-335-379-4 (PDF)
ISSN-L 1456-4491
ISSN 1456-4491
Lappeenranta 2019